Plasmonic Nanostructures and Film Crystallization in Perovskite Solar Cells

Michael Saliba

Department of Physics

University of Oxford

A thesis submitted for the degree of

Doctor of Philosophy

St Catherine's College

Trinity 2014

Plasmonic Nanostructures and Film Crystallization in Perovskite Solar Cells

Michael Saliba, St Catherine's College, Oxford, Trinity 2014

A thesis submitted for the degree of *Doctor of Philosophy*

Abstract

The aim of this thesis is to develop a deeper understanding and the technology in the nascent field of solid-state organic-inorganic perovskite solar cells.

In recent years, perovskite materials have emerged as a low-cost, thin-film technology with efficiencies exceeding 16% challenging the quasi-paradigm that high efficiency photovoltaics must come at high costs. This thesis investigates perovskite solar cells in more detail with a focus on incorporating plasmonic nanostructures and perovskite film formation.

Chapter 1 motivates the present work further followed by Chapter 2 which offers a brief background for solar cell fabrication and characterisation, perovskites in general, perovskite solar cells in specific, and plasmonics.

Chapter 3 presents the field of plasmonics including simulation methods for various core-shell nanostructures such as gold-silica and silver-titania nanoparticles.

The following Chapters 4 and 5 analyze plasmonic core-shell metal-dielectric nanoparticles embedded in perovskite solar cells. It is shown that using gold@silica or silver@titania NPs results in enhanced photocurrent and thus increased efficiency. After photoluminescence studies, this effect was attributed to an unexpected phenomenon in solar cells in which a lowered exciton binding energy generates a higher fraction of free charge. Embedding thermally unstable silver NPs required a low-temperature fabrication method which would not melt the Ag NPs. This work offers a new general direction for temperature sensitive elements.

In Chapters 6 and 7, perovskite film formation is studied. Chapter 6 shows the existence of a previously unknown crystalline precursor state and an improved surface coverage by introducing a ramped annealing procedure. Based on this, Chapter 7 investigates different perovskite annealing protocols. The main finding was that an additional 130°C flash annealing step changed the film crystallinity dramatically and yielded a higher orientation of the perovskite crystals. The according solar cells showed an increased photocurrent attributed to a decrease in charge carrier recombination at the grain boundaries.

Chapter 8 presents on-going work showing noteworthy first results for silica scaffolds, and layered, 2D perovskite structures for application in solar cells.

Acknowledgements

First of all, I want to thank Henry Snaith for his guidance, help, and never-ending stream of ideas. It was a thoroughly enjoyable experience and I am very grateful for having received such a great opportunity. Oxford is a fantastic place for solar cell research and it was a true privilege to be part of such a great team.

I want to thank the entire Oxford group (past and present) in no particular order: Clare Moloney, Simone Guarnera, Konrad Wojciechowski, James Ball, Sam Stranks, Mingzhen Liu, Severin Habisreutinger, Jacob Wang, Giles Eperon, Nakita Noel, Pablo Docampo, Tomas Leijtens, Michael Lee, Derek Hollman, James Kirkpatrick, Golnaz Sadoughi, Robert Gunning, Edward Crossland, Martina Congiu, Alba Pellaroque, Jiewei Liu, Agnese Abrusci, Jin Zhang, Andy Hey, Sandeep Pathak, Joël Teuscher.

Many thanks to my friends/colleagues/collaborators all over the world or in Oxford who helped me accomplish this work, gave valuable insight, and contributed in so many ways. I could not have done it without you. Just to mention a few (without being complete): Wei Zhang for the many helpful discussions and the fruitful collaboration over the years. Antonio Abate for the many espresso/cappuccino sessions. Kwan Tan who knows every possible route to the Oxford clean room now and paid back in full when I visited in Cornell. Giulia Granchini for her help at the beginning of my DPhil. Yao Sun for her magic synthesis skills. Michael Brown for proofreading. Maximilian Hoerantner for proofreading. Many thanks also to Andreas C. Lazar for his firm pro-existence stance.

I want to thank Ulrich Wiesner from Cornell University for having hosted me in his research group in 2012. It was a great opportunity to learn and develop! My time there was very enjoyable and productive thanks to the entire group: Xian Shi, Hiroaki Sai, Jörg Werner, Zihui Li, Tobias Hoheisel, Bruce Spencer, Sandra Cabanas Polo, Srikant Iyer, Rachel Dorin, Yibei Gu, Juho Song, Jennifer Drewes, Christina Cowman-Eggert, Kai Ma.

Many thanks to the Heinrich-Böll-Foundation for past support and St Catherine's College for the Light Senior Scholarship.

I would like to thank my family. In specific, my niece Sofia Elisabeth Saliba who braved much hardship at a very young age and is an inspiration to us all.

Thanks to my friends who had to suffer through my lengthy phone calls and were always there for me. (48 hours!)

Finally, I want to thank Kathrin Richter who, to borrow somebody else's words, must have the patience of an angel.

Contents

List of Figures

List of Tables

CHAPTER 1

Introduction

Motivation

The aim of this thesis is to develop a deeper understanding and the technology in the nascent field of perovskite solar cells. The general motivation to advance regenerative energy sources can be understood from Figure 1.1 which shows the overall primary energy production in 1973 and 2011 [1] documenting a doubling of production capacity in four decades and future projections predicting an ever increasing demand for more energy. Currently, the main energy source worldwide are fossil fuels (coal, oil, natural gas) with a contribution of over 80% which also come with a relatively abundant reserve [1]. Unfortunately, fossil energy also produces massive carbon dioxide emissions which are the main driver of global warming and climate change. A sustainable energy strategy for the generations to come has to drastically reduce the consumption of fossil fuels [2, 3]. Alternatively, nuclear power is considered because of the reduced carbon footprint. Accordingly, many countries have large nuclear sectors like the USA, France, Japan, Russia, the United Kingdom, China, Germany, etc. However, fission material is limited and highly toxic. Nuclear power plants are inherently risky because of the danger of a devastating chain reaction from a core meltdown. In the extreme case of the Chernobyl disaster, a radioactive dust cloud was released which encompassed multiple countries [4]. Even with very safe reactor types it remains challenging to build long-term nuclear power facilities such that they can withstand natural disaster, human error, or intentional manipulation/attack. Moreover, safe storage of nuclear waste over thousands of years is an unresolved (and expensive) problem. The growing public concern with fission energy has led many countries to reevaluate or even withdraw completely from nuclear energy.

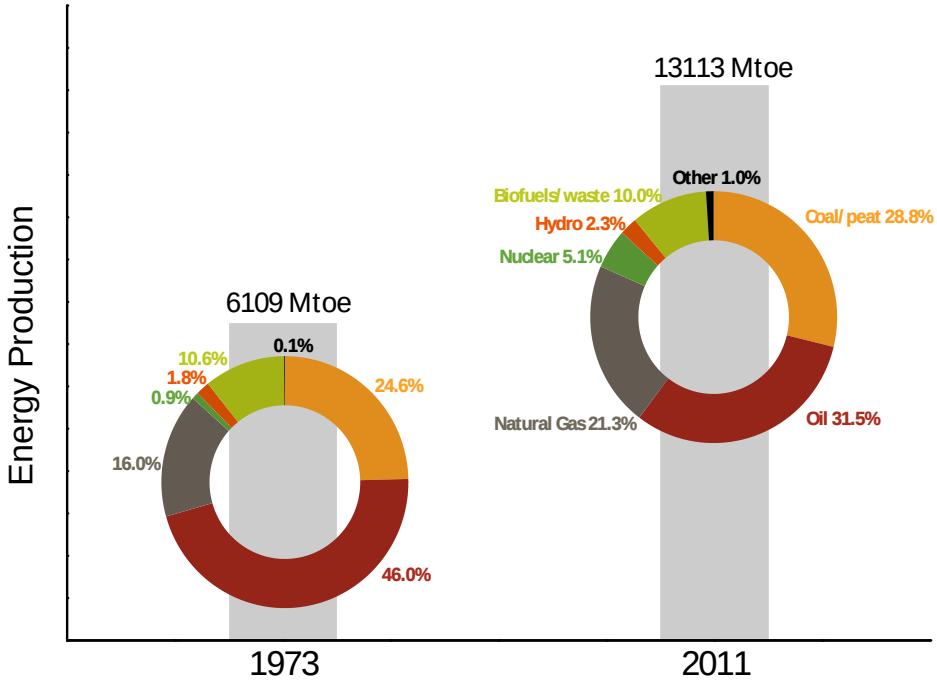

Fig. 1.1 Worldwide primary energy production in 1973 and 2011 expressed in the energy unit Mtoe (mega tonne of oil equivalent). The inset pie charts indicate the fraction of the different energy sources. The data is adapted from *Key World Energy Statistics 2013* published by the International Energy Agency [1].

A growing energy segment is from alternative energy sources like biofuels and hydroelectricity. As for biofuels, carbon neutrality remains doubtful and it is politically contentious to create a system where energy demand may cause food scarcity.

Hydroelectricity is of high interest because of its reliability, favourable carbon footprint, and profitability which need careful balancing against possible shortcomings such as endangering of ground water, damage to the ecosystem, loss of land, relocation of people, and the risk of facility failure (which can be catastrophic for large dams). Nevertheless, nowadays the main constraint for the very mature technology of hydroelectricity is further upscaling because of the limited amount of remaining locations (with suitable terrain), and thus reaching the economic point of diminishing returns.

So far all discussed energy sources have disadvantages of varying degrees. This motivates research on regenerative energy sources with reduced systemic risk and favourable carbon footprint directing the attention to the last remaining item in Figure 1.1: “Others” comprising geothermal, wind, ocean, and solar energy. While all approaches are under intense investigation, one aspect is intriguing: the sun is for free and the most abundant energy source in the solar system. The amount of sun light received on earth for only one hour is already the equivalent of the yearly energy output for the entire planet. Thus, tapping into even a small fraction of this potential could provide a long-term energy solution with a low carbon footprint. It is the aim of this thesis to contribute to this vision by investigating photovoltaic technology, i.e. the direct conversion of sun light into electricity.

Photovoltaics

Currently, inorganic single-crystal silicon solar cells are very efficient at utilizing the photoelectric effect with power conversion efficiencies (PCEs) up to 25% [5]. Mass production and extensive research have brought the price down but reductions are more challenging to achieve as costly high temperature steps for purification are needed in the fabrication process. Moreover, efficiencies are getting closer to the theoretical upper limit of about 33% for a single p-n junction silicon solar cell known as the Shockley-Queisser limit [6, 7].

It is derived by modelling the solar spectrum as a 6000 K black body radiator with missing absorption bands from the earth's atmosphere. Photons with energies higher than the solar cell's band gap cannot contribute to photoelectricity by more than the band gap with the excess energy turned into heat during thermal relaxation of the "hot electrons". The calculations relate the maximum attainable efficiency to the used band gap. From this the upper limit for a p-n junction is reached at ~33% efficiency for a band gap of 1.34 eV. The Shockley-Queisser limit applies for a single bandgap absorber and can be exceeded by multijunction (tandem) solar cells [8], light concentration [9], photon upconversion [10], or hot electron capture [11].

Among the most discussed inexpensive thin-film photovoltaic approaches are amorphous silicon with efficiencies of ~10% [12], Copper indium gallium selenide (CIGS) with ~20% [13], and cadmium telluride (CdTe) solar cells with ~19% [14]. Certified record efficiencies for various PV technologies can be found in the National Renewable Energy Laboratory (NREL) chart in Figure 1.2.

All these solar cell types have been investigated for many decades now with some of them showing great potential for commercialisation. It also seems that efficiency increases and cost reduction are becoming more and more gradual which may indicate that a certain threshold has been reached. However, more research is required for a fuller picture in order to provide as many approaches as possible to build the infrastructure for cost-efficient photovoltaic systems.

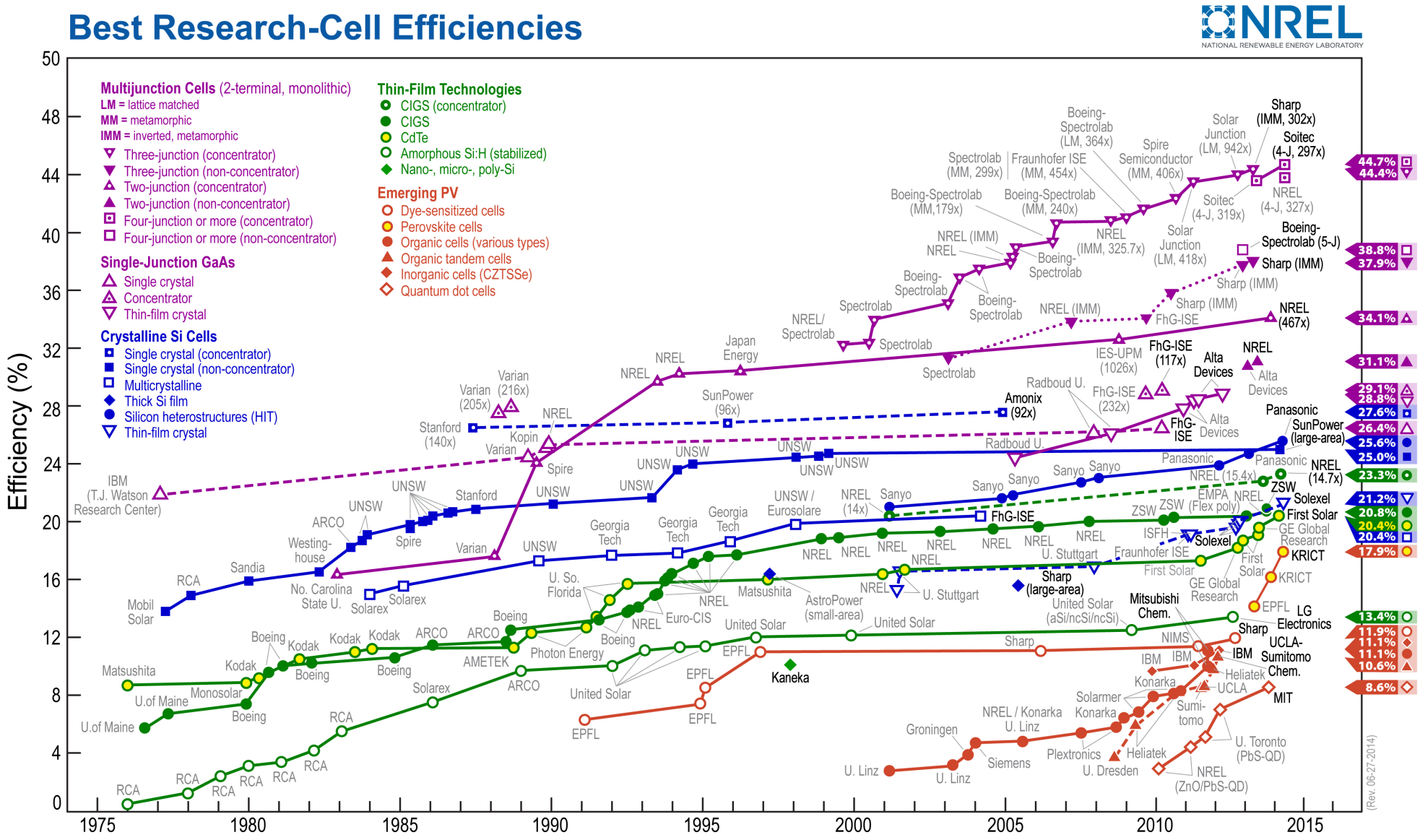

Fig. 1.2 Certified efficiencies for various photovoltaic technologies over the past 4 decades. This chart is issued by the National Renewable Energy Laboratory (NREL), USA [15].

Plasmonics

One strategy to improve solar cells is by inclusion of plasmonic nanostructures with a decreased volume/surface over reducing size. Fundamentally, at smaller length scales surface properties of materials determine the overall physical behaviour. This can be observed very prominently in the optical properties which can differ radically from the bulk material. For example, for millennia the colour play of stained church windows amazed people all over the world. Understanding of this came much later upon the realization that the glass was imbued with small metallic colloids which interacted with light in unexpected ways because of surface properties.

Incoming light can collectively excite the surface electron gas of such metallic nanoparticles into localized surface plasmon resonance (LSPR) modes. The plasmonic near-field exhibits strong local field enhancement.

Plasmonic nanostructures have the potential for fundamental enhancements in solar cell efficiency which could help to approach or even surpass the 1 sun Shockley-Queisser limit. Proposed strategies involve increasing the overall light harvest through extending the optical pathlength of incoming light, enhance absorption at particular wavelengths (antenna effect), or extend absorption of the solar spectrum which is otherwise out of reach [16–20].

Perovskite Solar Cells Overview

In recent years, "perovskite solar cells" have emerged in a spectacular fashion.

They are mainly comprised of solution-processable alkylammonium metal halides, such as methylammonium lead triiodide $CH_3NH_3PbI_3$ first synthesized by Weber et al. in 1978 [21]. The first photovoltaic application of this material was in a liquid dye-sensitized solar cell (DSSC) by Kojima et al. in 2009 [22] with PCEs of 3.8%. In only another four years spectacular improvements were made resulting in PCEs of over 15% [22–41]. Such rapid progress was highly unexpected and many research groups have now moved towards contributing to this new research field. This class of solar cells may challenge the long standing quasi-paradigm that high efficiency photovoltaics must come at high costs.

The main focus of this thesis is to advance the knowledge in the emerging field of perovskite solar cell research. To this end, Figure 1.3 shows an SEM cross section of a typical perovskite solar cell starting with glass which is covered with a transparent electron accepting layer (fluorine-doped tin oxide (FTO)) and a hole-blocking TiO_2 compact layer. An insulating mesoporous alumina scaffold infiltrated and capped with perovskite follows.

This is the photoactive area where light gets absorbed and transformed into electrons and holes. The electrons are carried through the perovskite to the (electron conducting) FTO layer. Holes are transported through a solid state hole transporter to the silver electrodes on the top.

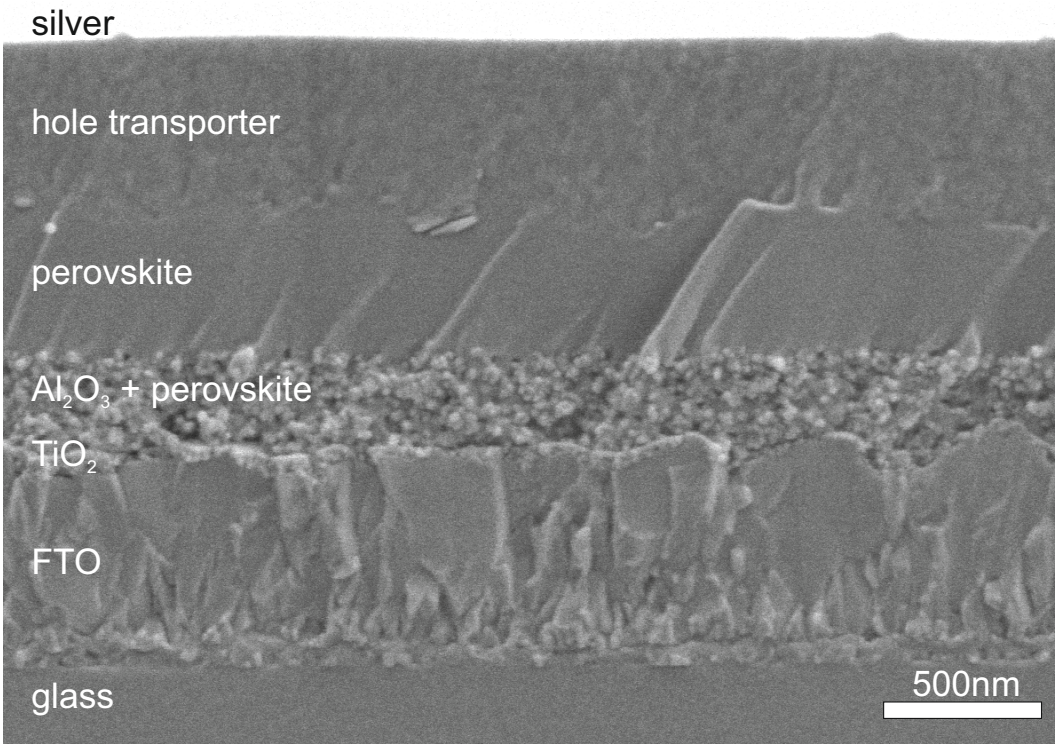

Fig. 1.3 SEM cross section of a perovskite solar cell with a mesoporous alumina layer. The scale bar is 500 nm.

In a nutshell, the main findings in this thesis were focused on embedding plasmonic core-shell nanoparticles (Au@SiO_2 or Ag@TiO_2) in the mesoporous scaffold; and the film formation of perovskite (with and without a scaffold) under different annealing parameters. After putting the object of study in plain sight, the outline of this thesis is as follows.

Thesis outline

Chapter 2 offers a brief background for solar cell fabrication and characterisation, perovskites in general, perovskite solar cells in specific, and plasmonics.

In Chapter 3 plasmonic behaviour of metal nanostructures is discussed. At first, a derivation for the optical cross sections is presented. Furthermore, the multiple multipole method (MMP) is introduced, i.e. a semi-analytical simulation method for solving the Maxwell equations numerically, with which the previously derived cross sections can be calculated. The simulation results for various core-shell nanostructures are shown and calculations are used for quality control of synthesized NPs. It is demonstrated how gold nanoparticles can act as sensors for the refractive index of an unknown solution. Also, simulations for gold-silica and silver-titania NPs at first buried in titania and then in a realistic DSSC photoactive layer are shown followed by an analysis of absorption and scattering behaviour.

In Chapter 4, gold-silica core-shell nanoparticles are embedded into perovskite solar cells resulting in a significant enhancement in photocurrent which, however, does not stem from enhanced light absorption. After a careful photoluminescence study, the increase in charge generation is attributed to a previously unexpected mechanism of reduced exciton binding energy in the presence of nanoparticles. This work was published in [32].

Based on this, in Chapter 5, thermally unstable silver-titania nanoparticles are embedded into perovskite solar cells. The fabrication is challenging as the previous fabrication procedure involved high-temperature steps which melt silver nanoparticles. Instead, a new low-temperature protocol is used and again an increase in photocurrent is observed.

In Chapter 6, perovskite thin-film formation is analysed with gracing incident wide angle x-ray spectroscopy (GIWAXS). The existence of a crystalline precursor state is discovered using different annealing protocols. Additionally, a slow ramp procedure is shown to improve perovskite film coverage. This work was published in [42].

Chapter 7 is motivated by observations made in Chapter 6. Different annealing protocols are used to show that a short flash annealing step at 130°C induces highly orientated perovskite crystals which are beneficial for device performance. This work was published in [43].

The following Chapter 8 presents on-going projects which show noteworthy first results for layered 2D perovskite structures as viable solar cell materials.

Finally, Chapter 9 presents a conclusion.

References

[1] *Key World Energy Statistics*. Paris: International Energy Agency, 2013.

[2] S. Solomon, *Climate change 2007-the physical science basis: Working group I contribution to the fourth assessment report of the IPCC*, vol. 4. Cambridge University Press, 2007.

[3] N. Nakicenovic and R. Swart, "Special report on emissions scenarios (sres)," *Intergovernmental Panel on Climate Change (IPCC)*, vol. 599, 2000.

[4] A. P. Møller and T. A. Mousseau, "Biological consequences of Chernobyl: 20 years on," *Trends in ecology & evolution*, vol. 21, no. 4, pp. 200–207, 2006.

[5] M. A. Green, "The path to 25% silicon solar cell efficiency: History of silicon cell evolution," *Progress in Photovoltaics: Research and Applications*, vol. 17, pp. 183–189, May 2009.

[6] W. Shockley and H. J. Queisser, "Detailed balance limit of efficiency of p-n junction solar cells," *Journal of Applied Physics*, vol. 32, no. 3, p. 510, 1961.

[7] H. J. Snaith, "Estimating the maximum attainable efficiency in dye-sensitized solar cells," *Advanced Functional Materials*, vol. 20, no. 1, pp. 13–19, 2010.

[8] A. De Vos, "Detailed balance limit of the efficiency of tandem solar cells," *Journal of Physics D: Applied Physics*, vol. 13, no. 5, p. 839, 1980.

[9] R. King, D. Law, K. Edmondson, C. Fetzer, G. Kinsey, H. Yoon, R. Sherif, and N. Karam, "40% efficient metamorphic GaInP/GaInAs/Ge multijunction solar cells," *Applied physics letters*, vol. 90, no. 18, pp. 183516–183516, 2007.

[10] T. Trupke, M. A. Green, and P. Würfel, "Improving solar cell efficiencies by up-conversion of sub-band-gap light," *Journal of Applied Physics*, vol. 92, no. 7, pp. 4117–4122, 2002.

[11] G. Conibeer, M. Green, R. Corkish, Y. Cho, E.-C. Cho, C.-W. Jiang, T. Fangsuwannarak, E. Pink, Y. Huang, T. Puzzer, T. Trupke, B. Richards, A. Shalav, and K. lung Lin, "Silicon nanostructures for third generation photovoltaic solar cells," *Thin Solid Films*, vol. 511-512, no. 0, pp. 654 – 662, 2006. EMSR 2005 - Proceedings of Symposium F on Thin Film and Nanostructured Materials for Photovoltaics EMRS 2005- Symposium F EMSR 2005 - Proceedings of Symposium F on Thin Film and Nanostructured Materials for Photovoltaics.

[12] M. A. Green, K. Emery, Y. Hishikawa, W. Warta, and E. D. Dunlop, "Solar cell efficiency tables (version 39)," *Progress in Photovoltaics: Research and Applications*, vol. 20, no. 1, pp. 12–20, 2012.

[13] S. Niki, M. Contreras, I. Repins, M. Powalla, K. Kushiya, S. Ishizuka, and K. Matsubara, "CIGS absorbers and processes," *Progress in Photovoltaics: Research and Applications*, vol. 18, no. 6, pp. 453–466, 2010.

[14] L. Kranz, S. Buecheler, and A. N. Tiwari, "Technological status of CdTe photovoltaics," *Solar Energy Materials and Solar Cells*, vol. 119, no. 0, pp. 278 – 280, 2013. Thin-film Photovoltaic Solar Cells.

[15] "National Renewable Energy Laboratory (NREL)." `http://www.nrel.gov/ncpv/images/efficiency_chart.jpg`, 2014. Accessed 27-July-2014.

[16] M. D. Brown, T. Suteewong, R. S. S. Kumar, V. D'Innocenzo, A. Petrozza, M. M. Lee, U. Wiesner, and H. J. Snaith, "Plasmonic dye-sensitized solar cells using core-shell metal-insulator nanoparticles," *Nano Letters*, vol. 11, no. 2, pp. 438–445, 2011.

[17] H. A. Atwater and A. Polman, "Plasmonics for improved photovoltaic devices.," *Nature Materials*, vol. 9, no. 3, pp. 205–13, 2010.

[18] X. H. Li, W. C. H. Choy, L. J. Huo, F. X. Xie, W. E. I. Sha, B. F. Ding, X. Guo, Y. F. Li, J. H. Hou, J. B. You, and Y. Yang, "Dual plasmonic nanostructures for high performance inverted organic solar cells," *Advanced Materials*, vol. 24, no. 22, pp. 3046–3052, 2012.

[19] D. M. Schaadt, B. Feng, and E. T. Yu, "Enhanced semiconductor optical absorption via surface plasmon excitation in metal nanoparticles," *Applied Physics Letters*, vol. 86, no. 6, 2005.

[20] J. Yang, J. You, C.-C. Chen, W.-C. Hsu, H.-r. Tan, X. W. Zhang, Z. Hong, and Y. Yang, "Plasmonic polymer tandem solar cell," *ACS Nano*, vol. 5, no. 8, pp. 6210–6217, 2011.

[21] D. Weber, "$CH_3NH_3PbX_3$, A Pb(II)-System with Cubic Perovskite Structure," *Zeitschrift fur Naturforschung Section B-A Journal of Chemical Sciences*, vol. 33, no. 12, pp. 1443–1445, 1978.

[22] A. Kojima, K. Teshima, Y. Shirai, and T. Miyasaka, "Organometal halide perovskites as visible-light sensitizers for photovoltaic cells," *Journal of the American Chemical Society*, vol. 131, pp. 6050–6051, Apr. 2009.

[23] J.-H. Im, C.-R. Lee, J.-W. Lee, S.-W. Park, and N.-G. Park, "6.5% efficient perovskite quantum-dot-sensitized solar cell," *Nanoscale*, vol. 3, no. 10, pp. 4088–4093, 2011.

[24] H. S. Kim, C. R. Lee, J. H. Im, K. B. Lee, T. Moehl, A. Marchioro, S. J. Moon, R. Humphry-Baker, J. H. Yum, J. E. Moser, M. Gratzel, and N. G. Park, "Lead iodide perovskite sensitized all-solid-state submicron thin film mesoscopic solar cell with efficiency exceeding 9%," *Scientific Reports*, vol. 2, 2012.

[25] J. H. Noh, S. H. Im, J. H. Heo, T. N. Mandal, and S. I. Seok, "Chemical management for colorful, efficient, and stable inorganic-organic hybrid nanostructured solar cells," *Nano Letters*, vol. 13, no. 4, pp. 1764–1769, 2013.

[26] L. Etgar, P. Gao, Z. Xue, Q. Peng, A. K. Chandiran, B. Liu, M. K. Nazeeruddin, and M. Grätzel, "Mesoscopic $CH_3NH_3PbI_3/TiO_2$ Heterojunction Solar Cells," *Journal of the American Chemical Society*, vol. 134, pp. 17396–17399, Oct. 2012.

[27] J. H. Heo, S. H. Im, J. H. Noh, T. N. Mandal, C.-S. Lim, J. A. Chang, Y. H. Lee, H.-j. Kim, A. Sarkar, N. K., M. Gratzel, and S. I. Seok, "Efficient inorganic-organic hybrid heterojunction solar cells containing perovskite compound and polymeric hole conductors," *Nature Photonics*, vol. 7, pp. 486–491, June 2013.

[28] H.-S. Kim, I. Mora-Sero, V. Gonzalez-Pedro, F. Fabregat-Santiago, E. J. Juarez-Perez, N.-G. Park, and J. Bisquert, "Mechanism of carrier accumulation in perovskite thin-absorber solar cells," *Nat Commun*, vol. 4, July 2013.

[29] M. M. Lee, J. Teuscher, T. Miyasaka, T. N. Murakami, and H. J. Snaith, "Efficient Hybrid Solar Cells Based on Meso-Superstructured Organometal Halide Perovskites," *Science*, vol. 338, pp. 643–647, Nov. 2012.

[30] J. M. Ball, M. M. Lee, A. Hey, and H. J. Snaith, "Low-temperature processed meso-superstructured to thin-film perovskite solar cells," *Energy & Environmental Science*, vol. 6, no. 6, pp. 1739–1743, 2013.

[31] E. Edri, S. Kirmayer, D. Cahen, and G. Hodes, "High Open-Circuit Voltage Solar Cells Based on Organic/Inorganic Lead Bromide Perovskite," *The Journal of Physical Chemistry Letters*, vol. 4, no. 6, pp. 897–902, 2013.

[32] W. Zhang, M. Saliba, S. D. Stranks, Y. Sun, X. Shi, U. Wiesner, and H. J. Snaith, "Enhancement of perovskite-based solar cells employing core-shell metal nanoparticles," *Nano Letters*, vol. 13, no. 9, pp. 4505–10, 2013. 23947387.

[33] G. E. Eperon, V. M. Burlakov, P. Docampo, A. Goriely, and H. J. Snaith, "Morphological Control for High Performance, Solution-Processed Planar Heterojunction Perovskite Solar Cells," *Advanced Functional Materials*, vol. 24, no. 1, pp. 151–157, 2014.

[34] S. Colella, E. Mosconi, P. Fedeli, A. Listorti, F. Gazza, F. Orlandi, P. Ferro, T. Besagni, A. Rizzo, G. Calestani, G. Gigli, F. De Angelis, and R. Mosca, "Mapbi$_{3-x}$cl$_x$ mixed halide perovskite for hybrid solar cells: The role of chloride as dopant on the transport and structural properties," *Chemistry of Materials*, vol. 25, pp. 4613–4618, Oct. 2013.

[35] J. Burschka, N. Pellet, S.-J. Moon, R. Humphry-Baker, P. Gao, M. K. Nazeeruddin, and M. Gratzel, "Sequential deposition as a route to high-performance perovskite-sensitized solar cells," *Nature*, vol. 499, pp. 316–319, July 2013.

[36] M. Liu, M. B. Johnston, and H. J. Snaith, "Efficient planar heterojunction perovskite solar cells by vapour deposition," *Nature*, vol. 501, pp. 395–398, Sept. 2013.

[37] B. Conings, L. Baeten, C. De Dobbelaere, J. D'Haen, J. Manca, and H.-G. Boyen, "Perovskite-based hybrid solar cells exceeding 10reproducibility using a thin film sandwich approach," *Advanced Materials*, vol. 26, no. 13, pp. 2041–2046, 2014.

[38] J.-Y. Jeng, Y.-F. Chiang, M.-H. Lee, S.-R. Peng, T.-F. Guo, P. Chen, and T.-C. Wen, "$CH_3NH_3PbI_3$ perovskite/fullerene planar-heterojunction hybrid solar cells," *Advanced Materials*, vol. 25, no. 27, pp. 3727–3732, 2013.

[39] S. D. Stranks, G. E. Eperon, G. Grancini, C. Menelaou, M. J. P. Alcocer, T. Leijtens, L. M. Herz, A. Petrozza, and H. J. Snaith, "Electron-Hole Diffusion Lengths Exceeding 1 Micrometer in an Organometal Trihalide Perovskite Absorber," *Science*, vol. 342, pp. 341–344, Oct. 2013.

[40] G. C. Xing, N. Mathews, S. Y. Sun, S. S. Lim, Y. M. Lam, M. Gratzel, S. Mhaisalkar, and T. C. Sum, "Long-range balanced electron- and hole-transport lengths in organic-inorganic $CH_3NH_3PbI_3$," *Science*, vol. 342, no. 6156, pp. 344–347, 2013.

[41] D. Liu and T. L. Kelly, "Perovskite solar cells with a planar heterojunction structure prepared using room-temperature solution processing techniques," *Nature Photonics*, vol. 8, pp. 133–138, Feb. 2014.

[42] K. W. Tan, D. T. Moore, M. Saliba, H. Sai, L. A. Estroff, T. Hanrath, H. J. Snaith, and U. Wiesner, "Thermally induced structural evolution and performance of mesoporous block copolymer-directed alumina perovskite solar cells," *ACS Nano*, vol. 0, no. ja, p. null, 2014.

[43] M. Saliba, K. W. Tan, H. Sai, D. T. Moore, T. Scott, W. Zhang, L. A. Estroff, U. Wiesner, and H. J. Snaith, "The influence of thermal processing protocol upon the crystallization and photovoltaic performance of organic-inorganic lead trihalide perovskites," *The Journal of Physical Chemistry C*, 2014.

CHAPTER 2

Background

This chapter introduces solar cell fabrication and characterisation methods.

This is followed by a discussion on perovskites in general giving an overview of the myriad of possible organic-inorganic materials. Then, perovskite solar cells are discussed introducing the main device architectures used to date. Lastly, the potential for plasmonics to enhance solar cell is discussed.

2.1 Core-Shell Nanoparticle Synthesis

The synthesis procedures for core-shell Au@SiO_2 and Ag@TiO_2 nanoparticles were originally developed by Yao Sun of Cornell University and can be found in Appendix A.

2.2 Solar Cell Fabrication and Synthesis Procedures

2.2.1 Deposition methods

Doctor blading evolved from the letterpress printing term "ductor blade" referring to the process of removing superfluous ink with a blade. A paste, for example titania nanoparticles in ethanol, was dropped between 2 scotch tape spacers. Then a smooth, rod-shaped object was swept at constant speed over the 2 spacer stripes yielding typical film thicknesses from 500-2000 nm depending on the spacer thickness, the speed of the doctor blade and dilution of the paste. Afterwards the mesolayer was usually smoothed further by exposure for up to a few minutes in an ethanol (EtOH) atmosphere. Subsequently, the substrate usually underwent a heating procedure to remove solvent, burn off organic components, or to induce a different phase of the material.

Screen printing utilizes a patterned mesh. The substrate rested underneath the mesh on which the paste was dropped. Then, a squeegee was moved slowly to distribute the paste on the mesh, i.e. "loading the mesh". Afterwards the mesh was pressed on the substrate and the squeegee was reapplied to pattern the underlying substrate. Again, the layer was usually exposed to an ethanol atmosphere for further smoothing. Subsequent heating steps as in the previous paragraph were applied as needed.

Spin coating is a very common method for smaller sized samples. The substrate was fixated (by a vacuum pump) on a chuck which was rotated by a motor at a given speed and acceleration. The paste was either dropped on the substrate before rotation referred to as the "static" method or during the rotation referred to as the "dynamic" method. There is no exact relationship for the final thickness which depends on the dilution of the paste, evaporation rate of the solvent, spin coating acceleration, speed, and method used. However, a useful empirical rule of thumb was proposed [1, 2]

$$t = c_1 \omega^{\alpha}$$

where t is the final thickness, ω is the angular velocity, and c_1 and α are empirical parameters which vary from system to system. In many systems the relationship $t \sim \omega^{-1/2}$ has been observed to be a useful starting point [2].

2.2.2 Device fabrication

Fluorine-doped Tin Oxide

A glass substrate of conducting fluorine-doped tin oxide (FTO) (Pilkington TEC 7, 7Ω/□) was used with typical dimensions of 11.2x11.2 cm^2 resulting in 64 devices of 1.4x1.4 cm^2. In order to prevent short circuiting of the devices, the electron and hole transporting metal electrodes had to be prevented from being contacted through the FTO. Thus, 0.45 cm on each device was FTO-free which was accomplished by putting stripes of scotch tape on the full FTO substrate so that the desired device dimensions were maintained. Then zinc powder was applied on the uncovered FTO. It acted as a catalyst for the subsequently dropped 2 M hydrochloric acid (HCl) solution which etched away the FTO leaving a striped pattern of non-conducting glass on the substrate. Afterwards, the scotch tape was removed and the substrate was sequentially cleaned in 2% hallmanex detergent solution in water, deionized water, acetone, and ethanol followed by plasma etching for 10 min.

Compact layer

A compact layer of titania (TiO_2), zinc oxide (ZnO), or alumunium-doped zinc oxide (AZO) was deposited on the FTO patterned glass substrate.

TiO_2

Mainly, two deposition methods for TiO_2 compact layers were used.

First, spray pyrolysis where a precursor solution of titanium diisopropoxide was diluted with ethanol (V:V, 1:10) and dispersed into fine droplets by a spraying setup under oxygen flow onto a 250°C hot substrate. A dense layer of titania formed (~50 nm) and turned into anatase after sintering to 500°C for 45 min.

Second, spin coating was employed as well. A precursor solution of 350 µl of titanium isopropoxide was diluted in mildly acidic 5 ml ethanol (130 mM HCl) and spin coated at 2000 rpm for 45 s. The substrate was dried at 150°C for 15 min and then sintered at 500°C for 45 min resulting in a final TiO_2 thickness of ~50 nm.

ZnO and AZO (aluminium-doped zinc oxide)

ZnO compact layer was deposited by spray pyrolysis of 0.1 M zinc acetate dihydrate (Sigma-Aldrich) diluted in methanol (~22 mg/ml) at 400°C.

AZO (aluminium-doped zinc oxide) was deposited with spray pyrolysis following the same procedure. Doping was accomplished by adding aluminium chloride ($AlCl_3$) (268 mM in methanol) to the ZnO precursor. The highest conductivity was reached at 2% Al/Zn ratio (see Figure 2.1).

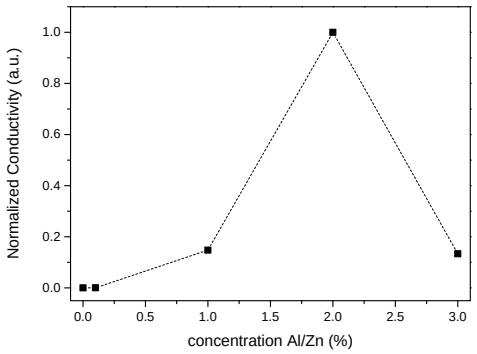

Fig. 2.1 Normalized conductivity of aluminium-doped ZnO layers over an increasing ratio of Al/Zn atoms.

Mesoporous layers

Mesoporous layers of TiO_2, ZnO, Al_2O_3, and silica (SiO_2) were deposited on the compact layer by the previously described methods (doctor blading, screen printing, spin coating). It should be noted that it was standard procedure to treat all pastes with an ultrasonic bath or horn ensuring optimal mixing.

Scaffold pastes

First, for traditional dye-sensitized solar cells (DSSCs) a highly interconnected anatase layer with good conductivity is crucial. This is generally accomplished by mixing TiO_2 nanoparticles with organic binders like cellulose. The Australian company Dyesol offers commercial solutions like the *18NR-T* paste, i.e. ~20 nm titania NPs in a mixture of ethyl cellulose and terpineol.

The mesoporous scaffold was spin coated on a substrate and the thickness was varied by the spin speed and Dyesol paste dilution with ethanol. Other deposition methods were doctor blading and screen printing where the paste was diluted by ethanol or terpineol depending on the desired film thickness. The spin coating method was slightly more repeatable than doctor blading or screen printing which required more manual control. However, using an automatized setup for doctor blading or screen printing remedied the lack in manual accuracy. Spin coating worked well for thinner films between 100-500 nm. Thicker films from 500-3000 nm were feasible for all three methods by adjusting the process parameters carefully.

The following sintering protocol was used after the Dyesol paste was deposited:

- 10 min ramp to 100°C and held for 10 min to evaporate ethanol.
- 5 min ramp to 150°C and held for 10 min to evaporate terpineol.
- 10 min ramp to 325°C and held for 30 min to burn the polymer.
- 5 min ramp to 450°C and held for 5 min.
- 10 min ramp to 500°C and held for 30 min.

Additionally, a $TiCl_4$ surface treatment was necessary for DSSCs (not for perovskite based devices), i.e. the samples were immersed in a 15-20 mM solution of $TiCl_4$ (concentration was adjustable by diluting the 2 M stock with DI water). The substrate was left in an oven at 70°C for 1 h. Subsequent rinsing in DI water, drying with compressed air and heating to 500°C for 45 min (and 30 min ramp) completed the procedure. The $TiCl_4$ procedure ensured good charge injection into the TiO_2 [3]. The 2 M $TiCl_4$ stock solution was prepared as follows. First, it has to be noted that the procedure is exothermic and must be conducted in a fume hood. 1 ml hydrochloric acid (35%) was added to 350 ml MQ water. The solution was cooled down in a freezer, taken back into the fume hood and left stirring in an ice bath. Then, 100 ml $TiCl_4$ (Sigma-Aldrich) was added into the mix *very* slowly and stopped whenever the mix bubbled excessively. The solution was stored in the freezer where it cleared up eventually.

Second, ZnO paste was made from a zinc oxide dispersion (40 wt% in ethanol, Sigma-Aldrich). Initially, a solution of 1.2 ml buthylamine was mixed with 20 g ZnO dispersion and left stirring for a few minutes. Then, 20 g terpineol (mixed isomers) was added and left stirring again. Ethyl cellulose solution (30 g) was added slowly. The paste was concentrated by using a rotary evaporator at 50°C for a few hours until most of the ethanol was gone.

The ethyl cellulose solution was prepared in the following manner: 170 ml ethanol was warmed up to 75°C and stirred with a magnetic bar. Then, 7.5 g of ethyl cellulose was added very slowly to the ethanol solution until complete dissolution.

Third, Al_2O_3 paste was made by adding 41.5 g butoxyethanol to 50 g of an Al_2O_3 dispersion (20% of 50 nm colloids in water, Sigma-Aldrich). The solution was stirred and ultrasonicated, and water was removed by a rotary evaporator at 40°C. The water-free solution was diluted 2 times with ethanol. Afterwards, 2 g of hydroxypropyl cellulose (HPC) solution mixed in 20 g ethanol was added slowly while the overall solution was constantly stirring. The paste was concentrated with rotary evaporation at 30°C removing the excess ethanol followed by shacking and ultrasonication. The alumina film thickness was adjusted by diluting the stock solution with ethanol.

Fourth, with the advent of perovskite solar cells, the mesostructure has not to be a good charge transport anymore for high performance devices (as was the case for DSSCs). Thus, simpler paste solutions without organic binders and extensive heating steps became suitable alternatives. One simple approach was spin coating TiO_2 NPs on a substrate where the thickness depended on the paste dilution and spin speed. The sample was left to dry at 150°C for 30 min. A detailed synthesis procedure for TiO_2 NPs can be found in Appendix A.

Fifth, an Al_2O_3 scaffold was achieved by spin coating a colloidal dispersion of <50 nm Al_2O_3 nanoparticles (Sigma-Aldrich, product number 702129) at 2500 rpm for 45 s, followed by drying at 150°C for 30 min. This method was developed by Ball et al. [4]

Sixth, spin coated SiO_2 NPs also formed a scaffold. The sample was usually left to dry at 150°C for 30 min. The synthesis procedure for SiO_2 NPs can be found in Appendix A.

Sensitizer

The photoactive area was applied on the mesoporous scaffold from the above protocols.

In the case of DSSCs, the titania mesostructure made from commercial Dyesol paste was the most relevant because the scaffold had to transport charge. The freshly sintered device substrate (after cooling down to room temperature) got immersed in a dye solution. The exposure time depended on the used dye (dissolved in tert-butanol:ACN), the mesoporous thickness, and experimental objectives. Afterwards the (now coloured) devices were taken out of the solution and rinsed in acetonitrile (ACN) to remove excess dye on the top surface.

The other mesostructures were mainly used with the new perovskite absorber. A 40 wt% perovskite precursor solution was prepared by mixing methylammonium iodide (CH_3NH_3I) and lead(II) chloride ($PbCl_2$, Sigma-Aldrich) in a 3:1 molar ratio in N,N-dimethylformamide (DMF).

Ethanol, methylamine (Sigma-Aldrich, 33 wt% in ethanol), and hydriodic acid (HI) (Sigma-Aldrich, 57 wt% in water) in a ratio of 10:2.4:1 (ethanol:methylamine:HI, V:V:V) was used for the methylammonium iodide synthesis as outlined in the following.
Methylamine was mixed in a stirring ethanol solution and left for 5 min. Afterwards HI was added dropwise and left stirring for 15 min. Leaving the solution on a hot plate at 100°C (no stirring) for a few hours led to crystallization into white methylammonium iodide powder. In order to remove unreacted material from the powder, it was washed in a diethyl ether solution and left stirring for 20 min (the crystals do not dissolve). The solution was filtered with a vacuum pump.
Recrystallization for a higher quality material was the next objective. For this, the filtered methylammonium iodide powder was added to a stirring solution of ethanol kept just below the boiling point (70°C). The aim was to get a saturated solution which determined the amount of ethanol needed (starting with a small quantity and gradual increase was a good strategy). Afterwards the mixture was put in the freezer and left overnight upon which the powder recrystallized (because of the reduced solubility in colder ethanol). Again, the solution was filtered followed by drying in a vacuum oven for 1 h. The white methylammonium iodide powder was one of the components for the above perovskite precursor solution.

The perovskite precursor was spin coated in nitrogen (or air) at 2000 rpm for 45 s. The "standard" protocol for annealing was at 100°C for 90 min in nitrogen (or 45 min in air).

Hole transporter

For DSSCs, the mesoporous layers were typically 1-2 µm in thickness. Each thickness needed an optimized hole transporting material (HTM). In most cases, this was spiro-OMeTAD with concentrations ranging from 60-100 mM dissolved in chlorobenzene (CB) with an added 13 mol% lithium bis(trifluoromethanesulfonyl)imide (Li-TFSI) (predissolved in ACN)

and 80 mol% tert-butylpyridine (tBP). The HTM was deposited via spin coating from 700-1200 rpm for 45 s yielding typical capping layers from 50-200 nm beyond the part infiltrating the mesostructure. The devices were then left in a light-tight desiccator overnight.

Perovskite solar cells had usually a maximum mesostructure thickness of ~500 nm. Spiro-OMeTAD was deposited by spin coating at 2000 rpm for 45 s. The typical concentration was 80 mM in CB with an added 30 mol% Li-TFSI (predissolved in ACN) and 80 mol% tBP yielding capping layers of up to 400 nm. The devices were then left in a light-tight desiccator overnight.

At this point, it is very apparent that perovskite solar cells have evolved organically from DSSCs as the manufacturing is almost identical with the main difference being that the perovskite replaces the dye. Thus, DSSC research can be directed with relative ease towards investigating and fabricating perovskite sensitized solar cells (PSSCs). However, the terminology changed later-on reflecting the transformation towards a new technology. This started when it was discovered that titania was not needed as a charge transporter anymore [5] and replaceable by an insulating alumina scaffold giving rise to the term meso-superstructured solar cells (MSSCs). Subsequently this concept was taken even further towards a thin-film technology by discarding the mesostructure completely which was possible due to the ambipolar charge transport properties of the perovskite absorber [6]. At this stage it would seem that perovskite-based solar cell can be developed into many different directions distinguishing them from the original DSSC design.

Electrodes

Finally, 150 nm thick silver (or gold) electrodes were evaporated onto the devices through a shadow mask under vacuum between 10^{-6} and 10^{-7} mbar.

2.3 Optical Characterization

UV-vis

UV-vis spectroscopy is an optical characterization method where light from 200-2000 nm is directed through a sample and then collected. Analyzing the light before and after it interacted with the sample is at the heart of this technique.

The incident and transmitted light intensities (I_0 and I_1 usually expressed as transmittance $T = I_1/I_0$) can be related to the absorption A, extinction coefficient ϵ, the absorber concentration c and the optical path length l through the sample via the Beer-Lambert law.

$$A = -\log(I_1/I_0) = \log(1/T) = \epsilon \cdot l \cdot c$$

The Beer-Lambert law is limited to homogeneous samples with negligible scattering. Also, a low concentration is usually needed as otherwise the incoming light interacts with the absorber and causes deviation.

Using an integrating sphere, i.e. a sphere with an inner diffuse reflection coating, helps to distinguish the contribution from diffuse and specular transmission or reflection.

First, the total transmission T_{tot} is measured by mounting the sample at the front of the integrating sphere (transmission port). Incoming light passes through the sample and gets diffusely reflected (and re-reflected) in the integrating sphere until it reaches the collection port (a small hole on the side of the sphere). Diffuse transmission through the sample is collected by opening a hole at the back of the integrating sphere (in direction of the incoming light beam). Thus, all specularly transmitted light is leaving the sphere without getting collected. Only the off-specular light contribution $T_{diffuse}$ remains. Second, the total reflection R_{tot} is measured by mounting the sample at the back of the integrating sphere on an 8° wedge. The incoming light passes through the sphere uninhibited until it reaches the sample. There it gets reflected at an angle of 8°. The specular and off-specular part of the light reflected this way remains within the sphere and gets eventually collected. The diffuse reflection is measured by using a 0° wedge. Now all on-axis reflected light is sent straight back through the entrance port without getting collected. Only diffuse reflection (off-axis) $R_{diffuse}$ remains in the integrating sphere and reaches the collection port. The scattered part of the light can be calculated by superposition of $T_{diffuse}$ and $R_{diffuse}$.

Accounting for all the light leads inevitably to

$$\textit{Reflection} + \textit{Transmission} + \textit{Absorbance} = 1$$

which can be written as

$$(R_{specular} + R_{diffuse}) + (T_{specular} + T_{diffuse}) + \text{Abs} = R_{tot} + T_{tot} + \text{Abs} = 100\%$$

Figure 2.2 shows the prescribed procedure for using the integrating sphere. In this thesis, UV-vis spectroscopy was mainly conducted with a Cary 300 Bio (Agilent Technologies) with an integrating sphere accessory.

2.4 Solar Cell Characterization

JV curves

Solar cells are typically characterized by measuring the current-voltage JV curve, i.e. the current density over applied voltage under illumination. The illumination follows *AM1.5G* standard test conditions (STC) at incident sunlight of 1000 W m^{-2}, an air mass (AM) of 1.5, and 25°C.

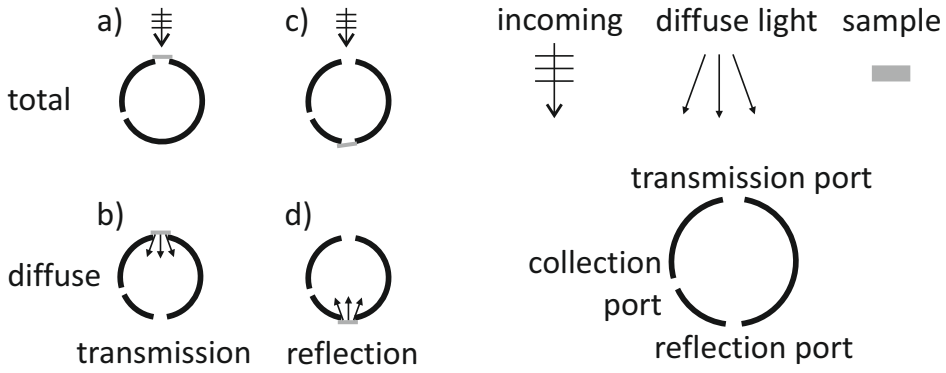

Fig. 2.2 UV-vis measurement with an integrating sphere. (a) Total transmission: the incoming light enters through the front port where the sample is mounted. The reflection port is closed. (b) Diffuse transmission: same as (a) but with the reflection port opened. (c) Total reflection: the incoming light passes through the front port until it reaches the sample which is mounted on the reflection port on an 8° wedge. (d) Diffuse reflection: same as (c) but with a 0° wedge. The light exits the integrating sphere through the collection port.

The main performance parameters for a solar cell are short-circuit current (J_{sc}), open-circuit voltage (V_{oc}), fill factor (FF) (or ff), and power conversion efficiency (PCE) (or η). Figure 2.3 is an illustration of a JV curve (black) under light irradiation where the short circuit current density J_{sc} is the y-axis intercept and the open circuit voltage V_{oc} is the x-intercept. The power output is calculated as $P = J \cdot V$ (red curve). Geometrically, the maximum power output $P_{\text{max}} = J_{\text{max}} \cdot V_{\text{max}}$ (shaded gray area) is the largest possible rectangle fitting under the JV curve. The short circuit current J_{sc} is the current measured when the cathode and anode are connected under short-circuit when no voltage is applied (zero load resistance). The open circuit voltage V_{oc} is the maximum voltage from a solar cell without drawing current (infinite load resistance). From these quantities the fill factor can be introduced, i.e. a measure for the squareness of the JV curve and thus the maximum obtainable power from J_{sc} and V_{oc}.

$$FF = \frac{J_{max}V_{max}}{J_{sc}V_{oc}}$$

FF is closely related to the PCE η expressing the overall fraction of light turned into electricity.

$$PCE = \eta = \frac{P_{max}}{P_{in}} = \frac{J_{sc}V_{oc} \cdot FF}{P_{in}}$$

where P_{in} is the power density of the incoming light.

The fill factor is negatively affected by parallel or shunt resistance R_{sh} where current leaks through alternative current pathways. Shunting resistance can be seen in an increased slope of the JV curve at 0 voltage. Additionally, series resistance R_{se} can come from within the cell, for example from resistance of metal contacts. It can be extracted from the slope of the JV curve at V_{oc}.

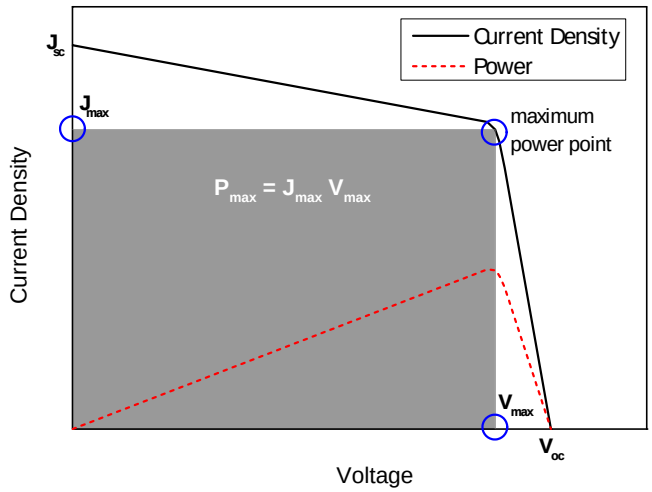

Fig. 2.3 Illustration of a current density-voltage curve (black) under light irradiation. The y-intercept is the short circuit current J_{sc} and the x-intercept is the open circuit voltage V_{oc}. The red curve is the calculated power output $P = J \cdot V$ where the peak is the maximum power point P_{max} with respective J_{max} and V_{max}. The rectangular grey area is $P_{max} = J_{max} \cdot V_{max}$ and depicts the highest possible power output from the solar cell.

Real solar cells with series and shunt resistance are often modeled with an equivalent circuit diagram as shown in Figure 2.4. The equivalent circuit contains a current source

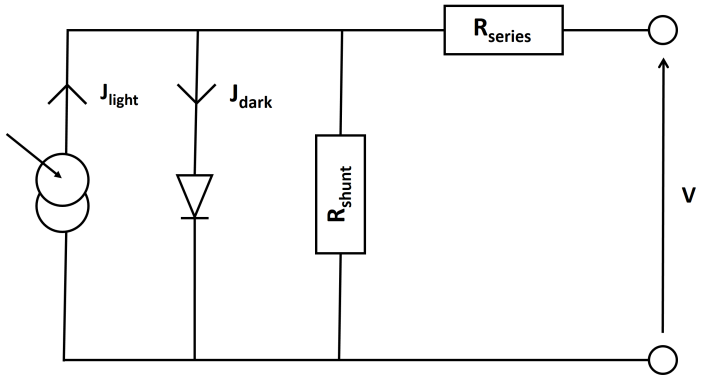

Fig. 2.4 Equivalent circuit diagram with series and shunt resistance.

generating J_{gen}, a diode with J_d, a parallel and series resistance collectively with J_{res}. The losses in current density due to the diode and resistance, the dark current density J_{dark}, is subtracted from the generated current density. The overall current density can be expressed in the following equation

$$J = J_{gen} - J_{dark} = J_{sc} - (J_d - J_{res}) = J_{sc} - J_0(e^{q(V+JR_{se})/kT} - 1) - \frac{V + JR_{se}}{R_{sh}}$$

with the temperature T, the Boltzmann constant k, and the reverse saturation current density J_0.

Spectral Response

The spectral response (SR) measures the ratio of the short circuit current density to the incident power P_{inc} at a given wavelength

$$SR(\lambda) = \frac{J_{sc}(\lambda)}{P_{inc}(\lambda)}$$

The incident photon-to-current conversion efficiency (IPCE) or external quantum efficiency (EQE) is defined as the ratio of collected electrons to the number incident photons.

$$IPCE(\lambda) = \frac{\#\ collected\ electrons}{\#\ incident\ photons}$$

SR and IPCE are related by

$$SR(\lambda) = \frac{q\lambda}{hc} IPCE(\lambda)$$

with the electric charge q, the Planck constant h, and the speed of light c.

The spectral response can be used to calculate the short circuit current [7]

$$J_{sc} = \int_{\lambda} \phi_{AM1.5}(\lambda) \cdot SR(\lambda)\, d\lambda$$

where $\phi_{AM1.5}(\lambda)$ in W/m^2/nm is the terrestrial solar spectrum under AM 1.5 global conditions shown in Figure 2.5 (red line). It also features the extraterrestrial spectrum (black line) which can be modelled by a black body at ~6000 K. The terrestrial irradiance is reduced in intensity because incoming light has to pass through the earth's atmosphere which absorbs strongly mainly due to ozone and water vapour. Another useful quantity is the ratio of collected electrons to absorbed photons which is known as the absorbed photon-to-current conversion efficiency (APCE) or internal quantum efficiency (IQE)

$$APCE(\lambda) = \frac{\#\ collected\ electrons}{\#\ absorbed\ photons}$$

IPCE and APCE are related by

$$APCE = \frac{IPCE}{A}$$

with A being the light absorbed in the photoactive layer.

Hence, APCE is always larger or equal to IPCE. APCE gives information on how well a solar cell converts photons into electrons. A low APCE, for example, would be a clear indication that the device is not turning photons into electrons efficiently. However, this is not necessarily true for a low IPCE where the losses may stem from transmitted or reflected light.

After having introduced the fabrication methods and main parameters for solar cells the next sections outlines the performance of perovskite solar cells beginning from the historic starting poing, i.e. dye-sensitized solar cells.

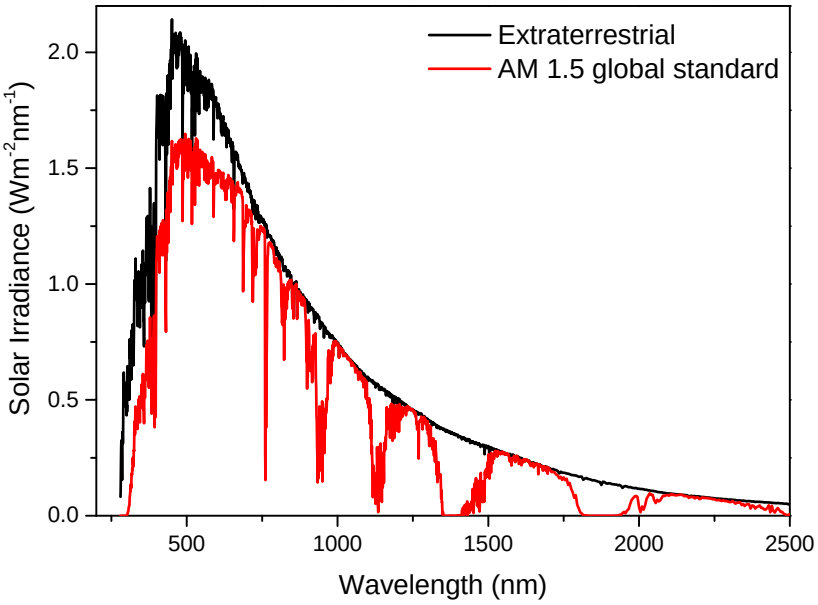

Fig. 2.5 Solar irradiance spectrum for extraterrestrial (black) and AM 1.5 global (red) conditions. The reduction for the terrestrial spectrum is mainly due to absorption by ozone and water vapour in the earth's atmosphere. The data is from the National Renewable Energy Laboratory (NREL) [8].

2.5 Dye-sensitized solar cells

Over the last two decades DSSCs have been studied intensively [9]. They are multilayer systems containing a light-absorbing dye sandwiched between layers for electron- and hole transport materials. The photoeffect occurs when the dye molecule gets excited by incoming light. The dye deexcites by surrendering an electron which diffuses towards an electron accepting layer. The dye is then regenerated by a hole transporter material. The electric circuit is established by contacting the electron and hole transporter layer with appropriate metallic electrodes. Figure 2.6 features the original embodiment of the DSSC as proposed by O'Regan and Graetzel in 1991 [9]. All DSSC layers can be modified and fine-tuned depending on the desired objective. This flexibility on one hand holds great potential for further improvements.

On the other hand, the complex, interdependent interface dynamics between the layers makes DSSC optimisation very challenging. Overall, DSSCs have great potential because they consist of inexpensive materials and current research shows efficiencies from 2-13% [9–14].

It should be noted that DSSCs need relatively large over-potentials of 200-300 meV to drive electron injection to the metal oxide (energy difference LUMO dye and conduction band of the metal oxide) and regenerate the oxidized dye (energy difference HOMO dye and oxidization potential of the hole transporter material). This results in a large loss-in-potential, i.e. the difference between the open circuit voltage (times elementary charge) and

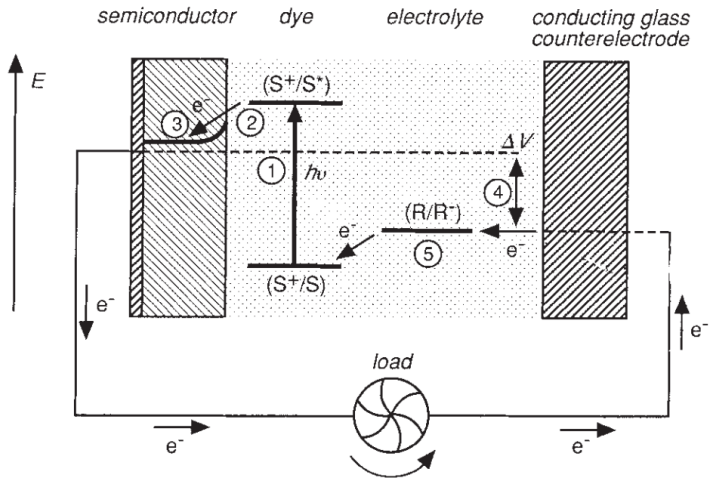

Fig. 2.6 DSSC schematics and basic operation principle of a dye-sensitized solar cell (DSSC). This image is from the seminal publication of O'Regan and Graetzel in 1991 [9]. Reprinted by permission from Macmillan Publishers Ltd: Nature 353: 737-740 ©1991

the optical bandgap, of more than 700 meV [15, 16] imposing a fundamental challenge for high efficiency devices.

The DSSC design is inherently suited for the perovskite absorber as replacing the dye with perovskite is already sufficient for high efficiency devices.

2.6 Perovskites in General

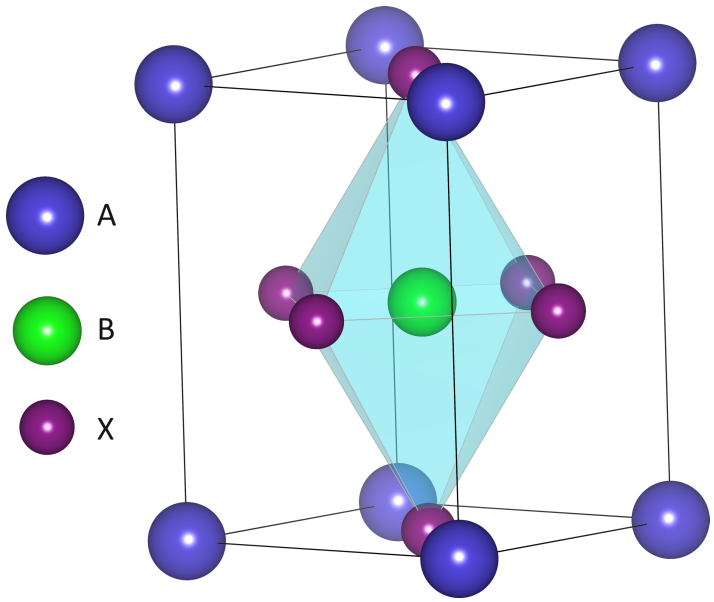

Fig. 2.7 Generic perovskite unit cell (tetragonal) with ABX_3 structure. Anion "A" is in the corners, cation "B" in the centre, and anions "C" in the face-centred positions of the unit cell. Every material conforming to this structure is called a perovskite.

The term perovskite was introduced by Gustav Rose who discovered the mineral calcium titanium oxide ($CaTiO_3$) in the Ural Mountains in 1839 [17] and named it after the Russian mineralogist Lev A. Perovski. It subsequently became the designation for any material adopting the crystal structure of $CaTiO_3$. The perovskite class of materials encompasses a huge amount of compounds of which many have remarkable physical properties (often due to subtle displacements within the crystal lattice) such as piezo- [18], thermo- [19], ferroelectricity [20], ferromagnetism [20], giant magnetoresistance [21], and superconductivity [22].

In a more generic formulation the perovskite unit cell is described as ABX_3 where "B" sits in the middle, "A" in the corners, and the "X" in the face-centred positions of a cubic unit cell (which can be distorted to orthorhombic or tetragonal). Figure 2.7 gives an illustration for a typical tetragonal unit cell.

The atomic radii of the different species can be used to check if a given set of atoms is likely to be consistent with a perovskite structure. Assuming an idealized cubic unit cell where all atoms touch, it follows geometrically that $R_A + R_X = \sqrt{2}(R_X + R_B)$ where R denotes the ionic radii of the respective atoms. From this reasoning and extended to permit for distortions in the unit cell the tolerance factor t was introduced by Victor Goldschmidt in 1926 [23].

$$t = \frac{R_A + R_X}{\sqrt{2}(R_B + R_X)} \tag{2.1}$$

This is an approximation assuming pure ionic bonding and ignoring covalent bonding [24, 25]. Deviations from $t = 1$ (perfect cubic unit cell) usually result in distorted lattices (rhombohedral, orthorhombic, teragonal [26–28], or hexagonal [29]). As a rule of thumb the following crystal structures are often observed for tolerance factors ranging from 0.76-1.13 [29].

$$0.76 < t \leq 0.88 \text{ (orthorhombic)}$$
$$0.88 < t \leq 1.00 \text{ (cubic)}$$
$$1.00 < t \leq 1.13 \text{ (hexagonal)}$$

Tolerance factors below 0.76 often conform to the trigonal crystal lattice of "ilmenite" ($FeTiO_3$) [30].

In 1978, Weber et al. discovered a new member of the perovskite family: organic-inorganic lead triiodide ($CH_3NH_3PbI_3$) [31, 32]. Many possible materials in this ABX_3 configuration were investigated ever since involving variations in every component (A, B, and X).

For example, the organic component (A) can encompass a whole range of molecules including methylammonium, formamidinium, longer alkylammonium chains, or mixtures of organic cations [33–38]. Possible metals (B) are Pb [31], Sn [39–46], Ge [47], Cu [48, 49],

Eu [50], Sb [51], Zn [52], Bi [53], Mn [54], Cd [55], Ni [37], Fe [37], or heterometallic mixtures [40, 56–63]. Finally, halides used with many of the described structures are Cl, Br, I, or mixtures.

Lead (Pb) has shown very promising photovoltaic properties in the past. Thus, for the remainder of this discussion, the perovskite structures discussed are mainly $APbX_3$. The physical effects of this material family are already tremendous [64, 65] displaying ferroelectric [43], luminescence [66], electroluminesence [67–69], LED [70–72], third-harmonic generation [73], photoconductive [74, 75], and transistor [76] properties. Furthermore, the exciton binding energies, dielectric constants, and band gap [33, 77–83] can be tuned by the organic chain length, or used halide which could be of interest for LED or LASER applications for example.

In addition, this material provides a whole array of synthesis methods for thin-film perovskite layers [84–89] utilizing spin-coating [37], dip-coating [90, 91], evaporation [92, 93], or chemical vapour deposition [94].

As a next step, eq. 2.1 is used to give an estimate for the maximum radius R_A fitting into an ideal cubic structure ($t = 1$) (see Table 2.1) with B = Ge, Sn, Pb and X = Cl, Br, I (with the ionic radii from [95]). Unsurprisingly the highest value $R_A = 2.59\,\text{Å}$ in the table is achieved when $R_B + R_X$ is the highest, i.e. for B = Pb and X = I. However, it should be noted that there is uncertainty about the ionic radius of Sn^{2+} which has been reported from 93-122 Å [96, 97].

Table 2.1 Resulting R_A when $t = (R_A + R_X)/(\sqrt{2}(R_B + R_X)) = 1$ for B = Ge, Sn, Pb and X = Cl, Br, I. The ionic radii are from [95, 96].

$R_B \backslash R_X$	Cl (1.81 Å)	Br (1.96 Å)	I (2.20 Å)
Ge (0.73 Å)	1.78 Å	1.84 Å	1.94 Å
Sn (0.93 Å)	2.06 Å	2.13 Å	2.23 Å
Pb (1.19 Å)	2.43 Å	2.49 Å	2.59 Å

A C-C (carbon-carbon) bond has about 1.5 Å bond length. Hence, only very few organic cations are sufficiently small (with 2-3 atoms) to fit into an ideal perovskite structure, e.g. methylamine (MA) (CH_3NH_3) and formamidinium (FA) ($NH_2CH{=}NH_2$). This configuration has all the metal centres (“B”) interconnected in vertical and horizontal direction and is known as a 3D perovskite structure.

Larger organic molecules such as $C_nH_{2n+1}NH_3$ result in layered structures (or so-called 2D perovskites) with inorganic planes [36] sandwiched between organic layers directed via self-assembly through van der Waals forces, and hydrogen bonds between the halogens in the inorganic layer and the organic layer. In principle 2D excitons in such systems have four times the binding energy of 3D excitons (due to the reduced kinetic energy). However, layered perovskites were observed to show even higher binding energies.

This can be explained qualitatively by considering that the organic layer is insulating (with a relatively low dielectric constant of about 2) while the inorganic layer acts as a semiconductor (with a relatively high dielectric constant of about 6) [83]. Thus, Coulomb interaction ($\sim 1/\varepsilon$) is less screened than in a 3D perovskite system which has no organic spacer layers. For excitons this means stronger interaction which is reflected in a higher than expected exciton binding energy [35], a phenomenon is known as the dielectric confinement effect [87]. A precise calculation for the binding energy in a dielectric quantum well environment utilizing the image charge method can be found in [98]. Highly excitonic materials with organic (insulating) layers have attracted considerable attention because of their high tunability, e.g. absorbtion onset, exciton binding energy. However, for solar cell application, a low exciton binding energy is desired in order to maximize free charge generation. Hence, the most promise so far is shown by the 3D perovskite $CH_3NH_3PbI_3$ or the mixed halide variation $CH_3NH_3PbI_{3-x}Cl_x$ with the relatively low exciton binding energy of ~50 meV [87].

In this thesis, the main perovskite absorber used for solar cell fabrication was methylammonium lead mixed halide. Figure 2.8a shows an absorption spectrum and Figure 2.8b an XRD pattern of ~400 nm thick $CH_3NH_3PbI_{3-x}Cl_x$ films fabricated from spin coating on a microscope slide and subsequent annealing at 100°C for 45 min. The absorptance is noteworthy because it is relatively high at ~80% and covers panchromatically almost all of the optical range from 400-800 nm with the cut-off at around 800 nm. The XRD pattern can be attributed to a tetragonal lattice with sharp peaks at 14.1° (1 1 0), 28.4° (2 2 0), and 43.1° (3 3 0) indicating a remarkably high crystallinity from the self-assembly process at such relatively low temperatures. The 14.1° peak is the perovskite signature peak signalling successful perovskite formation. A small peak at 12.8° (not present here) indicates the presence of PbI_2, one of the precursor materials, and suggests an incomplete reaction.

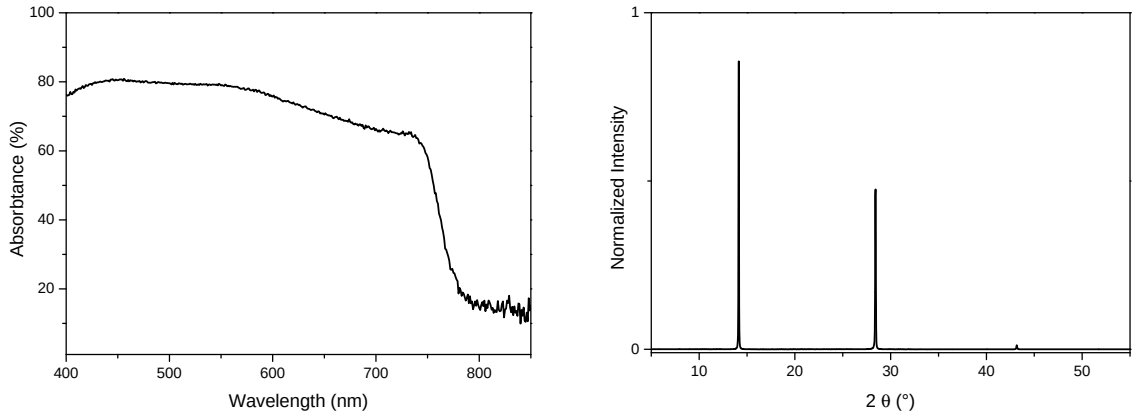

(a) Absorptance **(b)** XRD

Fig. 2.8 (a) Absorptance and (b) XRD of a ~400 nm thick $CH_3NH_3PbI_{3-x}Cl_x$ film on a flat microscope slide.

In the next section a summary of the recent development for perovskite solar cells is given.

2.7 Perovskite Solar Cells

The $CH_3NH_3PbI_3$ perovskite material was employed for photovoltaic applications for the first time in a liquid dye-sensitized solar cell (DSSC) by Kojima et al. in 2009 with PCEs up to 3.8% [99, 100]. Efficiencies then exhibited a step-change improvement by substituting the liquid electrolyte hole transporting material (HTM) with a solid state HTM, 2,2',7,7'-tetrakis(N,N-di-p-methoxyphenylamine)-9,9'-spirobifluorene (spiro-OMeTAD) [5, 101]. The perovskite was shown to support charge-transport of either electrons and holes respectively by replacing the mesoporous titania scaffold, a crucial element in the traditional DSSCs, with an inert Al_2O_3 scaffold [4, 5], termed a MSSC, or removal of the HTM [102]. Very high internal quantum efficiencies were also observed when the nanostructure was discarded completely, paving the way towards a conventional thin-film solar cell architecture [4, 6], showing that the perovskite can serve all the roles from light absorption to effective transport of both electrons and holes in an efficient p-i-n heterojunction solar cell. Additionally, perovskites prepared from a mixed or pure halide precursor [5] were observed to show remarkably long carrier diffusion lengths exceeding 1 µm [103, 104]. Further improvements to the processing of perovskite thin-films yielded remarkable PCEs exceeding 15% [6, 94, 105].

The change in perovskite solar cell architectures over time is reflected by the change in terminology. Initially, perovskite solar cells evolved "naturally" from DSSCs in which the dye was simply replaced by the perovskite absorber giving rise to the designation PSSC. Then, MSSCs was the term used when it was discovered that the titania scaffold could be replaced by insulating alumina [5]. Finally, this went even further towards a scaffold-less planar perovskite solar cell [6]. At this stage it seems that perovskite solar cell can be developed into many different directions branching off quite markedly from the initial DSSC design, an evolutionary fork so to speak.

2.8 Plasmonics

At very small length scales, typically in the nanometre range, the surface electrons of a metal-dielectric interface can oscillate collectively in so-called plasmonic surface resonance modes. These modes are highly sensitive to the environment (dielectric constant), type of metal, and geometry which gives them unique potential for tunability. As the object grows the collective excitation (which is in phase) is harder and harder to maintain until eventually the resonance mode breaks down.

Figure 2.9 illustrates a surface plasmon mode at an air-silver interface under plane wave excitation of $\lambda = 500\,\text{nm}$. The electric field travels along the dielectric-metal surface as a wave. The plasmonic near-field shows strong local field enhancement which diminishes exponentially. This effect has been investigated extensively in recent years with more and more refined manufacturing techniques, most notably electron-beam lithography (e-beam) [106],

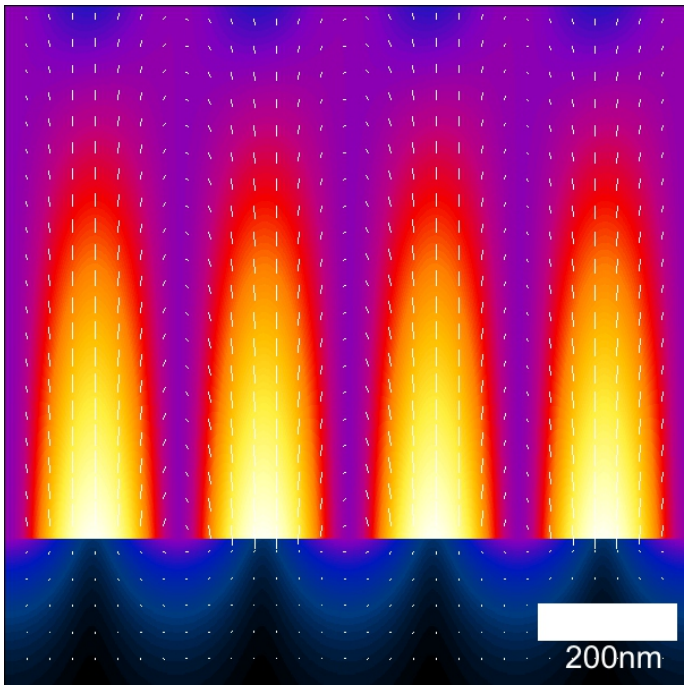

Fig. 2.9 Simulation of the electric field of a surface plasmon mode (SPP). A planar interface of air-silver is illuminated by a plane wave of $\lambda = 500\,\text{nm}$. The white lines follow the electric field.

focused ion beam lithography (FIB) [107], self-assembly [108, 109], or nanoimprinting [110]. Together with more and more powerful simulation methods [111, 112] this triggered a plethora of applications such as optical [113, 114] and electron microscopy [115], metamaterials [116], 3D plasmonic rulers [117], plasmonic oligomers [118], surface-enhanced Raman spectroscopy (SERS) [119, 120], or plasmonic wave guides [121].

Plasmonic nanostructures have the potential for fundamental enhancements in solar cell efficiency which could help to approach or even surpass the 1 sun Shockley-Queisser limit without any exotic operating principles. To date, several effective routes have been developed to incorporate metal NPs into solar cells, with most reports attributing enhancements to increased light absorption through plasmonic effects [122]. In a first route, the near field electric field enhancement of metal NPs upon surface plasmon excitation is employed to enhance the effective light absorption cross-section of a solar cell [123–128]. In a second route, light scattering off the plasmonic metal NPs is employed to re-direct light into a solar cell increasing the optical pathlength (antenna effect) [129]. In a third route, metal NPs are utilized as a sensitizer directly, to harvest light and inject photo-induced electrons to an electron acceptor [130]. The latter example by Reineck et al. is arguably the clearest demonstration of a "plasmonic solar cell" to date, since there is no ambiguity as to which component is responsible for absorbing the sun light. Although plasmonic light trapping and device performance enhancements are widely reported in many systems, there are very few examples where these photocurrent enhancements can be spectrally correlated to the plasmonic light coupling.

As already mentioned perovskite solar cells are exceptional candidates for low-loss photovoltaic operation demonstrating the great potential of perovskites as inexpensive and efficient absorber materials for solution processed photovoltaics. Even though the perovskite absorbers can already absorb sun light effectively in well operating solar cells, there are additional efficiency gains possible by enhancing the light absorption near the band edge and ensuing thinning of the solar cell.

2.9 Summary

This chapter gave an overview of the main solar cell fabrication methods used throughout this thesis. In particular it contained the following points

- Deposition methods for mesoporous layers (doctor blading, screen printing, spin coating)
- Solar cell fabrication protocol with details about
  - FTO patterning of glass
  - Compact layer deposition for TiO_2, ZnO, and AZO
  - Mesoporous layer made of TiO_2 (Dyesol), ZnO, TiO_2 NPs, Al_2O_3, and SiO_2
  - Dye or perovskite deposition
  - Hole transporter layer (Spiro-OMeTAD)
  - Metal electrode evaporation
- Synthesis protocols for nanoparticles such as TiO_2, SiO_2, Au@SiO_2, and Ag@TiO_2

Moreover, solar cells characterisation and main operational parameters were discussed.

In the last part a general introduction of perovskite was given with a focus on organic-inorganic trihalide perovskites. Then, perovskites for photovoltaic applications were discussed with an emphasis on the 3D methylammonium lead mixed halide material. This was followed by a outline on plasmonics nanostructures in solar cells.

References

[1] K. Norrman, A. Ghanbari-Siahkali, and N. B. Larsen, "6 studies of spin-coated polymer films," *Annu. Rep. Prog. Chem., Sect. C: Phys. Chem.*, vol. 101, pp. 174–201, 2005.

[2] D. Mitzi, *Solution processing of inorganic materials*. John Wiley & Sons, 2008.

[3] P. M. Sommeling, B. C. O'Regan, R. R. Haswell, H. J. P. Smit, N. J. Bakker, J. J. T. Smits, J. M. Kroon, and J. A. M. van Roosmalen, "Influence of a $ticl_4$ post-treatment on nanocrystalline tio_2 films in dye-sensitized solar cells," *The Journal of Physical Chemistry B*, vol. 110, no. 39, pp. 19191–19197, 2006.

[4] J. M. Ball, M. M. Lee, A. Hey, and H. J. Snaith, "Low-temperature processed meso-superstructured to thin-film perovskite solar cells," *Energy & Environmental Science*, vol. 6, no. 6, pp. 1739–1743, 2013.

[5] M. M. Lee, J. Teuscher, T. Miyasaka, T. N. Murakami, and H. J. Snaith, "Efficient Hybrid Solar Cells Based on Meso-Superstructured Organometal Halide Perovskites," *Science*, vol. 338, pp. 643–647, Nov. 2012.

[6] M. Liu, M. B. Johnston, and H. J. Snaith, "Efficient planar heterojunction perovskite solar cells by vapour deposition," *Nature*, vol. 501, pp. 395–398, Sept. 2013.

[7] J. Nelson, *The physics of solar cells*, vol. 57. World Scientific, 2003.

[8] "National Renewable Energy Laboratory (NREL)." `http://rredc.nrel.gov/solar/spectra/am1.5/`, 2014. Accessed 27-July-2014.

[9] B. O'Regan and M. Gratzel, "A low-cost, high-efficiency solar cell based on dye-sensitized colloidal TiO_2 films," *Nature*, vol. 353, pp. 737–740, Oct. 1991.

[10] U. Bach, D. Lupo, P. Comte, J. E. Moser, F. Weissortel, J. Salbeck, H. Spreitzer, and M. Gratzel, "Solid-state dye-sensitized mesoporous TiO_2 solar cells with high photon-to-electron conversion efficiencies," *Nature*, vol. 395, pp. 583–585, Oct. 1998.

[11] B. Li, L. Wang, B. Kang, P. Wang, and Y. Qiu, "Review of recent progress in solid-state dye-sensitized solar cells," *Solar Energy Materials and Solar Cells*, vol. 90, no. 5, pp. 549 – 573, 2006.

[12] A. Yella, H.-W. Lee, H. N. Tsao, C. Yi, A. K. Chandiran, M. K. Nazeeruddin, E. W.-G. Diau, C.-Y. Yeh, S. M. Zakeeruddin, and M. Grätzel, "Porphyrin-sensitized solar cells with cobalt (II/III)–based redox electrolyte exceed 12 percent efficiency," *Science*, vol. 334, no. 6056, pp. 629–634, 2011.

[13] M. R. Narayan, "Review: Dye sensitized solar cells based on natural photosensitizers," *Renewable and Sustainable Energy Reviews*, vol. 16, no. 1, pp. 208 – 215, 2012.

[14] S. Mathew, A. Yella, P. Gao, R. Humphry-Baker, C. F. E., N. Ashari-Astani, I. Tavernelli, U. Rothlisberger, N. Khaja, and M. Graetzel, "Dye-sensitized solar cells with 13% efficiency achieved through the molecular engineering of porphyrin sensitizers," *Nat Chem*, vol. 6, pp. 242–247, Mar. 2014.

[15] H. J. Snaith, A. J. Moule, C. Klein, K. Meerholz, R. H. Friend, and M. Grätzel, "Efficiency enhancements in solid-state hybrid solar cells via reduced charge recombination and increased light capture," *Nano Letters*, vol. 7, pp. 3372–3376, Nov. 2007.

[16] B. E. Hardin, H. J. Snaith, and M. D. McGehee, "The renaissance of dye-sensitized solar cells," *Nat Photon*, vol. 6, pp. 162–169, Mar. 2012.

[17] G. Rose, *De novis quibusdam fossilibus quae in montibus Uraliis inveniuntur*. Berlin: Berlin, 1839.

[18] H. Fu and R. E. Cohen, "Polarization rotation mechanism for ultrahigh electromechanical response in single-crystal piezoelectrics," *Nature*, vol. 403, pp. 281–283, Jan. 2000.

[19] I. Terasaki, Y. Sasago, and K. Uchinokura, "Large thermoelectric power in NaCo2O4 single crystals," *Physical Review B*, vol. 56, pp. 12685–12687, NOV 15 1997.

[20] J. Wang, J. B. Neaton, H. Zheng, V. Nagarajan, S. B. Ogale, B. Liu, D. Viehland, V. Vaithyanathan, D. G. Schlom, U. V. Waghmare, N. A. Spaldin, K. M. Rabe, M. Wuttig, and R. Ramesh, "Epitaxial $BiFeO_3$ multiferroic thin film heterostructures," *Science*, vol. 299, no. 5613, pp. 1719–1722, 2003.

[21] E. Dagotto, T. Hotta, and A. Moreo, "Colossal magnetoresistant materials: The key role of phase separation," *Physics Reports-Review Section of Physics Letters*, vol. 344, pp. 1–153, APR 2001.

[22] Y. Maeno, H. Hashimoto, K. Yoshida, S. Nishizaki, T. Fujita, J. Bednorz, and F. Lichtenberg, "Superconductivity in a layered perovskite without copper," *Nature*, vol. 372, pp. 532–534, DEC 8 1994.

[23] V. M. Goldschmidt, "Die Gesetze der Krystallochemie," *Naturwissenschaften*, vol. 14, no. 21, pp. 477–485, 1926.

[24] P. Garcia-Fernandez, J. Aramburu, M. Barriuso, and M. Moreno, "Key role of covalent bonding in octahedral tilting in perovskites," *The Journal of Physical Chemistry Letters*, vol. 1, pp. 647–651, Feb. 2010.

[25] K. Tkacz-Smiecha, A. Kolezynskia, and W. S. Ptak, "Chemical bond in ferroelectric perovskites," *Ferroelectrics*, vol. 237, pp. 57–64, Jan. 2000.

[26] J. Rodriguez-Carvajal, M. Hennion, F. Moussa, A. Moudden, L. Pinsard, and A. Revcolevschi, "Neutron-diffraction study of the Jahn-Teller transition in stoichiometric $LaMnO_3$," *Physical Review B*, vol. 57, no. 6, p. R3189, 1998.

[27] J. Greedan, M. Bieringer, J. Britten, D. Giaquinta, and H.-C. zur Loye, "Synthesis, crystal structure, and unusual magnetic properties of $InMnO_3$," *Journal of Solid State Chemistry*, vol. 116, no. 1, pp. 118–130, 1995.

[28] H. Y. Hwang, S.-W. Cheong, P. G. Radaelli, M. Marezio, and B. Batlogg, "Lattice effects on the magnetoresistance in doped $LaMnO_3$," *Phys. Rev. Lett.*, vol. 75, pp. 914–917, Jul 1995.

[29] N. Allan, M. Dayer, D. Kulp, W. Mackrodt, and R. Powell, "Atomistic lattice simulations of the ternary fluorides AMF_3 (A=Li,Na,K,Rb,Cs; M=Mg,Ca,Sr,Ba)," *Journal of Fluorine Chemistry*, vol. 54, no. 1–3, pp. 128 –, 1991.

[30] X. Liu, R. Hong, and C. Tian, "Tolerance factor and the stability discussion of ABO_3-type ilmenite," *Journal of Materials Science: Materials in Electronics*, vol. 20, no. 4, pp. 323–327, 2009.

[31] D. Weber, "$CH_3NH_3PbX_3$, A Pb(II)-System with Cubic Perovskite Structure," *Zeitschrift fur Naturforschung Section B-A Journal of Chemical Sciences*, vol. 33, no. 12, pp. 1443–1445, 1978.

[32] D. Weber, "$CH_3NH_3SnBr_xI_{3-x}$ (X = 0-3) - Sn(II)-System with Cubic Perovskite Structure," *Zeitschrift fur Naturforschung Section B-A Journal of Chemical Sciences*, vol. 33, no. 8, pp. 862–865, 1978.

[33] T. Ishihara, J. Takahashi, and T. Goto, "Optical properties due to electronic transitions in two-dimensional semiconductors $(C_nH_{2n+1}NH_3)_2PbI_4$," *Physical review B*, vol. 42, no. 17, p. 11099, 1990.

[34] G. Papavassiliou and I. Koutselas, "Structural, optical and related properties of some natural three- and lower-dimensional semiconductor systems," *Synthetic Metals*, vol. 71, pp. 1713–1714, Apr. 1995.

[35] G. C. Papavassiliou, "Synthetic Three-and Lower-Dimensional Semiconductors Based on Inorganic Units," *Molecular Crystals and Liquid Crystals Science and Technology. Section A. Molecular Crystals and Liquid Crystals*, vol. 286, pp. 231–238, July 1996.

[36] Y. Takeoka, K. Asai, M. Rikukawa, and K. Sanui, "Systematic Studies on Chain Lengths, Halide Species, and Well Thicknesses for Lead Halide Layered Perovskite Thin Films," *Bulletin of the Chemical Society of Japan*, vol. 79, no. 10, pp. 1607–1613, 2006.

[37] D. B. Mitzi, *Synthesis, Structure, and Properties of Organic-Inorganic Perovskites and Related Materials*, pp. 1–121. John Wiley & Sons, Inc., 2007.

[38] N. Pellet, P. Gao, G. Gregori, T.-Y. Yang, M. K. Nazeeruddin, J. Maier, and M. Gratzel, "Mixed-organic-cation perovskite photovoltaics for enhanced solar-light harvesting," *Angewandte Chemie International Edition*, vol. 53, no. 12, pp. 3151–3157, 2014.

[39] Y. Takahashi, R. Obara, Z.-Z. Lin, Y. Takahashi, T. Naito, T. Inabe, S. Ishibashi, and K. Terakura, "Charge-transport in tin-iodide perovskite $CH_3NH_3SnI_3$: origin of high conductivity.," *Dalton transactions (Cambridge, England : 2003)*, vol. 40, pp. 5563–8, May 2011.

[40] C. C. Stoumpos, C. D. Malliakas, and M. G. Kanatzidis, "Semiconducting tin and lead iodide perovskites with organic cations: Phase transitions, high mobilities, and near-infrared photoluminescent properties," *Inorganic Chemistry*, vol. 52, no. 15, pp. 9019–9038, 2013.

[41] D. Mitzi and K. Liang, "Synthesis, resistivity, and thermal properties of the cubic perovskite $NH_2CH{=}NH_2SnI_3$ and related systems," *Journal of Solid State Chemistry*, vol. 134, no. 2, pp. 376 – 381, 1997.

[42] D. B. Mitzi, C. A. Feild, W. T. A. Harrison, and A. M. Guloy, "Conducting tin halides with a layered organic-based perovskite structure," *Nature*, vol. 369, pp. 467–469, June 1994.

[43] D. Kruk, W. Medycki, J. Przesławski, S. Dacko, A. Piecha, and R. Jakubas, "Thermodynamic properties and molecular motions in ferroelectric $(C_3N_2H_5)_5Sb_2Br_{11}$," *Chemical Physics*, vol. 380, no. 1–3, pp. 86 – 91, 2011.

[44] F. Chiarella, P. Ferro, F. Licci, M. Barra, M. Biasiucci, a. Cassinese, and R. Vaglio, "Preparation and transport properties of hybrid organic-inorganic $CH_3NH_3SnBr_3$ films," *Applied Physics A*, vol. 86, pp. 89–93, Nov. 2006.

[45] J. L. Knutson, J. D. Martin, and D. B. Mitzi, "Tuning the band gap in hybrid tin iodide perovskite semiconductors using structural templating," *Inorganic chemistry*, vol. 44, no. 13, pp. 4699–4705, 2005.

[46] Y. Takahashi, H. Hasegawa, Y. Takahashi, and T. Inabe, "Hall mobility in tin iodide perovskite ch3nh3sni3: Evidence for a doped semiconductor," *Journal of Solid State Chemistry*, vol. 205, no. 0, pp. 39 – 43, 2013.

[47] D. B. Mitzi, "Synthesis, crystal structure, and optical and thermal properties of $(C_4H_9NH_3)_2MI_4$ (M = Ge, Sn, Pb)," *Chemistry of Materials*, vol. 8, no. 3, pp. 791–800, 1996.

[48] Z.-L. Xiao, H.-Z. Chen, M.-M. Shi, G. Wu, R.-J. Zhou, Z.-S. Yang, M. Wang, and B.-Z. Tang, "Preparation and characterization of organic-inorganic hybrid perovskite $(C_4H_9NH_3)_2CuCl_4$," *Materials Science and Engineering: B*, vol. 117, no. 3, pp. 313 – 316, 2005.

[49] C. Aruta, F. Licci, A. Zappettini, F. Bolzoni, F. Rastelli, P. Ferro, and T. Besagni, "Growth and optical, magnetic and transport properties of $(C_4H_9NH_3)_2MCl_4$ organic-inorganic hybrid films (M= Cu, Sn)," *Applied Physics A*, vol. 81, no. 5, pp. 963–968, 2005.

[50] D. B. Mitzi and K. Liang, "Preparation and properties of $(C_4H_9NH_3)_2EuI_4$: A luminescent organic-inorganic perovskite with a divalent rare-earth metal halide framework," *Chemistry of Materials*, vol. 9, no. 12, pp. 2990–2995, 1997.

[51] J. Zaleski and a. Pietraszko, "Structure at 200 and 298 K and X-ray investigations of the phase transition at 242 K of $[NH_2(CH_3)_2]_3Sb_2Cl_9$ (DMACA)," *Acta Crystallographica Section B Structural Science*, vol. 52, pp. 287–295, Apr. 1996.

[52] Y.-D. Huh, J. H. Kim, S. S. Kweon, W.-K. Kuk, C.-S. Hwang, J.-W. Hyun, Y.-J. Kim, and Y. Park, "Structure of the organic-inorganic hybrid $(C_6H_5C_2H_4NH_3)_2ZnBr_4$," *Current Applied Physics*, vol. 6, no. 2, pp. 219 – 223, 2006. Engineering Aspects of Nanomaterials and Technologies Engineering Aspects of Nanomaterials and Technologies.

[53] J. Jozkow, R. Jakubas, G. Bator, and A. Pietraszko, "Ferroelectric properties of $(C_5H_5NH)_5Bi_2Br_{11}$," *The Journal of Chemical Physics*, vol. 114, no. 16, pp. 7239–7246, 2001.

[54] J. Foster and N. S. Gill, "Complex halides of the transition metals. part iii. electronic spectra and ligand field parameters of octahedral and tetrahedral halogeno-complexes of manganese (ii)," *Journal of the Chemical Society A: Inorganic, Physical, Theoretical*, pp. 2625–2629, 1968.

[55] R. Mokhlisse, M. Couzi, N. Chanh, Y. Haget, C. Hauw, and A. Meresse, "Raman scattering and x-ray diffraction study of structural phase transitions in the perovskite-type layer compound $(C_3H_7NH_3)_2CdC_4$," *Journal of Physics and Chemistry of Solids*, vol. 46, no. 2, pp. 187–195, 1985.

[56] S. J. Jung, R.-Z. Yin, E. J. Oh, U.-I. Cho, K. H. Kim, and C. H. Yo, "Synthesis and characteristics of the organic layered structure material of $(C_4H_9NH_3)_2Fe_xPb_{1-x}Cl_4$," *Bulletin-Korean Chemical Society*, vol. 22, no. 7, pp. 703–708, 2001.

[57] W. Fang, C. Tang, R. Chen, D. Jia, W. Jiang, and Y. Zhang, "Polymeric heterometallic Pb–Ag iodometallates, iodoplumbates and iodoargentates with lanthanide complex cations as templates," *Dalton Transactions*, vol. 42, no. 42, pp. 15150–15158, 2013.

[58] Y. Ogomi, A. Morita, S. Tsukamoto, T. Saitho, N. Fujikawa, Q. Shen, T. Toyoda, K. Yoshino, S. S. Pandey, T. Ma, and S. Hayase, "$CH_3NH_3Sn_xPb_{1-x}I_3$ perovskite solar cells covering up to 1060 nm," *The Journal of Physical Chemistry Letters*, vol. 5, no. 6, pp. 1004–1011, 2014.

[59] W.-X. Chai, L.-M. Wu, J.-Q. Li, and L. Chen, "Silver iodobismuthates: Syntheses, structures, properties, and theoretical studies of $[Bi_2Ag_2I_{10}{}^{2-}]_n$ and $[Bi_4Ag_2I_{16}{}^{2-}]_n$," *Inorganic Chemistry*, vol. 46, no. 4, pp. 1042–1044, 2007. PMID: 17291103.

[60] W.-X. Chai, L.-M. Wu, J.-Q. Li, and L. Chen, "A series of new copper iodobismuthates: Structural relationships, optical band gaps affected by dimensionality, and distinct thermal stabilities," *Inorganic Chemistry*, vol. 46, no. 21, pp. 8698–8704, 2007. PMID: 17845032.

[61] L.-Q. Fan, L.-M. Wu, and L. Chen, "Syntheses, crystal structures, and properties of heterometallic iodoplumbates: Bicubane, ribbon, and chain configurations," *Inorganic Chemistry*, vol. 45, no. 8, pp. 3149–3151, 2006. PMID: 16602767.

[62] C. Feldmann, "$CuBi_7I_{19}(C_4H_8O_3H)_3(C_4H_8O_3H_2)$, a novel complex bismuth iodide containing one-dimensional $[CuBi_5I_{19}]^{3-}$ chains," *Inorganic Chemistry*, vol. 40, no. 4, pp. 818–819, 2001.

[63] M.-W. Yuan, L.-H. Li, and L. Chen, "Syntheses, structures, and theoretical studies of new mercury iodobismuthates: $(Et_4N)_4(Bi_4Hg_2I_{20})$ and $(nBu_4N)_2(Bi_2HgI_{10})$," *Zeitschrift fur anorganische und allgemeine Chemie*, vol. 635, no. 11, pp. 1645–1649, 2009.

[64] G. C. Papavassiliou, G. a. Mousdis, I. B. Koutselas, and G. J. Papaioannou, "Excitonic Bands in the Photoconductivity Spectra of Some Organic-Inorganic Hybrid Compounds Based on Metal Halide Units," *International Journal of Modern Physics B*, vol. 15, pp. 3727–3731, Dec. 2001.

[65] G. C. Papavassiliou, G. Pagona, N. Karousis, G. a. Mousdis, I. Koutselas, and A. Vassilakopoulou, "Nanocrystalline/microcrystalline materials based on lead-halide units," *Journal of Materials Chemistry*, vol. 22, no. 17, p. 8271, 2012.

[66] A. Kojima, M. Ikegami, K. Teshima, and T. Miyasaka, "Highly Luminescent Lead Bromide Perovskite Nanoparticles Synthesized with Porous Alumina Media," *Chemistry Letters*, vol. 41, no. 4, pp. 397–399, 2012.

[67] M. Era, S. Morimoto, T. Tsutsui, and S. Saito, "Organic-inorganic heterostructure electroluminescent device using a layered perovskite semiconductor $(C_6H_5C_2H_4NH_3)_2PbI_4$," *Applied Physics Letters*, vol. 65, no. 6, p. 676, 1994.

[68] K. Chondroudis and D. B. Mitzi, "Electroluminescence from an organic-inorganic perovskite incorporating a quaterthiophene dye within lead halide perovskite layers," *Chemistry of Materials*, vol. 11, no. 11, pp. 3028–3030, 1999.

[69] K. Gauthron, J.-S. Lauret, L. Doyennette, G. Lanty, a. Al Choueiry, S. J. Zhang, a. Brehier, L. Largeau, O. Mauguin, J. Bloch, and E. Deleporte, "Optical spectroscopy of two-dimensional layered $(C_6H_5C_2H_4NH_3)_2$-PbI_4 perovskite.," *Optics express*, vol. 18, pp. 5912–9, Mar. 2010.

[70] Z. Cheng, Z. Wang, R. Xing, Y. Han, and J. Lin, "Patterning and photoluminescent properties of perovskite-type organic/inorganic hybrid luminescent films by soft lithography," *Chemical Physics Letters*, vol. 376, pp. 481–486, July 2003.

[71] C. R. Kagan, D. B. Mitzi, and C. D. Dimitrakopoulos, "Organic-inorganic hybrid materials as semiconducting channels in thin-film field-effect transistors," *Science*, vol. 286, pp. 945–947, Oct. 1999.

[72] I. Koutselas, P. Bampoulis, E. Maratou, T. Evagelinou, G. Pagona, and G. C. Papavassiliou, "Some unconventional organic-inorganic hybrid low-dimensional semiconductors and related light-emitting devices," *The Journal of Physical Chemistry C*, vol. 115, no. 17, pp. 8475–8483, 2011.

[73] C. qing Xu, T. Kondo, H. Sakakura, K. Kumata, Y. Takahashi, and R. Ito, "Optical third-harmonic generation in layered perovskite-type material $(C_{10}H_{21}NH_3)_2PbI_4$," *Solid State Communications*, vol. 79, no. 3, pp. 245 – 248, 1991.

[74] C. Li, H. Deng, J. Wan, Y. Zheng, and W. Dong, "Photoconductive properties of organic-inorganic hybrid perovskite $(C_6H_{13}NH_3)_2(CH_3NH_3)_{m-1}Pb_mI_{3m+1}$:$TiO_2$ nanocomposites device structure," *Materials Letters*, vol. 64, pp. 2735–2737, Dec. 2010.

[75] C. Li, J. Wan, Y. Zheng, and W. Dong, "Tuning photoconductive properties of organic-inorganic hybrid perovskite nanocomposite device via organic layer's thickness," *Materials Letters*, vol. 76, no. 0, pp. 187 – 189, 2012.

[76] D. B. Mitzi, C. D. Dimitrakopoulos, and L. L. Kosbar, "Structurally Tailored Organic-Inorganic Perovskites: An Optical Properties and Solution-Processed Channel Materials for Thin-Film Transistors," *Chemistry of Materials*, vol. 13, pp. 3728–3740, Oct. 2001.

[77] N. A. Gippius, E. A. Muljarov, S. G. Tikhodeev, T. Ishihara, and L. V. Keldysh, "Dielectrically confined excitons and polaritons in natural superlattices -perovskite lead iodide semiconductors," *MRS Proceedings*, vol. 328, 1 1993.

[78] T. Kataoka, T. Kondo, R. Ito, S. Sasaki, K. Uchida, and N. Miura, "Magneto-optical study on excitonic spectra in $(C_6H_{13}NH_3)_2PbI_4$," *Physical Review B*, vol. 47, no. 4, p. 2010, 1993.

[79] N. Onoda-Yamamuro, T. Matsuo, and H. Suga, "Dielectric study of $CH_3NH_3PbX_3$ (X = Cl, Br, I)," *Journal of Physics and Chemistry of Solids*, vol. 53, no. 7, pp. 935 – 939, 1992.

[80] G. Papavassiliou, "Three- and low-dimensional inorganic semiconductors," *Progress in Solid State Chemistry*, vol. 25, no. 3–4, pp. 125 – 270, 1997.

[81] K. Tanaka, T. Takahashi, T. Ban, T. Kondo, K. Uchida, and N. Miura, "Comparative study on the excitons in lead-halide-based perovskite-type crystals $CH_3NH_3PbBr_3$ $CH_3NH_3PbI_3$," *Solid State Communications*, vol. 127, pp. 619–623, Sept. 2003.

[82] A. Poglitsch and D. Weber, "Dynamic disorder in methylammoniumtrihalogenoplumbates (II) observed by millimeter-wave spectroscopy," *The Journal of Chemical Physics*, vol. 87, no. 11, 1987.

[83] K. Tanaka and T. Kondo, "Bandgap and exciton binding energies in lead-iodide-based natural quantum-well crystals," *Science and Technology of Advanced Materials*, vol. 4, pp. 599–604, Nov. 2003.

[84] J. Calabrese, N. L. Jones, R. L. Harlow, N. Herron, D. L. Thorn, and Y. Wang, "Preparation and characterization of layered lead halide compounds," *Journal of the American Chemical Society*, vol. 113, pp. 2328–2330, Mar. 1991.

[85] L. Guo, Z. Sun, G. Zhao, X. Li, and H. Liu, "Synthesis and characterization of layered perovskite-type organic-inorganic hybrids $(R\text{-}NH_3)_2(CH_3NH_3)Pb_2I_7$," *Journal of Wuhan University of Technology-Mater. Sci. Ed.*, vol. 27, pp. 957–961, Oct. 2012.

[86] T. Ishihara, "Optical-properties of PbI-based perovskite structures," *Journal of Luminescence*, vol. 60-1, pp. 269–274, 1994.

[87] T. Ogawa and Y. Kanemitsu, *Optical properties of low-dimensional materials*, vol. 1. World Scientific, 1995.

[88] Y. Tabuchi, K. Asai, M. Rikukawa, K. Sanui, and K. Ishigure, "Preparation and characterization of natural lower dimensional layered perovskite-type compounds," *Journal of Physics and Chemistry of Solids*, vol. 61, pp. 837–845, June 2000.

[89] Y. Wei, P. Audebert, L. Galmiche, J.-S. Lauret, and E. Deleporte, "Synthesis, optical properties and photostability of novel fluorinated organic-inorganic hybrid $(R\text{-}NH_3)_2PbX_4$ semiconductors," *Journal of Physics D: Applied Physics*, vol. 46, p. 135105, Apr. 2013.

[90] K. Liang, D. B. Mitzi, and M. T. Prikas, "Synthesis and Characterization of Organic-Inorganic Perovskite Thin Films Prepared Using a Versatile Two-Step Dipping Technique," *Chemistry of Materials*, vol. 10, pp. 403–411, Jan. 1998.

[91] J. Burschka, N. Pellet, S.-J. Moon, R. Humphry-Baker, P. Gao, M. K. Nazeeruddin, and M. Gratzel, "Sequential deposition as a route to high-performance perovskite-sensitized solar cells," *Nature*, vol. 499, pp. 316–319, July 2013.

[92] M. Era and T. Hattori, "Self-Organized Growth of PbI-Based Layered Perovskite Quantum Well by Dual-Source Vapor Deposition," *Chemistry of Materials*, vol. 4756, no. 16, pp. 8–10, 1997.

[93] D. B. Mitzi, K. Chondroudis, and C. R. Kagan, "Organic-inorganic electronics," *IBM journal of research and development*, vol. 45, no. 1, pp. 29–45, 2001.

[94] Q. Chen, H. Zhou, Z. Hong, S. Luo, H.-S. Duan, H.-H. Wang, Y. Liu, G. Li, and Y. Yang, "Planar heterojunction perovskite solar cells via vapor-assisted solution process," *Journal of the American Chemical Society*, vol. 136, no. 2, pp. 622–625, 2014.

[95] R. Shannon, "Revised effective ionic radii and systematic studies of interatomic distances in halides and chalcogenides," *Acta Crystallographica Section A: Crystal Physics, Diffraction, Theoretical and General Crystallography*, vol. 32, no. 5, pp. 751–767, 1976.

[96] L. Ahrens, "The use of ionization potentials part 1. ionic radii of the elements," *Geochimica et Cosmochimica Acta*, vol. 2, no. 3, pp. 155 – 169, 1952.

[97] A. Wojakowska, "Phase equilibrium diagram for the tin(ii) bromide-copper(i) bromide system," *Journal of thermal analysis*, vol. 35, no. 1, pp. 91–97, 1989.

[98] E. Hanamura, N. Nagaosa, M. Kumagai, and T. Takagahara, "Quantum wells with enhanced exciton effects and optical non-linearity," *Materials Science and Engineering: B*, vol. 1, no. 3–4, pp. 255 – 258, 1988.

[99] A. Kojima, K. Teshima, Y. Shirai, and T. Miyasaka, "Organometal halide perovskites as visible-light sensitizers for photovoltaic cells," *Journal of the American Chemical Society*, vol. 131, pp. 6050–6051, Apr. 2009.

[100] J.-H. Im, C.-R. Lee, J.-W. Lee, S.-W. Park, and N.-G. Park, "6.5% efficient perovskite quantum-dot-sensitized solar cell," *Nanoscale*, vol. 3, no. 10, pp. 4088–4093, 2011.

[101] H. S. Kim, C. R. Lee, J. H. Im, K. B. Lee, T. Moehl, A. Marchioro, S. J. Moon, R. Humphry-Baker, J. H. Yum, J. E. Moser, M. Gratzel, and N. G. Park, "Lead iodide perovskite sensitized all-solid-state submicron thin film mesoscopic solar cell with efficiency exceeding 9%," *Scientific Reports*, vol. 2, 2012.

[102] L. Etgar, P. Gao, Z. Xue, Q. Peng, A. K. Chandiran, B. Liu, M. K. Nazeeruddin, and M. Grätzel, "Mesoscopic $CH_3NH_3PbI_3/TiO_2$ Heterojunction Solar Cells," *Journal of the American Chemical Society*, vol. 134, pp. 17396–17399, Oct. 2012.

[103] S. D. Stranks, G. E. Eperon, G. Grancini, C. Menelaou, M. J. P. Alcocer, T. Leijtens, L. M. Herz, A. Petrozza, and H. J. Snaith, "Electron-Hole Diffusion Lengths Exceeding 1 Micrometer in an Organometal Trihalide Perovskite Absorber," *Science*, vol. 342, pp. 341–344, Oct. 2013.

[104] G. C. Xing, N. Mathews, S. Y. Sun, S. S. Lim, Y. M. Lam, M. Gratzel, S. Mhaisalkar, and T. C. Sum, "Long-range balanced electron- and hole-transport lengths in organic-inorganic $CH_3NH_3PbI_3$," *Science*, vol. 342, no. 6156, pp. 344–347, 2013.

[105] G. E. Eperon, V. M. Burlakov, P. Docampo, A. Goriely, and H. J. Snaith, "Morphological Control for High Performance, Solution-Processed Planar Heterojunction Perovskite Solar Cells," *Advanced Functional Materials*, vol. 24, no. 1, pp. 151–157, 2014.

[106] K. Aydin, V. E. Ferry, R. M. Briggs, and H. A. Atwater, "Broadband polarization-independent resonant light absorption using ultrathin plasmonic super absorbers," *Nat Commun*, vol. 2, pp. 517–, Nov. 2011.

[107] E. Ozbay, "Plasmonics: Merging photonics and electronics at nanoscale dimensions," *Science*, vol. 311, no. 5758, pp. 189–193, 2006.

[108] K. Thomas, S. Barazzouk, B. Ipe, S. Joseph, and P. Kamat, "Uniaxial plasmon coupling through longitudinal self-assembly of gold nanorods," *Journal of Physical Chemistry B*, vol. 108, pp. 13066–13068, SEP 2 2004.

[109] J. A. Fan, C. Wu, K. Bao, J. Bao, R. Bardhan, N. J. Halas, V. N. Manoharan, P. Nordlander, G. Shvets, and F. Capasso, "Self-assembled plasmonic nanoparticle clusters," *Science*, vol. 328, no. 5982, pp. 1135–1138, 2010.

[110] A. Boltasseva, "Plasmonic components fabrication via nanoimprint," *Journal of Optics A: Pure and Applied Optics*, vol. 11, no. 11, p. 114001, 2009.

[111] L. Novotny and B. Hecht, *Principles of Nano-Optics.* Cambridge University Press, 2006.

[112] J. Smajic, C. Hafner, L. Raguin, K. Tavzarashvili, and M. Mishrikey, "Comparison of numerical methods for the analysis of plasmonic structures," *Journal of Computational and Theoretical Nanoscience*, vol. 6, pp. 763–774, MAR 2009.

[113] M. Mäder, T. Höche, J. W. Gerlach, S. Perlt, J. Dorfmüller, M. Saliba, R. Vogelgesang, K. Kern, and B. Rauschenbach, "Plasmonic activity of large-area gold-nanodot arrays on arbitrary substrates," *Nano Letters*, pp. 1–16, 2009.

[114] J. Gu, J. Demey, M. Moeremans, and J. M. Polak, "Sequential use of the pap and immunogold staining methods for the light microscopical double staining of tissue antigens : Its application to the study of regulatory peptides in the gut," *Regulatory Peptides*, vol. 1, no. 6, pp. 365–374, 1981.

[115] W. P. Faulk and G. M. Taylor, "Immunocolloid Method for electron microscope," *Immunochemistry*, vol. 8, no. 11, pp. 1081–&, 1971.

[116] N. Liu, H. Guo, L. Fu, S. Kaiser, H. Schweizer, and H. Giessen, "Three-dimensional photonic metamaterials at optical frequencies," *Nature Materials*, vol. 7, pp. 31–37, JAN 2008.

[117] N. Liu, M. Hentschel, T. Weiss, A. P. Alivisatos, and H. Giessen, "Three-dimensional plasmon rulers," *Science*, vol. 332, no. 6036, pp. 1407–1410, 2011.

[118] M. Hentschel, M. Saliba, R. Vogelgesang, H. Giessen, A. P. Alivisatos, and N. Liu, "Transition from isolated to collective modes in plasmonic oligomers," *Nano Letters*, vol. 10, no. 7, pp. 2721–2726, 2010.

[119] M. Fleischmann, P. J. Hendra, and A. J. McQuillan, "Raman spectra of pyridine adsorbed at a silver electrode," *Chemical Physics Letters*, vol. 26, no. 2, pp. 163–166, 1974.

[120] M. Fan, G. F. S. Andrade, and A. G. Brolo, "A review on the fabrication of substrates for surface enhanced Raman spectroscopy and their applications in analytical chemistry," *Analytica Chimica Acta*, vol. 693, pp. 7–25, MAY 5 2011.

[121] M. I. Stockman *et al.*, "Nanofocusing of optical energy in tapered plasmonic waveguides," *Physical review letters*, vol. 93, pp. 137404–137404, 2004.

[122] H. A. Atwater and A. Polman, "Plasmonics for improved photovoltaic devices.," *Nature Materials*, vol. 9, no. 3, pp. 205–13, 2010.

[123] S. D. Standridge, G. C. Schatz, and J. T. Hupp, "Distance dependence of plasmon-enhanced photocurrent in dye-sensitized solar cells," *Journal of the American Chemical Society*, vol. 131, no. 24, pp. 8407–8409, 2009.

[124] M. D. Brown, T. Suteewong, R. S. S. Kumar, V. D'Innocenzo, A. Petrozza, M. M. Lee, U. Wiesner, and H. J. Snaith, "Plasmonic dye-sensitized solar cells using core-shell metal-insulator nanoparticles," *Nano Letters*, vol. 11, no. 2, pp. 438–445, 2011.

[125] J. Yang, J. You, C.-C. Chen, W.-C. Hsu, H.-r. Tan, X. W. Zhang, Z. Hong, and Y. Yang, "Plasmonic polymer tandem solar cell," *ACS Nano*, vol. 5, no. 8, pp. 6210–6217, 2011.

[126] D. H. Wang, D. Y. Kim, K. W. Choi, J. H. Seo, S. H. Im, J. H. Park, O. O. Park, and A. J. Heeger, "Enhancement of donor-acceptor polymer bulk heterojunction solar cell power conversion efficiencies by addition of au nanoparticles," *Angewandte Chemie-International Edition*, vol. 50, no. 24, pp. 5519–5523, 2011.

[127] X. H. Li, W. C. H. Choy, L. J. Huo, F. X. Xie, W. E. I. Sha, B. F. Ding, X. Guo, Y. F. Li, J. H. Hou, J. B. You, and Y. Yang, "Dual plasmonic nanostructures for high performance inverted organic solar cells," *Advanced Materials*, vol. 24, no. 22, pp. 3046–3052, 2012.

[128] D. M. Schaadt, B. Feng, and E. T. Yu, "Enhanced semiconductor optical absorption via surface plasmon excitation in metal nanoparticles," *Applied Physics Letters*, vol. 86, no. 6, 2005.

[129] K. R. Catchpole and A. Polman, "Plasmonic solar cells," *Optics Express*, vol. 16, no. 26, pp. 21793–21800, 2008.

[130] P. Reineck, G. P. Lee, D. Brick, M. Karg, P. Mulvaney, and U. Bach, "A solid-state plasmonic solar cell via metal nanoparticle self-assembly," *Advanced Materials*, vol. 24, no. 35, pp. 4750–4755, 2012.

CHAPTER 3

Plasmonic Modelling and Simulation Results

This chapter provides the theoretical foundation for calculating optical cross sections and introduces the multiple multipole method (MMP) for simulating the electromagnetic field. More details can be found in previous work [1–3]. However, for this thesis only a brief summary is given.

The simulation results are presented and compared to experimental data. Calculations are used to evaluate the quality of synthesized nanoparticles (NPs), to demonstrate potential usage of NPs as plasmonic sensors for measuring an unknown index of refraction (IoR) of the surrounding medium, and for the optical cross sections of core-shell NPs in media closely resembling the photoactive layer of dye-sensitized solar cell (DSSCs).

3.1 Optical Cross Sections

This section outlines the derivation of the optical cross sections for absorption, scattering, and extinction which are accessible to both theory and experiment. In the next part, a general model for the dielectric constant for metals is presented and gold is shown as an example. This provides the framework for the multiple multipole method to simulate cross sections of non-trivial geometries which are used in the subsequent section to analyse experimental results.

The derivations follow my previous work [1–3], specifically [2] where more detailed analysis is provided. Here, only a concise summary is presented as to motivate and understand the underlying theory for the simulation method.

3.1.1 Maxwell Equations and Poynting theorem

Calculating the interaction of electromagnetic waves with metallic nanostructures translates into solving the Maxwell equations. However, analytical solutions are only available for simple geometries which often necessitates numerical approximations for more realistic scenarios. The aim is to get to an expression for the optical cross sections which can be measured experimentally with ultraviolet–visible spectroscopy (UV-vis).

The starting points are the macroscopic Maxwell equations in SI units for the case of *linear, isotropic, and homogenous media with plane wave solutions* [4]:

$$\mathbf{k} \cdot \mathbf{D}_0 = 0 \tag{3.1a}$$

$$\mathbf{k} \cdot \mathbf{B}_0 = 0 \tag{3.1b}$$

$$\mathbf{k} \times \mathbf{E}_0 = +\omega \mathbf{B}_0 \tag{3.1c}$$

$$\mathbf{k} \times \mathbf{H}_0 = -\omega \mathbf{D}_0 \tag{3.1d}$$

with the electric field $\mathbf{E}$, the electric displacement field $\mathbf{D} = \tilde{\varepsilon}\mathbf{E}$, the magnetic field $\mathbf{B}$, the magnetizing field $\mathbf{H} = \mu^{-1}\mathbf{B}$, the charge density ρ, and the current density $\mathbf{J} = \sigma\mathbf{E}$.

The complex dielectric constant can be written as $\tilde{\varepsilon} = \varepsilon + i\frac{\sigma}{\omega}$ where ε is absolute permittivity and σ is conductivity.

The plane wave solutions can be written as $\mathbf{E} = \mathbf{E}_0 \exp(+i\mathbf{kr}) \exp(-i\omega t)$ with the complex wave vector $\mathbf{k} = \mathbf{k}' + i\mathbf{k}''$ (propagation direction of the wave). $\mathbf{k}'$ expresses the oscillatory and $\mathbf{k}''$ the damping part of the wave.

From the Maxwell equations 3.1, a differential version of the *Poynting theorem*, i.e. the expression for energy conservation, can be derived. Detailed calculations can be found in most standard literature on electrodynamics [4].

$$\dot{U}_{em} + \mathcal{P}_e = W_{em} + \mathcal{P}_e = -\nabla \cdot \mathbf{S} \tag{3.2}$$

with the electric power density $\dot{U}_e = W_e$, the magnetic power density $\dot{U}_m = W_m$, the total electromagnetic power density $\dot{U}_{em} = W_{em}$, the Joule heating $\mathcal{P}_e$, and the Poynting vector $\mathbf{S}$ defined as

$$W_e = \mathbf{E} \cdot \dot{\mathbf{D}} \tag{3.3a}$$

$$W_m = \mathbf{H} \cdot \dot{\mathbf{B}} \tag{3.3b}$$

$$W_{em} = W_e + W_m \tag{3.3c}$$

$$\mathcal{P}_e = \mathbf{E} \cdot \mathbf{J} \tag{3.3d}$$

$$\mathbf{S} = \mathbf{E} \times \mathbf{H} \tag{3.3e}$$

Integrating over eq. 3.2 and using the Gauss theorem results in

$$\int_V W_{em} d^3r + \int_V \mathcal{P}_e d^3r = -\oint_{\partial V} \mathbf{n} \cdot \mathbf{S} d^2r \tag{3.4}$$

The integral version of the Poynting theorem states that the net flux of energy into a volume, given by the surface integral over the Poynting vector, is equal to the sum of Joule heating, which is the power dissipated in the volume, and the time rate change of the stored electromagnetic energy in the volume. From the integral it is clear that the Poynting theorem can be evaluated for any closed surface volume. Very often, a sphere is a suitable choice in order to simplify calculations.

In the next step, the time average of a time harmonic real field is defined as

$$\langle \mathbf{A_{real}} \rangle_t := \lim_{T \to \infty} \frac{1}{2T} \int_{-T}^{+T} \mathbf{A_{real}} dt \tag{3.5}$$

with $\mathbf{A_{real}} = Re[\mathbf{A} \cdot \exp(-i\omega t)]$ and the complex vector field $\mathbf{A}$.

The time harmonic factor is selected as $\exp(-i\omega t)$ creating consistency with the dielectric constant measurements by Johnson and Christy [5]. This selection is a convention and in principle $\exp(+i\omega t)$ is an equally valid choice.

With eq. 3.5 and 3.3e a time averaged version of the Poynting vector can be deduced [4]:

$$\langle \mathbf{S} \rangle_t = \frac{1}{2} Re[\mathbf{E} \times \mathbf{H}^*] \tag{3.6}$$

The index 't' denotes the time-average which is dropped for convenience in all further notations unless otherwise stated. Applying this averaging procedure to eq. 3.4, the Poynting theorem becomes

$$\int_V \langle W_{em} \rangle d^3r + \int_V \langle \mathcal{P}_e \rangle d^3r = -\oint_{\partial V} \mathbf{n} \cdot \langle \mathbf{S} \rangle d^2r \tag{3.7}$$

3.1.2 Absorption, scattering and extinction cross section

In this section, the assumption is a single particle in a non-absorbing medium illuminated by an electromagnetic wave. The wave propagates through the particle and gets scattered. The total field is comprised by the *inc*ident ($\mathbf{E}_{inc}$ and $\mathbf{H}_{inc}$) and *sca*ttered ($\mathbf{E}_{sca}$ and $\mathbf{H}_{sca}$) fields.

$$\mathbf{E} = \mathbf{E}_{inc} + \mathbf{E}_{sca} \quad (3.8a) \qquad \mathbf{H} = \mathbf{H}_{inc} + \mathbf{H}_{sca} \quad (3.8b)$$

The Poynting vector from eq. 3.4 can then be calculated by putting eq. 3.8a 3.8b, in eq. 3.6:

$$\langle \mathbf{S} \rangle = \frac{1}{2} Re[\mathbf{E} \times \mathbf{H}^*] = \langle \mathbf{S}_{inc} \rangle + \langle \mathbf{S}_{sca} \rangle + \langle \mathbf{S}_{ext} \rangle \quad (3.9)$$

where

$$\langle \mathbf{S}_{inc} \rangle = \frac{1}{2} Re[\mathbf{E}_{inc} \times \mathbf{H}^*_{inc}] \quad (3.10a)$$

$$\langle \mathbf{S}_{sca} \rangle = \frac{1}{2} Re[\mathbf{E}_{sca} \times \mathbf{H}^*_{sca}] \quad (3.10b)$$

$$\langle \mathbf{S}_{ext} \rangle = \frac{1}{2} Re[\mathbf{E}_{inc} \times \mathbf{H}^*_{sca} + \mathbf{E}_{sca} \times \mathbf{H}^*_{inc}] \quad (3.10c)$$

Equation 3.10c reveals *ext*inction ($\mathbf{S}_{ext}$) to be an interference effect between the *inc*ident ($\mathbf{S}_{inc}$) and *sca*ttered ($\mathbf{S}_{sca}$) field.

Absorption is the surface integral over the Poynting vector $\mathbf{S}$ which can be recalculated into the average Poynting theorem by using eq. 3.9 in eq. 3.7

$$W_{abs} = -\oint_{\partial V} \mathbf{n} \cdot \langle \mathbf{S} \rangle d^2 r = -\oint_{\partial V} \mathbf{n} \cdot [\langle \mathbf{S}_{inc} \rangle + \langle \mathbf{S}_{sca} \rangle + \langle \mathbf{S}_{ext} \rangle] \quad (3.11)$$

As already mentioned, the integration volume can be any closed surface enclosing the object. For this work a sphere is chosen. The unit normal vector on the integration area can be defined to show *out* of the sphere ensuring that the absorption is a positive quantity because the Poynting vector shows *into* the sphere. This is antiparallel to the choice of the normal unit vector. Equation 3.11 contains a minus sign and thus W_{abs} becomes positive.

Moreover, W_{inc}, W_{sca}, and W_{ext} are defined as

$$W_{inc} = -\oint_{\partial V} \mathbf{n} \cdot \langle \mathbf{S}_{inc} \rangle d^2 r = -\frac{1}{2} \oint_{\partial V} \mathbf{n} \cdot \langle \mathbf{E}_{inc} \times \mathbf{H}^*_{inc} \rangle d^2 r \quad (3.12)$$

$$W_{sca} = +\oint_{\partial V} \mathbf{n} \cdot \langle \mathbf{S}_{sca} \rangle d^2 r = +\frac{1}{2} \oint_{\partial V} \mathbf{n} \cdot \langle \mathbf{E}_{sca} \times \mathbf{H}^*_{sca} \rangle d^2 r \quad (3.13)$$

$$W_{ext} = -\oint_{\partial V} \mathbf{n} \cdot \langle \mathbf{S}_{ext} \rangle d^2 r = -\frac{1}{2} \oint_{\partial V} \mathbf{n} \cdot \langle \mathbf{E}_{inc} \times \mathbf{H}^*_{sca} + \mathbf{E}_{sca} \times \mathbf{H}^*_{inc} \rangle d^2 r \quad (3.14)$$

These quantities are positive because the unit normal vector was defined to show out of the sphere.

Using these definitions, eq. 3.11 can be written as

$$W_{abs} = W_{inc} - W_{sca} + W_{ext} \xrightarrow{W_{inc}=0} W_{ext} = W_{abs} + W_{sca} \quad (3.15)$$

Thus, for non-absorbing media ($W_{inc} = 0$), extinction is the sum of absorption and scattering. Finally, absorption, scattering and extinction cross section can be introduced [6] as

$$C_{abs} = W_{abs}/I_0 \tag{3.16a}$$

$$C_{sca} = W_{sca}/I_0 \tag{3.16b}$$

$$C_{ext} = C_{abs} + C_{sca} \tag{3.16c}$$

with $I_0 = \frac{1}{2}\sqrt{\frac{\varepsilon_m}{\mu_m}} \cdot |\mathbf{E}_0|^2$.

Frequently, $I_0 = 1$ is chosen which implies $|E_0|^2 = 2\sqrt{\frac{\varepsilon_m}{\mu_m}} = 2Z_m$ with the intrinsic wave impedance of the medium $Z_m = \sqrt{\frac{\varepsilon_m}{\mu_m}}$.

Gustav Mie in 1908 [7] derived an exact solution of the cross sections for the case of plane wave illumination of a sphere which is given in Appendix A. Additionally, it should be noted that for the quasistatic approximation, where the object is much smaller than the excitation wavelength, the Mie solution simplifies considerably resulting in the Fröhlich dipole resonance condition $Re(\epsilon(\omega)) = -2\epsilon_{medium}$.

There are also exact solutions for spheroidal [8] and cylindrical geometries [9]. For a detailed and modern presentation the book by Bohren and Huffman is recommended [6].

Equations 3.16 are sufficient for the following simulation work where cross sections are calculated by integration around a sphere as illustrated in Figure 3.1 where the larger (cut-out) sphere is the integration surface.

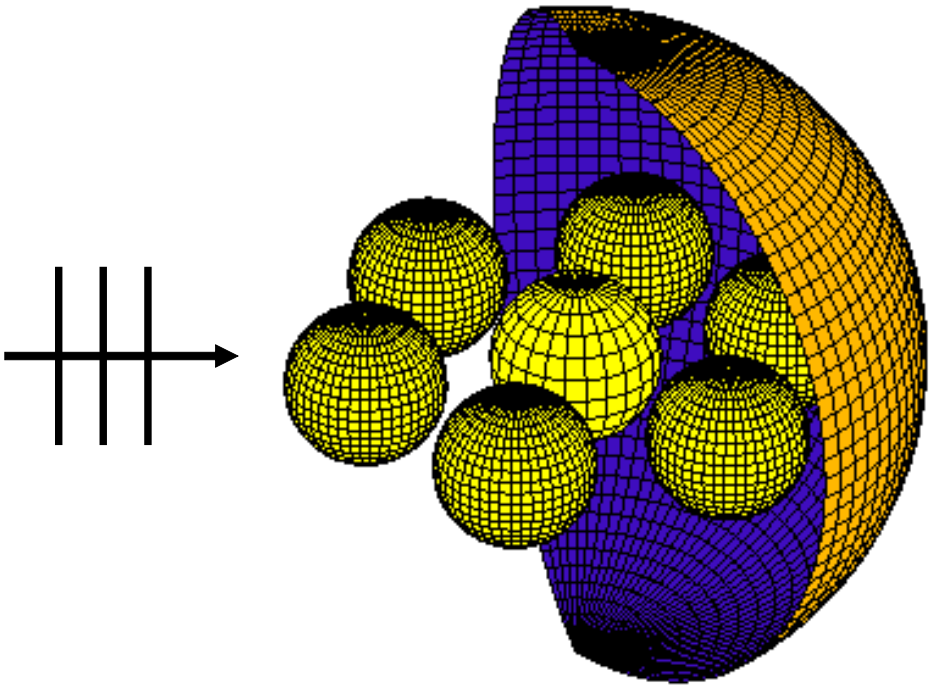

Fig. 3.1 Plane wave illumination of an assembly of spheres. The outer (cut-out) sphere, when completed to a full sphere, is one possible closed integration surface used according to eq. 3.16.

3.1.3 Modelling of the Dielectric Constant

Finding simple and differentiable formulas for the dielectric constant ε usually improves computation time because of time-consuming convolutions used by most simulation methods [10, 11]. This section presents a simple analytical model fitting the measured ε data [5] accurately. Gold is used as an example for all calculations but other metals like silver and copper can be treated in the same way.

For metals, the well-known Drude-Lorentz model is commonly used. However, it is relatively inaccurate for the complex part of the dielectric constant. Instead, the so-called critical point model gives an expression with relatively few parameters while providing more accuracy than the Drude-Lorentz model. Again, as already mentioned more detailed derivations can be found in my previous work [2].

Drude-Lorentz model

The Drude-Lorentz model assumes the metal electrons to be connected by springs motivating the idea of independent, identical and isotropic harmonic oscillators.

Two cases are usually distinguished. First, the *D*rude case, where the spring constant is zero, models intraband transitions of free electrons (within a band). Second, the *L*orentz case, where the spring constant is not zero, models interband transitions of bound electrons to higher energy photons within the metal.

The expression for the dielectric constant ε from the Drude-Lorentz model is well-known [4] and can be written as

$$\varepsilon = \varepsilon_\infty - \frac{\omega_{p,D}^2}{\omega^2 + i\omega\gamma_D} + \frac{\omega_{p,L}^2}{\omega_0^2 - \omega^2 - i\omega\gamma_L} \tag{3.17}$$

where ε_∞ accounts for the transition to higher order bands, $\omega_p^2 = ne^2/\varepsilon_0 m_0$ is the plasma frequency, n is the number density of either *free* or *bound* electrons per unit volume, m_0 is the effective mass, $\omega_0^2 = k/m_0$ (with the spring constant k) is the resonance frequency of the oscillator and γ the damping constant.

The Drude-Lorentz eq. 3.17 can be used for a best fit calculation to the experimental data. The exact parameters can be found in Appendix A (Table A.2) (obtained from my previous work [2]). Further down, in the next section, Figure 3.2 displays the measured [5] and calculated real and imaginary part of the dielectric constant of gold ε_{Au}.

Clearly, the real part of ε_{Au} in 3.2 is approximated well by the Drude-Lorentz model. However, this is not the case for the imaginary part which has a large offset across the spectrum. This motivates the introduction of a more advanced model: the critical point analysis.

Critical point model

The Drude-Lorentz model can be "extended" by adding more Lorentz terms to eq. 3.17. However, these new terms also provide more degrees of freedom which are hard to relate to physically meaningful quantities. In principle, any complete function set could also fit the experimental data but would obviously not be very insightful. This conundrum is beautifully encapsulated by John von Neumann's famous remark: *"With four parameters I can fit an elephant, and with five I can make him wiggle his trunk."* [12]

Critical point analysis modifies the interband transition term in eq. 3.17 by considering so-called critical points occurring when the dispersion relation has a first-order derivative of zero. Consequently, the density of states, which is inversely proportional to the gradient of the dispersion relation, exhibits a so-called van Hove singularity. The exact modelling can be found in [13, 14] where a new expression for the dielectric constant of metals is used with two critical points where '1' denotes the first and '2' the second critical point transition:

$$\varepsilon_{Au} = \varepsilon_\infty - \frac{\omega_{p,D}^2}{\omega^2 + i\omega\gamma_D} + \frac{\omega_{p,1}\exp(i\Phi_1)}{\omega_{0,1} - \omega - i\gamma_1} + \frac{\omega_{p,2}\exp(i\Phi_2)}{\omega_{0,2} - \omega - i\gamma_2} \tag{3.18}$$

where $\Phi_{1,2}$ is a phase. A best fit approximation is applied where the exact parameters can be found in Appendix A (Table A.3) (obtained from my previous work [2]).

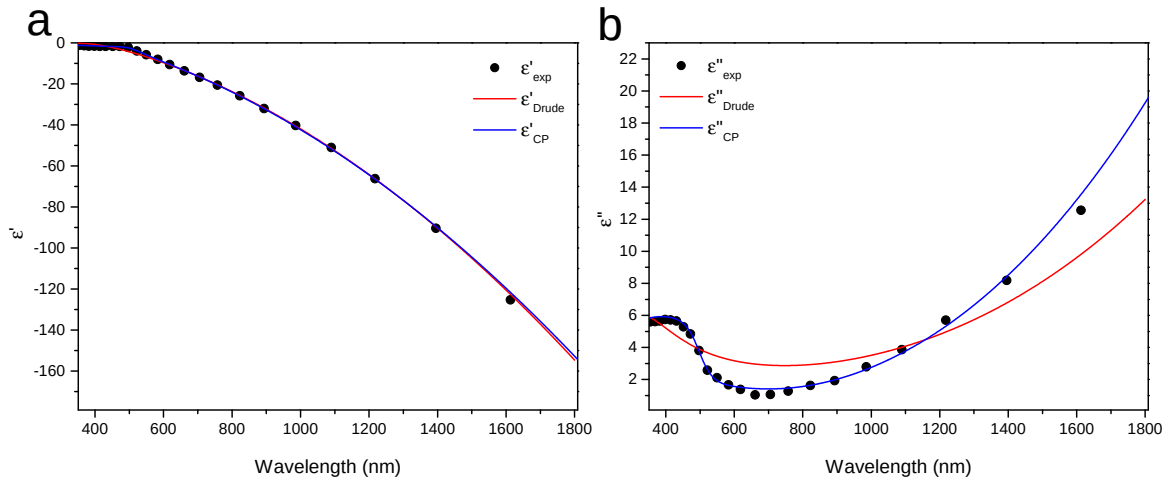

Fig. 3.2 (a) and (b): filled black circles: measured real (or imaginary part respectively) of gold from [5]; red line: Drude-Lorentz model (eq. 3.17); blue line: critical point analysis (eq. 3.18).

Figure 3.2 shows a clear improvement for the modelling of the imaginary part of ε_{Au} compared to the Drude-Lorentz model. Thus, within this work, the critical point analysis is used whenever the dielectric constant ε needs modelling.

3.1.4 Multiple Multipole Method (MMP)

The multiple multipole method (MMP) is a semi-analytical simulation technique for solving the Maxwell equations 3.1. MMP is implemented in a software package called the Multiple Multipole Program or MaX-1 [15, 16] (now available as the freeware "OpenMaXwell"). The abbreviation "MMP" refers to both the method and the software.

MMP is used for linear, homogeneous and isotropic spaces. The different media occupy disjunct three-dimensional volumes or "domains" which are separated by two-dimensional interfaces or "boundaries". The boundaries are discretized rather than the volume which makes simulations extremely efficient compared to volume discretization approaches [17].

MMP approximates the electromagnetic field by a terminated power series of the form

$$\text{FIELD} = \sum_i A_i \cdot \mathbf{B_i} + \text{ERROR} \tag{3.19}$$

Any known exact solution of the Maxwell equations can be used for the basis function $\mathbf{B_k}$ of the power series, e.g. plane waves, spherical multipoles, spherical Bessel functions, more complicated complex origin, ring or line multipoles [15, 18, 19]. *Multipoles* are used frequently as basis expansions and because of their being located at *multiple* sites the method is called the *multiple multipole method*. The coefficients A_k of the series are determined by minimizing the $ERROR$ at the boundaries which is calculated by checking the Maxwell boundary conditions in eq. 3.20 at the discretized surface.

$$\mathbf{n}_S \cdot \left(\mathbf{D}^I - \mathbf{D}^{II}\right) = \sigma \tag{3.20a}$$
$$\mathbf{n}_S \cdot \left(\mathbf{B}^I - \mathbf{B}^{II}\right) = 0 \tag{3.20b}$$
$$\mathbf{n}_S \times \left(\mathbf{E}^I - \mathbf{E}^{II}\right) = 0 \tag{3.20c}$$
$$\mathbf{n}_S \times \left(\mathbf{H}^I - \mathbf{H}^{II}\right) = \hat{\mathbf{J}} \tag{3.20d}$$

This also means there is direct feedback on the accuracy of the solution which can be rechecked by rediscretization of the surface (higher/lower resolution, or a different parametrization). Each rediscretization can then be checked separately in order to examine if the derived power series still fulfils the Maxwell boundary conditions.

The terminated power series is ambiguous and overall simulation time is drastically affected by the amount and types of multipoles used. Hence, good prior insight and experience is helpful for this simulation method. MMP is most efficient for geometries suited to its inner design such as planes, spheres, cylinders, or combinations of these. In principle, any arbitrary shaped object can be simulated because it is a matter of using sufficient expansions in the power series 3.19. However, for some geometries this can be extremely inefficient because the expansions do not fit the geometry. For example, using plane waves as response functions for spherical geometries is very time-consuming because of the high number of plane wave expansions required to resemble a single spherical Bessel function. This is specifically true for sharp corners and edges, where no exact solutions of the Maxwell equations are known. However, a significant amount of nanostructures

are rounded or can be approximated as rounded [20–22]. For such structures MMP is a well-suited method by design.

In order to simulate more arbitrary structures, MMP provides an automatic setting algorithm for the multipoles as illustrated in Figure 3.3. The field can be simulated by placing multipoles along a line closely following the boundary separating 2 media which are coloured grey (inside) and red (outside) here.

The inner (outer) medium is simulated by multipoles in the outside (inside) medium. This is due to multipoles exhibiting a singularity when they are within the domain upon which they act. Strategies to optimize the simulation include the exact proximity of the guiding line to the boundary, higher multipole density and finer discretization at points of increased surface curvature, etc.

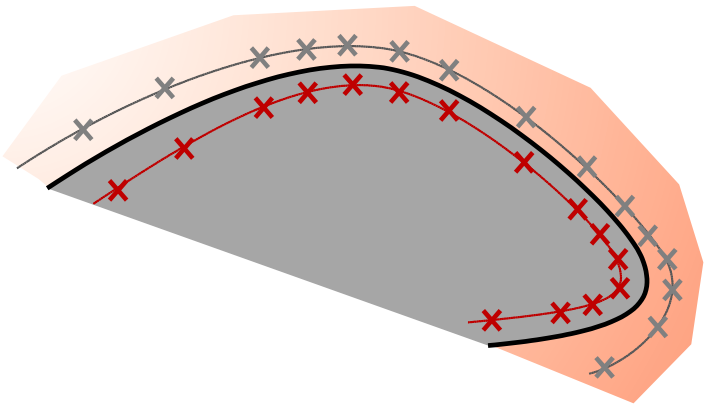

Fig. 3.3 Illustration of the automatic MMP setting routine. The solid black line is a boundary separating 2 different media. The dotted lines are guides to the eye on which the multipoles are placed (the crosses). Note that more multipoles are needed at sections of increased surface curvature. The electromagnetic field of the grey medium is fitted by the grey multipoles outside of the medium. The same holds true for the red medium which is fitted by the red coloured multipoles.

The next sections show examples of MMP simulations. At first, a simple planar and spherical interface is presented. Then, more complicated problems are treated, namely a plasmonic trimer and a nanoparticle buried into a dielectric layer (referred to as a “sombrero” structure).

3.1.5 Example I: Planar and Spherical Interface

A planar interface separating air and a medium of $n = 1.5$ is illuminated by a plane wave of $\lambda = 500\,\text{nm}$ propagating from the top at a $30°$ angle of incidence (the electric field polarization is in-plane). The total electric field simulation is shown in Figure 3.4a (obtained from my previous work [2]). An educated guess of a total field is needed. Here, the analytical solution is known from Snell's law and amplitudes can be calculated with the Fresnel coefficients. Consequently, only two more plane wave expansions are needed to model the total electromagnetic field, one for the transmitted and one for the reflected plane wave where the angles are calculated with Snell's law. The next step is to find the amplitudes of the transmitted and reflected plane wave. The MMP strategy is to discretize the plane interface and adjust the amplitudes until the boundary error, derived by checking the Maxwell boundary conditions, is small. The numerical solution is extremely accurate because the expansions used are implementations of the analytical solution of this problem. Note that an expansion other than a plane wave would have made it nearly impossible for MMP to minimize the error.

Next, a spherical interface is treated. As an example, Figure 3.4 shows the electric field of a 100 nm radius sphere with $n = 1.5$ in vacuum illuminated by a plane wave of $\lambda = 500\,\text{nm}$ propagating in x-direction and a y-polarized electric field [2]. There is, again, an analytical solution for this problem but it is not as simple as for planar interfaces. The sphere's response to a plane wave is an inside and outside (scattered) field [6, 7] and adding up excitation, scattering and inner field results in the total field. Analytically the inner field is a spherical Bessel function, representing a standing wave, and the scattered field is a spherical Hankel function, representing an outgoing wave. A graphical representation of spherical Bessel and Hankel functions can be found in Appendix A. MMP implements the spherical Bessel function as "3D Bessel" and the spherical Hankel function as "3D multipole" expansion. The solution of this problem requires only two expansions, a Bessel expansion for the inner field (placed in the centre of the sphere) and a multipole for the scattered field outside the sphere (also placed in the centre of the sphere). Because of its singularity in the origin, the Hankel function must always be located outside of the domain on which it acts upon. Again, the solution is very accurate because of the prior knowledge from Mie theory which guided the choice of this response function.

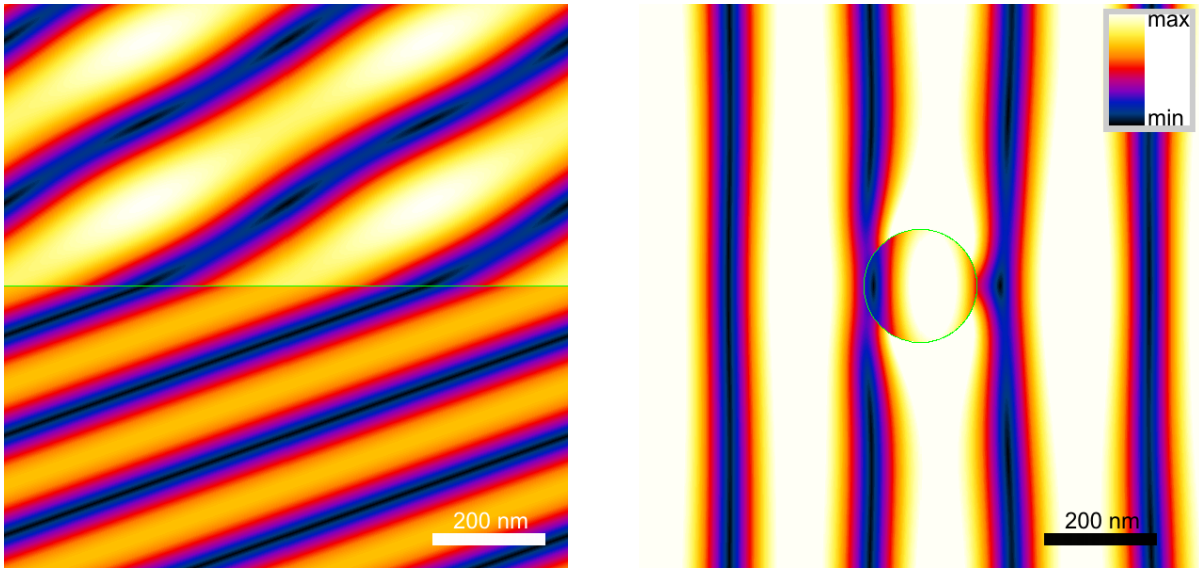

(a) total field planar interface **(b)** total field spherical interface

Fig. 3.4 Illustrations of planar and spherical interfaces. (a) A planar interface between air and a dielectric of $n = 1.5$ is illuminated by a plane wave of $\lambda = 500\,\text{nm}$ propagating from the top at $30°$ angle of incidence (the electric field polarization is in-plane). Two expansions are needed to model the response field: one transmitted, and one reflected plane wave. (b) A dielectric 100 nm radius sphere with $n = 1.5$ is excited by a plane wave at $\lambda = 500\,\text{nm}$ in vacuum propagating in x-direction and a y-polarized electric field. The electric field inside the sphere is modelled by a centrally located Bessel function and the outside field by a Hankel function which is also located in the centre of the sphere. The inset displays the colour scale used for the electric field. This figure is adapted from my previous work [2].

3.1.6 Example II: Trimer Structure

MMP can be expanded to simulate assemblies of individually solvable substructures. One example of this are plasmonic oligomers [3] where metallic spheres are assembled into structures resembling organic oligomers due to areas of field enhancement ("binding") and weakening ("anti-binding") between the spheres. As an example a trimer structure is presented, i.e. an equilateral triangle with 100 nm gold nanoparticles in the corners and 30 nm gaps between the particles (see Figure 3.5a). The surrounding medium is air and the excitation is by a plane wave with $\lambda = 500\,\text{nm}$ coming from the z-direction with an electric field polarization in x-direction. The response function in a first approximation contains the solutions of all substructures. Figure 3.5b depicts the Mie theory solutions for the individual spheres which is a Bessel function for the inner field (magenta square) and a Hankel function for the outer field (magenta cross) placed in the respective centres of the spheres. The individual solutions can be already sufficient for gaps (between the sphere's surfaces) larger than 10 nm. Indeed, for this particular assembly the boundary error is <1% and no further optimisation with automatic setting routines is needed.

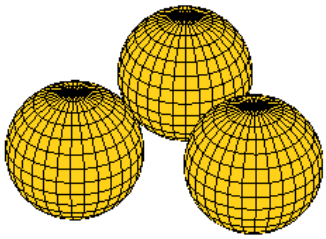

(a) 3D view of trimer

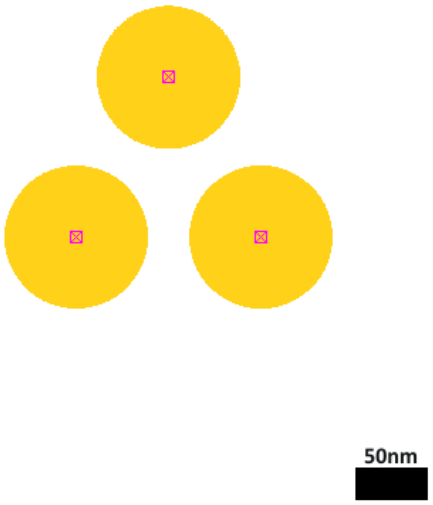

(b) Expansions

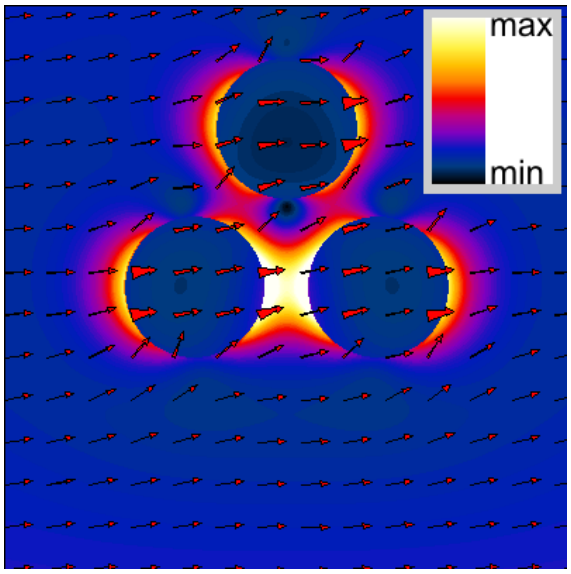

(c) Full field

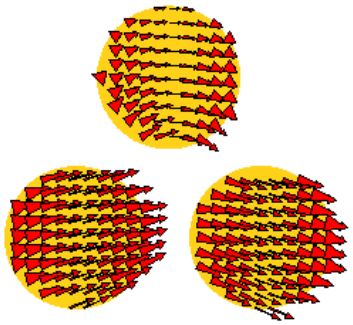

(d) Inner field

Fig. 3.5 (a) 3D view of 100 nm diameter gold spheres in an equilateral triangle in vacuum under plane wave excitation at $\lambda = 500\,\mathrm{nm}$ coming from the z-direction with an electric field polarisation in x-direction. The gap between the spheres is 30 nm. The grid lines on the spheres indicate the surface discretization used for the MMP simulation. (b) 2D cross view with expansions used to model the response function. Each sphere contains the individual Mie theory solutions in the respective centres which are Bessel functions (magenta squares) for the inner field and Hankel functions (magenta crosses) for the outer field. These solutions are already sufficient to model a complete field. (c) 2D cross view of the full time averaged electric field of the trimer assembly. The arrows follow the field lines. (d) 2D cross view with arrows showing the instantaneous electric field inside the spheres (sum of the Bessel functions).

As a result the total, time-averaged electric field is shown in Figure 3.5c where an electric field enhancement between the bottom 2 spheres can be seen (which are parallel to the electric field polarization). Finally, Figure 3.5d shows the field lines of the instantaneous inner field of the plasmonic trimer as constituted by the Bessel functions.

3.1.7 Example III: Sombrero structure

More sophisticated structures which go beyond composition of individual solutions are presented next. Gold nanoparticles (84 nm) buried at close distance to a sapphire surface of a substrate can be fabricated at relatively large scales [1] and exhibit interesting optical properties, e.g. as optical tweezers.

The substrate is modelled with the dielectric constant of sapphire (Al_2O_3) and the refractive index of gold is taken from Johnson and Christy [5]. Modelling this system is challenging because the spheres are very close (within a few nm) to the surface. This means three media (air, sapphire, gold) are in close proximity which can create triplet points causing the simulation to break down. One possible approach is to think of the covering sapphire surface as a "sombrero structure", i.e. a hat on top of a gold sphere. The sombrero can then be modelled relatively smoothly without sharp corners which have to be avoided for MMP simulations. Figure 3.6a shows the described situation where a sphere is covered with a sombrero interface which also depicts the boundary discretization used in later simulations. The boundaries are only the first step though. The object is illuminated from the top by a $\lambda = 942$ nm plane wave with an electric field polarization in x-direction. Finding the right expansions for an accurate response field is not obvious anymore. A first approach utilizes the individual solution for the interface elements. For the sphere, this is the now familiar Mie solution from the previous sections, although this time there are three media which necessitates additional multipoles for the third medium. The sombrero by itself (without the sphere) is also not a trivial exercise and requires automatized setting routines (see Figure 3.3) with multipoles increasing in density as they get closer and closer to the centre of the structure where an increased surface curvature is present. These are shown as blue crosses in Figure 3.6b. However, the most challenging part is the interaction between the sombrero and sphere. There is no analytical solution for this and drastic, hard to predict, field changes occur the closer the sphere and sombrero interface get. For this, a series of adaptive ring multipoles is used (magenta rings in Figure 3.6b) which contain individual mutipoles and can be highly tuned depending on the discretization used.

This underlines the versatility of the used multiple multipole simulation method. Very complex structures can be modelled in a short time after developing appropriate response functions. This chapter so far offers the theoretical foundation for cross section studies and a practical implementation for solving the Maxwell equations in an expedient manner. The next sections show simulation results for different core-shell nanostructures and comparison with experimental data. These structures are of general interest for solar cells as discussed in the following chapters.

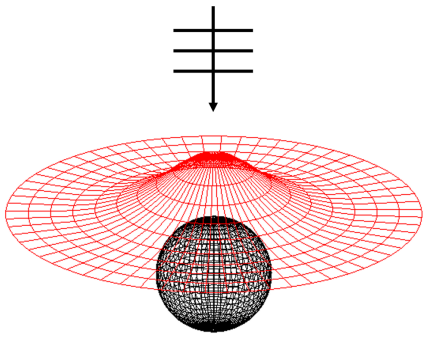

(a) Plane wave illumination

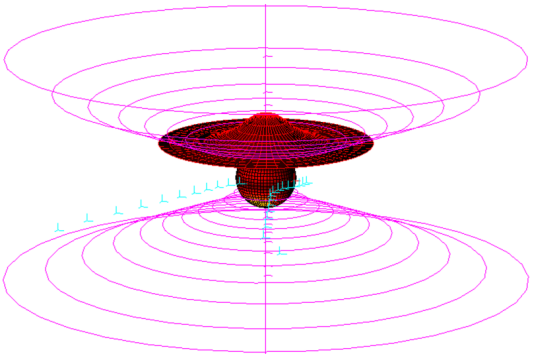

(b) Multipoles

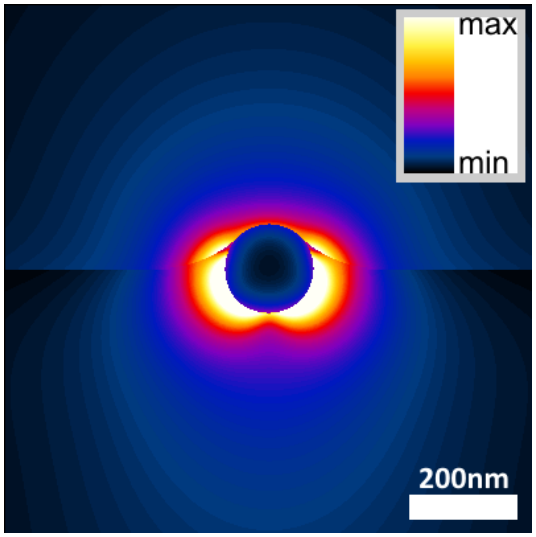

(c) 2D field simulation

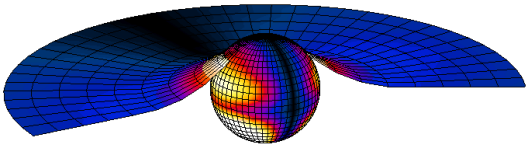

(d) 3D field simulation

Fig. 3.6 (a) Boundary modelling for a buried gold sphere of 84 nm diameter (black grid) embedded in a sapphire substrate approximated by a "sombrero" structure (red grid). Note that the discretization gets finer at the top where the field is the most complicated to model. (b) Multipoles used for the overall response field to a plane wave excitation (y-direction) with $\lambda = 942\,\mathrm{nm}$ and x-polarized electric field. The first solution is approximated by individual solutions for the nanoparticle (expansions not visible because they are inside the sphere) and the sombrero interface represented by the blue crosses placed by automatic setting algorithm (see Figure 3.3). Interaction between the sphere and sombrero, which has no analytical solution, is modelled by adaptive magenta coloured ring-multipoles. (c) 2D view of the electric field with an inset for the colour scale. (d) 3D view of the z-component of the electric field which is often measured experimentally. (The sombrero is cut out for illustration purposes.)
This modelling was partly used in my previous work [1].

3.2 Simulation Results and Discussion

Optical cross sections are accessible to MMP simulations and experiments. Accurate simulations can provide important feedback on nanostructures.

For example, as outlined in Appendix A, core-shell gold-silica or silver-titania nanoparticles can be synthesized at relative ease. With simulations the size of the core, the shell thickness, or the IoR of the surrounding medium can be analysed further.

The starting point for this discussion are more simple models helping to understand some qualitative features of metallic NP cross sections. This is followed by using simulations for quality control of previously synthesized gold NPs. Furthermore, a method to use gold NPs as sensors for the refractive index is presented.

Then, core-shell gold-silica structures in a titanium medium are presented. This scenario is extended to include a medium with the dielectric constant of a typical dye-sensitized solar cell (DSSC) photoactive layer followed by a discussion of gold-silica, silver-titania NPs of different sizes. Analysis of the cross sections gives an indication at which scale scattering dominates over absorption.

3.2.1 Cross Sections of Spherical Nanoparticles

Extinction spectra (according to eq. 3.16) for a bare gold nanoparticle of 20 nm diameter are shown in Figure 3.7 where the refractive index of the medium is increased from $n = 1.0-3.0$ The first thing to note is that the plasmonic dipole peak, reached when the Fröhlich condition $Re(\epsilon(\omega)) = -2\epsilon_{medium}$ is met, for all spectra displays a red-shift as the dielectric constant increases. This is a general observation for metallic nanoparticles where an optically denser medium leads to a red-shifted spectrum explained by the smaller effective wavelength (due to an increased polarizability of a medium with higher refractive index).

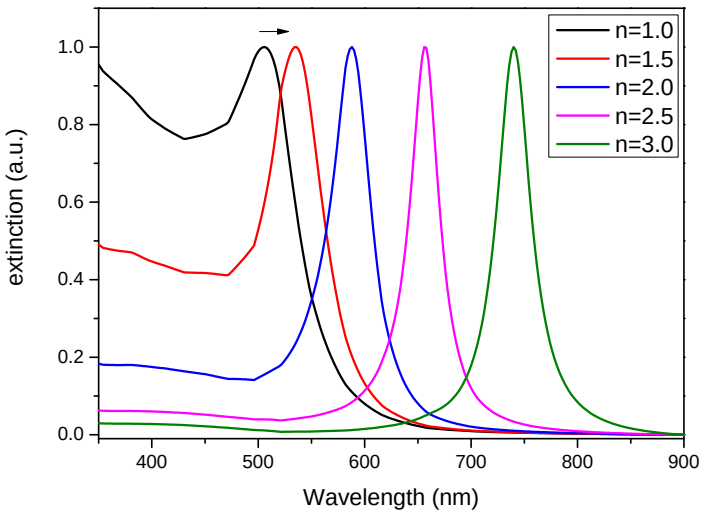

Fig. 3.7 Simulated, normalized extinction spectra for a gold nanoparticle of 20 nm diameter in media with refractive indices from $n = 1.0 - 3.0$ showing a red-shift.

As a next step, Figure 3.8 shows the extinction cross section simulations of a series of bare gold (solid lines) and gold-silica (dotted lines) NPs in a medium with $n = 1.33$ (water). The gold core diameter is varied from 40-150 nm, and the silica shell is kept constant at 10 nm. Again, there is a red-shift of the dipole peak as the gold core size increases for both

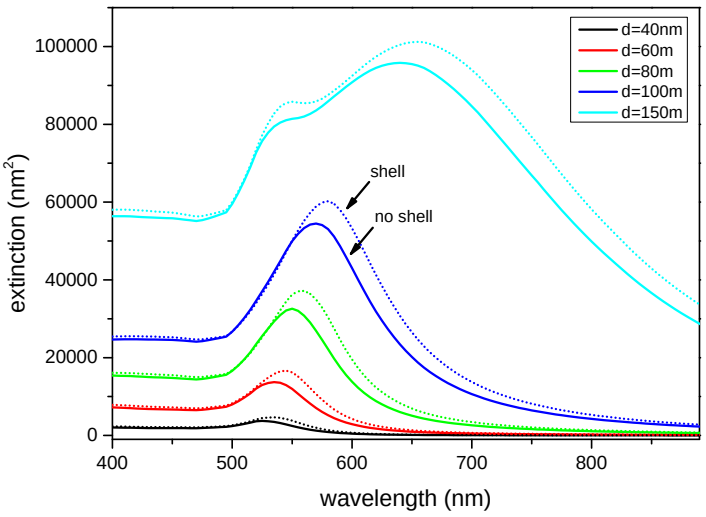

Fig. 3.8 MMP simulation of the extinction cross section according to eq. 3.16 of 40, 60, 80, 100, and 150 nm gold nanoparticles without (solid lines) and with a 10 nm SiO_2 shell (dotted lines) in a medium with $n = 1.33$ (water).

the bare and shelled particles. This is sometimes misattributed to an antenna effect where the resonance wavelength scales with length.

More accurately, for plasmonic surface waves on larger NPs, the incoming wavelength becomes more and more comparable to the size of the object, i.e. the quasistatic approximation is no longer valid. Thus, the excitation cannot displace the surface electrons over the entire nanoparticle homogeneously anymore, the phase is non-uniform and the spectrum is red-shifted [6, 23]. As the particle grows higher resonance modes appear, as can be seen for the 150 nm gold core which exhibits a quadrupole at around 520 nm. There is also a red-shift when the shell is present, explained by a local increase in refractive index (as already discussed above).

3.2.2 Quality Control

Cross section simulations can also be used to check the synthesis protocols. In Figure 3.9 the measured and simulated extinction spectra of gold NPs of presumed 60 and 100 nm diameter in water are shown. The 60 nm NPs match relatively well with the simulation in terms of spectral position. The broadening can be attributed to polydispersity. This could require additional purification of the solution. Especially the small peak at 740 nm is indicative for aggregation which can be removed by further centrifugation [24]. For the 100 nm NPs the simulation and experiment show slight discrepancies. The simulated 100 nm line shows good spectral agreement but does not match the width of the experimental data.

However, the tail part can be fitted with a 110 nm simulation. This indicates there is some polydispersity in the sample which contain a range of NPs from 100-110 nm NPs. Additional error sources could be imperfect spherical shape. This is a bigger problem for larger NPs because of the multiple seeding synthesis procedure where each step can introduce errors.

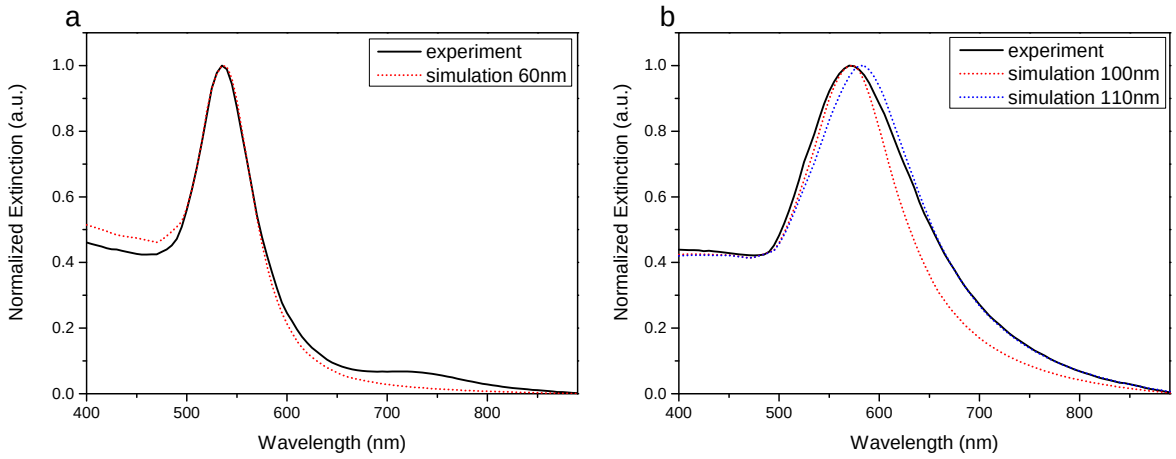

Fig. 3.9 (a) Synthesized Au NP (black) of assumed 60 nm diameter and checked for consistency with a simulated spectrum (dotted red). (b) Same consistency check for 100 nm (black) with simulated spectra a 100 (dotted red line) and 110 nm (dotted blue line) NP.

3.2.3 Gold Nanoparticles as Sensors

Simulations can be used to find the IoR of the surrounding medium because the spectral position of the plasmonic peaks is IoR-sensitive [25]. For example, from the TEM image of a Au NP in Figure 3.10 a 55 nm core can be estimated. With the known diameter and dielectric constant of gold, the refractive index of the surrounding medium can be estimated by fitting the extinction cross section to the experimental data as presented in Figure 3.10b where the best approximation resulted from a fit with $n = 1.35$. This in good agreement with the solvent used (ethanol with $n = 1.36$). The mismatch in line shape is due to the synthesis not yielding perfectly spherical nanoparticles [24]. Also, during the synthesis process, a small ratio of the NPs can aggregate and form lumps explaining the red-shifted broadening of the spectrum [24].

This demonstrates the principle of plasmonic sensors for the refractive index of the medium. The strategy is to put plasmonic NPs in a solution, measure the extinction cross section, and then the refractive index of the unknown solution can be derived from fitting. This is already a remarkable result underlining the effectiveness and importance of accurate modelling.

3.2.4 Cross Sections in DSSCs

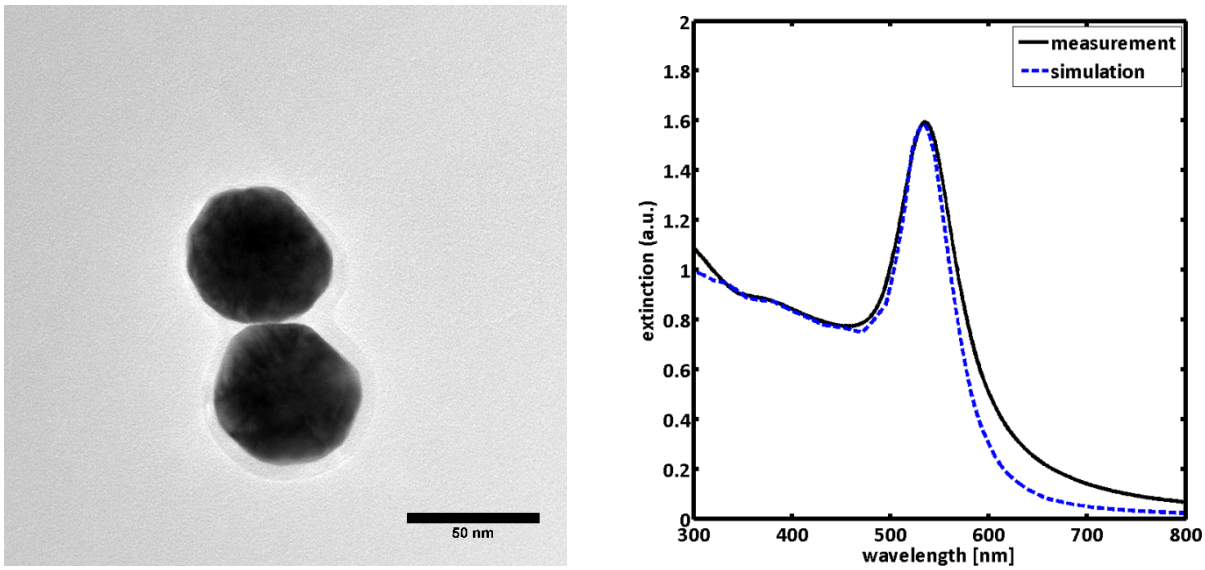

(a) Measurement **(b)** Simulation

Fig. 3.10 (a) Synthesized Au sphere with an estimated diameter of $d = 55$ nm. (b) measured and simulated extinction spectrum of (a). The MMP simulation assumes a diameter of 55 nm. The refractive index of the surrounding medium is used as a fitting parameter for the simulation. A best fit approximation is achieved for $n = 1.35$ which is very close to the used solvent's IoR (ethanol) of $n = 1.36$.

Simulated cross sections for more realistic solar cell scenarios are used, i.e. gold-silica core-shell nanoparticles. The first simulations are in a titania medium. Later, an effective medium of titania/dye/spiro is used which is very close to the photoactive layer in DSSCs.

The dielectric constant of gold is derived from the critical point analysis in the previous section. Refractive indices for silica or titania are from [26, 27], and the effective titania/dye/spiro medium from [28].

Figure 3.11 shows experimental absorption, scattering, and extinction cross sections of Au NPs embedded in TiO_2 and varying core diameters d_c from 50-250 nm with a fixed silica shell thickness of 3 nm .

There is a red-shift of the resonance modes in the spectrum with increasing diameter of the gold core following the same trend as in the previous section where it was explained by the non-uniform excitation over larger NPs. Furthermore, for larger core sizes higher resonance modes develop. It is noticeable that for small particles scattering becomes negligible compared to absorption. This is in good agreement with by the quasi-static approximation for small NPs (compared to the wavelength) where the following relation holds [6]

$$C_{sca} \sim r^6/\lambda^4 \qquad C_{abs} \sim r^3/\lambda$$

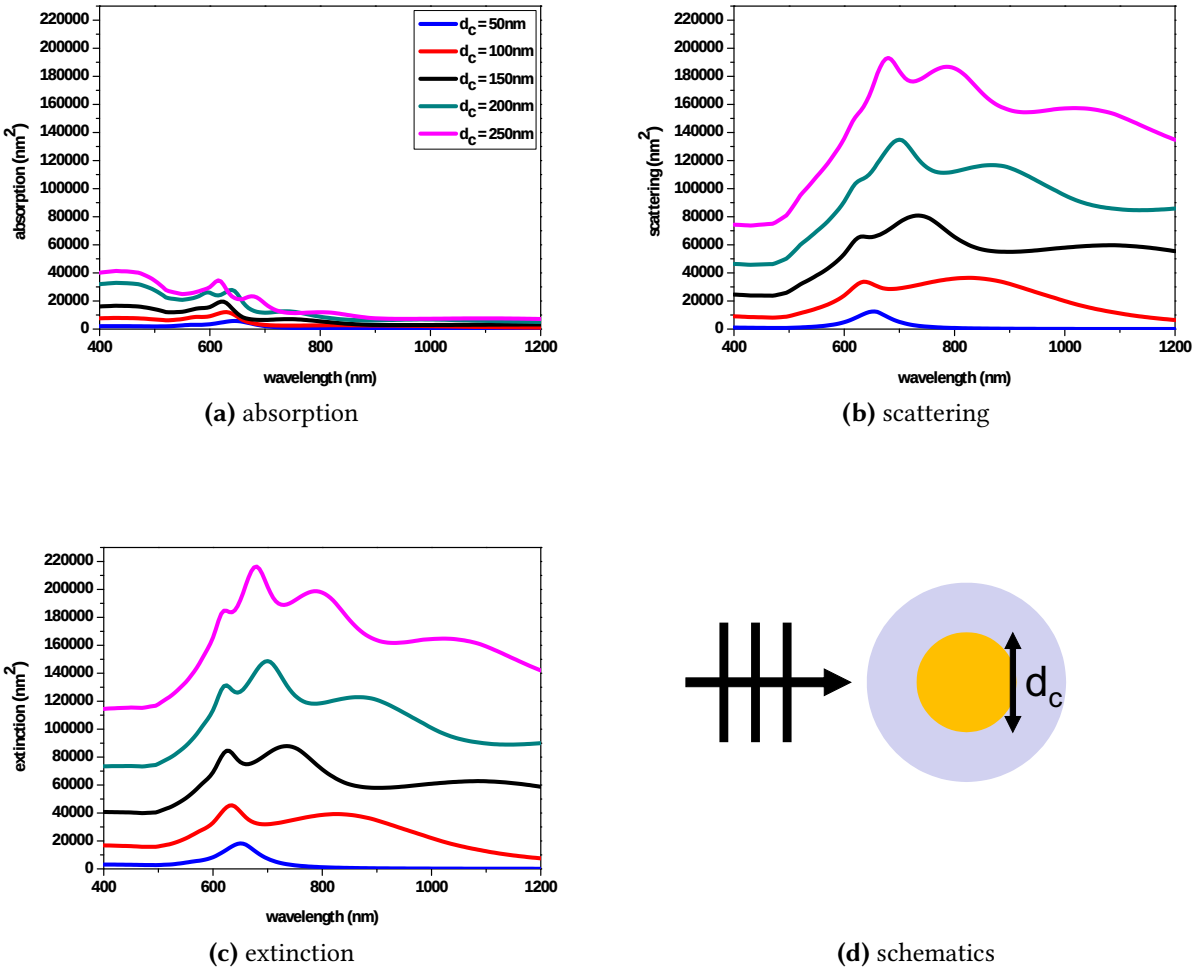

(a) absorption **(b)** scattering

(c) extinction **(d)** schematics

Fig. 3.11 Absorption, scattering and extinction cross sections of a single core-shell NPs embedded in a homogenous medium of TiO_2 under plane wave illumination. The gold core varies in diameter d_c from 50-250 nm. The Silica shell has a fixed thickness of 3 nm.

These simulations are a reference point from which more complex structures can be planned and designed.

As a next step, the scattering and absorption cross sections in DSSCs are simulated. This is of interest because scattering is redirection of light and can be used for an increased optical pathlength within a thin photovoltaic layer, which otherwise permits high transmission of incoming light.

Absorption at plasmon resonance on the other hand can be used to concentrate and localize incoming light, essentially acting as an antenna [29]. DSSCs are modelled by assuming an effective medium of titania/dye/spiro which was determined experimentally by ellipsometry by Moule et al [28].

An example for the absorption, scattering, and extinction cross section of a 100 nm gold core with a 3 nm shell is shown in Figure 3.12. Also, electric field simulations before, during, and after the dipole resonance are displayed as insets. It can be seen that in this

case of relatively large NPs scattering is dominating (just as in the previous discussion), and absorption is almost negligible.

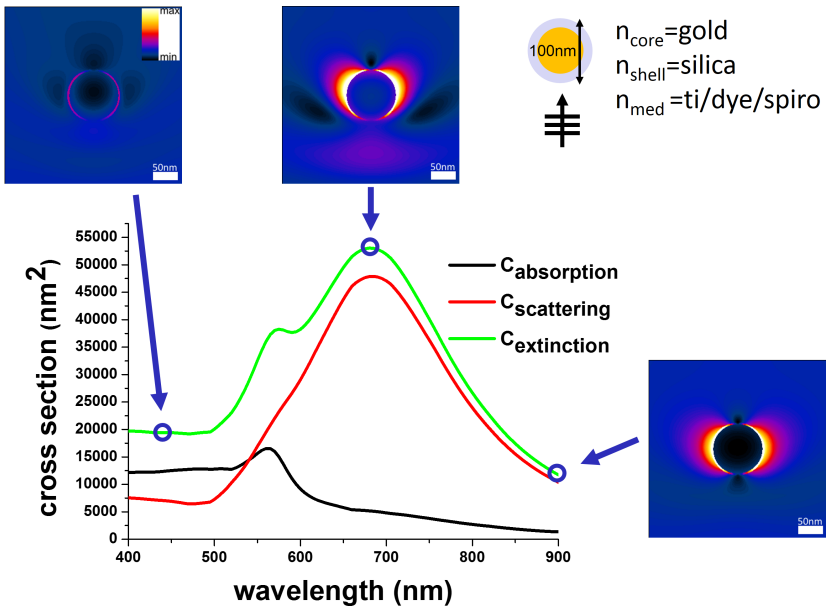

Fig. 3.12 Absorption, scattering, and extinction of a 100 nm gold core with a 3 nm silica shell in a photoactive layer of titania/dye/spiro. The inset images show the averaged electric field at the indicated positions.

Simulating the scattering cross sections of gold and silver cores from 60-140 nm (diameter) is presented in Figures 3.13a and 3.13b where again a red-shift is noticeable. Silver has blue-shifted dipolar resonance modes compared to gold, due to its different dielectric constant which is also modelled by the previously introduced critical point analysis.

Also, silver quadrupoles can be seen for the larger core sizes. A summary of the dipole modes of the different core sizes from 10-140 nm diameter is compiled in Figures 3.13c and 3.13d by tracking the wavelength (blue line) and scattering cross section values (gold: orange, silver: grey) over the core size illustrated by the blue circles in the scattering cross section. The blue-shifted dipole modes of Ag NPs (starting at 400 nm) compared to Au NPs (starting at 550 nm) are very evident here. Furthermore, silver is at first a stronger scatterer than gold for cores up to 80 nm diameter. Finally, Figures 3.13e and 3.13f present the absorption (dotted line) and scattering (solid line) cross sections over the core size for gold and silver as well as the corresponding scattering wavelength (blue line). From this, it is evident that scattering in the case of gold (in this particular medium) starts dominating at a core size of about 55 nm, and 25 nm for silver.

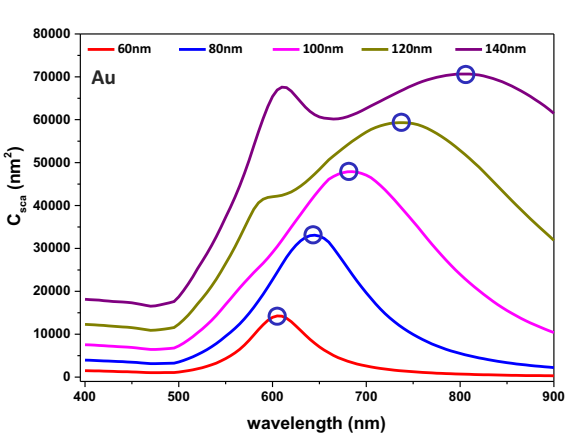

(a) Gold

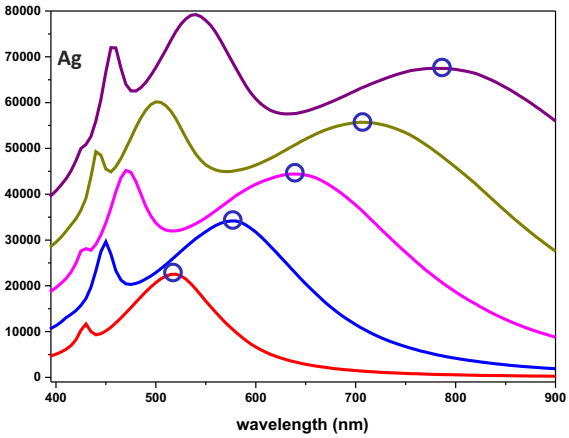

(b) Silver

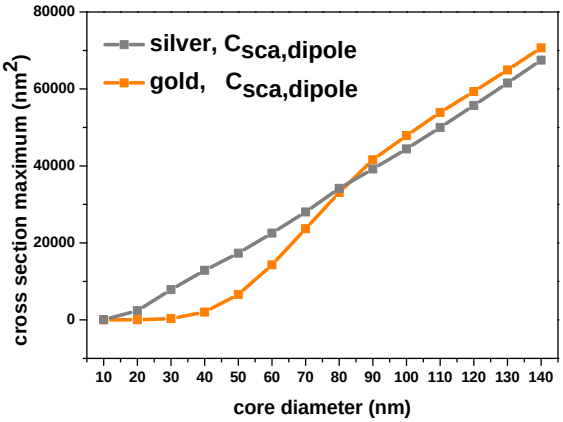

(c) Scattering maxima

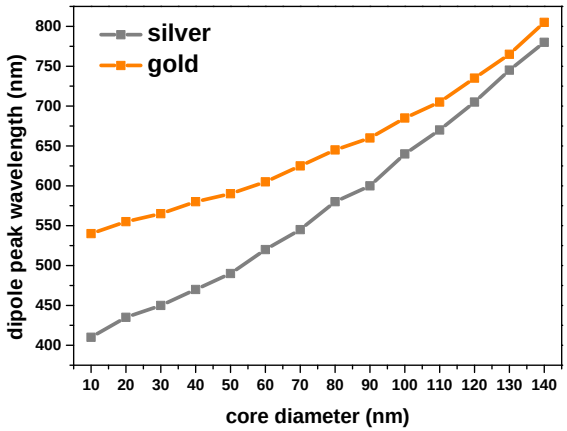

(d) Wavelength maxima

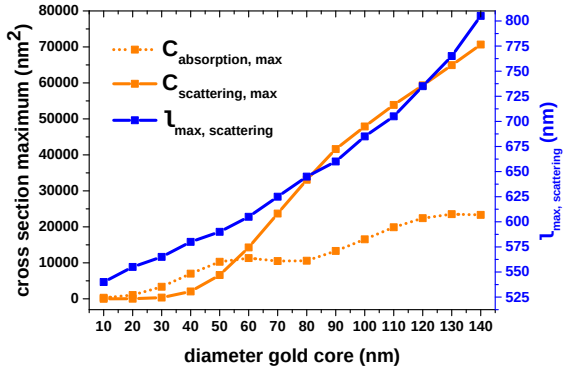

(e) Gold

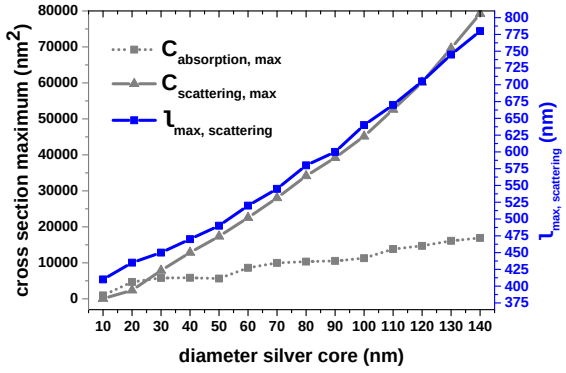

(f) Silver

Fig. 3.13 (a) Scattering cross sections of gold cores of 60, 80, 100, 120, and 140 nm with a 3 nm silica shell. The refractive index of the medium is from ellipsometric measurements of a titania/dye/spiro photoactive layer by Moule et al [28]. The inset circles (blue) track the wavelength and strength of the plasmonic dipole modes. (b) According simulations for silver cores. (c) Scattering cross section at the dipole wavelength for gold (orange) and silver (grey) over the core diameter. (d) The according dipole wavelength of gold (orange) and silver (grey) cores over the core diameter. (e) Absorption (dotted orange line) and scattering (solid orange line) cross section at the dipole wavelength are plotted over the diameter of the gold core. The scattering wavelength (blue line) is also shown. (f) Analogous simulation for silver cores.

3.3 Summary

The absorption, scattering and extinction cross section was derived from Maxwell's equations for energy conservation, i.e. the Poynting theorem. It states that the absorption or scattering cross section can be calculated whenever the total and scattered electromagnetic field is known by simply integrating the averaged Poynting vector over any closed surface volume around the object of interest. Absorption is calculated when the averaged, total Poynting vector is used and scattering for the averaged, scattered Poynting respectively. The extinction cross section follows by superposition of scattering and absorption.

The electromagnetic field can be simulated by the Multiple Multipole Method (MMP), a boundary element method solving the Maxwell equations in the case of linear, homogeneous and isotropic media. Additionally, a modified version of the Drude-Lorentz model for the dielectric constant of metals, the so-called critical point model, was introduced and showed increased accuracy.

Simulation results for various core-shell nanostructures were shown. Calculations helped to evaluate the quality of synthesized NPs and were used to demonstrate gold nanoparticles acting as sensors for the refractive index of an unknown solution. Furthermore, gold-silica NPs at first buried in titania and then in a realistic DSSC photoactive layer were shown which was extended to include silver-titania NPs as well. It was shown that scattering starts dominating for larger NPs, for gold it was at 55 nm and for silver at 25 nm. These simulations can be used for designing and guiding future experiments.

References

[1] M. Mäder, T. Höche, J. W. Gerlach, S. Perlt, J. Dorfmüller, M. Saliba, R. Vogelgesang, K. Kern, and B. Rauschenbach, "Plasmonic activity of large-area gold-nanodot arrays on arbitrary substrates," *Nano Letters*, pp. 1–16, 2009.

[2] M. Saliba, *Numerical Simulations of Near and Far Field Scattering Processes in Plasmonic Nanostructures (Diplomarbeit).* Stuttgart: Max Planck Institute for Solid State Research, 2009.

[3] M. Hentschel, M. Saliba, R. Vogelgesang, H. Giessen, A. P. Alivisatos, and N. Liu, "Transition from isolated to collective modes in plasmonic oligomers," *Nano Letters*, vol. 10, no. 7, pp. 2721–2726, 2010.

[4] J. Jackson, *Classical Electrodynamics.* 2 ed. New York Wiley, 1975.

[5] P. B. Johnson and R. W. Christy, "Optical constants of the noble metals," *Phys. Rev. B*, vol. 6, pp. 4370–4379, DEC 1972.

[6] C. F. Bohren and D. R. Huffman, *Absorption and Scattering of Light by Small Particles.* Wiley-VCH, 1983.

[7] G. Mie, "Beiträge zur Optik trüber Medien, speziell kolloidaler Metallösungen," *Annalen der Physik*, vol. 330, pp. 377–445, JAN 1908.

[8] R. Gans, "The shape of ultra microscopic gold particles," *Annalen der Physik*, vol. 37, pp. 881–900, APR 1912.

[9] L. Rayleigh, "On the electromagnetic theory of light," *Philos. Mag.*, vol. 12, p. 82, 1881.

[10] A. Vial, A. Grimault, D. Macias, D. Barchiesi, and M. de la Chapelle, "Improved analytical fit of gold dispersion: Application to the modeling of extinction spectra with a finite-difference time-domain method," *Physical Review B*, vol. 71, FEB 2005.

[11] A. Vial, "Implementation of the critical points model in the recursive convolution method for modelling dispersive media with the finite-difference time domain method," *Journal of Optics A-Pure and Applied Optics*, vol. 9, pp. 745–748, JUL 2007.

[12] F. Dyson, "A meeting with Enrico Fermi - How one intuitive physicist rescued a team from fruitless research.," *Nature*, vol. 427, p. 297, JAN 22 2004.

[13] J. Leng, J. Opsal, H. Chu, M. Senko, and D. E. Aspnes, "Analytic representations of the dielectric functions of materials for device and structural modeling," *THIN SOLID FILMS*, vol. 313, pp. 132–136, FEB 1998.

[14] P. G. Etchegoin, E. C. Le Ru, and M. Meyer, "An analytic model for the optical properties of gold," *JOURNAL OF CHEMICAL PHYSICS*, vol. 125, p. 164705, NOV 2006.

[15] C. Hafner, *Post-modern electromagnetics: using intelligent Maxwell solvers*. John Wiley, 1999. The software package OpenMaXwell is available at http://openmax.ethz.ch/.

[16] R. Ballisti and C. Hafner, "The multiple multipole method in electrostatic and magnetostatic problems," *IEEE Transactions on Magnetics*, vol. 19, pp. 2367–2370, NOV 1983.

[17] J. Smajic, C. Hafner, L. Raguin, K. Tavzarashvili, and M. Mishrikey, "Comparison of numerical methods for the analysis of plasmonic structures," *Journal of Computational and Theoretical Nanoscience*, vol. 6, pp. 763–774, MAR 2009.

[18] T. Sannomiya, J. Voeroes, and C. Hafner, "Symmetry decomposed multiple multipole program calculation of plasmonic particles on substrate for biosensing applications," *Journal of Computational and Theoretical Nanoscience*, vol. 6, pp. 749–756, MAR 2009.

[19] E. Moreno, D. Erni, C. Hafner, and R. Vahldieck, "Multiple multipole method with automatic multipole setting applied to the simulation of surface plasmons in metallic nanostructures," *Journal of the Optical Society of America A-Optics Image Science and Vision*, vol. 19, pp. 101–111, JAN 2002.

[20] J. Dorfmüller, R. Vogelgesang, R. T. Weitz, C. Rockstuhl, C. Etrich, T. Pertsch, F. Lederer, and K. Kern, "Fabry-Perot Resonances in One-Dimensional Plasmonic Nanostructures," *Nano Letters*, vol. 9, pp. 2372–2377, JUN 2009.

[21] T. Zentgraf, J. Dorfmüller, C. Rockstuhl, C. Etrich, R. Vogelgesang, K. Kern, T. Pertsch, F. Lederer, and H. Giessen, "Amplitude-and phase-resolved optical near fields of split-ring-resonatur-based metamaterials," *Optics Letters*, vol. 33, pp. 848–850, APR 15 2008.

[22] O. Schubert, J. Becker, L. Carbone, Y. Khalavka, T. Provalska, I. Zins, and C. Soennichsen, "Mapping the polarization pattern of plasmon modes reveals nanoparticle symmetry," *Nano Letters*, vol. 8, pp. 2345–2350, AUG 2008.

[23] U. Kreibig and L. Genzel, "Optical absorption of small metallic particles," *Surface Science*, vol. 156, Part 2, no. 0, pp. 678 – 700, 1985.

[24] V. Chegel, O. Rachkov, A. Lopatynskyi, S. Ishihara, I. Yanchuk, Y. Nemoto, J. P. Hill, and K. Ariga, "Gold nanoparticles aggregation: Drastic effect of cooperative functionalities in a single molecular conjugate," *The Journal of Physical Chemistry C*, vol. 116, no. 4, pp. 2683–2690, 2012.

[25] L. M. Liz-Marzan, M. Giersig, and P. Mulvaney, "Synthesis of nanosized gold-silica core-shell particles," *Langmuir*, vol. 12, pp. 4329–4335, Jan. 1996.

[26] I. Malitson, "Interspecimen comparison of refractive index of fused silica," *Journal of the Optical Society of America*, vol. 55, no. 10P1, pp. 1205–&, 1965.

[27] J. R. DeVore, "Refractive indices of rutile and sphalerite," *JOSA*, vol. 41, no. 6, pp. 416–417, 1951.

[28] A. J. Moule, H. J. Snaith, M. Kaiser, H. Klesper, D. M. Huang, M. Gratzel, and K. Meerholz, "Optical description of solid-state dye-sensitized solar cells. i. measurement of layer optical properties," *Journal of Applied Physics*, vol. 106, no. 7, p. 073111, 2009.

[29] H. A. Atwater and A. Polman, "Plasmonics for improved photovoltaic devices.," *Nature Materials*, vol. 9, no. 3, pp. 205–13, 2010.

Plasmonic Core-Shell Nanoparticles in Perovskite Solar Cells

CHAPTER 4

Enhancement of Perovskite-based Solar Cells Employing Core-Shell Gold-Silica Nanoparticles

Photocurrent and efficiency enhancement in meso-superstructure organometallic halide perovskite solar cells incorporating core-shell Au@SiO_2 nanoparticles (NPs) is demonstrated with device efficiencies of up to 11.4%. The enhancement is attributed to a previously unobserved and unexpected mechanism of reduced exciton binding energy, rather than improved light absorption. These findings represent a new aspect and lever for the application of metal nanoparticles in photovoltaics, and could lead to facile tuning of exciton binding energies in perovskite semiconductors. This work is published in [1].

This work was conducted in close collaboration with Wei Zhang from Oxford University and his contributions will be noted in the figure captions.

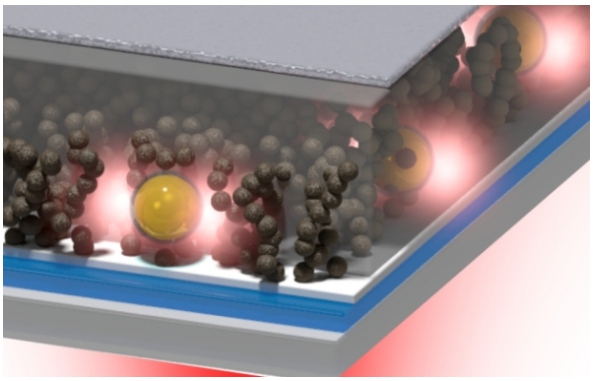

Fig. 4.1 Illustration of gold-silica nanoparticles with plasmonic field in a perovskite solar cell. This illustration was created with the help of Sven M. Hein of TU Berlin.

4.1 Experimental

General device making is described in Chapter 2.2. In this section, only some of the specific differences are outlined.

Nanoparticles synthesis for Au@SiO_2

80 nm gold nanoparticles with an 8 nm SiO_2 shell were synthesized in a three-step seeded growth method as outlined in Appendix A and adapted from [1–3]. The nanoparticles were provided by Yao Sun from Cornell University.

Au@SiO_2 incorporation

Here, the specific details for device fabrication incorporating Au@SiO_2 are outlined.

A thin layer of compact anatase TiO_2 of ~50 nm in thickness was formed through spray pyrolysis of titanium diisopropoxide bis(acetylacetonate) diluted in anhydrous ethanol at a volumetric ratio of 1:10 using oxygen as a carrier gas. The procedure was completed by sintering at 500°C for 45 min.
130 nm thick mesoporous Al_2O_3 layer was deposited by spin-coating Al_2O_3 paste (which contains organic binders and is prepared according to [4]) diluted further in anhydrous ethanol at 1:2 by weight at 2000 rpm for 45 s. To fabricate Au@SiO_2 devices, the Al_2O_3 precursor solution was replaced by a Au@SiO_2/Al_2O_3 mixture with weight ratio ranging from 0.45 to 1.8 wt%. The layer was then sintered in air at 500°C for 30 min. Once cooled, 100 µl of 30 wt% perovskite precursor solution was dispensed on the previously prepared mesostructure by spin-coating at 2000 rpm for 45 s in air. The coated films were then incubated in a small oven set at 100°C for 45 min.
Devices based on mesoporous TiO_2 films were fabricated with a similar procedure by spin-coating TiO_2 paste (Dyesol 18NR-T) diluted in anhydrous ethanol at 1:3.5 by weight at 1500 rpm for 30 s.

UV-vis spectroscopy

The samples for the UV-Vis study were prepared following exactly the same procedures as for the device fabrication. The absorptance of the active layer in the full device was measured on a Carry 300 Bio (Agilent Technologies) with an integrating sphere accessory. Four samples were used for each measurement and the average of all spectra is presented.

Steady-state and time-resolved photoluminescence spectra

Time-resolved and time-integrated photoluminescence (PL) spectra of devices without the spiro-OMeTAD or top electrodes were acquired using a time-correlated single photon

counting (TCSPC) setup (FluoTime 300, PicoQuant GmbH). Samples were photoexcited through the glass using a 507 nm laser head (LDH-P-C-510, PicoQuant GmbH) with pulse duration of 117 ps, fluence of ~0.03 nJ/cm^2, and a repetition rate of 40 MHz (TiO_2 samples) or between 2-5 MHz (Al_2O_3 samples). Time-resolved measurements were acquired from emission at 765 nm, and global bi-exponential fits across at least 4 devices were carried out using commercial fitting software (FluoFit v4.5.3, PicoQuant GmbH). Low temperature measurements were carried out using an Oxford Instruments OptistatDN cryostat with a specialized fitting for the TCSPC setup.

4.2 Results and Discussion

In this chapter, core-shell metal-dielectric nanoparticles within a thin-film solar cell technology are combined in a perovskite absorber. The structure of the solar cells is shown schematically in Figure 4.2a. A 50 nm thick, compact anatase TiO_2 layer is deposited on a conducting glass substrate to ensure selective collection of electrons at the fluorine doped tin oxide (FTO contact), which is followed by a mesoporous layer of Al_2O_3 of about 130 nm in thickness. To incorporate metal nanoparticles (NPs) into the solar cells, Au@SiO_2 core-shell NPs were mixed with the Al_2O_3 precursor solution at varying concentrations. The perovskite precursor solution was then spin-coated on the mesoporous layer and dried at 100°C in air. Notably, at the present concentrations of perovskite solution (30 wt% in DMF), a capping layer of solid-perovskite film was formed on top of the mesoporous alumina [4]. Finally, a layer of p-type organic hole-conductor, spiro-OMeTAD, was deposited on top via spin-coating to enable selective p-type contact to the perovskite absorber, and transport of holes to the thermally evaporated silver contact. For the rest of this discussion, the terms "MSSCs incorp/rating the Au@SiO_2 nanoparticles" and "Au@SiO_2 devices" are used interchangeably , and the standard MSSC (without gold nanoparticles) is referred to as "control" or "Al_2O_3-only" device. A representative TEM image of a Au@SiO_2 NP is shown in Figure 4.2b. The Au NPs of about 80 nm diameter are coated by an ~8 nm SiO_2 shell, with an absorption peak at ~550 nm in water, as shown in Figure 4.2c.

The slightly red shifted extinction spectrum of Au@SiO_2 NPs as compared to that of Au NPs is expected from the change in the local refractive index (see Chapter 2) [5]. Previously, it was shown that bare gold nanoparticles without insulating SiO_2 shells are unfavourable because of structural and thermal instability. In particular, the silica shell is needed to prevent Ostwald ripening, i.e. the tendency of metal nanoparticles to regroup into larger spheres when heated, and enables thermal processing during device fabrication [6–8].

More importantly, the insulating silica shell prevents direct contact between bare Au and the hole transporter spiro-OMeTAD, or the perovskite, inhibiting an unwanted charge recombination pathway within the devices.

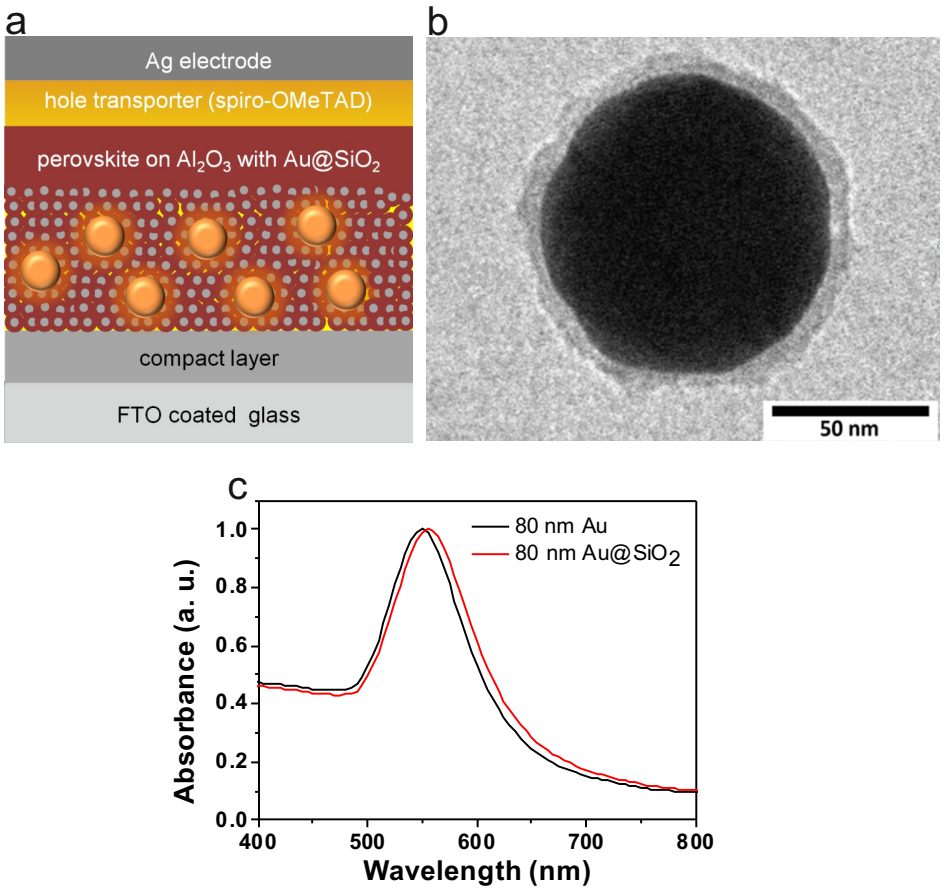

Fig. 4.2 (a) Device structure schematics for MSSCs with integrated Au@SiO_2 NPs (yellow circles). (b) TEM image of Au@SiO_2 NPs. (c) UV-Vis spectra in water of bare Au NPs as well as Au@SiO_2 NPs. The TEM and UV-Vis measurements were taken by Yao Sun from Cornell University.

To investigate the effect of Au@SiO_2 NPs on device performance, standard MSSCs were fabricated with only Al_2O_3 NPs as the scaffold, and then with Au@SiO_2 NPs at 0.45 to 1.8 wt% with respect to the Al_2O_3. Figure 4.3a presents the photocurrent density-voltage (JV) curves of the MSSCs with and without Au@SiO_2 NPs (with the same film thickness). The Al_2O_3-only device has a peak power conversion efficiency (PCE) of 10.7%, whereas the Au@SiO_2 device exhibited a PCE of 11.4%. Compared with the Al_2O_3-only device, the fill factor (FF) and open-circuit voltages (V_{oc}) were similar, while the short-circuit current density (J_{sc}) significantly increased from 14.8 mA/cm^2 to 16.9 mA/cm^2. The effect of Au@SiO_2concentration on device performance was further investigated. Figure 4.3b shows the average device performance parameters as the concentration of Au@SiO_2NPs varies from 0 to 1.8 wt%. To ensure reliability, 48 devices were made for each concentration.

At the optimum concentration of 0.9 wt%, an average PCE of 9.5% was achieved, which is 13% higher than the average control device efficiency of 8.4%. In addition, the average J_{sc} increased by 13.5% from 13.4 mA/cm^2 to 15.3 mA/cm^2. This validates that incorporation of Au@SiO_2 NPs has improved the device performance by enhancing the photocurrent.

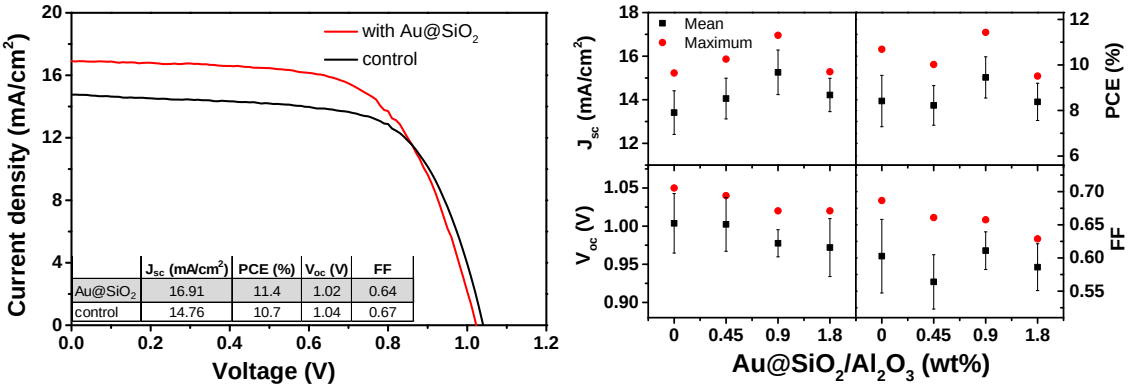

(a) JV curves **(b)** Device parameters

Fig. 4.3 (a) Representative JV curves for Al_2O_3-only and Au@SiO_2devices measured under AM1.5 simulated sunlight (100 mW/cm^2 irradiance). (b) Concentration dependence of Au@SiO_2 NPs on the device performance as measured over 48 devices for each concentration.
The devices were fabricated and characterized with the help of Wei Zhang from Oxford University.

After this work was conducted, hysteresis in perovskite solar cells was reported. This means the JV curve measurements depend on scanning speed and scanning direction, i.e. from short-circuit to forward bias (denoted as "SC-FB") and back ("FB-SC") [9–12]. In addition, the precise device architecture and processing conditions are of major importance as well [13–15].

The effect is not fully understood at the current stage but some key observations link hysteresis to [9]:

- the perovskite absorber as opposed to other materials within the solar cell.
- the contact material (interfaces).
- planar versus mesoporous heterojunction architecture.
- slower scan rates (~0.001 V s^{-1}) which seem to exacerbate hysteresis for planar devices.

Possible hypotheses for the hysteresis effect were suggested [9]:

- Defects in the perovskite material may act as traps for electrons and holes.
- Inorganic-organic perovskites have been shown to exhibit ferroelectric properties [16, 17]. Thus, there may be an innate polarization of the material depending on the applied bias.
- Within the perovskite absorber, there may be mobile excess ions, present as interstitial defects (iodide and methylammonium). Ion migration to either side of the film during device operation may contribute to the observed hysteresis.

Again, more research is needed to substantiate these suggestions.

As a remedy it was suggested to scan devices at "stabilized conditions". This means from a preliminary scan the maximum power point is inferred. Then the device is held at the voltage of the maximum power point under under AM1.5 sunlight. The short-circuit current is monitored over time until it finally settles. Consequently, a "stabilized efficiency" can be used as a measure for device performance.

The stabilized power output method was not developed at the time this work was conducted. However, Figure 4.4 shows the forward and backward scan for the devices in Figure 4.3a. As can be seen, for the control device the PCE for the SC-FB scan is at 7.5% as compared to the FB-SC scan with a PCE of 10.6%. The drop in efficiency is mainly due to fill factor. For the Au@SiO_2 device the PCE increases from 8.8% (SC-FB scan) to 11.4% (FB-SC scan) which is (again) mainly due to a fill actor decrease. It should be noted that the scan rate of ~0.001 V s^{-1} is relatively low which tends very often to coincide with the stabilized efficiencies. Thus, the above documented hysteresis values indicate a relatively small hysteresis effect within this experiment. Accordingly, the overall performances is likely to be between the two different scans. Moreover, all devices were scanned under the same conditions including the same scan direction and scan speed. This makes all results comparable to each other and the effect of hysteresis, while problematic, does not infringe on the overall comparison of control and Au@SiO_2 devices.

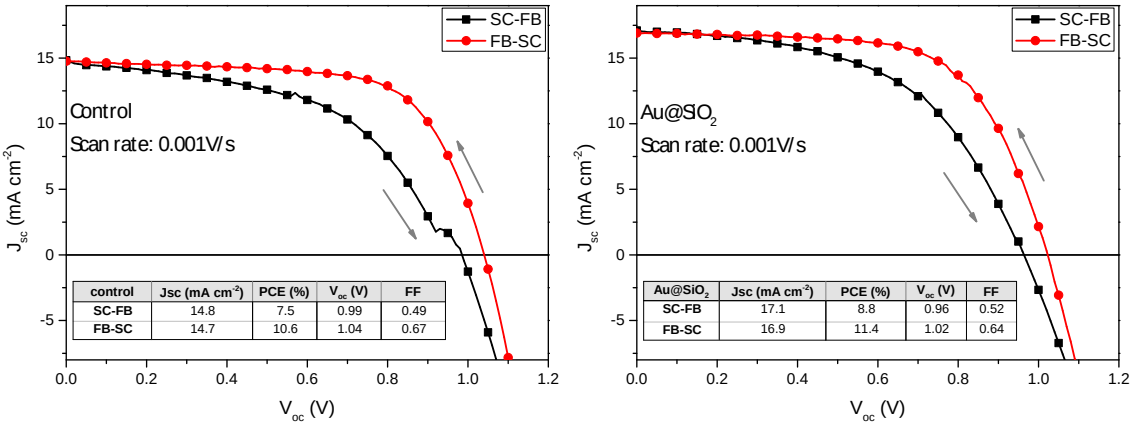

(a) Control **(b)** Au@SiO_2

Fig. 4.4 (a) Forward, denoted as "short circuit - forward bias" or "SC-FB", and backward ("FB-SC") scan for the control device from Figure (a). The scan rate is 0.001 V s^{-1}. (b) Same measurement for the Au@SiO_2 device.
The devices were fabricated and characterized with the help of Wei Zhang from Oxford University.

In order to confirm that the improvement of device performance is due to the effect of the Au core rather than the possible scattering enhancements or another electronic influence of the SiO_2 shell, a control experiment was performed by incorporating SiO_2 NPs (~100 nm in diameter) into the Al_2O_3 paste. Considering the density difference for Au

(ρ_{Au} = 19.30 g cm^{-3}) and SiO_2 (ρ_{SiO_2} = 2.648 g cm^{-3}), the concentration of SiO_2 NPs was correspondingly tuned from 0 to 0.24 wt%.

Both the J_{sc} and PCE decreased when SiO_2 NPs were incorporated as can be seen in Figure 4.5. Therefore, the enhancement of J_{sc} and PCE for the Au@SiO_2 devices is attributed to the presence of the gold core rather than to any effect from the SiO_2 shell. To demonstrate

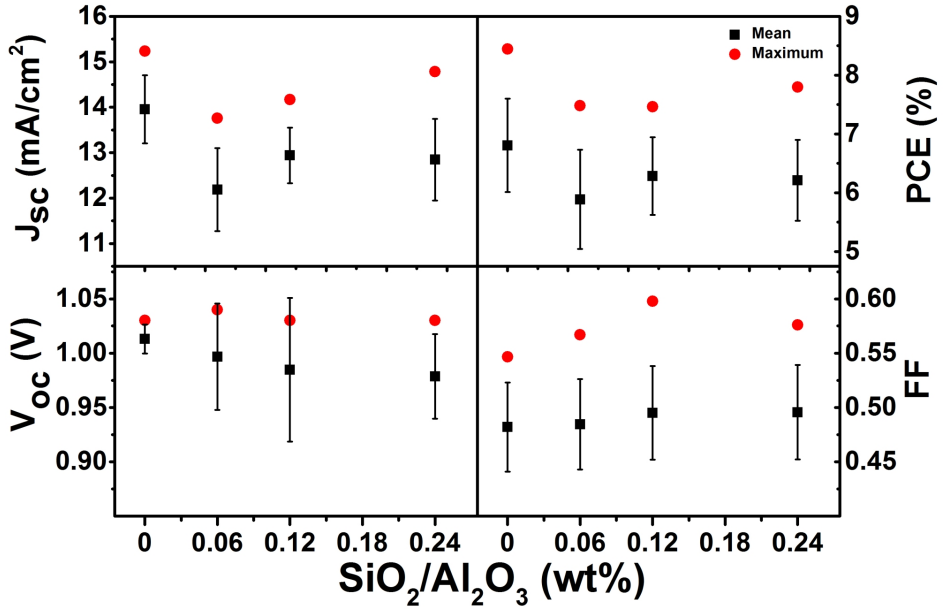

Fig. 4.5 Concentration dependence of SiO_2 NPs on the device performance. The devices were fabricated and characterized with the help of Wei Zhang from Oxford University.

broader applicability of this approach, mesoporous TiO_2-based devices were fabricated, where the device represents a perovskite sensitized solar cell (PSSC). Results are shown in Figure 4.6.

A similar enhancement trend is obtained for both J_{sc} (increased from 12.7 to 13.7 mA/cm^2) and PCE (increased from 6.0 to 7.2%) when Au@SiO_2 NPs are incorporated into the TiO_2. This trend of enhanced photocurrent was observed over tens of sets of devices over a period of more than 12 months of experimentation. As initially designed, it was expected to attribute the improvement in enhanced photocurrent to enhanced light harvesting through plasmonic light interaction in the metal nanoparticles. An integrating sphere accessory was used to measure the active layer in complete MSSCs (including Ag back electrode) with and without Au@SiO_2 NPs.

After careful absorptance measurements a plasmon enhanced light absorption cannot be justified as shown in Figure 4.7a where the light absorption in the Au@SiO_2 layers is indistinguishable from the control device.

This is due to the low loading of Au@SiO_2 NPs (0.9 wt%) in the Al_2O_3 film. In Figure 4.7b the incident photon-to-current conversion efficiency (IPCE) for typical devices is shown. The spectrum from the Au@SiO_2 device is increased over the whole wavelength range (400 - 750 nm), as compared to the control device.

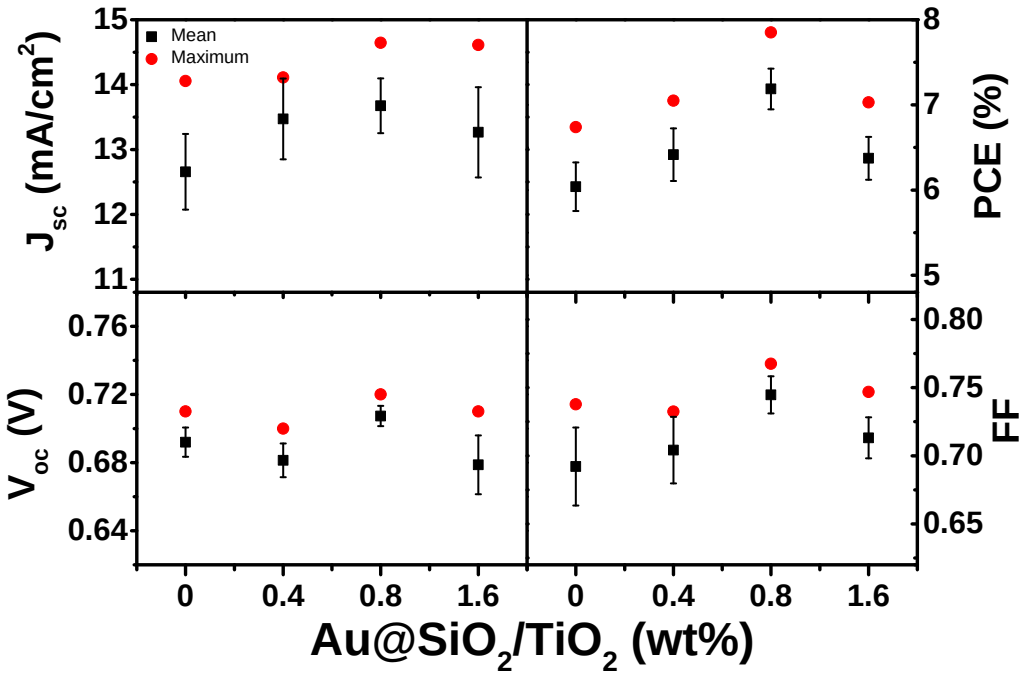

Fig. 4.6 Concentration dependence of $Au@SiO_2$ NPs on the device performance using a TiO_2 mesoporous film. The devices were fabricated and characterized with the help of Wei Zhang from Oxford University.

Based on Figure 4.7b, the increase in IPCE (ΔIPCE) with the addition of the $Au@SiO_2$ NPs is calculated and presented in Figure 4.7c.

Although there are some features in the spectrum, the enhancement is broadly distributed over the whole range and does not specifically follow the plasmon mode profile. A bias white light of ~50 mW cm^{-2} was also present in order to create similar conditions to the solar simulator measurement.

Again, enhanced photocurrent was observed unambiguously, but no significant change to the light harvesting. SiO_2 nanoparticles on their own do not enhance the photocurrent, but rather reduce it. Thus, the conclusion is that $Au@SiO_2$ NPs enhance the solar cell's internal conversion efficiency.

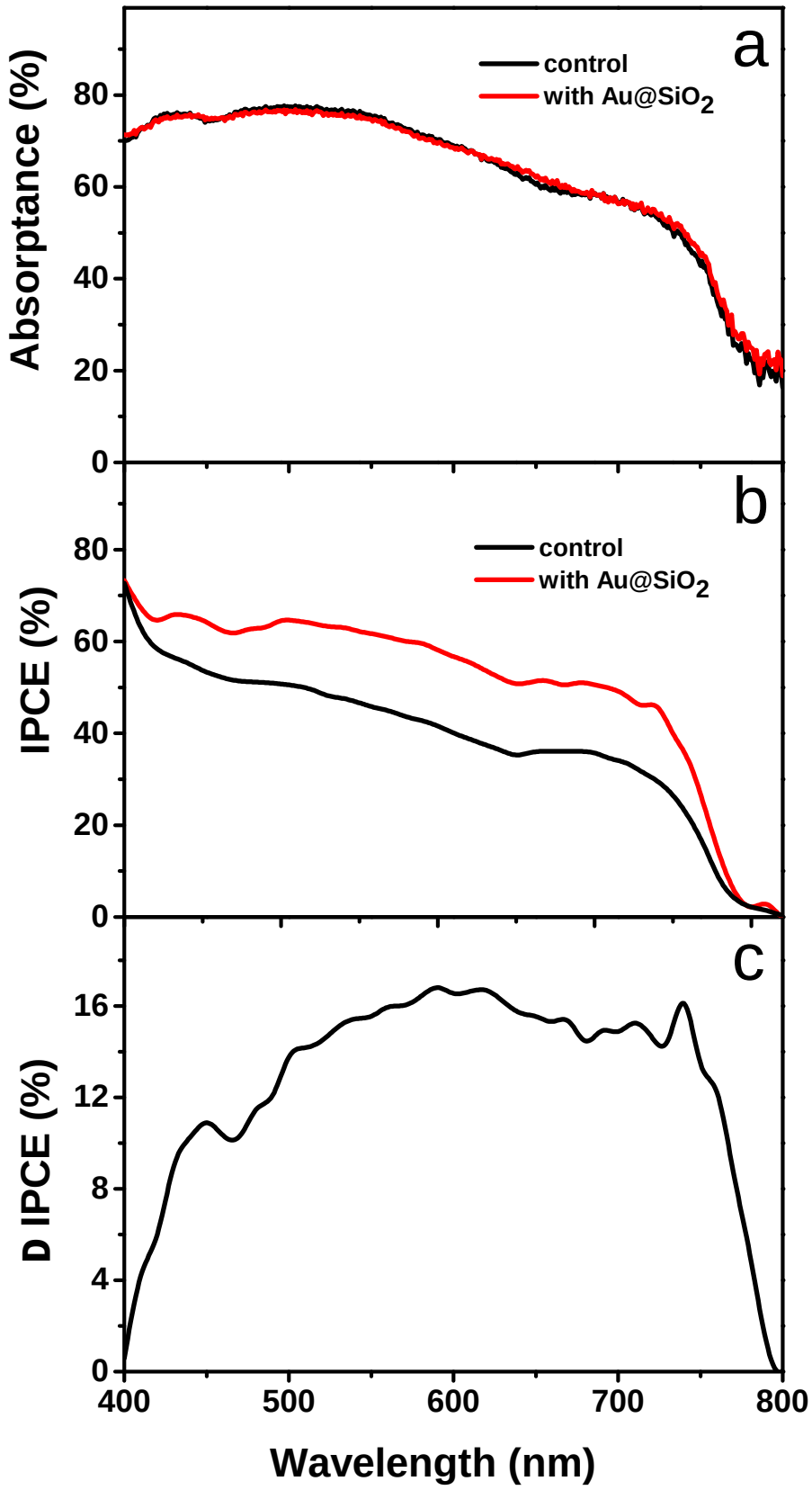

Fig. 4.7 (a) Absorptance of the active layer in Al_2O_3-based device without (control) and with Au@SiO_2 NPs. (b) IPCE spectra of control and Au@SiO_2 devices. (c) The increase in IPCE (ΔIPCE) with the addition of Au@SiO_2 NPs.

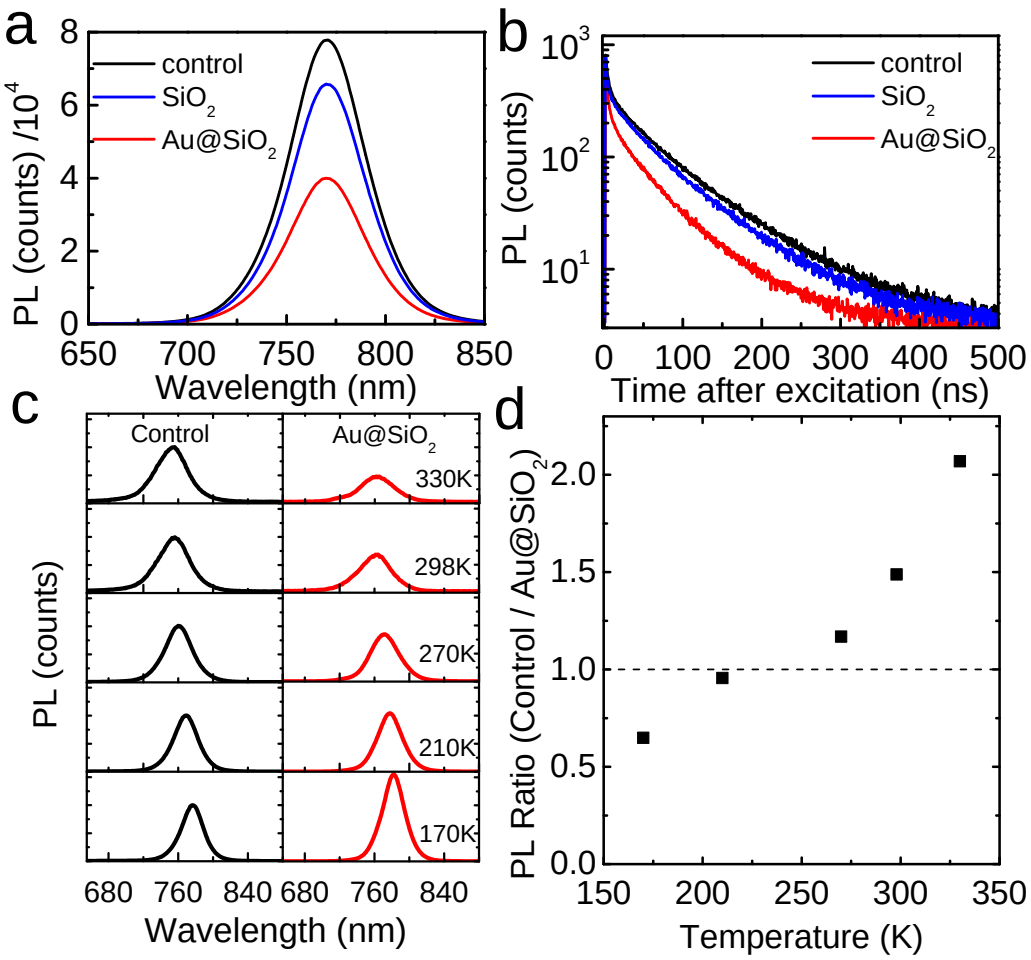

Fig. 4.8 (a) Time-integrated spectra and (b) time-resolved PL decays (detected at 765 nm), averaged across measurements from 16 samples, for perovskite coated on Al_2O_3-only (control) and films incorporating SiO_2 or Au@SiO_2 NPs. (c) Temperature dependence of time-integrated PL spectra for perovskite films coated on Al_2O_3-only (control) and films incorporating Au@SiO_2 NPs. The spectra for the controls have been normalized to the peak of the emission, and the films incorporating Au@SiO_2 NPs scaled accordingly. Both samples exhibit a considerable increase in absolute PL on reducing temperature. (d) Ratio of the wavelength integrated PL of the control and sample incorporating Au@SiO_2 NPs. The PL measurements were performed with the help of Samuel D. Stranks of Oxford University.

To probe any early time changes to the primary exciton or electron-hole pairs in the perovskite absorber, a series of time-resolved and steady state photoluminesence (PL) measurements were performed on perovskite-coated mesoporous alumina, with and without the addition of Au@SiO_2 NPs. Spiro-OMeTAD was not present in these films. Figure 4.8a shows the room temperature time-integrated PL spectra, averaged across 16 samples, revealing a significant reduction in the PL of the perovskite samples incorporating Au@SiO_2 NPs. The time-resolved measurements at the peak perovskite emission (765 nm) are shown in Figure 4.8b. Again an enhanced PL quenching rate with the Au@SiO_2 NPs was observed, with global bi-exponential fits to the 16 measurements giving time constants of $\tau_1 = 4.88 \pm 0.66$ ns and $\tau_2 = 71.25 \pm 1.45$ ns for the control (no Au@SiO_2 NPs) and shorter

values of $\tau_1 = 3.48 \pm 0.41$ ns and $\tau_2 = 50.94 \pm 1.32$ ns for the perovskite films coated on the mesoporous alumina scaffold containing the Au@SiO_2 NPs. By contrast, there is only a slight change in the PL decay dynamics and time-integrated spectra with the addition of solid SiO_2 NPs at a similar concentration. This result is reconfirmed in the titania mesoporous devices where the PL is clearly quenched for Au@SiO_2 and hardly any difference can be seen for the SiO_2 devices (see Figure 4.9).

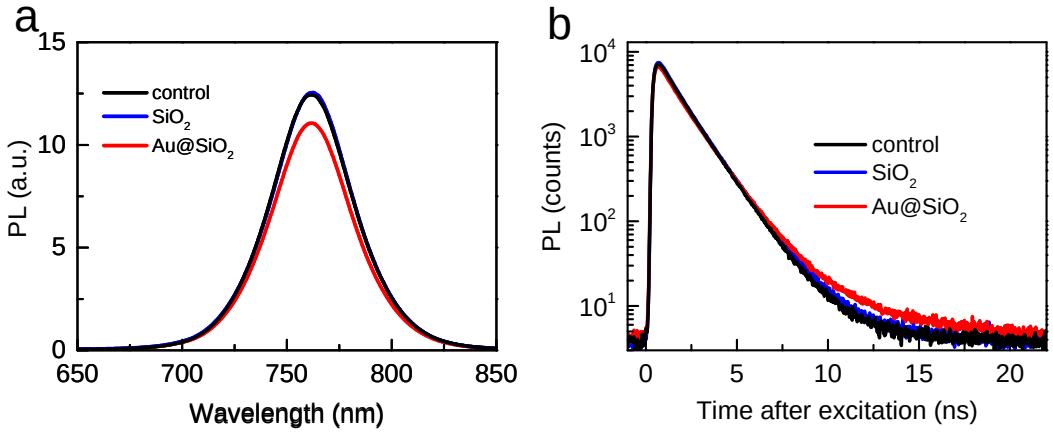

Fig. 4.9 (a) Time-integrated and (b) time-resolved (detected at 765 nm) PL spectra, averaged across measurements from 16 samples, for perovskite on TiO2-only and films incorporating SiO_2 or Au@SiO_2 NPs. The PL measurements were performed with the help of Samuel D. Stranks of Oxford University.

These results show that the presence of the metal nanoparticles quenches the photoluminescence at room temperature. If this was a system incorporating tightly bound Mott Excitons, such as organic semiconductors, the assumption would be that the excitons are being quenched by either energy transfer to the metal nanoparticles, a speeding up of the radiative or non-radiative decay rate, or via induced charge separation. Judging by the enhanced photocurrent in the devices, energy transfer to the metal nanoparticles is unlikely, and speeding up of the non-radiative or radiative decay rate is also unlikely to result in enhanced charge generation. Hence the conclusion is that ionization of the exciton and enhanced charge separation is occurring. With the perovskite system, the binding energy of the exciton has been reported to be ~50 meV [18], which should exhibit more delocalized Wannier-like exciton characteristics. However, this has only been estimated on $CH_3NH_3PbI_3$ in the low temperature orthorhombic phase, and if the exciton binding energy of the material here is larger, there may be coexistence of excitons and free charge and a certain fraction of geminate electron-hole recombination at room temperature, which would result in photoluminescence.

To probe the influence of the Au@SiO_2 NPs in more depth, a temperature dependent study of the photoluminescence was performed. As shown in Figure 4.8c and Figure 4.10, on reducing temperature the photoluminescence increases in magnitude considerably, likely due to an increased fraction of excitonic recombination (because the phonon energy decreases far below the exciton binding energy) [19], and also undergoes a red-shift.

The red-shift with reducing temperature is unusual for conventional semiconductors but has been previously reported for Pb-based compounds which exhibit a negative Varshni parameter [20–22]. One means to determine the exciton binding energy in conventional semiconductors [23, 24], which has been employed many times previously for semiconducting perovskites [19, 25], is to measure the absolute PL quenching of the exciton emission as a function of temperature, where the exciton PL from a material with a low exciton binding energy is rapidly quenched with increasing temperature, and a system with a larger exciton binding energy is more gradually quenched with increasing temperature.

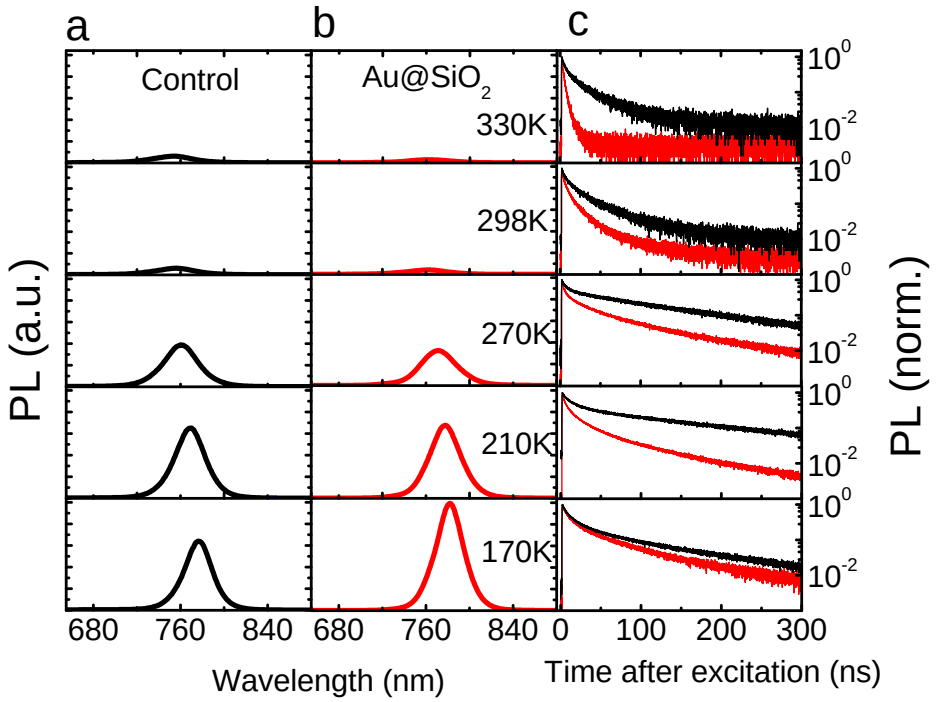

Fig. 4.10 Temperature dependence of time-integrated PL spectra on an absolute scale for perovskite on (a) Al_2O_3-only (control) and (b) films incorporating Au@SiO_2 NPs. Data are presented on the same scale. (c) Temperature dependence of the normalized time-integrated PL decays of the perovskite peak emission for the control (black) and films incorporating Au@SiO_2 NPs (red). The PL measurements were performed with the help of Samuel D. Stranks of Oxford University.

As can be seen in Figure 4.8c, the PL from the sample incorporating Au@SiO_2 NPs is considerably larger than that of the control at 170 K, but lesser in magnitude than the control at room temperature. Plotting the ratio of the wavelength-integrated PL intensity for the Au@SiO_2 samples over the control samples (Figure 4.8d), a steep gradient, going from just above 0.5 at low temperatures, to just above 2 at high temperatures was observed.

Firstly, the enhanced PL in the samples incorporating Au@SiO_2 NPs at low temperature indicates that the presence of the Au@SiO_2 nanoparticles is not enhancing any non-radiative recombination processes and, by contrast, results in a speeding up of the radiative decay rate [26]. If it is assumed that the majority of the PL is originating from radiative exciton recombination, then the data can be used to estimate the exciton binding energy for the two systems shown in Figure 4.11 [20, 25].

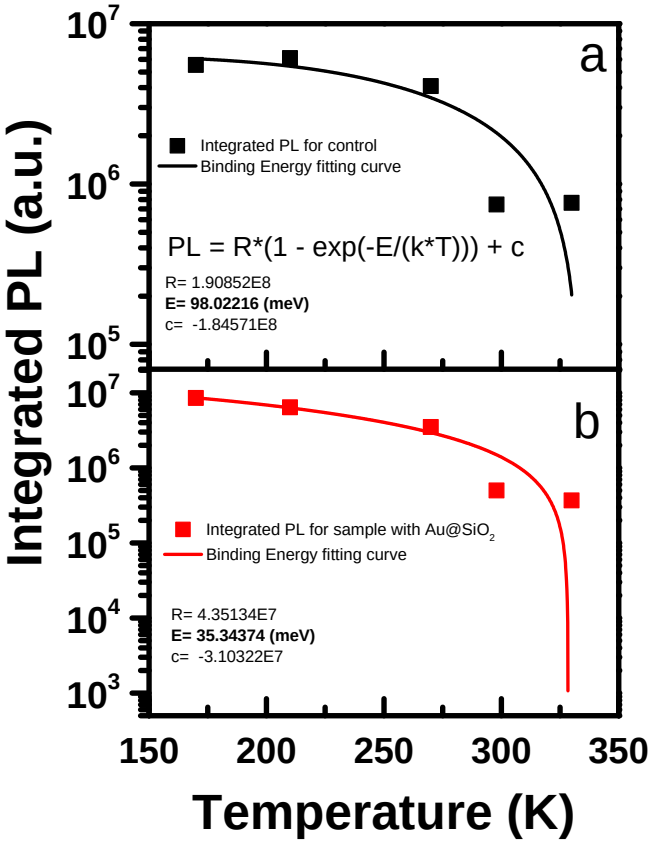

Fig. 4.11 Time-integrated PL spectra as a function of temperature for perovskite films on (a) Al_2O_3-only (control) and (b) Al_2O_3 films with Au@SiO_2 NPs. The solid lines in both figures are fits according to [20, 25]

By fitting the integrated PL the exciton binding energies can be estimated to be ~98 meV for the control samples and ~35 meV for the samples incorporating Au@SiO_2 NPs. The reduction in exciton binding energy in the proximity of surface plasmon modes has been previously demonstrated for Al-coated ZnO [27], but to the best of my knowledge, never observed before in any photovoltaic system. This is strong evidence for reduced exciton binding energy in the studied perovskite absorber with the incorporation of the core-shell metal nanoparticles, and consistent with the solar cell characteristics. However, these results rely on the assumption that the PL is predominantly from exciton recombination. Although this has been applied previously for similar perovskites [25], more detailed and extensive measurements of the fundamental exciton and charge dynamics in this largely uninvestigated perovskite semiconductor are required.

The precise mechanism which is responsible for reducing the exciton binding energy is also not fully understood and requires further experimental and theoretical investigation, but is likely to be due to the subtleties of exciton-plasmon coupling [26]. Also, a slight red-shift in PL position is observed for the Au@SiO_2 samples in comparison to the control films, which becomes more apparent at lower temperatures. Initially, the expectation is a blue-shift with reduced binding energy as observed in *conventional semiconductors*, since the exciton absorption should be just below the band gap.

However, at these relatively high temperatures, thermal broadening may mask these effects.

Another possible enhancement mechanism which has been proposed in the literature for other solar cells is plasmonic heating where local heating of the metal nanoparticles due to light absorption could result in improved operation of the solar cell due to increased temperature [28]. However, if this was the predominant influence then both PL quenching and a corresponding blue-shift at any given temperature should be seen, but they are not. Also some spectral signature mapping the absorption of the nanoparticles in the spectral response of the device would be expected. However, it has to be noted that a white light bias is used, which may mask this effect.

4.3 Summary

A successful strategy for incorporating core-shell metal-dielectric NPs into organometal halide perovskite solar cells was developed. At optimized conditions, the Au@SiO_2 device exhibited a significantly enhanced short-circuit photocurrent (J_{sc}) and average PCE of 9.5% as compared to the control device which showed an average PCE of 8.4%. Interestingly, at the optimum concentrations of Au@SiO_2nanoparticles, the light absorption in the complete devices is not significantly enhanced. Through a time-resolved and steady state temperature dependent photoluminescence study, the origin of the improved J_{sc} was attributed to a reduced exciton binding energy, and hence enhanced generation of free charge carriers with the incorporation of the metal nanoparticles. This represents a new enhancement mechanism for metal nanoparticles incorporated into photovoltaics, and may prove to be exceptionally useful for this new family of perovskite semiconductors where the exciton binding energy is in the order of 100 meV. Further work is required to fully understand the mechanism which is driving the enhanced solar cell performance.

CHAPTER 5

Plasmonic Silver-Titania Nanoparticles in Low-Temperature processed Perovskite Solar Cells

The previous chapter focused on integrating gold nanoparticles into perovskite solar cells. This directs the attention to other metals exhibiting similar plasmonic behaviour such as silver NPs which can be synthesized into many different shapes by employing inexpensive synthesis methods.

However, silver NPs show unstable behaviour under high temperature processing which makes integration into many of the conventional solar cell designs challenging. Here, for the first time, a successful low-temperature processing route is demonstrated for embedding temperature-sensitive core-shell silver-titania nanoparticles into a perovskite-based solar cell. The device efficiencyiy is enhanced from 11.4% to 13.7%. This provides a general strategy for incorporating thermally sensitive components for future enhancements of this solar cell type.

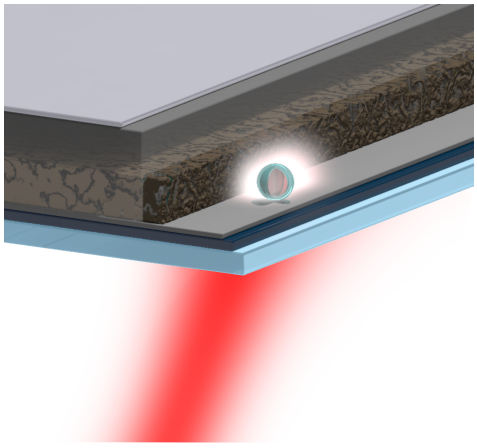

Fig. 5.1 Illustration of silver-titania nanoparticle with plasmonic field in a perovskite solar cell. This illustration was created with the help of Sven M. Hein of TU Berlin.

Introduction

Although gold is a well-known plasmonic material and has been intensively studied for a plethora of applications [29–33], it is still of interest to replace it with a cheaper metal for large scale photovoltaic applications. In general, silver is a preferred material for plasmonic applications because of its high quality factor over a broad spectral range, outperforming most metals [34, 35]. Moreover, silver NPs can be deposited on substrates with relative ease due to self-assembly properties, whilst synthesis is inexpensive via wet chemistry procedures leading to many different shapes like triangles, cubes, stars, rods, etc. allowing a myriad of optical properties [36]. Silver, however, is less thermally stable than gold or other metals. This limits its applicability whenever high temperature processing is involved [37]. For example, it is standard practice for DSSC to sinter the mesoporous TiO_2 layer at 500°C. Thus, in this study, temperature-sensitive Ag@SiO_2 core-shell nanoparticles are incorporated into perovskite solar cells fabricated with a *low* temperature procedure by Ball et al. [4], boosting device efficiencies. This route opens the door to other temperature sensitive design elements.

5.1 Experimental

Steady-state, time-resolved photoluminescence, and UV-vis spectra were taken according to the previous chapter.

Nanoparticles synthesis for Ag@TiO_2

30-40 nm Ag NPs with a 2-3 nm TiO_2 shell were synthesized by a polyol method, according to a reported procedure with slight modifications [38]. A detailed description can be found in Appendix A. The nanoparticles for this study were provided by Yao Sun from Cornell University.

Ag@TiO_2 incorporation

The general device making is described in Chapter 2.2. In the following, the specific details for device fabrication incorporating Ag@TiO_2 are outlined.

A TiO_2 compact layer was deposited by spin coating a 253 mM titanium isopropoxide precursor (diluted in a mildly acidic anhydrous ethanol solution) at a speed of 2000 rpm for 60 s followed by drying at 150°C for 15 min and then sintering at 500°C for 45 min. The final thickness is ~50 nm.

After cooling to room temperature an Al_2O_3 scaffold was spin coated at 2500 rpm for 45 s from a colloidal dispersion of <50 nm Al_2O_3 nanoparticles (no organic binders), followed by drying at 150°C for 30 min. Throughout all experiments the scaffold thickness was kept constant at about 350 nm by diluting the Al_2O_3 NPs with ethanol in a 1:2 volume ratio. This method was developed by James M. Ball from Oxford University [4].

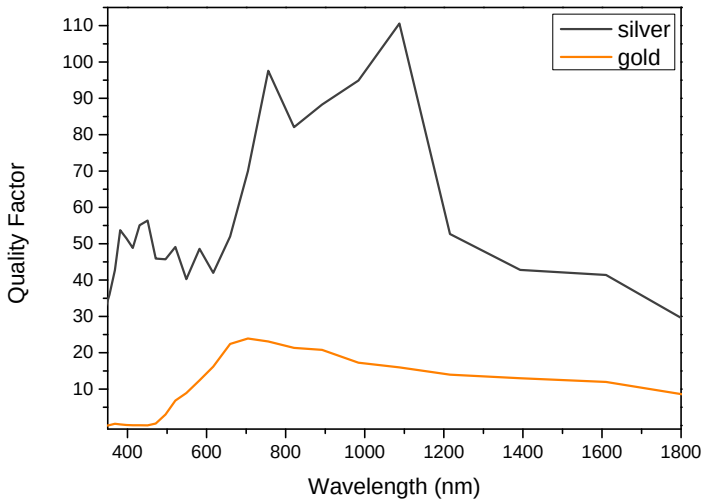

Fig. 5.2 Quality factor $Q = \omega \frac{\partial Re(\varepsilon)}{\partial \omega} / 2Im(\varepsilon)$ as calculated from experimental data of the dielectric constant [35, 42].

Silver nanoparticles dispersed in ethanol were incorporated into the Al_2O_3 scaffold by replacing appropriate amounts of ethanol used for the Al_2O_3 dilution such that the weight ratio of $Ag@TiO_2/Al_2O_3$ ranged from 1.1 to 4.4 wt%. All dispersions were put in an ultrasonic bath for at least 10 min to ensure optimal mixing. Note that the Ag NPs are not exposed to temperatures exceeding 150°C.

Simulations

Simulations of the electromagnetic field were conducted with the software package OpenMaXwell [39], i.e. a semianalytical Maxwell solver using multiple multipoles comprised of exact solutions of the Maxwell equations to model the overall time-harmonic electromagnetic field as outlined in Chapter 3. The calculations assumed plane wave excitation with the following refractive indices: 1.76 for alumina, 2.5 for titania, 2.55 for perovskite [40, 41], and n_{silver} from Johnson and Christy [42].

5.2 Results and Discussion

Silver is usually preferred over gold because of lower costs and a higher quality factor (see Figure 5.2). In this work, the concentration of $Ag@TiO_2$ in the active layer of a device processed at <150°C was optimized to show a significant device performance enhancement with a record PCE of 14.9% as compared to a control device. This study opens the door to investigate the effect of plasmonic silver nanomaterials in solar cells and provides a general strategy for integration of thermally sensitive components in electronic devices for various applications.

Figure 5.3a shows an SEM cross section image of a meso-superstructured solar cell (MSSC). A 50 nm thick TiO_2compact layer is on top of an electron collecting fluorine-doped tin oxide (FTO) electrode, followed by an insulating Al_2O_3 scaffold. This scaffold is infiltrated and capped by $CH_3NH_3PbI_{3-x}Cl_x$ perovskite which forms the photoactive area where electrons and holes are separated under solar irradiation. The holes are transported through the HTM (Spiro-OMeTAD) and collected at the silver electrode. Silver nanoparticles with titania shell (Ag@TiO_2, 40 nm@2 nm), as shown in Figure 5.3b, were blended into the Al_2O_3 scaffold at different weight concentrations up to 4.4 wt% (Ag@TiO_2/Al_2O_3) while keeping the overall thickness constant.

Figure 5.3c shows the absorption spectrum of the Ag NPs with (red) and without (black) titania shell in ethanol. A narrow plasmonic peak is observed at around 410 nm for the bare Ag NPs whilst the peak at 510 nm can be explained by formation of larger silver clusters from agglomeration during the synthesis process. These larger clusters are removed in the subsequent purification process before the encapsulation with the titania shell, resulting in a single sharp peak (red curve). The slight red-shift of the plasmonic peak is expected in the presence of the TiO_2 shell because of the increased effective refractive index [43].

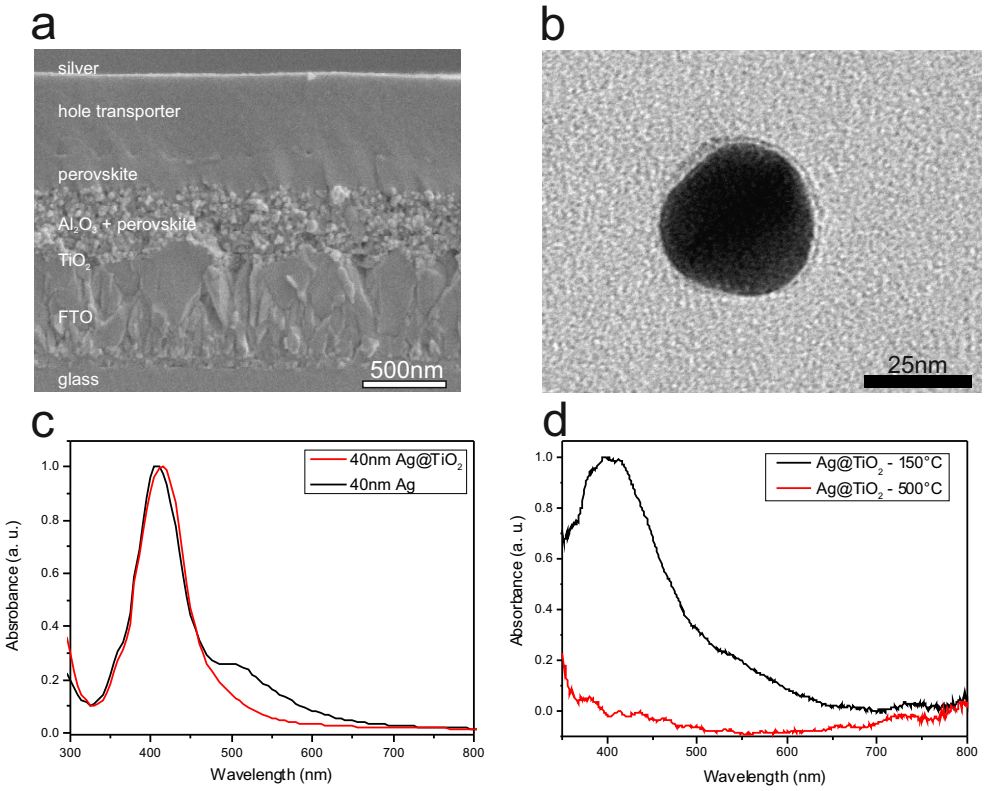

Fig. 5.3 (a) SEM cross section of a meso-superstructured perovskite solar cell (MSSC). The scale bar is 500 nm. (b) TEM cross section of a 40 nm silver core with a 2 nm TiO_2 shell. The scale bar is 25 nm. (c) Absorbance of silver nanoparticles without (solid black line) and with titania shell (red) in ethanol. (d) Absorbance of high concentration of Ag@TiO_2 NPs in an Al_2O_3 thin film deposited on FTO glass and heated to 150°C (black) and 500°C (red). The plasmonic peak of Ag@TiO_2 NPs disappears completely upon sintering at 500°C. The TEM image in (b) and UV-vis data in (c) were taken by Yao Sun from Cornell University.

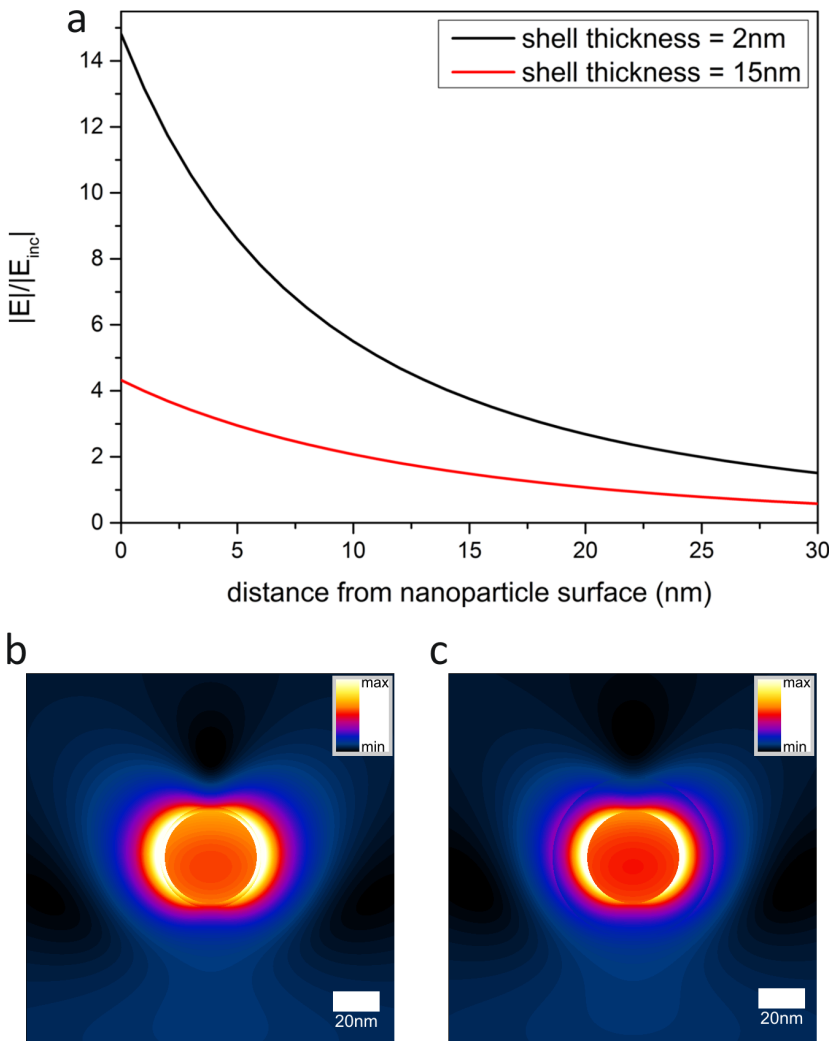

Fig. 5.4 (a) Electric field enhancement $|\mathbf{E}| \,/\, |\mathbf{E}_{inc}|$ over the distance from the nanoparticle shell for a 20 nm silver core and a 2 nm titania shell (black) and a 15 nm titania shell (red) in a mixed medium of perovskite/Al_2O_3 with respective electric field simulation for (b) the 2 nm, and (c) 15 nm shell at the corresponding dipole frequencies.

For photovoltaic applications, it is necessary to coat the Ag NPs with a titania shell which contributes to chemical stability and prevents bare Ag NPs from acting as charge carrier recombination centres in the photoactive layer [8]. Generally, the plasmonic optical near-field only extends to a few tens of nanometres and thus thinner shells around Ag NPs screen less of the plasmonic field as can be seen in the electromagnetic simulations in Figure 5.4 for a 2 nm and 15 nm thick titania shell. At the same time, thick shells are advantageous for increased thermal stability. The trade-off of these two effects imposes an inherent limit for shell thicknesses.

In fact, a 1-2 nm titania shell, as used in this study, is insufficient for thermal protection of the silver core at 500°C as demonstrated in Figure 5.3d where the plasmonic peak vanishes precluding these Ag@TiO_2 NPs from high temperature processing steps in device fabrication.

It is well-documented that the surface atoms in metals start diffusing out at temperatures far below the bulk melting point resulting in a liquid, premelted surface layer which facilitates the overall melting process [44, 45].

This is further influenced by the local surface curvature of the NPs [46], vapour pressure of the material [37] and substrate support [47]. Thus, shape change of nanoparticles already starts at low temperatures [48]. Ag NPs in particular, due to a relatively low bulk melting point of 961°C and high vapour pressure [37], can be very sensitive towards heating temperatures [49] and even complete loss of optical properties as observed here.

An additional example highlighting the temperature sensitivity of non-spherical NPs of even more stable metals like gold is shown in Figure 5.5 displaying the absorbance spectrum of ~40 nm gold nanorods with ~10 nm thick silica shell before and after heating at 300°C. The inset is a TEM image of a representative particle at room temperature. Nanorods before heating (black line) show two distinct resonance frequencies, one transversal and one longitudinal mode. The transversal mode depends on the thickness of the rod and corresponds to a sphere with such diameter. The longitudinal mode on the other hand depends on the length of the rod and changes accordingly (analogous to an antenna).

When heated at only 300°C (red line) the rod starts to melt and reshape into a sphere in order to minimize surface energy seen in the absorbance spectrum where the longitudinal peak disappears and only the transversal mode remains. The change is discernible by bare eye as the samples change colour from dark blue to red.

At this stage, it can be clearly concluded from Figure 5.3d that the used Ag@TiO_2 NPs remain stable at drying temperatures of 150°C making them compatible with the low temperature processing technique for perovskite solar cells.

The devices were fabricated such that none of the heating steps exceeded 150°C after addition of Ag@TiO_2 NPs into the mesostructure. Table 5.1 shows the main device performance parameters: short circuit current (J_{sc}), open circuit voltage (V_{oc}), fill factor (FF), and power conversion efficiency (PCE) for different concentrations (from 0 to 4.4 wt%) of Ag@TiO_2 mixed into the Al_2O_3 colloid solution.

Table 5.1 Short circuit current density (J_{sc}), open circuit voltage (V_{oc}), fill factor (FF) and power conversion efficiency (PCE) with standard deviations for different concentrations of Ag@TiO_2/Al_2O_3 (wt%) ranging from 0.0-4.4 wt% over at least 8 devices for each group.

Ag/alumina (wt%)	Short-circuit current density (mW/cm^2)	Open-circuit voltage (V)	Fill factor	PCE (%)
0.0	17.3 ± 1.2	1.03 ± 0.03	0.64 ± 0.06	11.4 ± 1.3
1.1	18.0 ± 1.6	1.01 ± 0.01	0.64 ± 0.02	11.6 ± 1.3
2.2	19.7 ± 1.6	1.04 ± 0.01	0.67 ± 0.01	13.7 ± 1.2
3.3	20.2 ± 0.6	1.03 ± 0.02	0.65 ± 0.02	13.5 ± 0.6
4.4	19.9 ± 2.0	1.01 ± 0.03	0.59 ± 0.08	11.8 ± 2.7

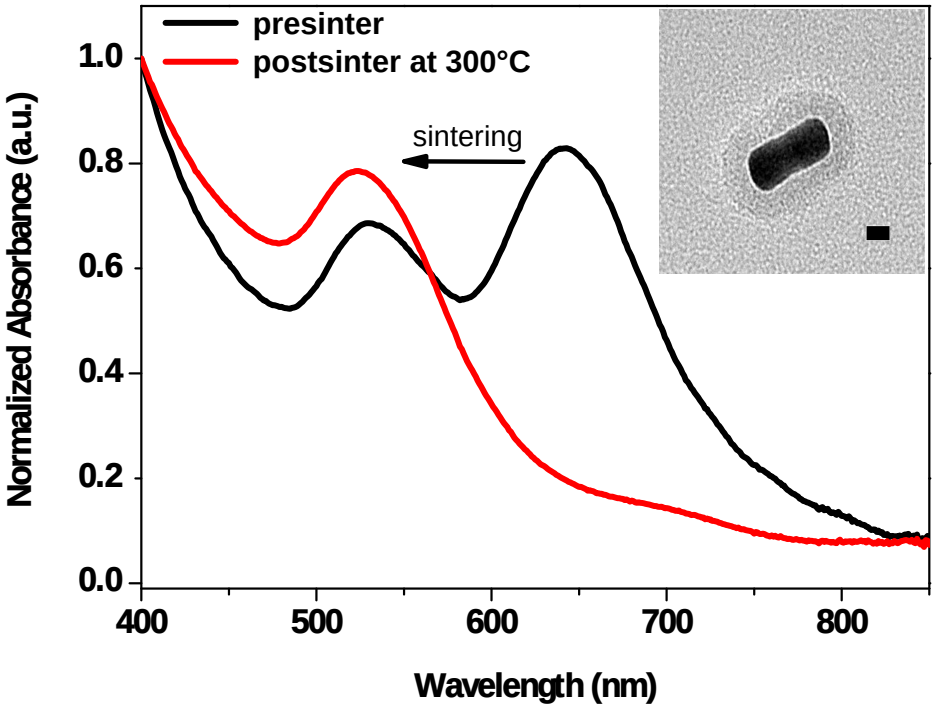

Fig. 5.5 Normalized absorbance of a ~40 nm gold nanorod with ~10 nm thick silica shell before sintering (black line) and after sintering (red line) at 300°C upon which the longitudinal mode vanishes. The inset shows a TEM image of a representative nanorod with a scale bar of 10 nm The TEM image was taken by Simon Fairclough of Oxford University.

The control devices (0 wt% Ag@TiO_2) are around 11.4% PCE on average which is in good agreement with previous reports [4]. A ~20% PCE increase from 11.4% to 13.7% is observed for the optimized Ag@TiO_2 concentration (2.2 wt%). This is consistent with the trend in the previous Chapter [1] where a similar efficiency increase by 13% from 8.4% for the control to 9.5% for the Au@SiO_2 devices is observed. The improvement is even more pronounced for the Ag@TiO_2 devices, which indicates that silver is a more promising material than gold in terms of plasmonic properties due to the higher control device efficiency presented in this work. Figure 5.6 shows the champion solar cells, along with an inset of the device parameters, for the control and optimal 2.2 wt% Ag@TiO_2 devices exhibiting PCEs of up to 14.9% which is consistent with the trend from the averaged device data.

For the rest of this work, unless otherwise stated, "Ag@TiO_2 devices" refers to the optimized 2.2 wt% Ag@TiO_2 concentration. The improvement is mainly from enhanced short circuit current. Figure 5.7 presents data for over 32 devices for both the control and the optimized 2.2 wt% concentration and reconfirms the overall increase to be mainly from J_{sc}.

These results are cross-checked by using similarly sized pure titania beads mixed into the Al_2O_3 scaffold at ratios equivalent to the molarity of the Ag@TiO_2 devices. Figure 5.8 shows there is no significant difference between control devices and devices incorporating titania beads, leading to the conclusion that the silver core is essential for the observed enhancement. Thus, plasmonic effects have to be taken into account for this study.

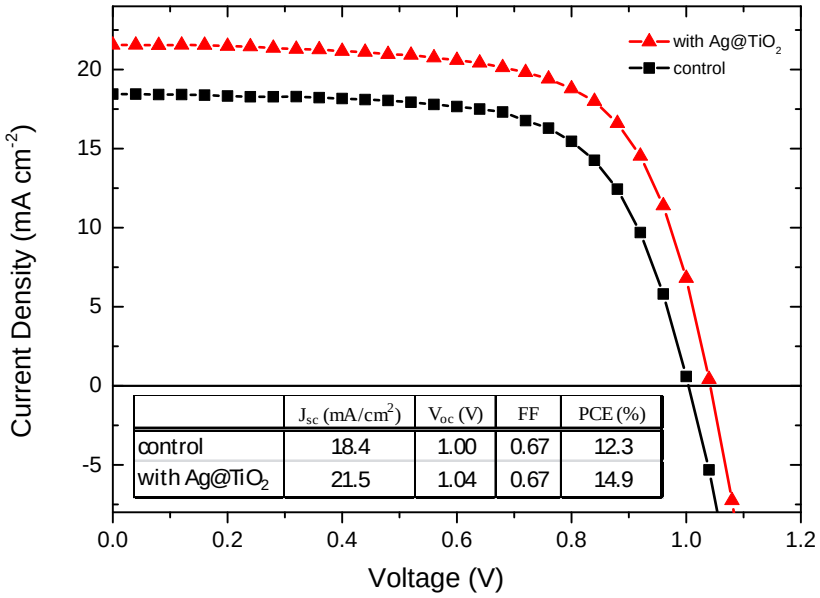

Fig. 5.6 Current density-voltage characteristics for the best control device and a device with optimised 2.2 wt% $Ag@TiO_2$ concentration.

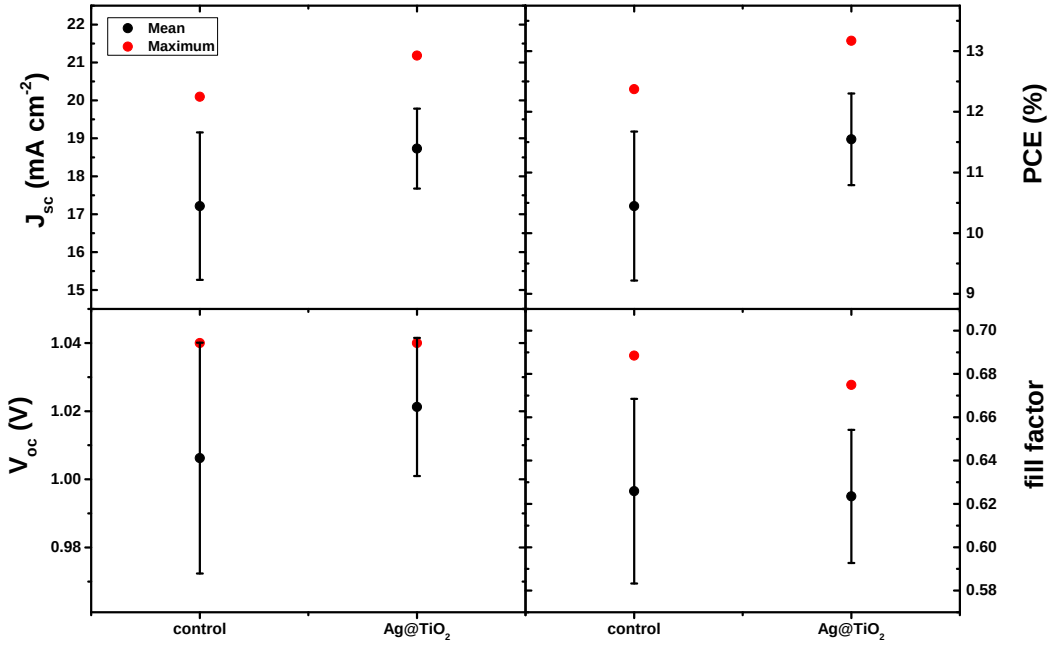

Fig. 5.7 Short circuit current density (J_{sc}), open circuit voltage (V_{oc}), power conversion efficiency (PCE), and fill factor for devices without silver NPs (control) and with optimized concentration ($Ag@TiO_2$). The data was averaged over 32 individual devices for each parameter.

The optical effect of the silver NPs on device performance was studied through measuring the light harvesting efficiency of full perovskite solar cells with silver back contacts [1, 4].

In Figure 5.9a, UV-vis spectra (obtained with an integrating sphere) of control and $Ag@TiO_2$ devices are shown; no obvious difference is observed. As the next step, the Incident Photon-to-Current Conversion Efficiency (see Figure 5.9b) is measured.

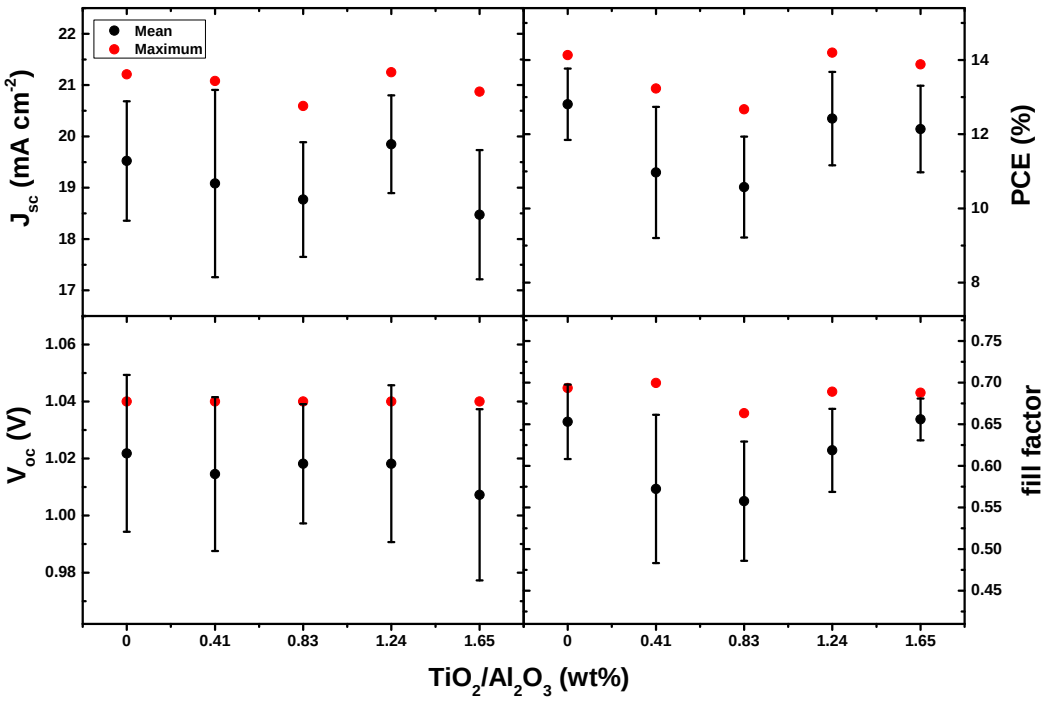

Fig. 5.8 Device performance parameters for different wt% of TiO_2 NPs averaged over 11 devices per concentration. Due to the different density of pure titania beads, the weight ratio was adjusted to correspond to the amount of $Ag@TiO_2$ NPs of the concentration dependence in Table 5.1.

The $Ag@TiO_2$ devices outperform the control devices as expected from the device data in Table 1. However, the enhancement is broad-band (between 400-750 nm) displaying no sharp peaks which can be matched in an obvious way to the optical spectrum of the Ag NPs.

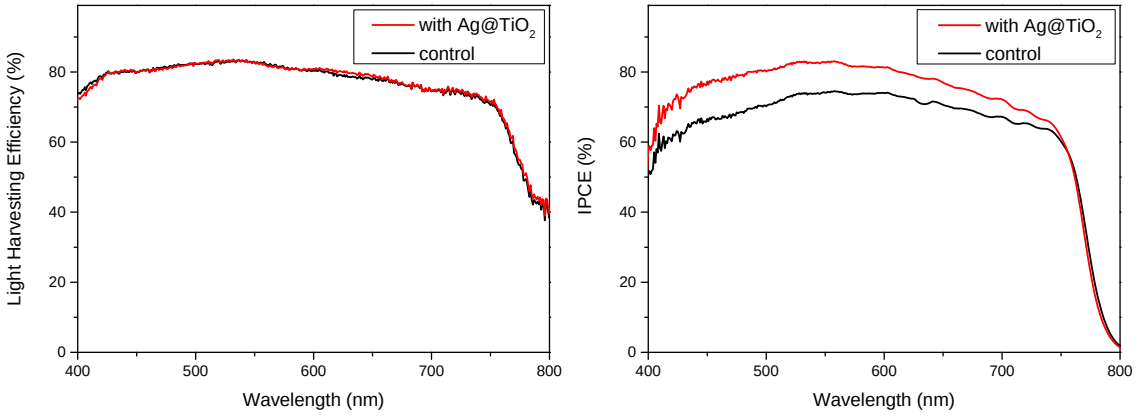

(a) Light harvesting efficiency **(b)** IPCE

Fig. 5.9 (a) Light harvesting efficiency of the photoactive layer for the control (black) and $Ag@TiO_2$ (red) devices measured according to reference [4]. (b) Incident Photon-to-Current Conversion Efficiency (IPCE) for respective devices without (black) and with silver NPs (red).

Proposal for Mechanism

In order to understand the enhancement mechanism, time resolved and steady-state photoluminesence measurements were taken. A clear quenching of both the steady state (Figure 5.10a) and time-resolved (Figure 5.10b) PL for the Ag@TiO_2 devices is observed.

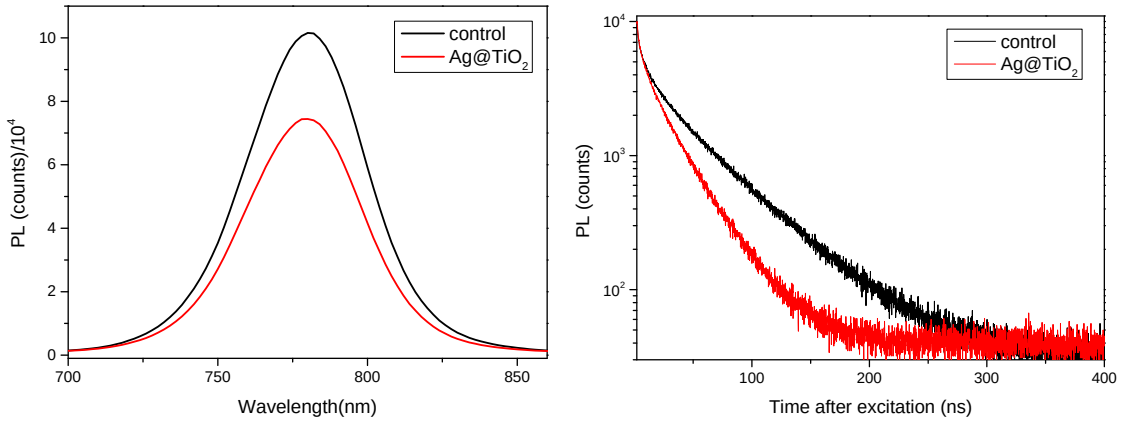

(a) Steady-state **(b)** Time-resolved PL

Fig. 5.10 (a) Steady-state photoluminescence for control (black) and optimized Ag@TiO_2 (red) containing devices. (b) Time-resolved PL data for the same devices averaged over 8 devices.

The following mechanism discussion was conducted with Victor Burlakov of Oxford University. It is still being developed and needs further experimental evidence. Here, it is proposed that the Ag@SiO_2 act as antennas in the presence of excitons and increase the optical pathlength of photons from recombining electron-hole pairs. This is schematically presented in Figure 5.11.

Theory

The steady-state PLQE (photoluminescence quantum efficiency) dependence on temperature can be explained by the influence of two factors associated with the presence of metallic nanoparticles. These are 1) high polarizability of the nanoparticles (see [50]), and 2) change in exciton radiation geometry as illustrated in Figure 5.11, which may result in either increase or decrease of radiation reabsorption depending on the overlap of the absorption and exciton spectrum at a given temperature. The first factor simply means that exciton radiation can be mediated by nanoparticles, which acquire high dipole moment induced by electric field associated with the dipole moment of an exciton in the vicinity of the NP [50]. The second factor takes into account the fact that the induced dipole moment may be oriented differently from dipole moment of the exciton (d_{exc}) resulting in a different radiation direction. Thus, the nanoparticles act as antennas redirecting the photons.

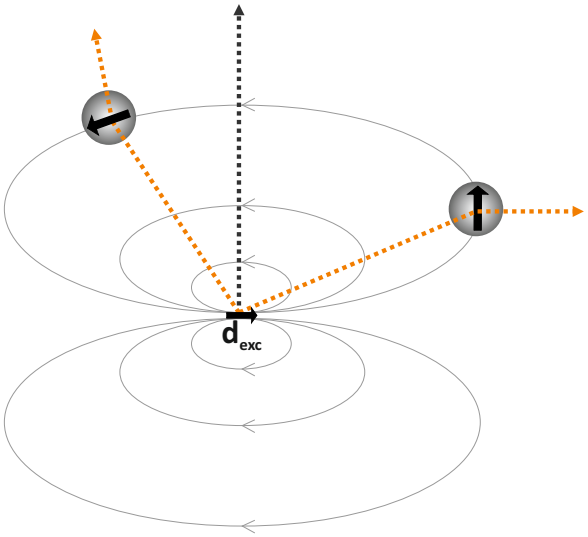

Fig. 5.11 Proposed mechanism for the photocurrent increase. The exciton with dipole moment d_{exc} (illustrated by the grey lines) polarizes the metallic nanoparticles inducing a dipole moment (arrows in the grey spheres) [50]. A photon is emitted when the exciton recombines and due to the presence of the induced dipoles the radiation direction changes (from the black to the orange dotted path) which makes exciton reabsorption more likely. The mechanism study was conducted with Victor Burlakov of Oxford University.

Now, the above mentioned factors are considered separately. Radiation of dipoles representing photoluminescance I_{PL} of the material without NPs can be expressed as

$$I_{PL} = n_{exc} R_0 \exp(-\alpha(T)\, l_0) \tag{5.1}$$

where n_{exc} is the exciton concentration, R_0 is the exciton radiative decay rate, and $\alpha(T)$ is the temperature-dependent absorption coefficient of the pure material. l_0 is an effective optical path length for outgoing radiation. In the next step, both R_0 and l_0 are renormalized in the presence of NP and written in the form

$$R_l = R_0(1 + k_0\, n_{NP}) \tag{5.2a}$$

$$l_l = l_0(1 + k_1\, n_{NP}) \tag{5.2b}$$

where k_0 and k_1 are constants defining the increase in the radiation rate and in effective optical path, respectively, and n_{NP} is the NP concentration.

The perovskite absorption and exciton spectrum at different temperatures was measured in [51] which is shown Figure 5.12 also containing an inset with the overlap integral of the product of the exciton and absorption spectrum over temperature. The overlap shows a clear drop as the temperature decreases.

Here, the main interest is in the change of PL properties relative to the control sample (without NPs). Therefore the ratio of the PL intensity determined by eq. 5.3 with R_0 and l_0 replaced by R_1 and l_1, respectively, resulting in

$$I_{Rel} = (1 + k_0\, n_{NP}) \exp(-\alpha(T)\, k_1\, n_{NP}\, l_0) \tag{5.3}$$

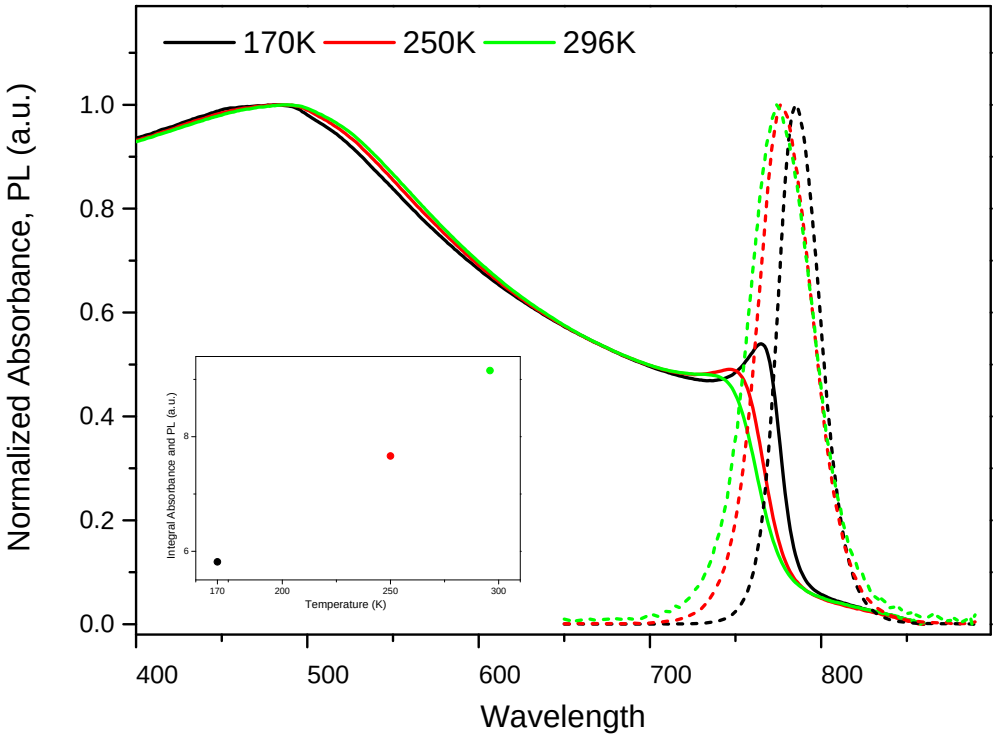

Fig. 5.12 Absorption and exciton spectrum at 296 K, 250 K, and 170 K as adapated from [51]. The inset is the overlap integral of the product of the exciton and absorption spectrum. Reprinted by permission from Macmillan Publishers Ltd: Nature Communications 5: 3586 ©2014)

With this expression, the relative PL intensity can be fitted at various temperatures using k_0 and k_1 as fit parameters. The results are presented in Figure 5.13a. The data for the absorption coefficient $\alpha_0(T)$ was derived from Figure 5.12.

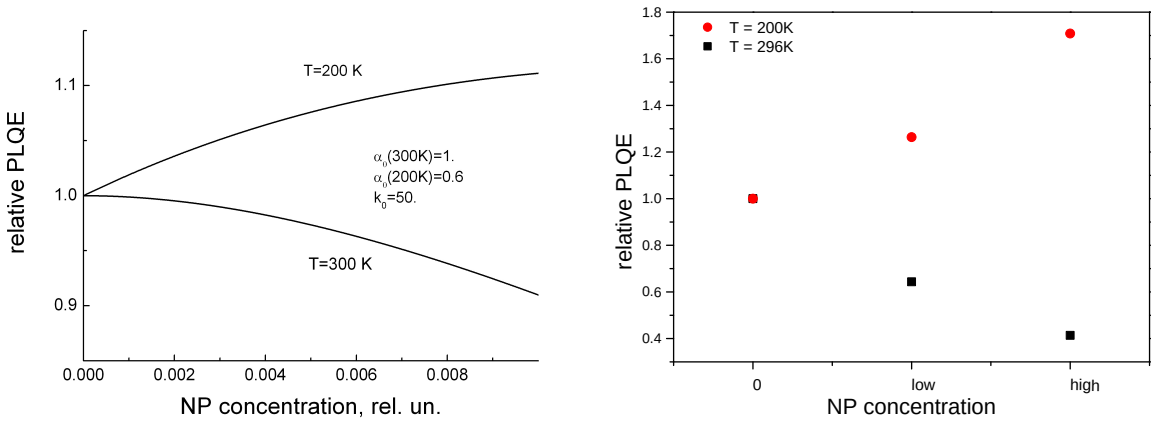

(a) theory **(b)** experiment

Fig. 5.13 Relative PLQE over NP concentration at different temperature for (a) theory and (b) experiment. The data for the absorption coefficient α_0 was adapted from [51]. The mechanism study was conducted with Victor Burlakov of Oxford University.

Experimental data is shown in Figure 5.13b with the normalized PLQE at 200 K and 296 K reiterating the same trend as the theoretical prediction. More experiments are currently conducted to repeat the trend and provide further evidence for the model. Nevertheless, this model already shows promise for explaining the mechanism for increased photocurrent.

5.3 Summary

Thermally sensitive silver nanoparticles were embedded into perovskite-based high-efficiency solar cells at temperatures below 150°C. An efficiency increase by ~18% from 11.4% for control to 13.7% for 2.2 wt% optimized Ag@TiO_2 devices was observed. In a first model an increased exciton reabsorption was identified as a possible mechanism for the enhanced photocurrent.

The lowered processing temperatures decrease manufacturing costs and open the door to new, interesting applications which were previously inaccessible because of high temperature conditions. Particularly readily available non-spherical nanoparticles which are notoriously hard to stabilize against temperature-induced shape change can now be processed and used with relative ease. Hence, a very promising route for future enhancements is mapped out.

References

[1] W. Zhang, M. Saliba, S. D. Stranks, Y. Sun, X. Shi, U. Wiesner, and H. J. Snaith, "Enhancement of perovskite-based solar cells employing core-shell metal nanoparticles," *Nano Letters*, vol. 13, no. 9, pp. 4505–10, 2013. 23947387.

[2] C. Ziegler and A. Eychmuller, "Seeded growth synthesis of uniform gold nanoparticles with diameters of 15-300 nm," *Journal of Physical Chemistry C*, vol. 115, no. 11, pp. 4502–4506, 2011.

[3] C. Graf, D. L. J. Vossen, A. Imhof, and A. van Blaaderen, "A general method to coat colloidal particles with silica," *Langmuir*, vol. 19, no. 17, pp. 6693–6700, 2003.

[4] J. M. Ball, M. M. Lee, A. Hey, and H. J. Snaith, "Low-temperature processed meso-superstructured to thin-film perovskite solar cells," *Energy & Environmental Science*, vol. 6, no. 6, pp. 1739–1743, 2013.

[5] J. Rodriguez-Fernandez, I. Pastoriza-Santos, J. Perez-Juste, F. J. G. de Abajo, and L. M. Liz-Marzan, "The effect of silica coating on the optical response of sub-micrometer gold spheres," *Journal of Physical Chemistry C*, vol. 111, no. 36, pp. 13361–13366, 2007.

[6] W. Ostwald, M. Bodenstein, K. Clusius, K. Bonhoeffer, and H. Falkenhagen, *Zeitschrift fur physikalische Chemie*. No. v. 22, Akademische Verlagsgesellschaft Geest & Portig, 1897.

[7] L. Ratke and P. W. Voorhees, *Growth and coarsening: Ostwald ripening in material processing*. Springer, 2002.

[8] M. D. Brown, T. Suteewong, R. S. S. Kumar, V. D'Innocenzo, A. Petrozza, M. M. Lee, U. Wiesner, and H. J. Snaith, "Plasmonic dye-sensitized solar cells using core-shell metal-insulator nanoparticles," *Nano Letters*, vol. 11, no. 2, pp. 438–445, 2011.

[9] H. J. Snaith, A. Abate, J. M. Ball, G. E. Eperon, T. Leijtens, N. K. Noel, S. D. Stranks, J. T.-W. Wang, K. Wojciechowski, and W. Zhang, "Anomalous hysteresis in perovskite solar cells," *The Journal of Physical Chemistry Letters*, vol. 5, no. 9, pp. 1511–1515, 2014.

[10] R. S. Sanchez, V. Gonzalez-Pedro, J.-W. Lee, N.-G. Park, Y. S. Kang, I. Mora-Sero, and J. Bisquert, "Slow dynamic processes in lead halide perovskite solar cells. characteristic times and hysteresis," *The Journal of Physical Chemistry Letters*, vol. 5, no. 13, pp. 2357–2363, 2014.

[11] R. Gottesman, E. Haltzi, L. Gouda, S. Tirosh, Y. Bouhadana, A. Zaban, E. Mosconi, and F. De Angelis, "Extremely slow photoconductivity response of $CH_3NH_3PbI_3$ perovskites suggesting structural changes under working conditions," *The Journal of Physical Chemistry Letters*, vol. 5, pp. 2662–2669, 2014.

[12] M. Xiao, F. Huang, W. Huang, Y. Dkhissi, Y. Zhu, J. Etheridge, A. Gray-Weale, U. Bach, Y.-B. Cheng, and L. Spiccia, "A fast deposition-crystallization procedure for highly efficient lead iodide perovskite thin-film solar cells," *Angewandte Chemie*, vol. 126, no. 37, pp. 10056–10061, 2014.

[13] Y. Wu, A. Islam, X. Yang, C. Qin, J. Liu, K. Zhang, W. Peng, and L. Han, "Retarding the crystallization of PbI_3 for highly reproducible planar-structured perovskite solar cells via sequential deposition," *Energy Environ. Sci.*, vol. 7, no. 9, pp. 2934–2938, 2014.

[14] A. Dualeh, T. Moehl, N. Tétreault, J. Teuscher, P. Gao, M. K. Nazeeruddin, and M. Grätzel, "Impedance spectroscopic analysis of lead iodide perovskite-sensitized solid-state solar cells," *ACS Nano*, vol. 8, no. 1, pp. 362–373, 2014.

[15] A. T. Barrows, A. J. Pearson, C. K. Kwak, A. D. F. Dunbar, A. R. Buckley, and D. G. Lidzey, "Efficient planar heterojunction mixed-halide perovskite solar cells deposited via spray-deposition," *Energy Environ. Sci.*, vol. 7, no. 9, pp. 2944–2950, 2014.

[16] H.-R. Zhao, D.-P. Li, X.-M. Ren, Y. Song, and W.-Q. Jin, "Larger spontaneous polarization ferroelectric inorganic-organic hybrids: $[PbI_3]_\infty$ chains directed organic cations aggregation to kagomé-shaped tubular architecture," *Journal of the American Chemical Society*, vol. 132, no. 1, pp. 18–19, 2010. PMID: 20014843.

[17] T. Hang, W. Zhang, H.-Y. Ye, and R.-G. Xiong, "Metal-organic complex ferroelectrics," *Chem. Soc. Rev.*, vol. 40, pp. 3577–3598, 2011.

[18] H. J. Lian, A. Yang, M. L. W. Thewalt, R. Lauck, and M. Cardona, "Effects of sulfur isotopic composition on the band gap of PbS," *Phys. Rev. B*, vol. 73, p. 233202, Jun 2006.

[19] T. Ishihara, "Optical-properties of PbI-based perovskite structures," *Journal of Luminescence*, vol. 60-1, pp. 269–274, 1994.

[20] Z. Chen, C. L. Yu, K. Shum, J. J. Wang, W. Pfenninger, N. Vockic, J. Midgley, and J. T. Kenney, "Photoluminescence study of polycrystalline $CsSnI_3$ thin films: Determination of exciton binding energy," *Journal of Luminescence*, vol. 132, no. 2, pp. 345–349, 2012.

[21] A. Olkhovets, R.-C. Hsu, A. Lipovskii, and F. W. Wise, "Size-dependent temperature variation of the energy gap in lead-salt quantum dots," *Phys. Rev. Lett.*, vol. 81, pp. 3539–3542, Oct 1998.

[22] N. Ashcroft and N. Mermin, *Solid State Physics*. Brooks Cole, 1976.

[23] Y. Varshni, "Temperature dependence of the energy gap in semiconductors," *Physica*, vol. 34, no. 1, pp. 149–154, 1967.

[24] M. Leroux, N. Grandjean, B. Beaumont, G. Nataf, F. Semond, J. Massies, and P. Gibart, "Temperature quenching of photoluminescence intensities in undoped and doped gan," *Journal of Applied Physics*, vol. 86, no. 7, pp. 3721–3728, 1999.

[25] N. Kitazawa, M. Aono, and Y. Watanabe, "Synthesis and luminescence properties of lead-halide based organic–inorganic layered perovskite compounds $(C_nH_{2n+1}NH_3)_2PbI_4$ (n=4, 5, 7, 8 and 9)," *Journal of Physics and Chemistry of Solids*, vol. 72, no. 12, pp. 1467–1471, 2011.

[26] M. Achermann, "Exciton-plasmon interactions in metal-semiconductor nanostructures," *The Journal of Physical Chemistry Letters*, vol. 1, no. 19, pp. 2837–2843, 2010.

[27] Y. J. Fang, Y. W. Wang, L. Gu, R. Lu, and J. Sha, "Effect of the defect on photoluminescence property of Al-coated ZnO nanostructures," *Optics Express*, vol. 21, no. 3, pp. 3492–3500, 2013.

[28] W.-L. Liu, F.-C. Lin, Y.-C. Yang, C.-H. Huang, S. Gwo, M. H. Huang, and J.-S. Huang, "The influence of shell thickness of Au@TiO_2 core-shell nanoparticles on the plasmonic enhancement effect in dye-sensitized solar cells," *Nanoscale*, vol. 5, pp. 7953–7962, 2013.

[29] M. Hentschel, M. Saliba, R. Vogelgesang, H. Giessen, A. P. Alivisatos, and N. Liu, "Transition from isolated to collective modes in plasmonic oligomers," *Nano Letters*, vol. 10, no. 7, pp. 2721–2726, 2010.

[30] J. N. Anker, W. P. Hall, O. Lyandres, N. C. Shah, J. Zhao, and R. P. Van Duyne, "Biosensing with plasmonic nanosensors.," *Nature Materials*, vol. 7, pp. 442–53, 2008.

[31] T. Ergin, N. Stenger, P. Brenner, J. B. Pendry, and M. Wegener, "Three-dimensional invisibility cloak at optical wavelengths.," *Science*, vol. 328, pp. 337–9, 2010.

[32] N. Liu, M. Hentschel, T. Weiss, A. P. Alivisatos, and H. Giessen, "Three-dimensional plasmon rulers," *Science*, vol. 332, no. 6036, pp. 1407–1410, 2011.

[33] J.-S. Huang, T. Feichtner, P. Biagioni, and B. Hecht, "Impedance matching and emission properties of nanoantennas in an optical nanocircuit.," *Nano Letters*, vol. 9, pp. 1897–902, 2009.

[34] M. Rycenga, C. M. Cobley, J. Zeng, W. Y. Li, C. H. Moran, Q. Zhang, D. Qin, and Y. N. Xia, "Controlling the synthesis and assembly of silver nanostructures for plasmonic applications," *Chemical Reviews*, vol. 111, no. 6, pp. 3669–3712, 2011.

[35] M. I. Stockman, "Nanoplasmonics: past, present, and glimpse into future," *Optics Express*, vol. 19, no. 22, pp. 22029–22106, 2011.

[36] T. C. Deivaraj, N. L. Lala, and J. Y. Lee, "Solvent-induced shape evolution of pvp protected spherical silver nanoparticles into triangular nanoplates and nanorods.," *Journal of colloid and interface science*, vol. 289, pp. 402–9, 2005.

[37] Y. Khalavka, C. Ohm, L. Sun, F. Banhart, and C. Sonnichsen, "Enhanced thermal stability of gold and silver nanorods by thin surface layers," *Journal of Physical Chemistry C*, vol. 111, pp. 12886–12889, 2007. Nanorods, different vapor pressures.

[38] J. F. Qi, X. N. Dang, P. T. Hammond, and A. M. Belcher, "Highly efficient plasmon-enhanced dye-sensitized solar cells through metal@oxide core-shell nanostructure," *ACS nano*, vol. 5, no. 9, pp. 7108–7116, 2011.

[39] C. Hafner, *Post-modern electromagnetics: using intelligent Maxwell solvers*. John Wiley, 1999. The software package OpenMaXwell is available at http://openmax.ethz.ch/.

[40] M. Hirasawa, T. Ishihara, T. Goto, K. Uchida, and N. Miura, "Magnetoabsorption of the lowest exciton in perovskite-type compound $CH_3NH_3PbI_3$," *Physica B*, vol. 201, pp. 427–430, 1994.

[41] K. Tanaka, T. Takahashi, T. Ban, T. Kondo, K. Uchida, and N. Miura, "Comparative study on the excitons in lead-halide-based perovskite-type crystals $CH_3NH_3PbBr_3$ $CH_3NH_3PbI_3$," *Solid State Communications*, vol. 127, pp. 619–623, Sept. 2003.

[42] P. B. Johnson and R. W. Christy, "Optical constants of the noble metals," *Phys. Rev. B*, vol. 6, pp. 4370–4379, DEC 1972.

[43] C. F. Bohren and D. R. Huffman, *Absorption and Scattering of Light by Small Particles*. Wiley-VCH, 1983.

[44] P. Buffat and J. P. Borel, "Size effect on the melting temperature of gold particles," *Physical Review A*, vol. 13, no. 6, pp. 2287–2298, 1976. PRA.

[45] P. R. Couchman and W. A. Jesser, "Thermodynamic theory of size dependence of melting temperature in metals," *Nature*, vol. 269, no. 5628, pp. 481–483, 1977.

[46] R. Kofman, P. Cheyssac, A. Aouaj, Y. Lereah, G. Deutscher, T. Bendavid, J. M. Penisson, and A. Bourret, "Surface melting enhanced by curvature effects," *Surface Science*, vol. 303, no. 1-2, pp. 231–246, 1994.

[47] K. K. Nanda, "Size-dependent melting of nanoparticles: Hundred years of thermodynamic model," *Pramana-Journal of Physics*, vol. 72, no. 4, pp. 617–628, 2009.

[48] H. Petrova, J. Perez Juste, I. Pastoriza-Santos, G. V. Hartland, L. M. Liz-Marzán, and P. Mulvaney, "On the temperature stability of gold nanorods: comparison between thermal and ultrafast laser-induced heating.," *Physical chemistry chemical physics : PCCP*, vol. 8, pp. 814–21, 2006. Already shape change of Au NR at 200C.

[49] R.-X. Dong, C.-C. Chou, and J.-J. Lin, "Synthesis of immobilized silver nanoparticles on ionic silicate clay and observed low-temperature melting," *Journal of Materials Chemistry*, vol. 19, p. 2184, 2009. Lowered melting on clay.

[50] P. M. Bendix, L. Jauffred, K. Norregaard, and L. B. Oddershede, "Optical trapping of nanoparticles and quantum dots," *Selected Topics in Quantum Electronics, IEEE Journal of*, vol. 20, no. 3, pp. 1–12, 2014.

[51] V. D'Innocenzo, G. Grancini, M. J. P. Alcocer, A. R. S. Kandada, S. D. Stranks, M. M. Lee, G. Lanzani, H. J. Snaith, and A. Petrozza, "Excitons versus free charges in organo-lead tri-halide perovskites," *Nature Communications*, vol. 5, pp. –, Apr. 2014.

Perovskite Film Crystallization

CHAPTER 6

Thermally Induced Structural Evolution and Performance of Mesoporous Block Copolymer-directed Alumina Perovskite Solar Cells

Structure control in solution-processed hybrid perovskites is crucial to design and fabricate highly efficient solar cells. Here, in situ gracing incident wide angle x-ray spectroscopy (GIWAXS) and scanning electron microscopy was used to investigate the structural evolution and film morphologies of methylammonium lead triiodide/chloride ($CH_3NH_3PbI_{3-x}Cl_x$) in mesoporous block copolymer derived alumina superstructures during thermal annealing. It is shown that $CH_3NH_3PbI_{3-x}Cl_x$ material evolution can be characterized by three distinct structures: a crystalline precursor structure not described previously, a 3D perovskite structure, and a mixture of compounds resulting from degradation. Finally, it can be demonstrated how understanding the processing parameters provides the foundation needed for optimal perovskite film morphology and coverage, leading to enhanced block copolymer-directed perovskite solar cell performance. This work is published in [1].

The work in this chapter was performed in close collaboration with Kwan W. Tan from the group of Ulrich Wiesner at Cornell University. Kwan has spent about 8 weeks at Oxford University and I have spent about 8 weeks at Cornell as part of an EPSRC funded project. During my stay in Cornell I fabricated and characterised many of the materials. However, the synchrotron became only available after I had left Cornell. Hence, some of the characterisation and experiments were conducted solely by Kwan W. Tan. This will be noted in the figure captions and text.

Introduction

Harnessing sunlight to generate photovoltaic electricity based on thin film solar cell technologies is desirable to deliver green, sustainable energy at reduced materials and fabrication cost [2, 3]. Thin film hybrid solar cells using solution-processable materials [3] such as semiconductor nanocrystals, [4, 5] organic polymers, [6, 7] or dye-sensitized solar cells [8–10] have achieved 7-12% power conversion efficiencies (PCEs). As already mentioned, perovskite solar cells have been reported with PCEs above 15% [11–31].

This material class is highly attractive for thin-film photovoltaics due to the ease of solution processing and excellent absorption properties in the near-infrared spectrum to generate charge carriers [11, 13, 14, 19]. Moreover, ambipolar charge transport properties and long carrier lifetimes enable the direct transport of both photogenerated electron and hole charge carriers to the respective collecting electrodes [15, 16, 19, 20, 29, 30].

The photovoltaic device architecture provides an alternative approach to enhance device performance [32–34]. In particular, block copolymer (BCP) self-assembly-directed materials have improved charge transport and light management of mesoscopic solar cells via control of morphology, [34–41] porosity and pore size, [41–45] material crystallinity, [46, 47] electronic [35, 47] and optical [42, 48] properties. For example, well-ordered bicontinuous BCP gyroid morphologies enable easy backfilling of the hole transport materials and complete mesopore interconnectivity in solid-state dye-sensitized solar cells [35, 36]. Moreover, porous BCP nanostructures provide control over single crystal epitaxial nanostructures, [46] and may enable tuning the feature size and morphology of well-defined $CH_3NH_3PbX_3$ nanocrystallites to achieve excellent photovoltaic device performance [20, 25]. Combining BCP structure control with the organic-inorganic hybrid perovskite, observation of structural evolution at multiple length scales is expected to be key to establishing structure-property correlations. To the best of my knowledge, such evolution of thermally annealed hybrid perovskites obtained via a single-step spin coating process has not been reported.

6.1 Experimental

Materials

All materials were used as received. Anhydrous grades of toluene,*n*-butanol, tetrahydrofuran, chloroform, N,N-dimethylformamide (DMF) and terpineol, 97% aluminum tri-*sec*-butoxide, >97% titanium isopropoxide, 20 wt% aluminum oxide nanoparticles in isopropanol (<50 nm, product number 702129), 57 wt% hydroiodic acid in water, 33 wt% methylamine solution in ethanol, and lead chloride were obtained from Sigma-Aldrich. 70% nitric acid and 37% hydrochloric acid were obtained from Mallinckrodt Baker and EMD Millipore, respectively. 10 cP and 46 cP ethyl cellulose were obtained from TCI America.

Mesoporous block copolymer-directed alumina (MBCP-Al_2O_3) and titania (MBCP-TiO_2) films

MBCP-Al_2O_3 films were prepared as described in Appendix A. This project was in close collaboration with Kwan W. Tan of Cornell University who prepared the MBCP samples in this study.

Mesoporous alumina nanoparticle (NP) films

Mesoporous Al_2O_3 nanoparticle (NP) thin films were prepared as described in Chapter 2.2. Very briefly, the binder-free mesoporous Al_2O_3 NP film was prepared by spin coating 6.67 wt% Al_2O_3 NPs in isopropanol on silicon at 2500 rpm (60 s), and dried at 150°C (1 h).

Moreover, the 2 wt% Al_2O_3 NP/binder paste was prepared by mixing 1 g of Al_2O_3 NPs, 3.33 g terpineol, 1 g 10 cP ethyl cellulose and 1 g 46 cP ethyl cellulose in 43.67 g isopropanol. The mixture was stirred vigorously at 70°C for 30 min. The mesoporous Al_2O_3 NP film with binder was prepared by spin coating the Al_2O_3 NP/binder mixture on silicon at 2500 rpm (60 s), and calcined at 500°C (3 h) with a ramp rate of 1 °C/ min.

Mesoporous alumina thin film characterization

Scanning electron microscopy (SEM) images were acquired on Au-Pd coated mesoporous alumina thin films using LEO 1550 and TESCAN MIRA3-LM field emission SEMs equipped with in-lens detectors. atomic force microscopy (AFM) images were obtained on a Veeco Mulitmode II SPM with a Nanoscope III controller in tapping mode at ambient conditions.

GISAXS was measured at the G1 beamline of the Cornell High Energy Synchrotron Source (CHESS). The G1 beamline setup consists of a multilayer monochromator of $\lambda = 0.1225$ nm with a CCD area detector with a 71.73 µm pixel size and a total of 1024x1024 pixels. The sample-to-detector distance was 2.745 m. The incident angle of the beam was varied between 0.1° and 0.3° with typical exposure times <2 s. GISAXS patterns were analysed with an in-house software [49] and the FIT2D program [50].

The SEM images and GISAXS data in this study were taken by Kwan W. Tan of Cornell University.

Wide-angle X-ray scattering measurements of $CH_3NH_3PbI_{3-x}Cl_x$

Methylammonium iodide (CH_3NH_3I) was prepared using 57 wt% hydroiodic acid (HI) in water and 33 wt% methylamine solution (CH_3NH_3) in ethanol as reported in Chapter 2.2. 5-40 wt% of methylammonium iodide (CH_3NH_3I) and lead chloride ($PbCl_2$) (3:1 by molarity) dissolved in N,N-dimethylformamide was dispensed on the MBCP-Al_2O_3 and flat glass coverslip substrates by spin coating at 3000 rpm (45 s) in air. For *ex situ* measurements, the

hybrid perovskite samples were annealed by a slow temperature ramp of 10°C / 10 min and held at 100°C for 45 min in a nitrogen atmosphere.

The annealed perovskite films were carefully scratched from the substrate and powdered for X-ray diffraction (XRD) analysis. The XRD characterization was performed on a Scintag theta-theta X-ray diffractometer equipped with Cu-K_α radiation and a Ge solid-state detector operating at 40 kV and 40 mA.

For in situ GIWAXS measurements, after spin coating the sample was immediately loaded on a temperature-controlled stage at the D1 beamline of CHESS. The D1 beamline setup consists of a multilayer monochromator of $\lambda = 0.1161$ nm. GIWAXS patterns were collected on Fuji image plates placed in a holder at a distance of 177 mm from the sample. The incident beam angle was above the silicon critical angle (~0.25°) with exposure times <5 s. The direct beam was blocked with lead tape. The exposed plates were scanned for digital processing with a GE Healthcare Typhoon FLA-7000 image plate reader. Digital images were analyed using the FIT2D program [50]. The resolution of the letter-sized image plate is 2000x2500 pixels with a 100 μm pixel size. The measurements in nitrogen were conducted in a custom-made environmental chamber mounted on the temperature-controlled stage [51].

The GIWAXS data in this study was taken by Kwan W. Tan of Cornell University.

Isothermal-time-dependent (ITD) perovskite crystallization

A 20 wt% precursor solution was dispensed on the MBCP-Al_2O_3 substrate by spin coating and immediately loaded on the temperature-stage held at 100°C at the D1 beamline. GIWAXS measurements were taken at different time intervals over a dwell of 50 min. The measurements were conducted in ambient air and nitrogen.

Time-temperature-dependent (TTD) perovskite crystallization

A 20 wt% precursor solution was dispensed on the MBCP-Al_2O_3 substrate by spin coating and loaded on the temperature-stage held at 30°C at the D1 beamline. The stage was slowly heated at a ramp rate of 10°C/10 min to the final temperature of 100°C. The MBCP-Al_2O_3 perovskite sample was held at 100°C for 60 min. The GIWAXS measurements were taken at different time intervals in nitrogen.

MBCP-Al_2O_3 hybrid perovskite solar cell assembly.

MBCP-Al_2O_3 perovskite solar cells (>20 cells for each annealing history) were fabricated according to Chapter 2.2. The MBCP-Al_2O_3 hybrid films were prepared by spin coating on the TiO_2/FTO substrates at 2000 rpm (45 s).

The substrates were baked at 50°C (2 h), 100°C (2 h), and 130°C (2 h) sequentially in the drybox and calcined at 450°C (3 h) with a ramp rate of 1 °C/ min.

A 40 wt% perovskite precursor solution was dispensed on the MBCP-Al_2O_3 scaffold by spin coating at 2000 rpm (45 s). For the ITD-air processed MBCP-Al_2O_3 perovskite solar cells, the devices were fabricated in ambient air and heated in a conventional oven at 100°C for 45 min. For the TTD-nitrogen processed MBCP-Al_2O_3 perovskite solar cells, the devices were fabricated in a nitrogen glovebox. After drying at ambient temperature for at least 20 min, the samples were slowly heated on a hotplate from ambient temperature to 100°C at a ramp rate of 5°C/5 min, and held at 100°C for 45 min. The electron blocking layer was formed by spin coating 80 mM spiro-OMeTAD in chlorobenzene solution with 80 mol% tBP and 30 mol% Li-TFSI additives and aged overnight in a dessicator (in air). Silver contact electrodes of 150 nm were thermally evaporated to complete the devices.

MBCP-Al_2O_3 hybrid perovskite solar cell characterization

More than 20 solar cells were measured for each annealing condition (ITD versus TTD) with a Keithley 2400 under AM 1.5G 100 mW/cm^2 simulated sunlight (Abet Technologies Sun 2000) calibrated against an NREL certified KG5 filtered silicon reference diode. The cells were masked with a square aperture defining an active area of typically 0.07 cm^2 and measured in a light-tight sample holder.

6.2 Results and Discussion

GIWAXS of $CH_3NH_3PbI_{3-x}Cl_x$ Perovskites

One of the key advantages of the $CH_3NH_3PbX_3$ hybrid perovskite photovoltaic devices is the ease of solution-processing. The organic (CH_3NH_3I) and inorganic precursors ($PbCl_2$) are dissolved in a common solvent (DMF), deposited on a substrate by spin coating, and annealed at relatively low temperatures of 90-100°C for 5-120 min to induce perovskite crystallization [13–24, 26–28]. However, crystallographic data obtained from one-dimensional (1D) powder XRD provides only limited structural information, in particular for the highly oriented perovskite thin films [13, 14, 19, 20, 23–27].

To this end, GIWAXS was employed with 2D detection capability to probe the crystallographic orientations of planar $CH_3NH_3PbI_{3-x}Cl_x$ perovskite thin films.

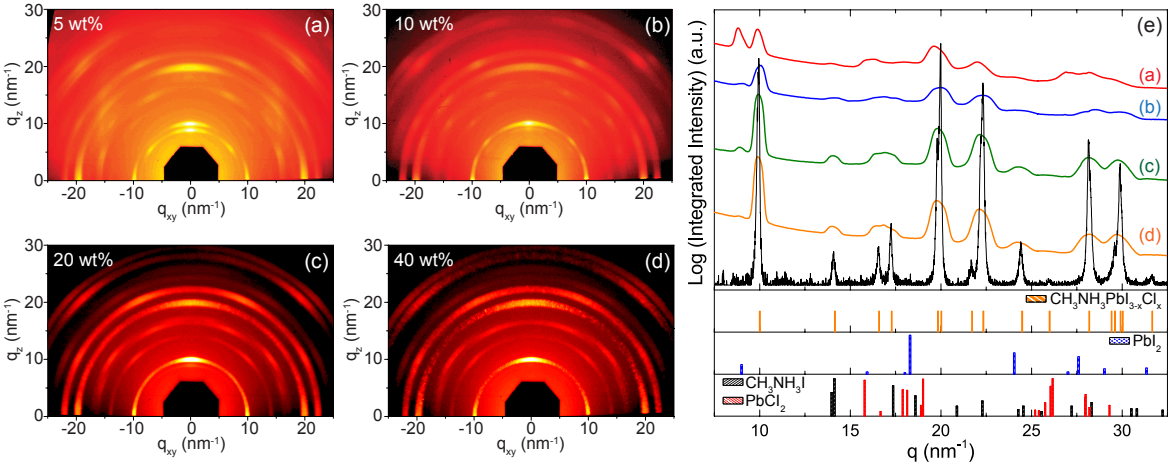

Fig. 6.1 2D GIWAXS profiles of $CH_3NH_3PbI_{3-x}Cl_x$ perovskite films on flat substrates prepared from (a) 5 wt%, (b) 10 wt%, (c) 20 wt%, (d) 40 wt% precursor solutions, and annealed at 100°C for 45 min. (e) Azimuthally integrated intensity plots of the GIWAXS patterns. The bottom black curve is the XRD spectrum of the $CH_3NH_3PbI_{3-x}Cl_x$ perovskite measured in powdered form. The measurements in this figure were taken by Kwan W. Tan of Cornell University.

Figure 6.1 shows GIWAXS profiles of crystalline perovskite thin films on microscope slides prepared from precursor solutions of different concentrations and annealed at 100°C for 45 min in nitrogen atmosphere. The 5 wt% and 10 wt% perovskite films are observed to exhibit a mixture of scattered secondary spots and rings (Figure 6.1a and b), indicating that crystalline domains are highly oriented in the in-plane direction. Similar GIWAXS profiles were observed for the thicker 20 wt% and 40 wt% perovskite films. The presence of strongly scattered rings in Figure 6.1c and d indicates that crystalline domains are predominantly polycrystalline, i.e. randomly oriented relative to the plane of the substrate. The azimuthally integrated scattering intensity of the different GIWAXS patterns is plotted against the scattering vector q in Figure 6.1e, where $q = 4\pi \sin(\theta)/\lambda$, θ is half of the scattering angle, and λ is the X-ray wavelength (0.1161 nm). The 2D GIWAXS integrated intensity curves correspond well to the crystallographic peaks of the 1D X-ray diffraction pattern of a $CH_3NH_3PbI_{3-x}Cl_x$ powdered sample (black curve) [24], and are distinctly different from those of the CH_3NH_3I (PDF 00-10-0737) and $PbCl_2$ (PDF 00-050-0536) precursors (see bottom of Figure 6.1e). The lattice parameters for the tetragonal *I4/mcm* $CH_3NH_3PbI_{3-x}Cl_x$ powdered sample are $a = 8.868(1)$ Å and $c = 12.659(2)$ Å [24, 52–54].

It should be noted that while the broad GIWAXS scattering peaks do not allow precise structural assignments, distinct peaks observed for different species enable determination of the predominant sample structure in real time. The scattering peak at $q = 10\,\mathrm{nm}^{-1}$ was assigned to the (1 1 0) peak observed for the perovskite structure [19, 24].

The scattering peak at $q = 9\,\mathrm{nm}^{-1}$ assigned to the (0 0 1) plane of PbI_2 (PDF 00-007-0235) was present only in the 5 wt% perovskite film, suggesting thinner films underwent a more rapid degradation into PbI_2 [14, 24].

Characterization of Block Copolymer-directed Al_2O_3 Thin Films

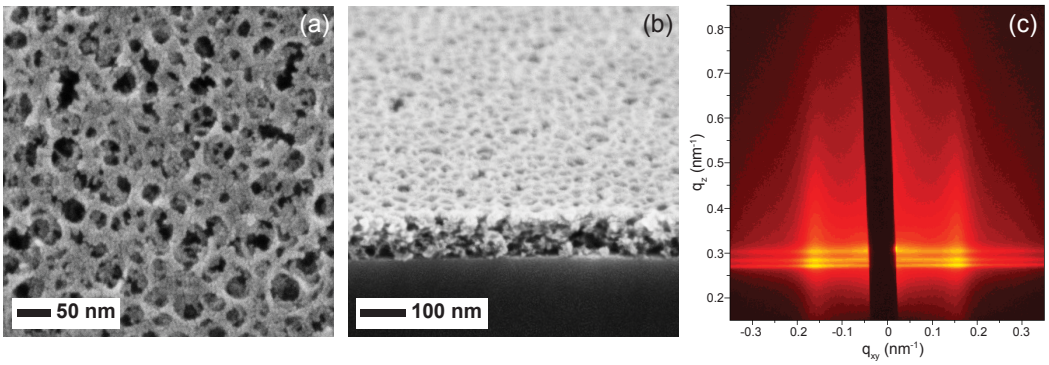

Fig. 6.2 (a) Plan view and (b) cross-sectional SEM images, and (c) 2D GISAXS profile at incidence angle of 0.16° of MBCP-Al_2O_3 film after calcination. The measurements in this figure were taken by Kwan W. Tan of Cornell University.

In a solvent mixture of non-polar toluene and polar n-butanol, the structure directing polyisoprene-*block*-polystyrene-*block*-polyethylene oxide (PI-*b*-PS-*b*-PEO) triblock terpolymer forms micelles with the hydrophobic PI and PS in the core, and a hydrophilic PEO corona [41–44]. The added Al_2O_3 sol is selectively attracted to the PEO corona by hydrogen bonds [37]. Upon solvent evaporation, the organic/inorganic micelles self-assemble into a randomly packed arrangement. Mesoporous block copolymer-directed alumina (MBCP-Al_2O_3) thin films with interconnected porosity are generated when the organic components are removed by calcination as evidenced by the scanning electron microscopy (SEM) and AFM images in Figures 6.2 and 6.3, respectively.

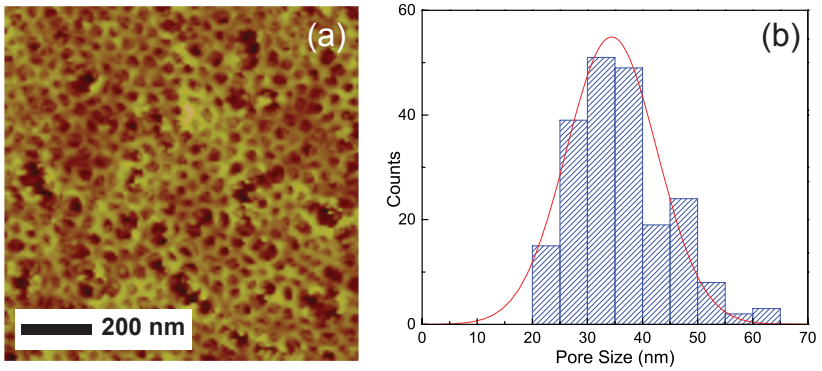

Fig. 6.3 (a) AFM surface profile of the MBCP-Al_2O_3 film. (b) Histogram of the MBCP-Al_2O_3 pore size distribution. A Gaussian fitting curve is added to guide the eye. The measurements in this figure were taken by Kwan W. Tan of Cornell University.

The MBCP-Al_2O_3 pores are interconnected in both in-plane and out-of-plane directions. From SEM and AFM, the pore diameter is ~36 nm and the film thickness is 70-80 nm after calcination. In 2D gracing incident scattering angle x-ray spectroscopy (GISAXS) patterns, two intense diffraction peaks are observed at $q_{xy} = \pm 0.157\,\mathrm{nm}^{-1}$ (Figure 6.2c) consistent with a disordered mesoporous material with a macroscopically homogenous in-plane d-spacing of $2\pi/q_{xy} \approx 40\,\mathrm{nm}$ [44].

The oscillations at the diffraction peaks are attributed to the form factor of the film thickness [55]. In contrast, the porosity of Al_2O_3 nanoparticulate films is macroscopically inhomogeneous as shown in Figure 6.4 [19–21].

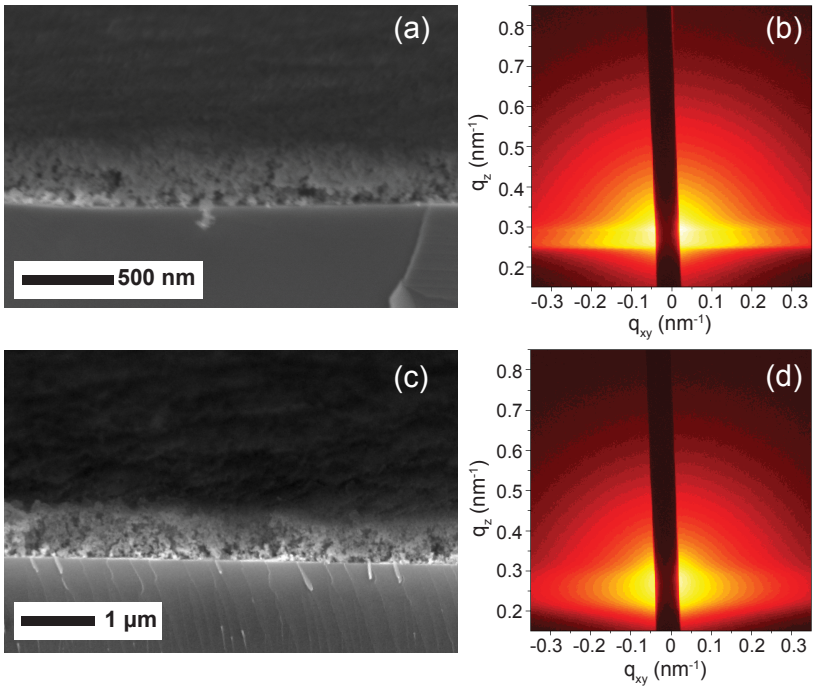

Fig. 6.4 Cross-sectional SEM micrographs and GISAXS profiles of (a, b) binder-free Al_2O_3 and (c, d) Al_2O_3 with binder measured at incidence angle of 0.18°. The in-plane porosity in the Al_2O_3 NP films is macroscopically inhomogeneous. The measurements in this figure were taken by Kwan W. Tan of Cornell University.

In situ X-ray of MBCP-Al_2O_3 Perovskite Structural Evolution

The mesoporous support in solution-processed nanostructured $CH_3NH_3PbX_3$ perovskite solar cells fulfils multiple roles. For example, mesoporous TiO_2 acts as the distributed heterojunction with large surface areas for the generation of charges by the $CH_3NH_3PbI_3$ perovskite absorber, and collects and transports the electrons to the collecting electrode [11–18, 25]. Moreover, mesoporous superstructures improve the coating of perovskite material to enhance coverage and light harvesting efficiency [20], and act as a physical barrier to prevent the formation of "shunt paths" by direct contact of the hole transport material and electron selective layer [19–23]. In situ GIWAXS was applied to study the structural evolution of solution-processed $CH_3NH_3PbI_{3-x}Cl_x$ perovskite on MBCP-Al_2O_3 thin films during annealing in real time. A 20 wt% perovskite precursor solution was deposited on the MBCP-Al_2O_3 thin film for isothermal-time-dependent (ITD) annealing in air and nitrogen, respectively. The precursor solution filled the interconnected mesopores and formed a "wet capping layer" on the superstructure scaffold with incomplete solvent removal.

After deposition the sample was immediately loaded on a sample-stage held at 100°C. It should be noted that in this way the ITD MBCP-Al_2O_3 perovskite samples underwent

an immediate jump from ambient temperature to 100°C. GIWAXS measurements were collected in real time over a dwell of 50 min. In the employed beam configuration, GIWAXS measured the perovskite material within the MBCP-Al_2O_3 scaffold and capping layer as the incidence angle of the incoming X-ray beam was above the critical angle of the silicon substrate. In situ 2D GIWAXS profiles and azimuthally integrated intensity plots of the ITD MBCP-Al_2O_3 perovskite structural evolution in nitrogen and air, respectively, are shown in Figure 6.5.

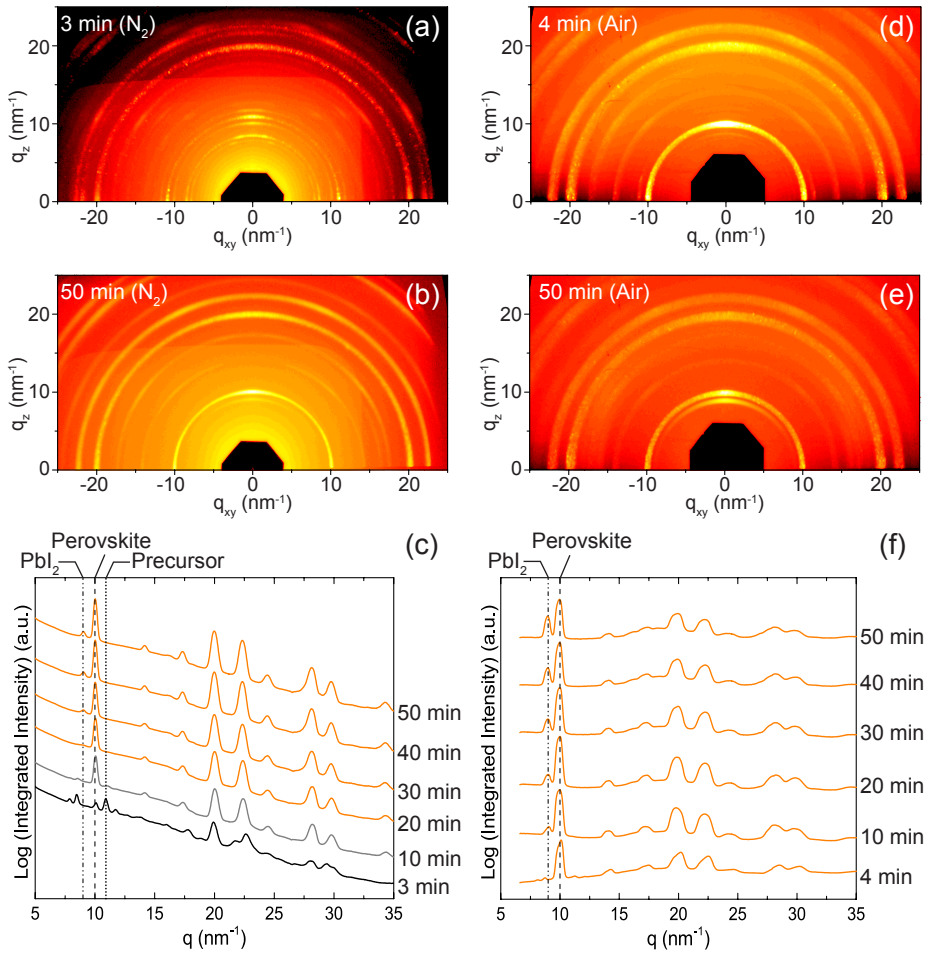

Fig. 6.5 2D GIWAXS profiles for ITD annealing of MBCP-Al_2O_3 perovskite films at 100°C in (a, b) nitrogen and (d, e) air for different time points as indicated, together with (c, f) respective azimuthally integrated intensity plots. The dotted line at $q \approx 11\,\mathrm{nm}^{-1}$, dashed line at $q = 10\,\mathrm{nm}^{-1}$, and dash-dotted line at $q = 9\,\mathrm{nm}^{-1}$ denote the signature scattering peaks for the crystalline precursor, perovskite, and PbI_2 structures, respectively. The measurements in this figure were taken by Kwan W. Tan of Cornell University.

For the study of the ITD MBCP-Al_2O_3 perovskite's behaviour in nitrogen, the wet sample was loaded into a custom-made environmental chamber on the heated stage at 100°C under flowing nitrogen [51]. Under these conditions, the wet sample exhibits multiple orders of scattering rings in the GIWAXS profile (Figure 6.5a), indicating the formation of crystalline material. Interestingly, from the integrated intensity plots in Figure 6.5c, at short times

(3 min time point) a distinct set of scattering peaks at lower q values (<9 nm^{-1}) are observed that are neither characteristic for CH_3NH_3I, $PbCl_2$, PbI_2, nor for the $CH_3NH_3PbI_{3-x}Cl_x$ perovskite structure. After 10 min the expected peaks for the mixed halide perovskite are observed (compare Figure 6.5c with Figure 6.1e). This observation suggests the formation of a distinct crystalline structure, which in the following discussion will be refered to as the "crystalline precursor structure". The peak at $q \approx 11\,nm^{-1}$ is assigned as the signature scattering peak for this crystalline precursor structure.

Further investigation is currently underway to identify the structure of this crystalline precursor material. However, during the revision of this work, a highly relevant article was published by Dualeh et al. [56] which also identified the precursor state and suggested lead(II) oxychloride as a possible candidate [57]. Somewhere between 3 and 10 min of annealing in nitrogen under the set conditions, the film underwent a transition to form the mixed halide perovskite structure, at which point the intensity of the peak at $q \approx 11\,nm^{-1}$ for the crystalline precursor in Figure 6.5c vanishes. The film started to degrade into PbI_2 after about 20-30 min of annealing, as indicated by the appearance of a scattering peak at $q = 9\,nm^{-1}$.

The degradation may be attributed to the presence of moisture in the chamber [14, 23, 24, 52, 54], but at this point X-ray beam induced damage cannot be excluded either. For comparison, Figure 6.5b shows the GIWAXS profile of the MBCP-Al_2O_3 perovskite film after 50 min annealing in nitrogen at 100°C. From the beginning of ITD annealing at 100°C in air, multiple orders of scattering rings in the GIWAXS profile are observed (Figure 6.5d), consistent with the rapid formation of a polycrystalline perovskite phase in the presence of MBCP-Al_2O_3. Figure 6.5f shows the azimuthally integrated intensity plot of the ITD experiments in air with the perovskite signature peak at $q = 10\,nm^{-1}$. Within 10 min at 100°C, the perovskite started to degrade to PbI_2 as signified by the new peak formed at $q = 9\,nm^{-1}$. The degradation is likely to initiate from the perovskite film surface [54] and may be attributed to moisture in the air [14, 23, 24, 52] and X-ray beam induced damage. Over the dwell of 50 min at 100°C, the scattering peaks remained in the same positions as shown in Figure 6.5e and f, suggesting minimal reorientation changes to the perovskite structure. Under air the perovskite structure already showed first indications of degradation via the peak at $q = 9\,nm^{-1}$ by the 10 min time point. The absence of the crystalline precursor structure is suspected to be due to a more rapid transition in air as compared to nitrogen.

Similar behaviour is observed, i.e. the absence of the crystalline precursor for the mixed halide perovskite on a MBCP-TiO_2 superstructure annealed in air, albeit with more severe degradation into PbI_2 (Figure 6.6).

To delineate how individual parameters contribute to the structural evolution of $CH_3NH_3PbI_{3-x}Cl_x$ on MBCP-Al_2O_3, time-temperature-dependent (TTD) GIWAXS measurements were conducted with a slow temperature ramp applied to the wet MBCP-Al_2O_3

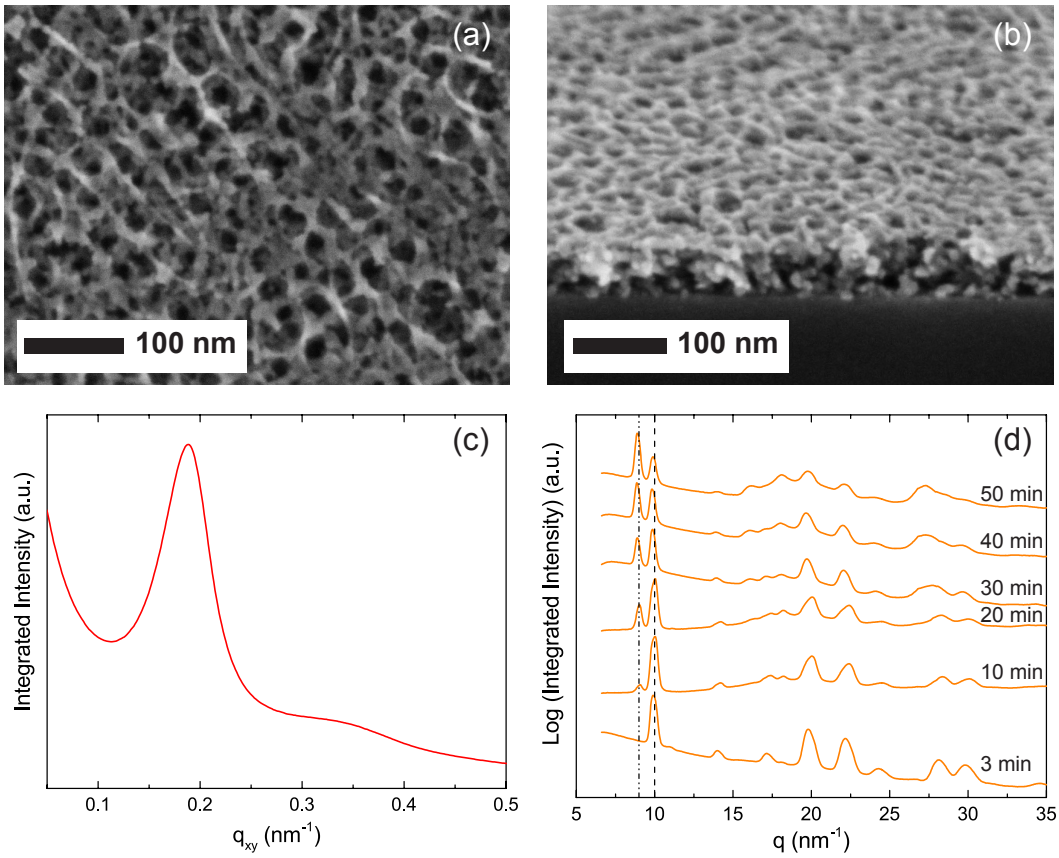

Fig. 6.6 Plan view and (b) cross-sectional SEM micrographs of MBCP-TiO_2 film. (c) Integrated intensity plots of GISAXS profile of MBCP-TiO_2 measured at an incidence angle of 0.16°. The first scattering peak at q_{xy} = 0.189 nm^{-1} provides a macroscopically homogeneous in-plane d-spacing of $2\pi/q_{xy} \approx 33$ nm. (d) In situ GIWAXS azimuthally integrated intensity plots of $CH_3NH_3PbI_{3-x}Cl_x$ perovskite on MBCP-TiO_2 as observed under isothermal-time-dependent (ITD) annealing at 100°C in air. The measurements in this figure were taken by Kwan W. Tan of Cornell University.

perovskite sample in nitrogen. To that end, 20 wt% precursor solution was deposited on the MBCP-Al_2O_3 thin film and loaded into the environmental chamber held at 30°C under flowing nitrogen. The temperature of the heating stage was raised by 10°C at every 10 min time interval. It took approximately 2-3 min for the heated stage to reach the set temperature. Figure 6.7 displays four representative 2D GIWAXS profiles (a-d) while the integrated intensity plots (e) reveal the TTD structural evolution of the MBCP-Al_2O_3 perovskite sample from 30-100°C over the dwell of 120 min.

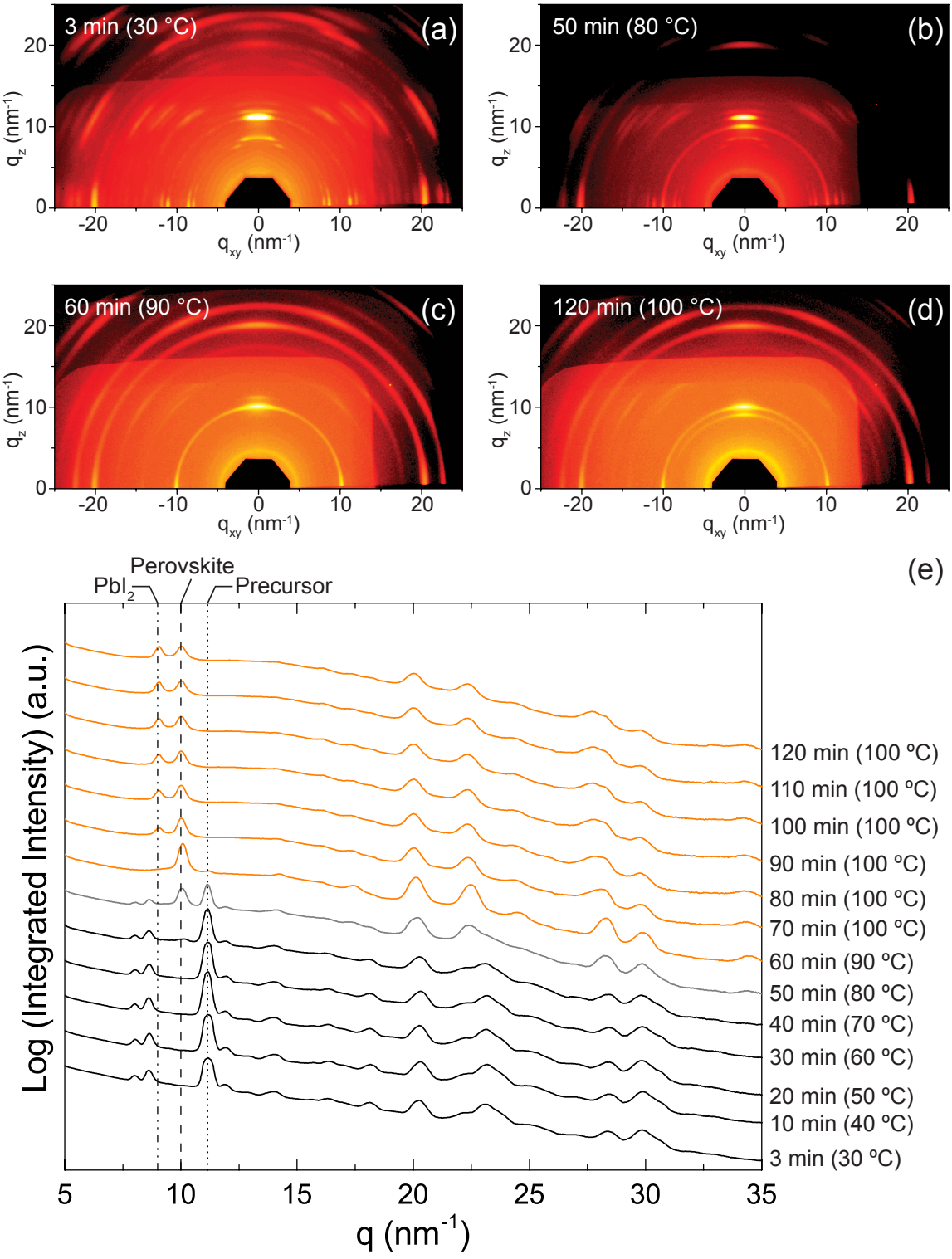

Fig. 6.7 2D GIWAXS profiles for TTD annealing of MBCP-Al_2O_3 perovskite films in nitrogen after (a) 3 min, (b) 50 min, (c) 60 min and (d) 120 min, together with (e) azimuthally integrated intensity plots. The dotted line at $q \approx 11\,\mathrm{nm}^{-1}$, dashed line at $q = 10\,\mathrm{nm}^{-1}$, and dash-dotted line at $q = 9\,\mathrm{nm}^{-1}$ denote the signature scattering peaks for the crystalline precursor, perovskite, and PbI_2 structures, respectively. The difference in background brightness of the GIWAXS patterns is a shadow artifact of the experimental setup. The measurements in this figure were taken by Kwan W. Tan of Cornell University.

At the beginning of the experiment, the crystalline precursor was detected in the GIWAXS profile via the peak at $q \approx 11\,\mathrm{nm}^{-1}$, see also GIWAXS pattern in Figure 6.7a showing results for the 3 min (30°C) time point. At the 50 min time point (80°C) a scattering ring appeared at $q = 10\,\mathrm{nm}^{-1}$ (Figure 6.7b), indicating the transition from the crystalline precursor to polycrystalline perovskite. This structural transition was completed at the 60 min time point (90°C, Figure 6.7c), similar to the 10 min time point for the ITD annealed MBCP-Al_2O_3 perovskite at 100°C in nitrogen (compare with Figure 6.5c). Perovskite film degradation was observed at the 70 min time point after the temperature was raised to the final value of 100°C, and progressed till the final time point at 120 min (Figure 6.7d). Similar to the ITD annealing in nitrogen, three distinct structures were identified during the TTD processing of $CH_3NH_3PbI_{3-x}Cl_x$ in MBCP-Al_2O_3 superstructures: (1) crystalline precursor, (2) perovskite, and (3) PbI_2 as a perovskite degradation product.

From the present and previous work, it is concluded that transitions between these different structures are driven by a combination of annealing temperature, environmental atmosphere and film thickness [23, 27, 28]. A yet-to-be identified crystalline precursor structure was observed upon spin coating the $CH_3NH_3PbI_{3-x}Cl_x$ precursor solution on MBCP-Al_2O_3 which displayed noteworthy thermal stability during the TTD ramp annealing. It is postulated that the crystalline precursor undergoes a solid-solid phase transformation to the 3D perovskite structure at 80°C. This transition occurs relatively rapidly (<10 min) and is largely completed at 90°C. To the best of my knowledge, this is the first experimental observation of a transformation from a crystalline precursor to the perovskite crystal structure for methylammonium lead trihalide perovskite materials, suggesting a phase transformation pathway consistent with Ostwald's "Rule of Stages" in which a metastable precursor is first formed, followed by transformation into the more stable product [58, 59].

Furthermore, the macroscopic coverage of the substrate with perovskite layers is largely affected by the heat treatment profile. In plan view SEM images (Figure 6.8a and b) large (>2 µm) perovskite crystallite islands are observed as well as pores in the capping layer on MBCP-Al_2O_3 under ITD annealing conditions.

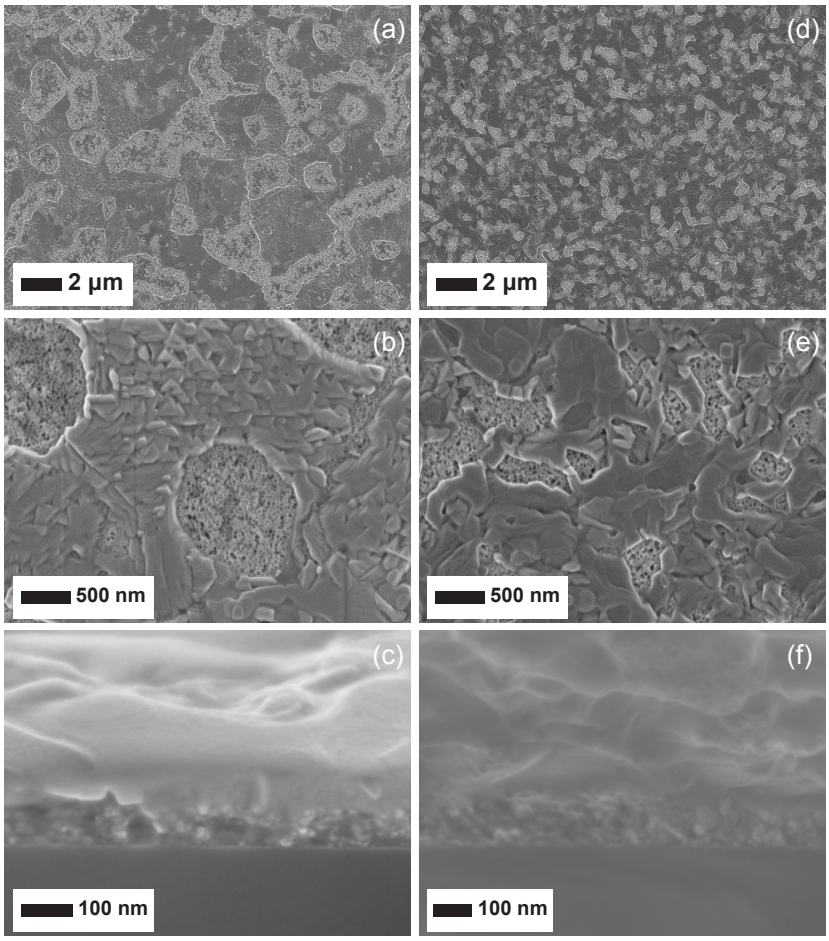

Fig. 6.8 Plan view and cross-sectional SEM micrographs of 20 wt% perovskite on MBCP-Al_2O_3 prepared by (a-c) isothermal-time-dependent (100°C for 45 min), and (d-f) time-temperature-dependent (5°C/5 min ramp rate, 100°C for 45 min) annealing in nitrogen. Large perovskite crystallite islands and pore regions were observed for the ITD annealed MBCP-Al_2O_3 perovskite films compared to the TTD annealed samples. The SEM images in this figure were taken by Kwan W. Tan of Cornell University.

In contrast, the discrete perovskite islands and pores are on the sub-micron length scale for the TTD annealed MBCP-Al_2O_3 perovskite film shown in Figure 6.8d and e. Since the only difference in the heat treatment profile is at the initial stage before perovskite formation, this result suggests that the crystalline precursor coverage and the subsequent phase transformation contributes significantly to the final film coverage, which in turn greatly affects device performance (see below).

MBCP-Al_2O_3 Perovskite Solar Cell Performance

Figure 6.9 shows SEM images of MBCP-Al_2O_3 perovskite films prepared from 40 wt% precursor solutions and annealed either instantaneously at 100°C (ITD), or with a slow temperature ramp to 100°C (TTD) in nitrogen. While the crystallite domain sizes are very similar for the ITD and TTD annealed films (Figure 6.9c and d), the capping film coverage is drastically different.

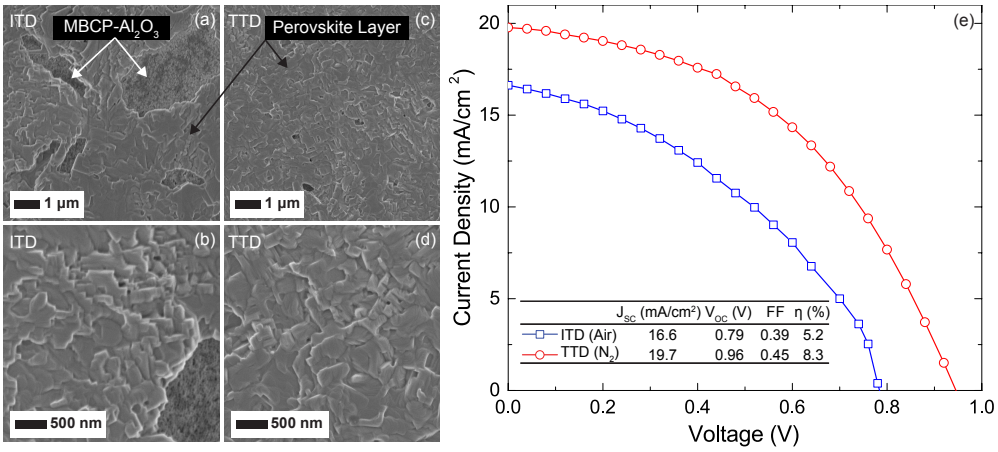

Fig. 6.9 Plan view SEM micrographs of perovskite crystallization in MBCP-Al_2O_3 annealed under (a, b) ITD, and (c, d) TTD conditions. (e) Current density/voltage curves of best performing MBCP-Al_2O_3 perovskite solar cells measured under stimulated AM1.5 sunlight of 100 mW/cm^2 irradiation for different annealing conditions (ITD versus TTD). The SEM images in this figure were taken by Kwan W. Tan of Cornell University.

Figure 6.9a shows that large pores (>1 μm) were formed in the capping layer of the MBCP-Al_2O_3 perovskite films annealed instantly at 100°C (ITD). In contrast, when the MBCP-Al_2O_3 perovskite film was annealed with a slow temperature ramp of 5°C/5 min in nitrogen to 100°C and held for 45 min at the final temperature (TTD), significantly better perovskite film coverage was achieved. The 40 wt% perovskite film morphology is highly similar to the 20 wt% perovskite films (see Figure 6.8). The crystalline precursor which is present for a longer dwell period during TTD annealing is hypothesized to promote film formation with fewer macroscopic defects than in ITD annealed films.

MBCP-Al_2O_3 perovskite solar cells annealed under ITD and TTD conditions were fabricated (see Table 6.1). Comparing the best performing MBCP-Al_2O_3 perovskite solar cells in Figure 6.9e, the values of short-circuit current density (J_{sc}), open-circuit voltage (V_{oc}) and fill factor (FF) of the TTD-N_2 device increased by at least 15% relative to the ITD-air device. At the same time, the power conversion efficiency increased from 5.2% to 8.3%. The device performance improvement was attributed to the enhanced perovskite film morphology and coverage, enabling more uniform charge generation and collection, and reduced leakage with fewer available shunt paths [20, 23, 27, 28]. This trend is reconfirmed by calculating the shunt R_{sh} and series resistance R_{se} according to Chapter 2. For typical ITD-air devices, this is $R_{sh} = 60.5\ \Omega\,\text{cm}^2$ and $R_{se} = 133\ \Omega\,\text{cm}^2$; and $R_{sh} = 16.7\ \Omega\,\text{cm}^2$ and $R_{se} = 425\ \Omega\,\text{cm}^2$ for TTD devices respectively.

Table 6.1 MBCP-Al_2O_3 perovskite solar cell performance parameters averaged over a batch of at least 20 devices measured under 100 mW/cm^2 stimulated AM1.5 sunlight irradiation.

	Short-circuit current density (mA/cm^2)	Open-circuit voltage (V)	Fill factor	PCE (%)
ITD-annealed in air	13.7 ± 1.7	0.73 ± 0.08	0.36 ± 0.06	3.6 ± 1.0
TTD-annealed in N_2	15.7 ± 2.9	0.94 ± 0.02	0.44 ± 0.05	6.3 ± 1.2

6.3 Summary

In conclusion, in situ 2D GIWAXS was employed in combination with SEM to follow the structural evolution of $CH_3NH_3PbI_{3-x}Cl_x$ perovskite on mesoporous block copolymer Al_2O_3 thin films under thermal annealing.

Solution-processed perovskite films underwent transitions between three distinct crystalline structures during thermal annealing: a crystalline precursor, a perovskite and a degradation product in the form of PbI_2. Finally, it was demonstrated that by annealing the MBCP-Al_2O_3 perovskite films with a well-controlled temperature ramp in a dry environment the perovskite capping film coverage and the power conversion efficiency of block copolymer-directed alumina perovskite solar cells can be greatly improved. To the best of this my knowledge, the crystalline precursor has not previously been described and its exact structure is currently unknown. The evolution between these structures markedly depends on the annealing conditions.

This chapter highlights the critical dependence of device performance on the annealing protocol used for the perovskite film formation. This motivates the next chapter where 2 distinct annealing protocols are used. Both utilize a ramp procedure to 100°C which was proven here to yield better surface coverage. The difference between the protocols is the last step after the ramp: one uses a dwell time at 100°C for 45 min and the other procedure a quick 130°C flash anneal for 5 min. As a result, the film crystallinity changes dramatically exhibiting different device performances.

CHAPTER 7

The Influence of Thermal Processing Protocol upon the Crystallization and Photovoltaic Performance of Organic-Inorganic Lead Trihalide Perovskites

The previous chapter highlighted the critical dependence of perovskite film formation on the precise annealing procedure. This motivates the current chapter which investigates the thermally-induced morphological and crystalline development of methylammonium lead mixed halide perovskite ($CH_3NH_3PbI_{3-x}Cl_x$) thin films and photovoltaic device performance with mesosuperstructured and planar heterojunction architectures. The main finding is that a short rapid thermal annealing at 130°C leads to the growth of large micron-sized textured perovskite domains and improves the short circuit currents and power conversion efficiencies up to 13.5% for the planar heterojunction perovskite solar cells. This work highlights once more the criticality of controlling the thin film crystallization mechanism of hybrid perovskite materials for high-performing photovoltaic applications. This work is published in [60].

The work in this chapter was performed in close collaboration with Kwan W. Tan from the group of Ulrich Wiesner at Cornell University. Kwan has spent about 8 weeks at Oxford University and I have spent about 8 weeks at Cornell as part of an EPSRC funded project. During my stay in Cornell I fabricated and characterised the materials. However, the synchrotron became only available after I had left Cornell. Hence, some of the characterisation and experiments were conducted solely by Kwan W. Tan. This will be noted in the figure captions and text.

Introduction

Recent investigations into the perovskite film morphology formation have provided insights towards identifying key parameters to attain consistently high-performing solar cells. Park and co-workers spin coated 10-40 wt% of $CH_3NH_3PbI_3$ dissolved in γ-butyrolactone on a 5.5 µm thick mesoporous titania photoanode, forming 2-3 nm perovskite nanocrystals after annealing at 40-160°C [12]. Graetzel and colleagues utilized a two-step sequential process by first depositing PbI_2 on a 350 nm thick mesoporous TiO_2 layer, and subsequent dip-coating into a solution of CH_3NH_3I precursor in isopropanol to grow ~22 nm $CH_3NH_3PbI_3$ nanocrystallites [25, 61]. The nanoporous nature and large surface area of the titania film enabled ultrafast growth of perovskite crystals within the pores and high performing devices of over 15% PCE [25]. Even the removal of the mesoporous scaffold did not deter high performances of planar heterojunction perovskite-based solar cells and recent investigations of vapour deposition [26] and solution processing [31] have demonstrated over 15% PCE. Despite the distinction in the state of the precursors (liquid versus vapour), the resulting hybrid perovskite films to date fulfil similar criteria: high film uniformity and coverage, and large perovskite crystallites (100-1000 nm) to harness the excellent carrier properties [1, 23, 26–31, 62–64].

In this work, methylammonium lead mixed halide ($CH_3NH_3PbI_{3-x}Cl_x$) perovskites with different crystal domain sizes were prepared via a direct single-step spin coating process, followed by growth under different thermal annealing conditions. The resulting film morphologies were subsequently correlated with performances in alumina-based meso-superstructured and planar heterojunction solar cell architectures.

7.1 Experimental

Fabrication of mesoporous block copolymer-directed alumina thin films, mesoporous alumina nanoparticle thin films of ~100 nm, perovskite solar cell assembly, and solar cell characterization were outlined in in Appendix A and Chapter 2.2. This project was in close collaboration with Kwan W. Tan of Cornell University who took the GIWAXS data, SEM images, and prepared the MBCP sample in this study.

UV-vis spectroscopy and photoluminescence characterization were outlined in the previous chapters.

Annealing protocols of the perovskite films

All of the following procedures were conducted in a nitrogen atmosphere. A 40 wt% solution of methylammonium iodide (CH_3NH_3I) and lead chloride ($PbCl_2$) (3:1 by molarity) dissolved in DMF was spin coated on the BCP-Al_2O_3 films, Al_2O_3-NP films and silicon substrates at 2000 rpm for 45 s. The wet perovskite samples were allowed to dry at ambient temperature for at least 20 min. All samples were slowly heated from ambient temperature to 100°C at

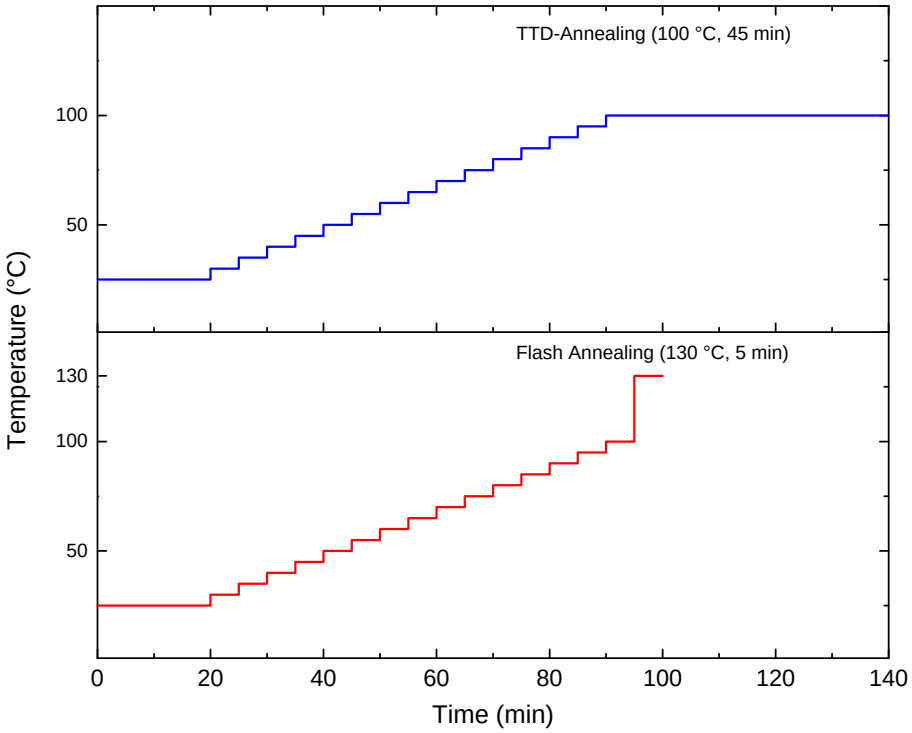

Fig. 7.1 Representative plot of TTD and flash thermal annealing protocols

a ramp rate of 5°C/5 min on a Fisher Scientific hotplate (product code: 10049552), i.e. the hotplate temperature was increased by 5°C after every 5 min dwell.

After the annealing procedure the samples were taken off the hot plate and put on a metallic surface at room temperature. The final annealing step was modified to prepare different crystalline perovskite thin film samples. In the "time-temperature-dependent" annealing procedure, the sample was held at 100°C for 45 min. In the "flash" annealing procedure, the samples were first held at 100°C for 5 min, then rapidly heated to the final value of 130°C (<3 min), and held there for another 5 min. The thermally annealed perovskite samples were removed from the hot plate and quenched on a metal block heatsink at ambient temperature. The different annealing procedures are displayed in Figure 7.1. It should be noted that the time-temperature-dependent annealing step here is not the usual annealing step employed in previous studies. Unless otherwise stated the coated substrates were placed directly in an oven or on a hot plate already set at the crystallization temperature, i.e. a very short ramp time. Within this manuscript time-temperature-dependent is referring to the slow ramp to 100°C.

Scanning electron microscopy and grazing incidence wide-angle X-ray characterization (GIWAXS)

The perovskite surface area coverage was estimated from SEM images using the ImageJ software [23]. Grazing incidence wide-angle X-ray scattering (GIWAXS) was measured at the D1 beamline of the Cornell High Energy Synchrotron Source (CHESS). The D1 beamline setup consists of a multilayer monochromator of $\lambda = 0.14715$ nm. GIWAXS patterns were

collected on a Dectris Pilatus 300k area detector mounted vertically at a distance of ~142 mm from the sample.

The incident beam angle was above the silicon critical angle (~0.25°) and exposure times <5 s. The resolution of the area detector was 487x619 pixels with a 172 µm pixel size. The GIWAXS patterns were analysed using the FIT2D software [50] and displayed in scattering vector q coordinates, where $q = 4\pi \sin(\theta)/\lambda$, θ is half of the scattering angle, and λ is the X-ray wavelength. The SEM images and GIWAXS data in this study were taken by Kwan W. Tan of Cornell University.

7.2 Results and Discussion

Characterization of $CH_3NH_3PbI_{3-x}Cl_x$ perovskites

The organic-inorganic nature of $CH_3NH_3PbX_3$ allows high flexibility and simple processing by either vapour deposition, solution processing, or a combination of both. Various groups investigated different processing parameters to optimize the perovskite film formation via single-step spin coating, for example probing solute concentration, solvent selection, environmental atmosphere, spin coating speed and annealing conditions [1, 23, 27, 28]. The previous chapter postulates the existence of a "crystalline precursor structure" present in films of the mixed halide ($CH_3NH_3PbI_{3-x}Cl_x$) hybrid material prior to a phase transformation to the final perovskite structure during thermal annealing [1]. There, it is argued that the crystalline precursor promotes more controlled perovskite film formation on mesoporous block copolymer-directed alumina (BCP-Al_2O_3) superstructures and planar substrates by annealing via a ramp rate.

Figure 7.2 shows results of grazing incidence wide-angle X-ray scattering (GIWAXS) measurements of $CH_3NH_3PbI_{3-x}Cl_x$ perovskite films prepared on different substrates by controlled ramp thermal annealing. A 40 wt% perovskite solution was deposited on ~100 nm mesoporous alumina nanoparticle thin films (NP-Al_2O_3, Figure 7.2a, b, 70-80 nm mesoporous block copolymer-directed alumina thin films (BCP-Al_2O_3, Figure 7.2c) and planar silicon substrates (Figure 7.2d) in nitrogen atmosphere. After drying at ambient temperature, all the perovskite samples were slowly heated from ambient temperature to 100°C at a ramp rate of 5°C/5 min to promote uniform film formation (see Figure 7.1) [1].

To ensure complete phase transformation of the precursors into the perovskite structure, the "time-temperature-dependent" (TTD) annealing treatment is applied holding the NP-Al_2O_3 perovskite sample at 100°C for 45 min. The corresponding GIWAXS profile in Figure 7.2a displays scattering rings for all seven reflections along q, indicating the NP-Al_2O_3 perovskite film is polycrystalline. Similar polycrystalline scattering patterns were reported for the same thermal treatment of BCP-Al_2O_3 perovskite samples and perovskite films on planar substrates [1]. Interestingly when a "flash" annealing is applied by rapidly increas-

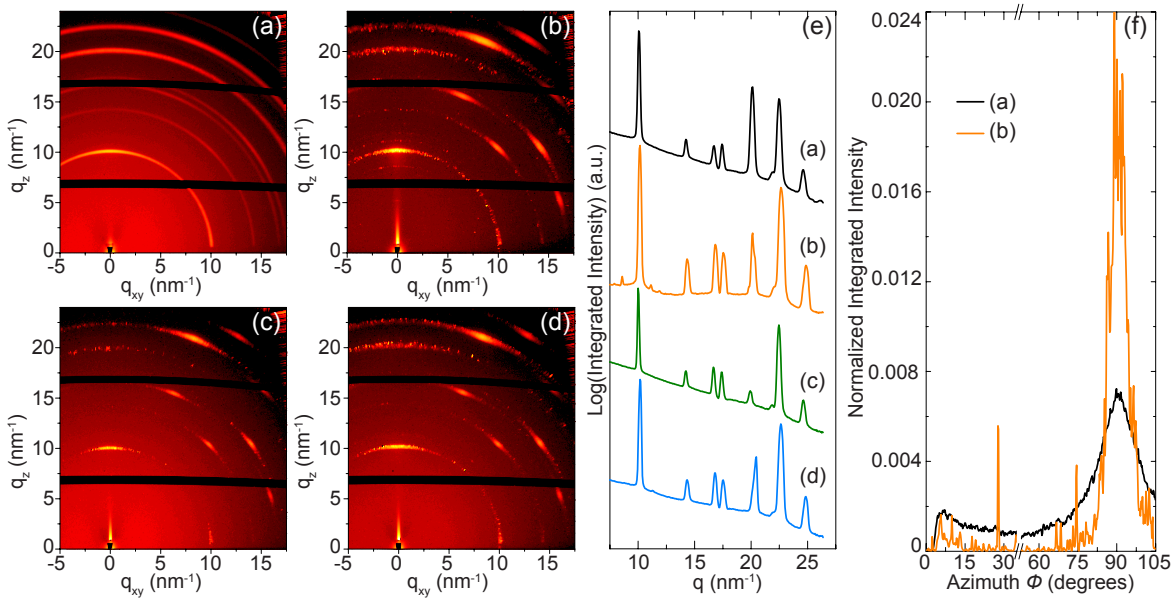

Fig. 7.2 GIWAXS profiles of $CH_3NH_3PbI_{3-x}Cl_x$ perovskite films (a) TTD annealed at 100°C for 45 min on NP-Al_2O_3; flash annealed at 130°C for 5 min on (b) NP-Al_2O_3, (c) BCP-Al_2O_3, and (d) planar silicon substrates. (e) Azimuthally and (f) radially integrated intensity plots from the corresponding GIWAXS patterns (a-d). The measurements in this figure were taken by Kwan W. Tan of Cornell University.

ing the temperature to 130°C for 5 min after the ramp to 100°C (see Figure 7.1), GIWAXS results for all perovskite samples (Figure 7.2b-d) exhibited "spotty" patterns, signifying the formation of highly textured perovskite crystal domains.

The azimuthally integrated scattering intensity plots versus scattering vector q (Figure 7.2e) for the different GIWAXS patterns are consistent with the $CH_3NH_3PbI_{3-x}Cl_x$ crystallographic pattern [1, 24].

The azimuthal scattering intensity distribution of the peak at $q = 10\,\mathrm{nm}^{-1}$ suggests an orientation in the in-plane direction relative to the substrate. To illustrate the degree of orientation of the perovskite crystal domains in the in-plane direction, radial integration over the peak at $q = 10\,\mathrm{nm}^{-1}$ of the two NP-Al_2O_3 perovskite samples (Figure 7.2a, b) was conducted, and results were plotted against the azimuth angle (Figure 7.2f). The comparison shows that after the ramp annealing to 100°C there already is a preferential in-plane orientation, which gets significantly more pronounced after the flash annealing.

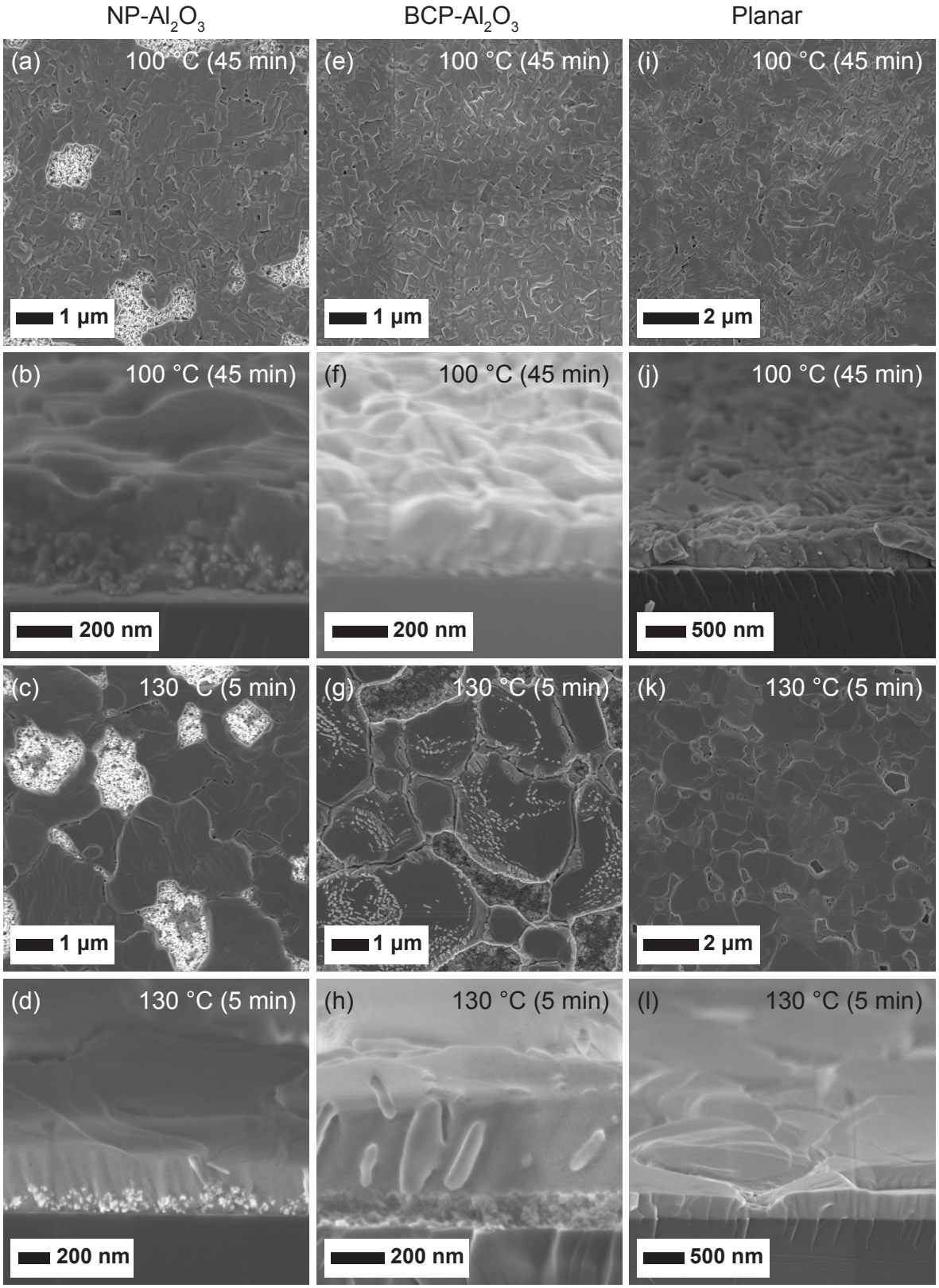

Fig. 7.3 Plan view and cross-sectional SEM micrographs of perovskite films on (a-d) NP-Al_2O_3, (e-h) BCP-Al_2O_3 and (i-l) planar silicon substrates prepared by the respective thermal annealing procedures as indicated. The SEM images in this figure were taken by Kwan W. Tan of Cornell University.

SEM images in Figure 7.3 reveal distinctly different perovskite crystal domain sizes depending on the annealing procedure. The TTD annealed perovskite samples at 100°C for 45 min on NP-Al_2O_3 (Figure 7.3a), BCP-Al_2O_3 (Figure 7.3e) and silicon substrates (Figure 7.3i) display a broad distribution of crystal domain sizes from about 100 to 1000 nm. This is consistent with the polycrystalline pattern observed for the NP-Al_2O_3 perovskite sample in the GIWAXS measurement (Figure 7.2a). From the cross-sectional SEM images (Figure 7.3b, f, j), the polycrystalline domains form a relatively rough surface. When the perovskite samples were flash annealed to 130°C, a very different film morphology consisting of micron-sized crystal domains (Figure 7.3c, g, k) emerged. This is consistent with the highly oriented spotty patterns obtained from GIWAXS (Figure 7.2b-d). All the resulting perovskite films have a maximum thickness of approximately 400 nm after thermal annealing.

Perovskite-based hybrid solar cell performances

Cell fabrication was conducted for $CH_3NH_3PbI_{3-x}Cl_x$ meso-superstructured (MSSC) and planar heterojunction perovskite solar cells on the mesoporous NP-Al_2O_3 superstructure and on a planar TiO_2 compact layer, annealed by TTD (100°C for 45 min) and flash (130°C for 5 min) procedures after the slow temperature ramp. In the following, the thermally annealed samples are designated by X-Y, where X represents substrate (NP or planar) and Y is the highest temperature at which the perovskite was annealed. Figure 7.4 displays the schematic and current density/voltage plots of the respective best performing perovskite solar cells along with a table inset of their performance parameters.

Table 7.1 summarizes the average device performance parameters: short-circuit current (J_{sc}), open-circuit voltage (V_{oc}), fill factor (FF) and power conversion efficiency (PCE) of the TTD 100°C and flash 130°C annealed samples.

Table 7.1 Meso-superstructured (14 devices) and planar heterojunction (22 devices) perovskite solar cell performance parameters measured under 100 mW/cm^2 stimulated AM1.5 sunlight irradiation.

	Short-circuit current density (mA/cm^2)	Open-circuit voltage (V)	Fill factor	Power conversion efficiency (%)
NP-100	17.7 ± 2.9	0.92 ± 0.04	0.53 ± 0.05	8.4 ± 1.8
NP-130	17.5 ± 1.7	0.91 ± 0.07	0.44 ± 0.09	6.9 ± 1.6
Planar-100	17.9 ± 2.2	0.92 ± 0.03	0.61 ± 0.05	9.9 ± 1.5
Planar-130	19.0 ± 1.6	0.91 ± 0.02	0.63 ± 0.04	10.7 ± 1.3

It should be noted that in this study 100 nm thick mesoporous scaffolds were used, which are thinner than for the best MSSCs thus far which employed 300-400 nm thick mesoporous Al_2O_3 [20, 25, 65, 66]. Here, a perovskite capping layer was formed on the ~100 nm NP-Al_2O_3 thin films (see Figure 7.3b, d).

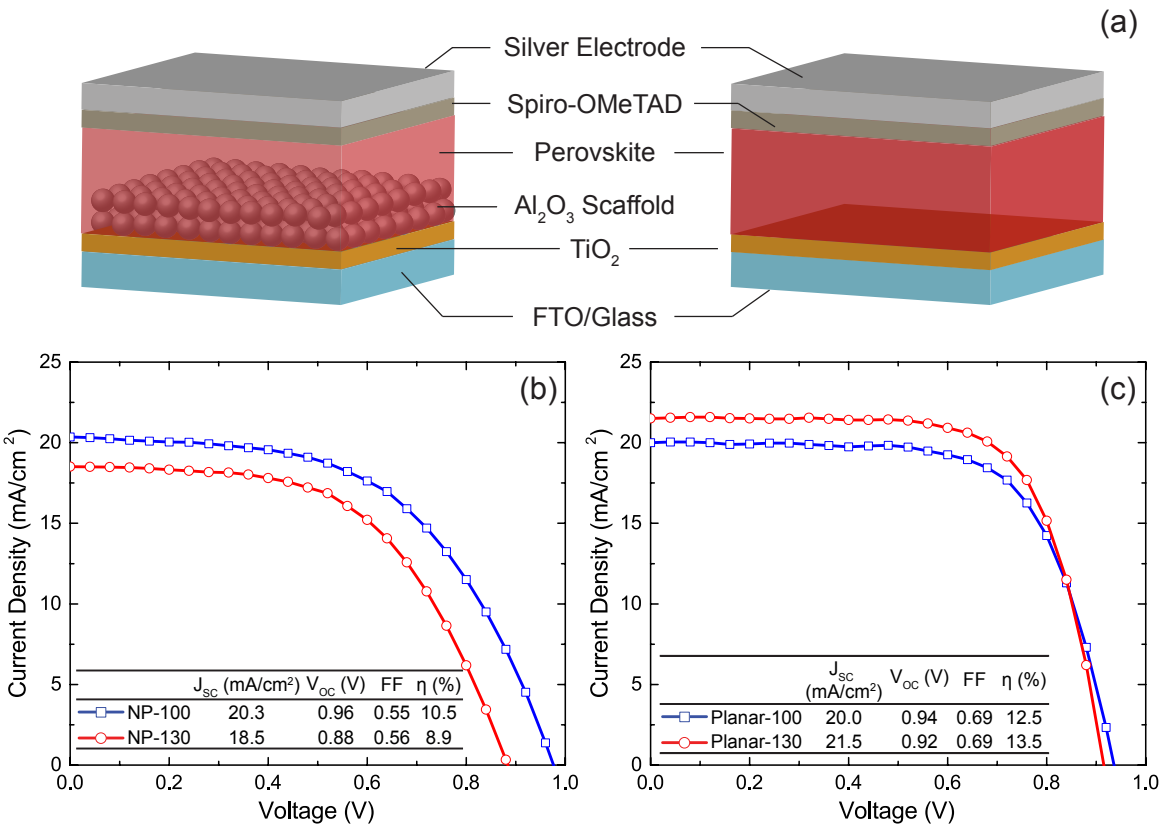

Fig. 7.4 (a) Schematic of meso-superstructured and planar heterojunction perovskite solar cells. Current density/voltage curves of differently annealed (b) NP-Al_2O_3 MSSC and (c) planar heterojunction perovskite solar cells measured under stimulated AM1.5 sunlight of 100 mW/cm^2 irradiation. The schematics in this figure were drawn with the help of Kwan W. Tan of Cornell University.

All NP-Al_2O_3 perovskite MSSCs exhibited similar average values for J_{sc} ~18mA/cm^2 and V_{oc} around 0.9 V. However, the average FF (0.53 to 0.44) and PCE (8.4% to 6.9%) decreased for the NP-130 MSSCs compared to NP-100 devices. The best performing NP-Al_2O_3 perovskite MSSC was annealed at 100°C for 45 min achieving a PCE of 10.5% (Figure 7.4b). When the Al_2O_3 perovskite MSSC was flash annealed at 130°C for 5 min, the PCE decreased to 8.9% due to lower V_{oc} and J_{sc} values (Figure 7.4b).

The lower FFs and PCEs for the NP-130 MSSC devices were attributed to the reduced perovskite surface coverage [20, 23]. The higher 130°C annealing temperature (albeit with shorter annealing duration) led to larger pores in the perovskite capping layer and exposed the mesoporous Al_2O_3 scaffold layer (see Figure 7.3a and c). From plan view SEM images, the perovskite capping layer coverage was estimated to reduce by 5% (from ~82% to ~77%) for the NP-130 perovskite films compared to TTD annealed samples (Figure 7.5).

Moreover, the cross-sectional SEM images in Figure 7.6 indicate that the NP-Al_2O_3 regions with no perovskite capping layer are only partially filled and may permit direct contact of the hole-transporter with the TiO_2 compact layer, resulting in lower shunt resistance [20, 23].

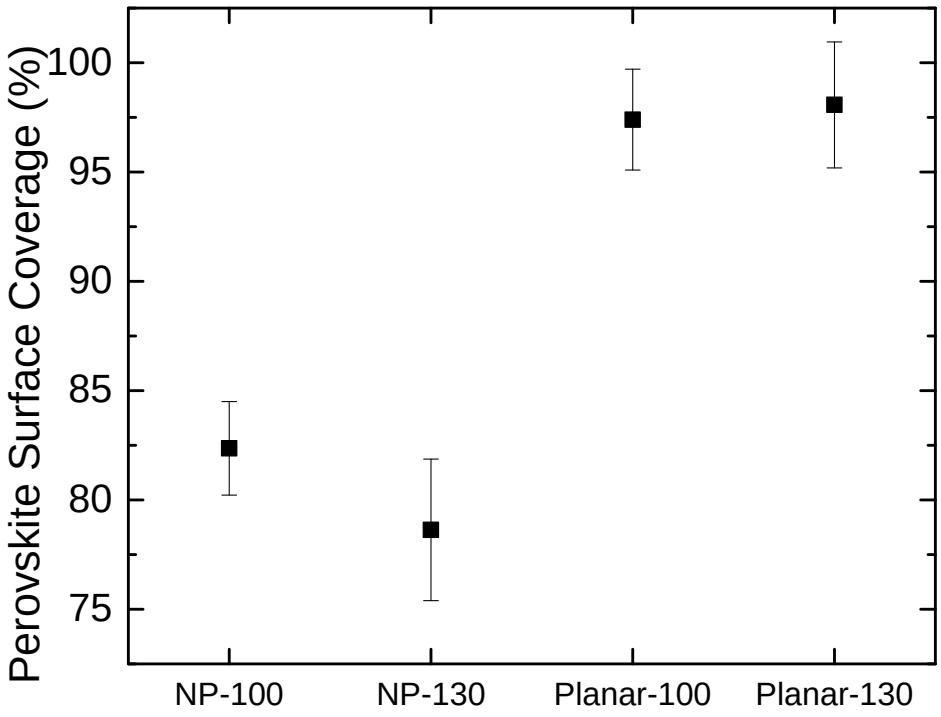

Fig. 7.5 Perovskite surface coverage on NP-Al_2O_3 and planar surfaces prepared by TTD and flash thermal annealing. The calculations in this figure were conducted with the help of Kwan W. Tan of Cornell University.

This trend is reconfirmed by calculating the shunt R_{sh} and series resistance R_{se}. For typical NP-100 devices, this is $R_{sh} = 877\ \Omega\,\mathrm{cm}^2$ and $R_{se} = 14.4\ \Omega\,\mathrm{cm}^2$; and $R_{sh} = 586\ \Omega\,\mathrm{cm}^2$ and $R_{se} = 16.9\ \Omega\,\mathrm{cm}^2$ for NP-130 devices respectively. This is in stark contrast to planar devices which show $R_{sh} = 1318\ \Omega\,\mathrm{cm}^2$ and $R_{se} = 7.6\ \Omega\,\mathrm{cm}^2$ for Planar-100 devices; and $R_{sh} = 1428\ \Omega\,\mathrm{cm}^2$ and $R_{se} = 7.5\ \Omega\,\mathrm{cm}^2$ for Planar-130 devices.

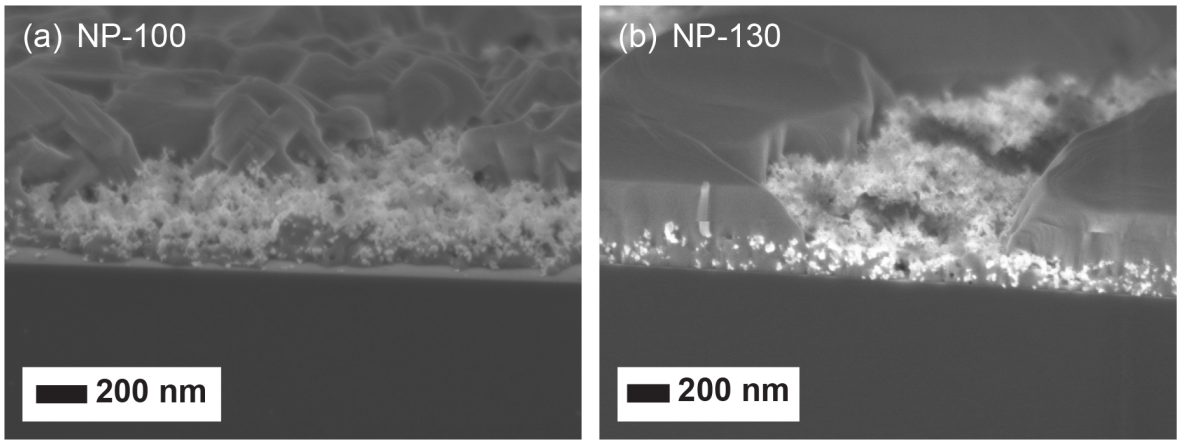

Fig. 7.6 SEM images of a cross section of perovskite capping layer-free regions on NP-Al_2O_3 thin films prepared by (a) TTD and (b) flash thermal annealing. The SEM images in this figure were taken by Kwan W. Tan of Cornell University.

Identical thermal annealing procedures were applied to planar heterojunction perovskite solar cells formed directly on TiO_2 compact layer with the average device parameters also summarized in Table 7.1.

The first clear observation is that they performed much better than the equivalent MSSCs of the same study. Comparing between the different annealing protocols, while the average V_{oc} (~0.9 V) and FFs (~0.6) are indistinguishable for differently annealed planar perovskite devices, the average J_{sc} and PCE of planar-130 devices improved from 17.9 to 19.0 mA/cm^2 and 9.9% to 10.7%, respectively, as compared to the planar-100 devices. The current density/voltage curves of the best performing devices are plotted in Figure 7.4c. In particular, the FF of 0.69 for the best single-step spin coating processed, thermally annealed planar heterojunction perovskite solar cells are in good agreement or even exceeding other champion perovskite photovoltaic devices prepared by sequential solution processing [25, 31], vapour deposition [26, 64], and combined solution-vapour-processing [62].

The high FF (~0.6) and PCE (>10%) for the planar heterojunction perovskite solar cells can be attributed to the formation of a uniform perovskite absorber layer with a reduced number of pores by a controlled ramp from ambient temperature to 100°C (see Figure 7.3i and k) [1, 23, 26–28, 62]. Indeed, as Figure 7.5 shows perovskite surface coverage greater than 95% for both planar perovskite films thermally annealed at 100°C for 45 min and 130°C for 5 min. The higher J_{sc} and PCE values of the planar-130 with respect to planar-100 perovskite solar cells are likely due to the formation of more uniform, micron-sized textured perovskite domains as observed via GIWAXS (Figure 7.2d) and SEM (Figure 7.3k).

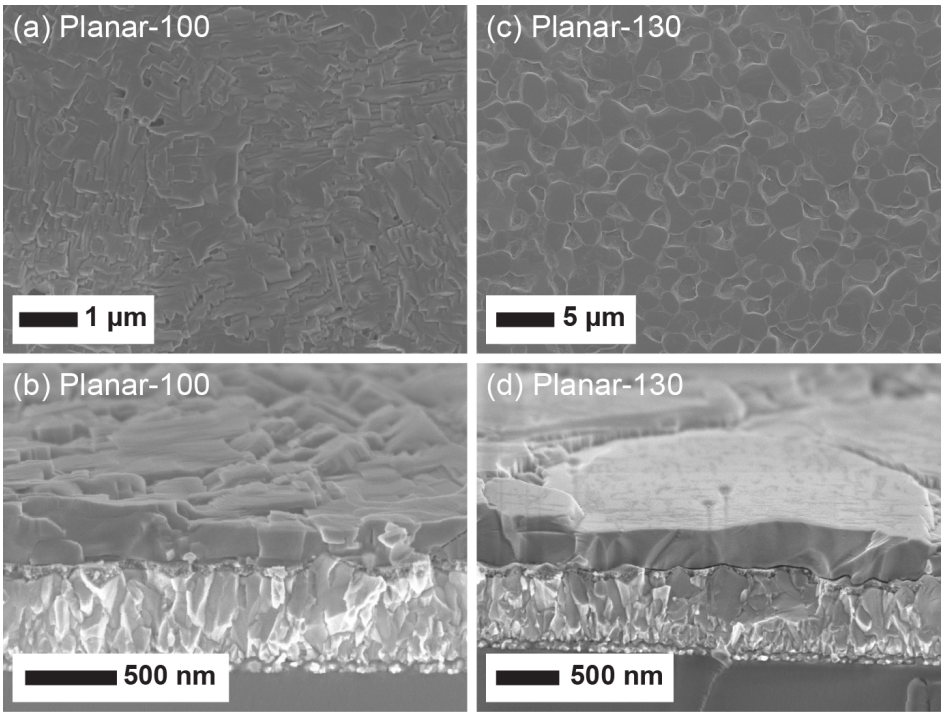

Fig. 7.7 Cross sections and coverage. The SEM images in this figure were taken by Kwan W. Tan of Cornell University.

Figure 7.7 displays similar planar perovskite film morphologies on TiO_2 compact layer/FTO glass substrates synthesized by TTD and flash thermal annealing. UV-vis absorbance plots for planar-100 and planar-130 perovskite films in Figure 7.8 display similar light absorption spectra for both planar-100 and planar-130 perovskite films.

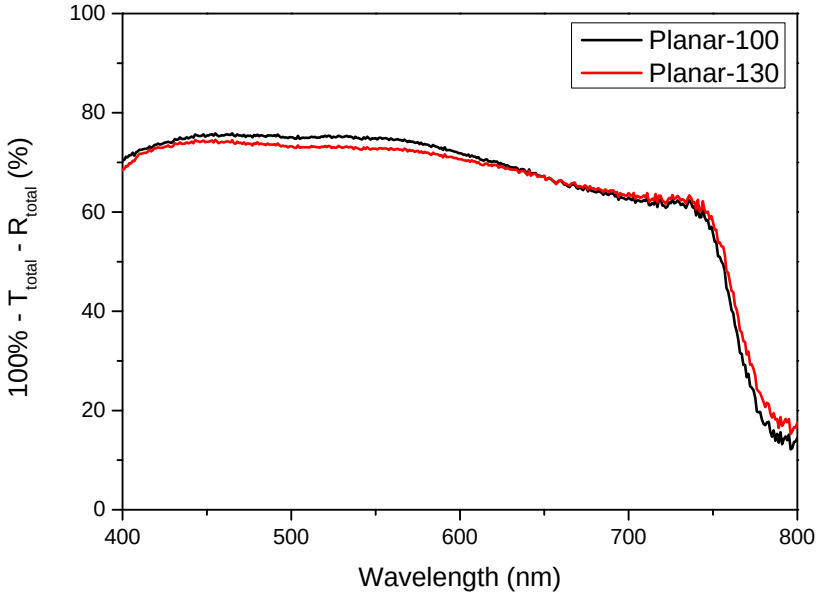

Fig. 7.8 UV-vis absorbance measurement with an integrating sphere accessory. Absorbance over wavelength is shown for the planar-100 (black) and planar-130 (red) perovskite films.

Non-radiative recombination of charge carriers is likely to occur at the grain boundaries, which can be reasoned from faster photoluminescence decay for perovskite films with smaller crystalline domains [20, 29, 67].

Indeed, longer PL lifetimes and higher steady-state PL intensities for the flash annealed planar-130 films, see Figure 7.9, are observed. However, it should be noted that there could be additional influences of the flash anneal beyond changes to the domain size, such as changes to the stoichiometry of the perovskite material, which could also be influencing the PL lifetime.

Whether the charge carrier mobility is strongly influenced by domain size is yet to be observed. In addition, the precise nature of the electronic contact at the perovskite/TiO_2 and perovskite/spiro-OMeTAD interfaces may be strongly influenced by the crystallinity of the perovskite at these contacts [62]. All considered, it appears that the larger domain sizes are advantageous for more optimum photovoltaic operation, as would be expected for a conventional thin film semiconductor. The proviso is that the macroscopic film morphology also has to be as uniform as possible, absent from pinholes.

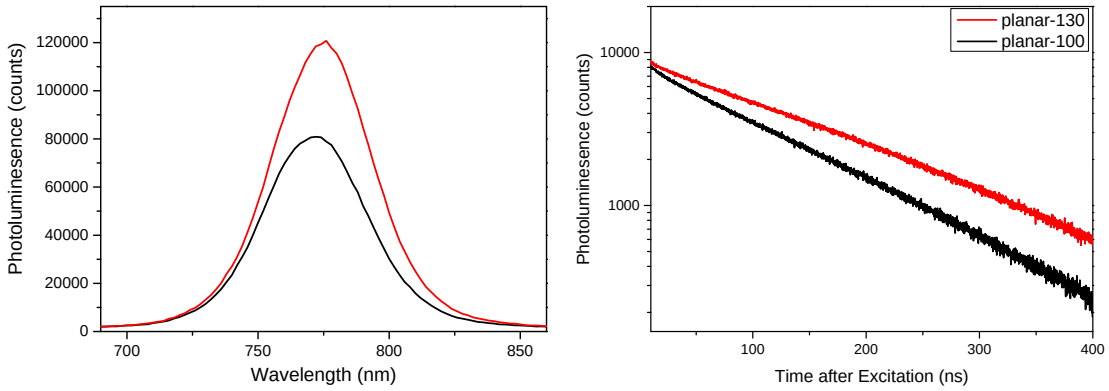

(a) Steady-state PL **(b)** Time-resolved PL

Fig. 7.9 (a) Steady-state and (b) time-resolved photoluminescence plots for planar-130 (red) and planar-100 (black) perovskite films

7.3 Summary

Film morphology control was demonstrated in $CH_3NH_3PbI_{3-x}Cl_x$ perovskite thin films by tuning the thermal annealing conditions after a slow ramp. Using grazing incidence wide-angle X-ray scattering and scanning electron microscopy, it was found that a short rapid annealing at 130°C promoted the growth of highly uniform micron-sized textured perovskite domains, while a longer dwell at 100°C resulted in 100-1000 nm polycrystalline perovskite domains. The rapid 130°C and longer 100°C thermal annealing resulted in very different perovskite solar cell performances with the meso-superstructured and planar heterojunction device architectures. In general, the 100°C annealed MSSC devices performed better than 130°C annealed samples attributed to the higher perovskite surface coverage. The planar perovskite devices outperformed the MSSC mesostructured counterparts mainly due to higher fill factor and short circuit currents, obtained from >95% perovskite surface coverage. Moreover, the 130°C flash thermal annealing resulted in planar heterojunction solar cells with highly textured perovskite domains and power conversion efficiency improvement from 9.9 to 10.7% compared to the 100°C annealed planar devices. The improvement was postulated to arise from reduced losses at the grain boundaries. The best performing planar heterojunction perovskite solar cell achieved a high power conversion efficiency of 13.5%. This study highlights the importance of simultaneously controlling both the macroscopic morphology and the crystalline domain size.

References

[1] K. W. Tan, D. T. Moore, M. Saliba, H. Sai, L. A. Estroff, T. Hanrath, H. J. Snaith, and U. Wiesner, "Thermally induced structural evolution and performance of mesoporous block copolymer-directed alumina perovskite solar cells," *ACS Nano*, vol. 0, no. ja, p. null, 2014.

[2] A. Cho, "Energy's Tricky Tradeoffs," *Science*, vol. 329, pp. 786–787, Aug. 2010.

[3] M. Graetzel, R. A. J. Janssen, D. B. Mitzi, and E. H. Sargent, "Materials interface engineering for solution-processed photovoltaics," *Nature*, vol. 488, pp. 304–312, Aug. 2012.

[4] A. H. Ip, S. M. Thon, S. Hoogland, O. Voznyy, D. Zhitomirsky, R. Debnath, L. Levina, L. R. Rollny, G. H. Carey, A. Fischer, K. W. Kemp, I. J. Kramer, Z. J. Ning, A. J. Labelle, K. W. Chou, A. Amassian, and E. H. Sargent, "Hybrid passivated colloidal quantum dot solids," *Nature Nanotechnology*, vol. 7, no. 9, pp. 577–582, 2012.

[5] Z. Ning, D. Zhitomirsky, V. Adinolfi, B. Sutherland, J. Xu, O. Voznyy, P. Maraghechi, X. Lan, S. Hoogland, Y. Ren, and E. H. Sargent, "Graded Doping for Enhanced Colloidal Quantum Dot Photovoltaics," *Advanced Materials*, vol. 25, no. 12, pp. 1719–1723, 2013.

[6] R. F. Service, "Outlook Brightens for Plastic Solar Cells," *Science*, vol. 332, p. 293, Apr. 2011.

[7] J. You, L. Dou, K. Yoshimura, T. Kato, K. Ohya, T. Moriarty, K. Emery, C.-C. Chen, J. Gao, G. Li, and Y. Yang, "A polymer tandem solar cell with 10.6% power conversion efficiency," *Nat Commun*, vol. 4, p. 1446, Feb. 2013.

[8] I. Chung, B. Lee, J. He, R. P. H. Chang, and M. G. Kanatzidis, "All-solid-state dye-sensitized solar cells with high efficiency," *Nature*, vol. 485, pp. 486–489, May 2012.

[9] L. Han, A. Islam, H. Chen, C. Malapaka, B. Chiranjeevi, S. Zhang, X. Yang, and M. Yanagida, "High-efficiency dye-sensitized solar cell with a novel co-adsorbent," *Energy & Environmental Science*, vol. 5, no. 3, pp. 6057–6060, 2012.

[10] A. Yella, H.-W. Lee, H. N. Tsao, C. Yi, A. K. Chandiran, M. K. Nazeeruddin, E. W.-G. Diau, C.-Y. Yeh, S. M. Zakeeruddin, and M. Grätzel, "Porphyrin-sensitized solar cells with cobalt (II/III)–based redox electrolyte exceed 12 percent efficiency," *Science*, vol. 334, no. 6056, pp. 629–634, 2011.

[11] A. Kojima, K. Teshima, Y. Shirai, and T. Miyasaka, "Organometal halide perovskites as visible-light sensitizers for photovoltaic cells," *Journal of the American Chemical Society*, vol. 131, pp. 6050–6051, Apr. 2009.

[12] J.-H. Im, C.-R. Lee, J.-W. Lee, S.-W. Park, and N.-G. Park, "6.5% efficient perovskite quantum-dot-sensitized solar cell," *Nanoscale*, vol. 3, no. 10, pp. 4088–4093, 2011.

[13] H. S. Kim, C. R. Lee, J. H. Im, K. B. Lee, T. Moehl, A. Marchioro, S. J. Moon, R. Humphry-Baker, J. H. Yum, J. E. Moser, M. Gratzel, and N. G. Park, "Lead iodide perovskite sensitized all-solid-state submicron thin film mesoscopic solar cell with efficiency exceeding 9%," *Scientific Reports*, vol. 2, 2012.

[14] J. H. Noh, S. H. Im, J. H. Heo, T. N. Mandal, and S. I. Seok, "Chemical management for colorful, efficient, and stable inorganic-organic hybrid nanostructured solar cells," *Nano Letters*, vol. 13, no. 4, pp. 1764–1769, 2013.

[15] L. Etgar, P. Gao, Z. Xue, Q. Peng, A. K. Chandiran, B. Liu, M. K. Nazeeruddin, and M. Grätzel, "Mesoscopic $CH_3NH_3PbI_3/TiO_2$ Heterojunction Solar Cells," *Journal of the American Chemical Society*, vol. 134, pp. 17396–17399, Oct. 2012.

[16] J. H. Heo, S. H. Im, J. H. Noh, T. N. Mandal, C.-S. Lim, J. A. Chang, Y. H. Lee, H.-j. Kim, A. Sarkar, N. K., M. Gratzel, and S. I. Seok, "Efficient inorganic-organic hybrid heterojunction solar cells containing perovskite compound and polymeric hole conductors," *Nature Photonics*, vol. 7, pp. 486–491, June 2013.

[17] E. J. W. Crossland, N. Noel, V. Sivaram, T. Leijtens, J. A. Alexander-Webber, and H. J. Snaith, "Mesoporous TiO_2 single crystals delivering enhanced mobility and optoelectronic device performance," *Nature*, vol. 495, pp. 215–219, Mar. 2013.

[18] H.-S. Kim, I. Mora-Sero, V. Gonzalez-Pedro, F. Fabregat-Santiago, E. J. Juarez-Perez, N.-G. Park, and J. Bisquert, "Mechanism of carrier accumulation in perovskite thin-absorber solar cells," *Nat Commun*, vol. 4, July 2013.

[19] M. M. Lee, J. Teuscher, T. Miyasaka, T. N. Murakami, and H. J. Snaith, "Efficient Hybrid Solar Cells Based on Meso-Superstructured Organometal Halide Perovskites," *Science*, vol. 338, pp. 643–647, Nov. 2012.

[20] J. M. Ball, M. M. Lee, A. Hey, and H. J. Snaith, "Low-temperature processed meso-superstructured to thin-film perovskite solar cells," *Energy & Environmental Science*, vol. 6, no. 6, pp. 1739–1743, 2013.

[21] E. Edri, S. Kirmayer, D. Cahen, and G. Hodes, "High Open-Circuit Voltage Solar Cells Based on Organic/Inorganic Lead Bromide Perovskite," *The Journal of Physical Chemistry Letters*, vol. 4, no. 6, pp. 897–902, 2013.

[22] W. Zhang, M. Saliba, S. D. Stranks, Y. Sun, X. Shi, U. Wiesner, and H. J. Snaith, "Enhancement of perovskite-based solar cells employing core-shell metal nanoparticles," *Nano Letters*, vol. 13, no. 9, pp. 4505–10, 2013. 23947387.

[23] G. E. Eperon, V. M. Burlakov, P. Docampo, A. Goriely, and H. J. Snaith, "Morphological Control for High Performance, Solution-Processed Planar Heterojunction Perovskite Solar Cells," *Advanced Functional Materials*, vol. 24, no. 1, pp. 151–157, 2014.

[24] S. Colella, E. Mosconi, P. Fedeli, A. Listorti, F. Gazza, F. Orlandi, P. Ferro, T. Besagni, A. Rizzo, G. Calestani, G. Gigli, F. De Angelis, and R. Mosca, "$Mapbi_{3-x}cl_x$ mixed halide perovskite for hybrid solar cells: The role of chloride as dopant on the transport and structural properties," *Chemistry of Materials*, vol. 25, pp. 4613–4618, Oct. 2013.

[25] J. Burschka, N. Pellet, S.-J. Moon, R. Humphry-Baker, P. Gao, M. K. Nazeeruddin, and M. Gratzel, "Sequential deposition as a route to high-performance perovskite-sensitized solar cells," *Nature*, vol. 499, pp. 316–319, July 2013.

[26] M. Liu, M. B. Johnston, and H. J. Snaith, "Efficient planar heterojunction perovskite solar cells by vapour deposition," *Nature*, vol. 501, pp. 395–398, Sept. 2013.

[27] B. Conings, L. Baeten, C. De Dobbelaere, J. D'Haen, J. Manca, and H.-G. Boyen, "Perovskite-based hybrid solar cells exceeding 10reproducibility using a thin film sandwich approach," *Advanced Materials*, vol. 26, no. 13, pp. 2041–2046, 2014.

[28] J.-Y. Jeng, Y.-F. Chiang, M.-H. Lee, S.-R. Peng, T.-F. Guo, P. Chen, and T.-C. Wen, "$CH_3NH_3PbI_3$ perovskite/fullerene planar-heterojunction hybrid solar cells," *Advanced Materials*, vol. 25, no. 27, pp. 3727–3732, 2013.

[29] S. D. Stranks, G. E. Eperon, G. Grancini, C. Menelaou, M. J. P. Alcocer, T. Leijtens, L. M. Herz, A. Petrozza, and H. J. Snaith, "Electron-Hole Diffusion Lengths Exceeding 1 Micrometer in an Organometal Trihalide Perovskite Absorber," *Science*, vol. 342, pp. 341–344, Oct. 2013.

[30] G. C. Xing, N. Mathews, S. Y. Sun, S. S. Lim, Y. M. Lam, M. Gratzel, S. Mhaisalkar, and T. C. Sum, "Long-range balanced electron- and hole-transport lengths in organic-inorganic $CH_3NH_3PbI_3$," *Science*, vol. 342, no. 6156, pp. 344–347, 2013.

[31] D. Liu and T. L. Kelly, "Perovskite solar cells with a planar heterojunction structure prepared using room-temperature solution processing techniques," *Nature Photonics*, vol. 8, pp. 133–138, Feb. 2014.

[32] A. Polman and H. A. Atwater, "Photonic design principles for ultrahigh-efficiency photovoltaics," *Nature Materials*, vol. 11, no. 3, pp. 174–177, 2012.

[33] R. R. Lunt, T. P. Osedach, P. R. Brown, J. A. Rowehl, and V. Bulović, "Practical roadmap and limits to nanostructured photovoltaics," *Advanced Materials*, vol. 23, no. 48, pp. 5712–5727, 2011.

[34] M. C. Orilall and U. Wiesner, "Block copolymer based composition and morphology control in nanostructured hybrid materials for energy conversion and storage: solar cells, batteries, and fuel cells," *Chem. Soc. Rev.*, vol. 40, pp. 520–535, 2011.

[35] E. J. Crossland, M. Kamperman, M. Nedelcu, C. Ducati, U. Wiesner, D.-M. Smilgies, G. E. Toombes, M. A. Hillmyer, S. Ludwigs, U. Steiner, *et al.*, "A bicontinuous double gyroid hybrid solar cell," *Nano Letters*, vol. 9, no. 8, pp. 2807–2812, 2008.

[36] P. Docampo, M. Stefik, S. Guldin, R. Gunning, N. A. Yufa, N. Cai, P. Wang, U. Steiner, U. Wiesner, and H. J. Snaith, "Triblock-terpolymer-directed self-assembly of mesoporous TiO_2: High-performance photoanodes for solid-state dye-sensitized solar cells," *Advanced Energy Materials*, vol. 2, no. 6, pp. 676–682, 2012.

[37] M. Templin, A. Franck, A. Du Chesne, H. Leist, Y. Zhang, R. Ulrich, V. Schädler, and U. Wiesner, "Organically modified aluminosilicate mesostructures from block copolymer phases," *Science*, vol. 278, no. 5344, pp. 1795–1798, 1997.

[38] C. Guo, Y.-H. Lin, M. D. Witman, K. A. Smith, C. Wang, A. Hexemer, J. Strzalka, E. D. Gomez, and R. Verduzco, "Conjugated block copolymer photovoltaics with near 3% efficiency through microphase separation," *Nano Letters*, vol. 13, no. 6, pp. 2957–2963, 2013.

[39] M. Kuemmel, D. Grosso, C. Boissière, B. Smarsly, T. Brezesinski, P. A. Albouy, H. Amenitsch, and C. Sanchez, "Thermally stable nanocrystalline γ-alumina layers with highly ordered 3d mesoporosity," *Angewandte Chemie International Edition*, vol. 44, no. 29, pp. 4589–4592, 2005.

[40] H. Oveisi, X. Jiang, M. Imura, Y. Nemoto, Y. Sakamoto, and Y. Yamauchi, "A mesoporous gamma-alumina film with vertical mesoporosity: The unusual conversion from a $Im\bar{3}m$ mesostructure to vertically oriented gamma-alumina nanowires," *Angewandte Chemie International Edition*, vol. 50, no. 32, pp. 7410–7413, 2011.

[41] X. Jiang, N. Suzuki, B. P. Bastakoti, K. C.-W. Wu, and Y. Yamauchi, "Synthesis of continuous mesoporous alumina films with large-sized cage-type mesopores by using diblock copolymers," *Chemistry–An Asian Journal*, vol. 7, no. 7, pp. 1713–1718, 2012.

[42] S. Guldin, M. Kolle, M. Stefik, R. Langford, D. Eder, U. Wiesner, and U. Steiner, "Tunable mesoporous bragg reflectors based on block-copolymer self-assembly," *Advanced Materials*, vol. 23, no. 32, pp. 3664–3668, 2011.

[43] I. E. Rauda, R. Buonsanti, L. C. Saldarriaga-Lopez, K. Benjauthrit, L. T. Schelhas, M. Stefik, V. Augustyn, J. Ko, B. Dunn, U. Wiesner, *et al.*, "General method for the synthesis of hierarchical nanocrystal-based mesoporous materials," *ACS nano*, vol. 6, no. 7, pp. 6386–6399, 2012.

[44] R. Buonsanti, T. E. Pick, N. Krins, T. J. Richardson, B. A. Helms, and D. J. Milliron, "Assembly of ligand-stripped nanocrystals into precisely controlled mesoporous architectures," *Nano Letters*, vol. 12, no. 7, pp. 3872–3877, 2012.

[45] M. Nedelcu, J. Lee, E. J. Crossland, S. C. Warren, M. C. Orilall, S. Guldin, S. Hüttner, C. Ducati, D. Eder, U. Wiesner, *et al.*, "Block copolymer directed synthesis of mesoporous tio2 for dye-sensitized solar cells," *Soft Matter*, vol. 5, no. 1, pp. 134–139, 2009.

[46] H. Arora, P. Du, K. W. Tan, J. K. Hyun, J. Grazul, H. L. Xin, D. A. Muller, M. O. Thompson, and U. Wiesner, "Block copolymer self-assembly–directed single-crystal homo-and heteroepitaxial nanostructures," *Science*, vol. 330, no. 6001, pp. 214–219, 2010.

[47] S. Guldin, S. Hüttner, P. Tiwana, M. C. Orilall, B. Ülgüt, M. Stefik, P. Docampo, M. Kolle, G. Divitini, C. Ducati, *et al.*, "Improved conductivity in dye-sensitised solar cells through block-copolymer confined tio2 crystallisation," *Energy & Environmental Science*, vol. 4, no. 1, pp. 225–233, 2011.

[48] K. Hur, Y. Francescato, V. Giannini, S. A. Maier, R. G. Hennig, and U. Wiesner, "Three-dimensionally isotropic negative refractive index materials from block copolymer self-assembled chiral gyroid networks," *Angewandte Chemie International Edition*, vol. 50, no. 50, pp. 11985–11989, 2011.

[49] D.-M. Smilgies and D. R. Blasini, "Indexation scheme for oriented molecular thin films studied with grazing-incidence reciprocal-space mapping," *Journal of Applied Crystallography*, vol. 40, no. 4, pp. 716–718, 2007.

[50] A. Hammersley, S. Svensson, M. Hanfland, A. Fitch, and D. Hausermann, "Two-dimensional detector software: from real detector to idealised image or two-theta scan," *International Journal of High Pressure Research*, vol. 14, no. 4-6, pp. 235–248, 1996.

[51] K. Bian, J. J. Choi, A. Kaushik, P. Clancy, D.-M. Smilgies, and T. Hanrath, "Shape-anisotropy driven symmetry transformations in nanocrystal superlattice polymorphs," *ACS nano*, vol. 5, no. 4, pp. 2815–2823, 2011.

[52] T. Baikie, Y. N. Fang, J. M. Kadro, M. Schreyer, F. X. Wei, S. G. Mhaisalkar, M. Graetzel, and T. J. White, "Synthesis and crystal chemistry of the hybrid perovskite $CH_3NH_3PbI_3$ for solid-state sensitised solar cell applications," *Journal of Materials Chemistry A*, vol. 1, no. 18, pp. 5628–5641, 2013.

[53] A. Poglitsch and D. Weber, "Dynamic disorder in methylammoniumtrihalogenoplumbates (II) observed by millimeter-wave spectroscopy," *The Journal of Chemical Physics*, vol. 87, no. 11, 1987.

[54] C. C. Stoumpos, C. D. Malliakas, and M. G. Kanatzidis, "Semiconducting tin and lead iodide perovskites with organic cations: Phase transitions, high mobilities, and near-infrared photoluminescent properties," *Inorganic Chemistry*, vol. 52, no. 15, pp. 9019–9038, 2013.

[55] P. Busch, M. Rauscher, D.-M. Smilgies, D. Posselt, and C. M. Papadakis, "Grazing-incidence small-angle x-ray scattering from thin polymer films with lamellar structures-the scattering cross section in the distorted-wave born approximation," *Journal of applied crystallography*, vol. 39, no. 3, pp. 433–442, 2006.

[56] A. Dualeh, N. Tétreault, T. Moehl, P. Gao, M. K. Nazeeruddin, and M. Grel, "Effect of annealing temperature on film morphology of organicinorganic hybrid pervoskite solid-state solar cells," *Advanced Functional Materials*, vol. 24, no. 21, pp. 3250–3258, 2014.

[57] R. Edwards, R. Gillard, P. Williams, and A. Pollard, "Studies of Secondary Mineral Formation in the PbO-H2O-HCl System," *Mineralogical Magazine*, vol. 56, pp. 53–65, MAR 1992.

[58] J. J. De Yoreo and P. G. Vekilov, "Principles of crystal nucleation and growth," *Reviews in mineralogy and geochemistry*, vol. 54, no. 1, pp. 57–93, 2003.

[59] P. G. Vekilov, "Nucleation," *Crystal growth & design*, vol. 10, no. 12, pp. 5007–5019, 2010.

[60] M. Saliba, K. W. Tan, H. Sai, D. T. Moore, T. Scott, W. Zhang, L. A. Estroff, U. Wiesner, and H. J. Snaith, "The influence of thermal processing protocol upon the crystallization and photovoltaic performance of organic-inorganic lead trihalide perovskites," *The Journal of Physical Chemistry C*, 2014.

[61] K. Liang, D. B. Mitzi, and M. T. Prikas, "Synthesis and Characterization of Organic-Inorganic Perovskite Thin Films Prepared Using a Versatile Two-Step Dipping Technique," *Chemistry of Materials*, vol. 10, pp. 403–411, Jan. 1998.

[62] Q. Chen, H. Zhou, Z. Hong, S. Luo, H.-S. Duan, H.-H. Wang, Y. Liu, G. Li, and Y. Yang, "Planar heterojunction perovskite solar cells via vapor-assisted solution process," *Journal of the American Chemical Society*, vol. 136, no. 2, pp. 622–625, 2014.

[63] J. You, Z. Hong, Y. M. Yang, Q. Chen, M. Cai, T.-B. Song, C.-C. Chen, S. Lu, Y. Liu, H. Zhou, and Y. Yang, "Low-temperature solution-processed perovskite solar cells with high efficiency and flexibility," *ACS Nano*, vol. 8, pp. 1674–1680, Jan. 2014.

[64] O. Malinkiewicz, A. Yella, Y. H. Lee, G. M. Espallargas, M. Graetzel, M. K. Nazeeruddin, and H. J. Bolink, "Perovskite solar cells employing organic charge-transport layers," *Nature Photonics*, vol. 8, pp. 128–132, Feb. 2014.

[65] J. T.-W. Wang, J. M. Ball, E. M. Barea, A. Abate, J. A. Alexander-Webber, J. Huang, M. Saliba, I. Mora-Sero, J. Bisquert, H. J. Snaith, and R. J. Nicholas, "Low-temperature processed electron collection layers of Graphene/TiO_2 nanocomposites in thin film perovskite solar cells," *Nano Letters*, vol. 14, pp. 724–730, Dec. 2013.

[66] K. Wojciechowski, M. Saliba, T. Leijtens, A. Abate, and H. J. Snaith, "Sub-150C processed meso-superstructured perovskite solar cells with enhanced efficiency," *Energy & Environmental Science*, vol. 7, no. 3, pp. 1142–1147, 2014.

[67] C. Wehrenfennig, G. E. Eperon, M. B. Johnston, H. J. Snaith, and L. M. Herz, "High charge carrier mobilities and lifetimes in organolead trihalide perovskites," *Advanced Materials*, vol. 26, no. 10, pp. 1584–1589, 2014.

On-going Projects and Conclusion

CHAPTER 8

On-going Projects

This chapter discusses on-going work including silica scaffolds which can be used for perovskite solar cells instead of titania or alumina mesolayers. Additonally, first results for 2D layered organic-inorganic perovskites are presented. The 2D materials are synthesized and used to demonstrate working solar cells for the first time to my knowledge. These findings have the potential to open the entire lead halide perovskite family (different only in the organic component) for further photovoltaic research offering an interesting direction for future work.

8.1 SiO_2 Scaffold

The main mesoporous scaffolds for perovskite solar cell are comprised of Al_2O_3 and TiO_2 NPs. Increasing the amount of possible materials is of general interest as each material has different properties providing more flexibility for experimental designs. For example, in previous chapters core-shell NPs were used to enhance photocurrent in perovskite solar cells. The dielectric shell material, which was either TiO_2 or SiO_2, was necessary for chemical protection and to prevent the core from acting as a recombination centre for free charges. In order to determine that the metallic core was necessary for the enhancement, an additional experiment utilizing a pure dielectric NP (TiO_2 or SiO_2) of the size of the core-shell structure was needed. This complication could be avoided if the mesoporous scaffold was made of NPs of the same material (and ideally size) as the dielectric shell. In the case of a dielectric TiO_2 shell this implies a (charge transporting) titania scaffold which, however, is of disadvantage for high efficiency devices with the mixed halide perovskite [1, 2]. For SiO_2, which is a very typical shell material for metallic cores, the scaffold would have to be comprised of insulating SiO_2 NPs. However, there are no reports (to my knowledge) on the feasibility of SiO_2 as a mesoporous layer for perovskite solar cells.

In an initial study, SiO_2 NPs are tested as a mesoporous scaffold material. The ~20 nm diameter SiO_2 NPs were provided by Jin Zhang and synthesised according to the procedure in Appendix A. The devices are fabricated according to Chapter 2.2 where the alumina mesolayer is replaced by a silica mesolayer of various thicknesses deposited via spin coating a solution of the SiO_2 NPs (dissolved in EtOH) on a substrate.

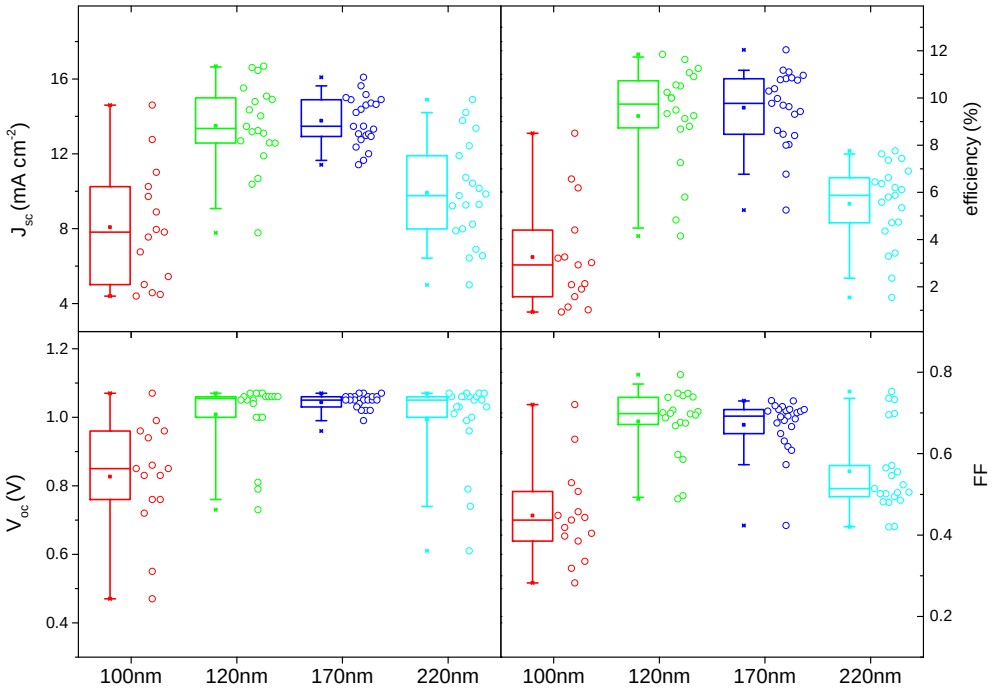

Fig. 8.1 Device performance parameters for SiO_2 scaffolds with thicknesses from 100-220 nm.

Figure 8.1 presents the solar cell performance parameter for perovskite solar cells with 100, 120, 170, and 220 nm thick silica scaffolds. There is an optimum between 120 and 150 nm SiO_2 thickness with efficiencies up to ~12%. These performances are comparable to the optimized Al_2O_3 scaffold [3] and thus proofing the principle of silica scaffolds working in high performance perovskite solar cells.

Then, Ag@SiO_2 (6-7 nm core, 6-7 nm shell) were embedded in the SiO_2 scaffold by mixing the NPs with the scaffold solution. The Ag@SiO_2 NPs were provided by Yao Sun of Cornell University.

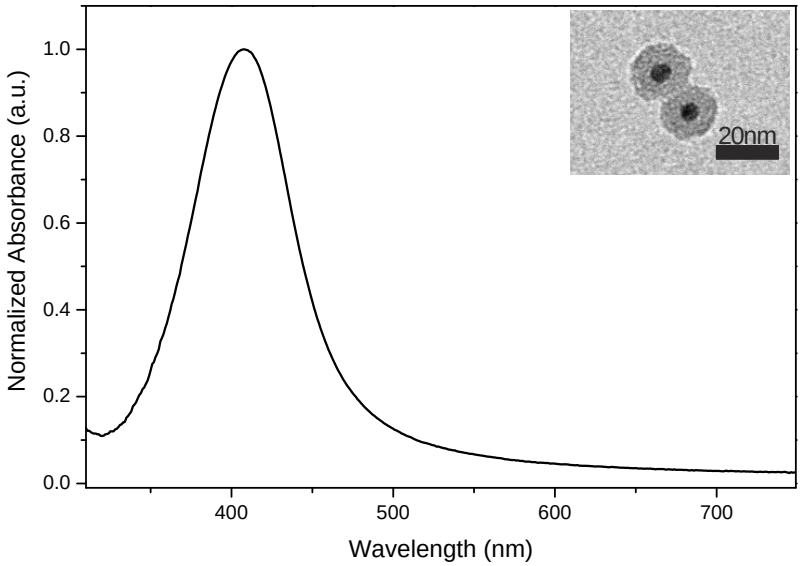

Fig. 8.2 UV-vis of Ag@SiO_2 (6-7 nm core, 6-7 nm shell) NPs with an inset TEM image. The TEM image was taken by Yao Sun of Cornell University.

Figure 8.2 shows the UV-vis spectrum of the used Ag@SiO_2 NPs with a plasmonic peak at ~400 nm and a corresponding TEM inset. Unfortunately, there was no photocurrent improvement after adding the Ag@SiO_2. This may be attributed to the relatively thick silica shell of 6-7 nm which is comparable to the size of the metallic core and thus screens out a significant proportion of the electromagnetic near-field. For future research a thinner SiO_2 (~2-3 nm) shell should be used which, however, is hard to synthesize for such small cores. Replacing successfully the alumina with a silica scaffold provides more flexibility for future research and is an encouraging finding.

8.2 2D Perovskites

The main perovskite investigated until now was methylammonium lead triiodide which is a 3D structure of interconnected metallic planes. The most commonly used organic components sufficiently small to fit into a 3D $APbI_3$ lattice are methylamine (MA) and the slightly larger formamidinium (FA) [4–7]. Introducing larger organic chains is incompatible with

the tolerance factor for an ideal cubic structure and hence a 2D A_2PbI_4 perovskite is formed where the metallic planes (series of corner-sharing $[PbI_6]^{4-}$ octahedra) are sandwiched between organic layers (see Figure 8.3).

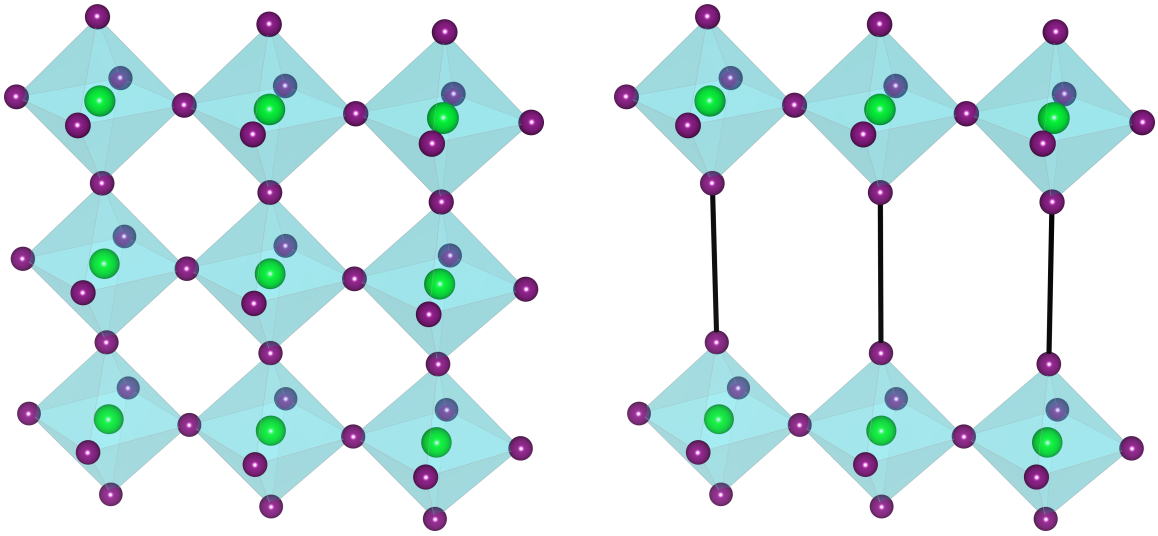

(a) 3D **(b)** 2D

Fig. 8.3 (a) 1 layer of a 3D perovskite structure with interconnected metallic $[PbI_6]^{4-}$ octahedra. The spaces between the octahedra (not shown) are filled with sufficiently small cations, e.g. $CH_3NH_3^+$, $HC(NH_2)_2^+$ or Cs^+. (b) Corresponding 2D perovskites where the metallic layers are connected by organic chains illustrated by vertically connecting lines.

Extensive research was conducted regarding the band gap, absorption, and photoluminescence with respect to the length and type of the organic component [5, 8, 9]. Exciton binding energies, for examples, can be varied from 50-600 meV [10, 11]. In general, excitons confined to a 2D system have larger binding energy than in a 3D system due to the decreased kinetic energy. This effect is amplified in a layered perovskite system where the metallic plane lies between organic layers of a relatively low dielectric constant resulting in an increased Coulomb interaction between electrons and holes (known as the dielectric confinement effect) [10, 12]. Excitons with lower binding energies are more likely to get separated into free electrons and holes by thermal ionization. This is one reason why 3D perovskites have performed so well in photovoltaic applications as the exciton binding energy of ~50 meV for MA-PbI_3 [13] is among the lowest in the respective perovskite family and comparable to room temperature phonons (~25 meV) [14].

However, the higher exciton binding energy for 2D perovskite does not necessarily rule them out for photovoltaic application as demonstrated by Im et al. in 2012 featuring a 2D perovskite solar cell with 2.4% efficiency based on the longer chained ethylamine (EA) in a liquid DSSC architecture [15]. However, this is one of the few examples showing explicitly photovoltaic viability which leaves the large family of 2D perovskites open for further research. This is of particular interest because of the vast array of already established 2D perovskite synthesis methods, depositions techniques, and theoretical models [5, 10, 11].

For example, 2D perovskites come in different colours which is of aesthetic interest for building integrated photovoltaics (BIPV). The band gap can also be tuned which is very important for tandem devices where the top cell needs to have a complementary band gap to the bottom cell in order to convert more incoming light into electricity.

Moreover, this offers the opportunity to study fundamental effects of high binding energy excitons at room temperature. The exact charge separation mechanism, charge carrier recombination, and charge transport may offer valuable insight for further optimization throughout the entire perovskite family. Also, 2D and 3D perovskite solar cell advances are closely related to advances for LED [16, 17] and LASER [18, 19] applications as they show remarkable luminescence behaviour [20].

Additionally, it has been observed that MA-PbI_3 reacts very sensitively to the precursor solvent, thermal annealing time, or annealing environment; and deposition methods such as single-step spin-coating, sequential solution processing, thermal evaporation, chemical vapour deposition, or combined solution-vapour-processing [21–26]. Thus, different precursor components for 2D perovskites provide more flexibility in solar cell fabrication. In single-step spin coating this can make solvents other than DMF or DMSO available opening new possibilities in multilayered architectures which are otherwise sensitive to such solvents. Another benefit is the changed film wettability, film coverage, and film formation speed permitting for more tunability and optimization. For chemical vapour deposition (CVD) or thermal evaporation the vapour rate is highly dependent on the melting point of the precursor components and thus more flexibility is gained by exploring the different perovskite materials.

As a next step, in order to narrow down the myriad of possible organic components, some of the most common amines used for lead iodide perovskites are presented in Figure 8.4. The longer chained alkylamines fit into a 2D perovskite structure of the generic form $(C_nH_{2n+1}NH_3)_2PbI_4$ with n = 2, 3, ... (abbreviated as C_nPbI_4 in the following). Indeed, the presented molecules have all been shown to form a layered perovskite: pentylamine (PeA) [27, 28], butylamine (BA) [29–31], propylamine (PA) [32], and ethylamine (EA) [15]. The corresponding perovskites for MA and FA are the 3D MA-PbI_3 and FA-PbI_3. Also, non-alkylamines like phenethylamine (PhE) [33] or guanidinium (GA) [34–37] can form the 2D $(PhE)_2PbI_4$ or $(GA)_2PbI_4$ perovskite. Mixtures of different organic components can also be used like MA and PhE forming $MA(PhE)_2Pb_2I_7$ [11, 38]. In the following, first experiments are shown on: $(PhE)_2PbI_4$, $MA(PhE)_2Pb_2I_7$, and $(GA)_2PbI_4$. The last two perovskites are used for solar cell fabrication and result for the first time (to my knowledge) in functioning solar cells.

Amine	3D structure	2D structure	Perovskite
phenethylamine (PhE)	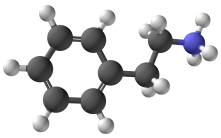	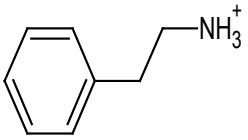	$(PhE)_2PbI_4$
pentylamine (PeA)	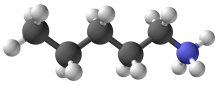		$(PeA)_2PbI_4$
butylamine (BA)	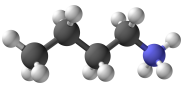	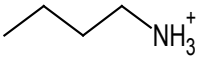	$(BA)_2PbI_4$
propylamine (PA)	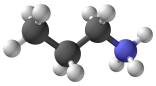	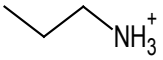	$(PA)_2PbI_4$
ethylamine (EA)	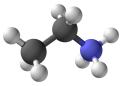	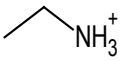	$(EA)_2PbI_4$
methylamine (MA)			$MA\text{-}PbI_3$
formamidinium (FA)	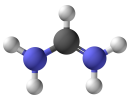	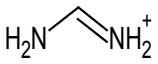	$FA\text{-}PbI_3$
guanidinium (GA)	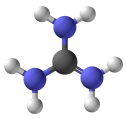	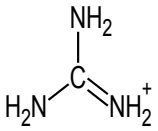	$(GA)_2PbI_4$

Fig. 8.4 Different organic amine groups in perovskite structures where Pb occupies the central and I the face centred position. (first column) amines. (second and third column) 3D and 2D structure of the corresponding amine cation. (Fourth column) Observed perovskite structure. Only formamidinium and methylamine results in a 3D structure where all the metallic planes are interconnected.

8.2.1 Experimental

$(PhE)_2PbI_4$ was synthesized by dissolving stoichiometric ratios of phenethylammonium iodide (PhE-I) and PbI_2 (Sigma-Aldrich) in N,N-dimethylformamide (DMF) for a 40 wt% solution.

PhE-I was synthesized analogously to methylammonium iodide (MA-I) which is outlined in Chapter 2.2. A perovskite film thickness of ~400 nm on a planar substrate was accomplished by spin coating at 2000 rpm for 45 s followed by heating at 100°C for 5 min.

$MA(PhE)_2Pb_2I_7$ was synthesized by dissolving different molar ratios of MA-I, PhE-I and PbI_2 (Sigma-Aldrich) in DMF for a 40 wt% solution. Devices were fabricated as outlined in Chapter 2.2. In short, a titania compact layer was deposited on FTO patterned glass. For devices requiring a mesostructure, TiO_2 (Dyesol) paste was spin coated resulting in thicknesses from 100-500 nm (tuned by appropriate ethanol dilution) followed by a $TiCl_4$ treatment.

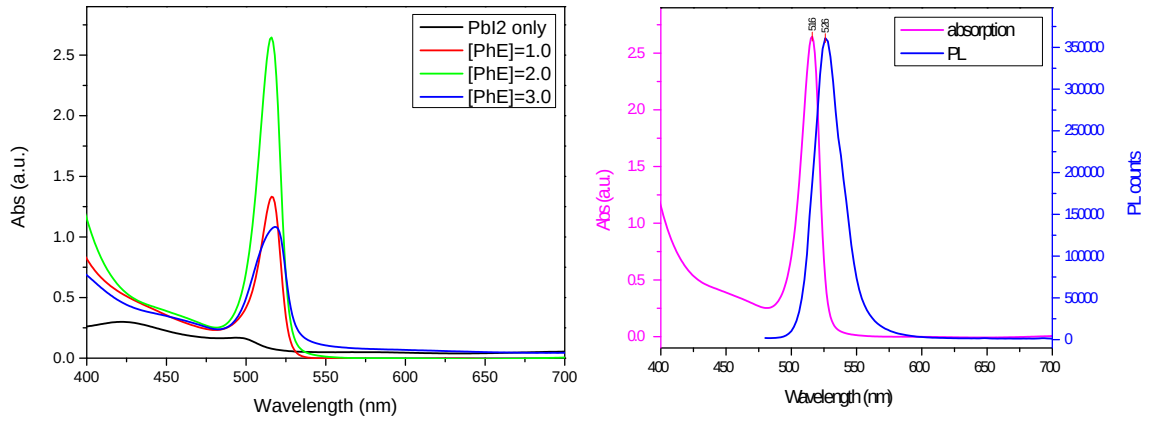

(a) UV-vis **(b)** PL

Fig. 8.5 (a) UV-vis (b) PL of a $(PhE)_2PbI_4$ film ([PhE]=2.0).

The remaining procedure was conducted in a nitrogen filled glove box. A 40 wt% perovskite film thickness of 400-500 nm on a planar substrate was accomplished by spin coating at 2000 rpm for 45 s followed by heating at 100°C for 5-40 min and a quick heating step at 130°C for 1 min.

Spiro-OMeTAD was deposited by spin coating at 2000 rpm for 45 s (in a glove box). The typical concentration was 80 mM in CB with an added 30 mol% Li-TFSI (predissolved in ACN) and 80 mol% tBP.

8.2.2 Results and Discussion

$(PhE)_2PbI_4$

The starting point for this investigation was the synthesis of a $(PhE)_2PbI_4$ precursor by mixing PhE-I and PbI_2 in DMF such that a 40 wt% solution is maintained. Yellow coloured perovskite films of ~400 nm were formed in the glove box via spin coating and subsequent annealing at 100°C for 5 min. Figure 8.5a shows the UV-vis absorption for a series of different molar ratios of [PhE-I]:[PbI_2] for 3:1, denoted as [PhE]=3.0, 2:1 ([PhE]=2.0), and 1:1 ([PhE]=1.0). The strongest signal is from the stoichiometric ratio ([PhE]=2.0) with a distinct peak at 516 nm, and there is also a 10 nm Stokes shift, as concluded from Figure 8.5b where the PL spectrum has a peak at 526 nm. This is in good agreement with literature [11, 39] and thus stoichiometric ratio is kept for future experiments. In order to confirm the successful formation of the $(PhE)_2PbI_4$ perovskite film, SEM and XRD data is shown in Figure 8.6. The SEM image reveals smooth film formation with a high surface coverage. The XRD peaks were assigned to an orthorhombic unit cell with $a = 8.895(4)$ Å, $b = 8.915(8)$ Å, and $c = 32.654(6)$ Å. The large unit cell is consistent with the long organic phenethylamine molecule which is also observed in literature (with almost precisely the same peak positions) [27, 39, 40].

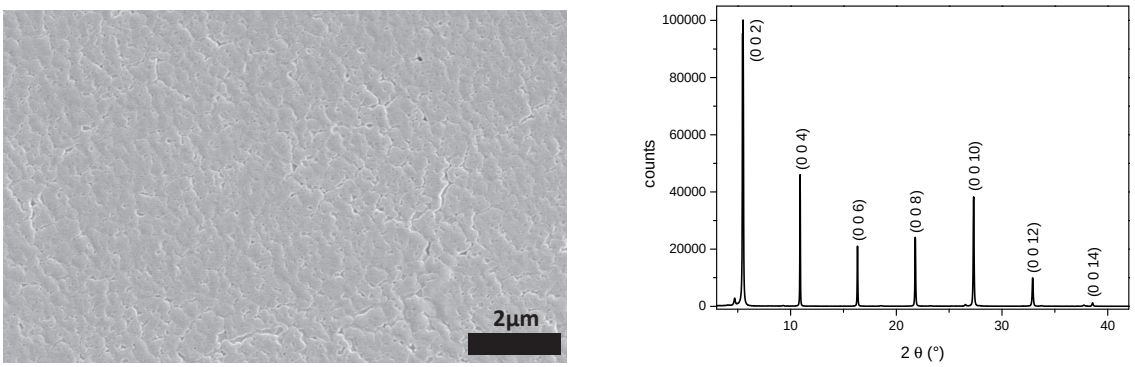

(a) SEM **(b)** XRD

Fig. 8.6 (a) SEM and (b) XRD of a $(PhE)_2PbI_4$ film. The peaks are assigned to an orthorhombic lattice.

In a next step, full solar cells were fabricated which, unfortunately, did not work even with the assistance of a charge transporting titania mesolayer.

This could be due to the relatively high exciton binding energy of 220 meV in this system which might inhibit good charge separation [11]. However, the lack of even poorly working devices could be an indication to revisit this perovskite compound with a more refined device fabrication routine.

Still, the successful perovskite synthesis is an encouraging first result and the acquired techniques are the basis for the following work on $MA(PhE)_2Pb_2I_7$.

$MA(PhE)_2Pb_2I_7$

The same procedure as in the case of $(PhE)_2PbI_4$ was followed. Again, the overall concentration was kept at 40 wt%. This time MA-I was added to a 1:1 molar solution of PhE-I and PbI_2 in order to prepare 5 different concentrations: [0:2:2] with [MA-I:PhE-I:PbI_2] abbreviated as [MA]=0, 0.5:2:2 ([MA]=0.5), 1.0:2:2 ([MA]=1.0), 2.0:2:2 ([MA]=2.0), and 3.0:2:2 ([MA]=3.0).

Red perovskite films of ~400 nm on a planar substrate were formed by spin coating at 2000 rpm for 45 s followed by annealing at 100°C for 20 min and a quick heating step at 130°C for 1 min. The SEM image in Figure 8.7a shows films with high surface coverage. Additionally, the UV-vis data in Figure 8.7b shows the [MA]=0-3.0 series. For [MA]=0 the absorption spectrum results in the $(PhE)_2PbI_4$ from the previous section (with a peak at 516 nm). With the addition of MA-I the initial peak red-shifts slightly and a second peak at 564 nm appears which is the signature peak for $MA(PhE)_2Pb_2I_7$ [11]. Interestingly, the 564 nm was the most pronounced for [MA=2.0]. The non-stoichiometric ratio with an excess of MA-I has been observed before to be necessary for formation in similar compounds [38, 41]. One reason for this could be the higher solubility and lower melting point of MA-I compared to PhE-I which changes the thin-film formation dynamics. The subsequent annealing procedure then needs excess amounts of MA-I which otherwise is gone before the film is formed. Thus, for the following devices a 40 wt% perovskite precursor with [MA]=2.0 ratio was used.

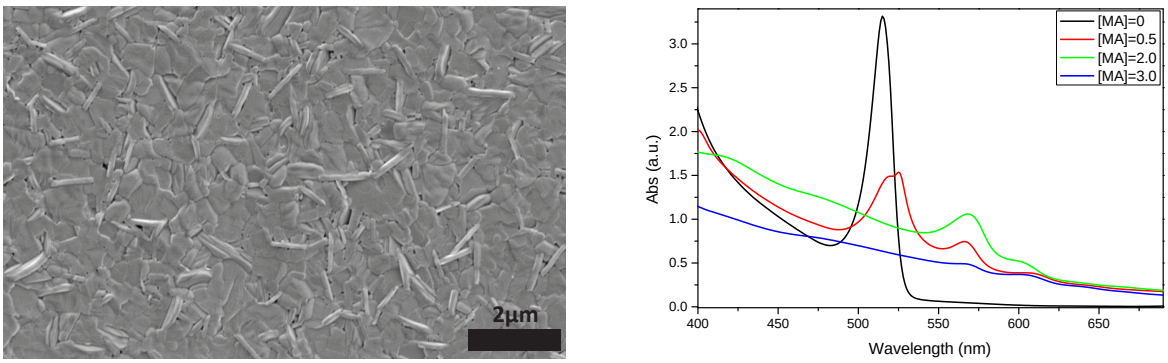

(a) SEM **(b)** XRD

Fig. 8.7 (a) SEM and (b) UV-vis for perovskite films with different MA-I concentrations. [MA]=0 is short for the molar ratio of [0:2:2] between [MA-I:PhE-I:PbI_2]. [MA]=0.5-3.0 is the respective series for an increase in MA-I concentration.

Figure 8.8a shows device data for $MA(PhE)_2Pb_2I_7$ perovskite films with (and without) a titania mesostructure (prepared in the same way as for DSSCs) of 0 nm (planar), 100 nm, 200 nm and 500 nm thickness. Remarkably, for the first time, working solar cells for each thickness can be shown which is further highlighted with representative JV curves in Figure 8.8c. Also, the EQE in Figure 8.8d for the best performing 2D perovskite device has an onset at around 570 nm following the UV-vis data. From the device data it is clear that the support from the conducting mesostructure is crucial as planar devices are at PCEs below 0.2% which changes drastically for a 100 nm mesolayer thickness where a maximum short circuit current of up to 4 mA/cm^2 is observed. It is noteworthy that the fill factor of up to 0.8 is comparable to the 3D perovskite devices. As the titania layer gets thicker, the device performance drops. This trend is also observed for the 3D perovskite material where thicker mesolayers were counterproductive due to an increased pathlength during charge transport which can induce higher charge recombination [3].

As a next step, the annealing protocol is optimized with a fixed titania mesolayer thickness of 100 nm. The annealing protocol has 2 steps. At first all devices are held at 100°C for 5, 10, 20, 30, and 40 min followed by a flash annealing step at 130°C for 1 min. Figure 8.8b reveals an optimum in J_{sc} and V_{oc} for the 20 min annealing time. The trend is not followed for the average fill factor, albeit the maximum fill factor for the 20 min procedure is still comparable to average values of the 40 min anneal time. Also, the flash annealing step is dropped for the "5min*" devices showing worse performance on average for J_{sc} and V_{oc} compared to the "5min" devices. However, this trend is not followed by the fill factor which drops considerably from 0.6 to 0.4. For further optimization, the 20 min anneal procedure is suggested as a starting point.

At this point, there are two key messages. First, the successful proof of principle that this 2D perovskite can produce working solar cells which was not observed previously. Second, the preliminary data is an important step for further experiments. Especially

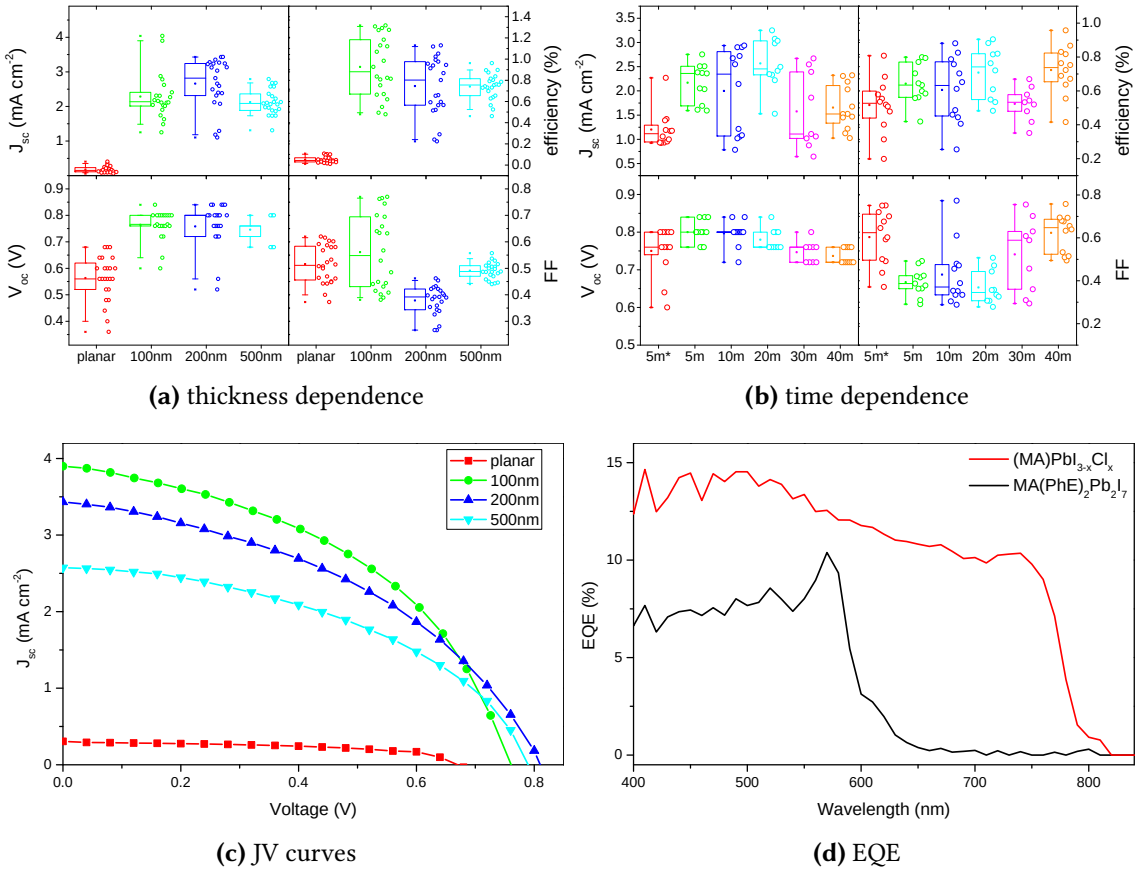

(a) thickness dependence **(b)** time dependence

(c) JV curves **(d)** EQE

Fig. 8.8 (a) Mesoporous TiO_2 thickness dependence of $MA(PhE)_2Pb_2I_7$ devices. (b) Annealing time dependence with a fixed mesoporous thickness of 100 nm. All devices are annealed at 100°C for 5-40 min followed by a quick heating step at 130°C for 1 min. Only "5 min*" is without the flash annealing step. (c) Representative JV curves for (b). (d) EQE for MA-$PbI_{3-x}Cl_x$ (red) and $MA(PhE)_2Pb_2I_7$ on a 100 nm thick titania mesostructure (black).

the annealing protocol may have great potential for improvement. The longer chained phenethylamine might require a higher anneal temperature for optimal devices as in the case of the formamidinium [42]. Also, a systematic investigation of the flash annealing step could help to optimize the film formation as it has for the 3D structures in the previous two chapters.

$(GA)_2PbI_4$

The same procedure as mentioned above was followed. The overall concentration was kept at 40wt%. GA-I was added in a 2:1 molar ratio to PbI_2 in DMF. A yellow ~400nm perovskite film formed after spin coating the precursor at 2000rpm for 45s followed by annealing at 150°C for 10min. It should be noted that the reference followed in this work [34] claims the formation of the 3D perovskite by using the appropriate molar ratio. However, using a 1:1 molar ratio yielded no significantly different results which could be due a change in synthesis route as an aqueous solution of lead acetate and GA-I was used in the previous work.

For the initial device making a 40wt% precursor solution was used on planar devices which, however, did not result in working devices. Figure 8.9a shows an SEM image which again has good surface coverage. In a next step, the precursor solution was diluted for a concentration dependence from 5-40%. The planar devices can be seen in Figure 8.9b. The only working device results were for 5 and 10% precursor concentration. Possibly, the thinner films form the perovskite phase more quickly during the 10min anneal step and the thicker films contain more unreacted precursor components. This may also affect film formation which might be more beneficial for the thinner films in general. At this stage, more experiments are needed to draw clear conclusions. Especially XRD data for the different thicknesses could help determining if there still is a precursor state. Also, using a mesoporous titania layer is a logical next step as already assisted device performance for the previous perovskite absorber. Additionally, the annealing protocol needs separate optimization.

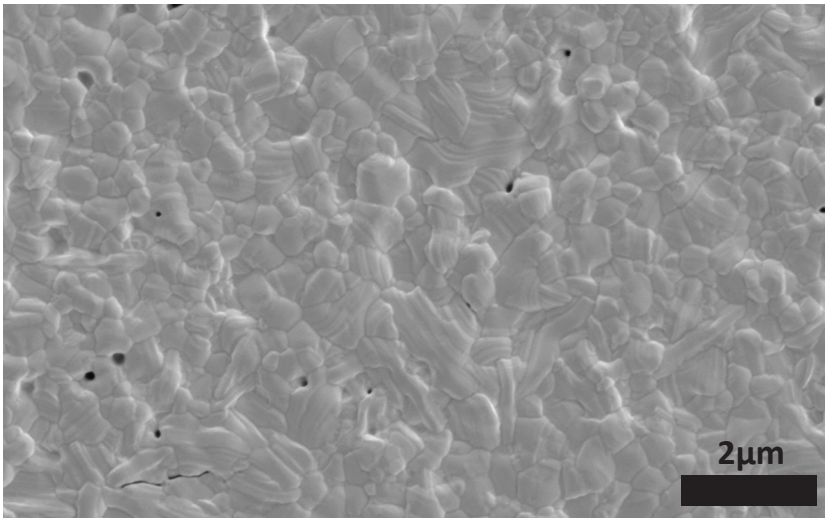

(a) SEM

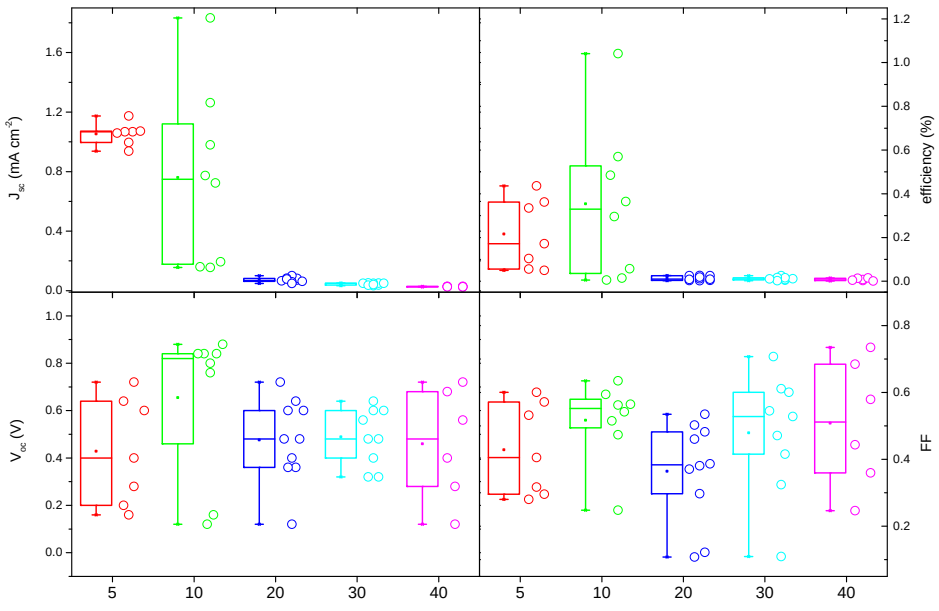

(b) device parameters

Fig. 8.9 (a) SEM image and (b) thickness dependence of $(GA)_2PbI_4$

8.2.3 Summary

The aim of this chapter was to demonstrate that 2D perovskite absorbers are suitable candidates for solar cells. This is motivated by the desire to find differently coloured perovskites for aesthetic reasons, complimentary band gaps for tandem solar cells, and changing the precursor's chemical components or solvent system in order to tap into the versatile manufacturing methodology for the 2D perovskite families.

The precursor materials tested were phenethylamine and a mixture of methylamine/phenethylamine which each replaced the methylamine group in the 3D $CH_3NH_3PbI_3$ to form a 2D A_2PbI_4 perovskite.

In a series of preliminary experiments the successful formation of yellow $(PhE)_2PbI_4$ was demonstrated but unfortunately no working solar cells were fabricated.

Then, based on the previous synthesis techniques, the red $MA(PhE)_2Pb_2I_7$ perovskite was synthesized. Solar cells with up to 4 mA/cm^2 short circuit current were manufactured in a DSSC architecture with a mesoporous titania layer of 100 nm.

Systematic follow-up experiments for further improvements are needed including XRD characterisation, annealing protocol optimization, mesoporous thickness dependence, and general device making.

The main message from these initial results is the proof of principle that 2D perovskites can operate as solar cells. This is an important stepping stone for future experiments for the entire perovskite family which is of major research interest.

CHAPTER 9

Conclusion

For many years, it has been a quasi-paradigm that solar cells are either expensive and efficient, or inexpensive and inefficient. Perovskite solar cells have broken this trend in a spectacular fashion with efficiencies already exceeding 15% after a remarkably short time. Currently, a whole new body of research is being built at dazzling speed with an increase in publication frequency from monthly at the beginning of this thesis to a weekly figure.

This thesis contributes to the understanding and improvement of perovskite photovoltaics by focusing on incorporating plasmonic nanostructures into the photoactive area and on analyzing thin-film formation under different annealing parameters.

In a first step the multiple multipole method (MMP) was introduced, i.e. a simulation technique to solve the Maxwell equations for plasmonic core-shell (metal-dielectric) nanostructures. This was used to simulate optical near fields and calculate absorption, scattering, and extinction cross sections.

MMP facilitates a deeper understanding for plasmonic effects of metallic nanostructures at small length scales (in the nm-range) where surface properties become more and more important. Under such conditions the surface electron gas can be collectively excited by incoming light resulting in new optical phenomena tunable by the geometry, materials used, and the surrounding medium. In this thesis, especially gold and silver nanoparticles with thin dielectric shells of silica and titania were analyzed as these systems could be integrated with relative ease into solar cells. Calculations revealed that increased core sizes resulted in a red-shifted optical spectrum which was explained by the excitation not being uniform across the whole particle anymore. A red-shift was also observed after adding the dielectric shell or increasing the medium's dielectric constant. The simulations were used to assess the synthesis quality of gold or silver nanoparticles by comparison to UV-vis measurements.

This was also used to demonstrate how the refractive index of an unknown solution can be determined by matching the calculated to the measured resonances (by adjusting the refractive index). Moreover, the plasmonic near-field enhancement in a realistic DSSC environment was simulated with special emphasis on the absorption and scattering properties of gold, silver, gold-silica, and silver-titania NPs. It was shown that silver had a blue-shifted spectrum compared to gold and started scattering at smaller core sizes than gold.

From this experience, NPs were integrated into perovskite solar cells. At first, this was done for gold-silica NPs which were mixed into the mesoporous alumina layer. Introducing a dielectric shell was crucial because it contributed to chemical stability and prevented the bare gold cores from acting as charge carrier recombination centres in the photoactive layer. It was discovered that at optimized concentrations, the devices with gold NPs exhibited an increased short-circuit photocurrent with an average PCE of 9.5% as compared to the control devices with an average PCE of 8.4%. However, the light absorption was not significantly increased. Through a time-resolved and steady state temperature dependent photoluminescence study, the origin of the improved short-circuit photocurrent was attributed to a reduced exciton binding energy, and hence enhanced generation of free charge carriers. This represents a new enhancement mechanism for metal nanoparticles incorporated into photovoltaics, and may prove to be exceptionally useful for perovskite solar cells where the exciton binding energy is in the order of 100 meV.

Motivated by this work, silver-titania NPs with a higher quality factor and different optical properties than gold were integrated into perovskite solar cells. This was a more challenging task because the silver NPs melted if processed with the same high temperature steps as the aforementioned gold-silica NPs. Hence, a new low-temperature fabrication procedure (<150°C) was employed which would not melt the Ag NPs. With this the perovskite solar cell efficiency increased from 11.4% to 13.7% for the optimized silver NP concentration. This opens the door to new applications which were previously inaccessible because of the high temperature conditions. In particular, readily available non-spherical nanoparticles which are notoriously hard to stabilize against temperature-induced shape change can now be processed and used with relative ease. Thus, a very promising route for future enhancements is mapped out.

The other main focus of this thesis was perovskite thin-film formation. First, using grazing incidence wide-angle X-ray scattering (GIWAXS), it was discovered that solution-processed perovskite films underwent a distinct crystalline precursor state at 80°C which has previously not been described. Furthermore, it was demonstrated that perovskite film coverage improved greatly with a well-controlled temperature ramp which was also beneficial for solar cell performance. This emphasizes the critical dependence of device performance on the exact annealing protocols.

Second, motivated by the previous work, film morphology control was demonstrated in perovskite thin films by tuning the thermal annealing conditions after a slow ramp.

Using GIWAXS and scanning electron microscopy, it was found that a short rapid annealing at 130°C promoted the growth of highly uniform micron-sized textured perovskite domains, while a longer dwell at 100°C resulted in 100-1000 nm polycrystalline perovskite domains. The rapid 130°C and longer 100°C thermal annealing resulted in very different perovskite solar cell performances with the meso-superstructured and planar heterojunction device architectures. In general, the 100°C annealed MSSC devices performed better than 130°C annealed samples attributed to the higher perovskite surface coverage. The planar perovskite devices outperformed the MSSC mesostructured counterparts mainly due to higher fill factor and short circuit currents, obtained from >95% perovskite surface coverage. Moreover, the 130°C flash thermal annealing resulted in planar heterojunction solar cells with highly textured perovskite domains and power conversion efficiency improvement from 9.9 to 10.7% compared to the 100°C annealed planar devices. The improvement was postulated to arise from reduced losses at the grain boundaries. The best performing planar heterojunction perovskite solar cells achieved a high power conversion efficiency of 13.5%. Again, this study highlights the importance of simultaneously controlling both the macroscopic morphology and the crystalline domain size.

In the last part of this thesis, future work with 2D perovskite absorbers was discussed for potential viability as solar cells. This is motivated by the desire to find differently coloured perovskites for aesthetic reasons, complimentary band gaps for tandem solar cells, and changing the precursor's chemical components or solvent in order to tap into the versatile manufacturing methodology for the 2D perovskite families. As an initial example, phenethylamine was used to form the red 2D $(MA)(PhE)_2Pb_2I_7$ perovskite. In a first demonstration working solar cells with up to 4 mA/cm^2 short circuit current in a DSSC architecture and a mesoporous titania layer of 100 nm were shown.

The main message from these initial results is the proof of principle that 2D perovskites can operate as solar cells. This is an important stepping stone for future experiments for the entire perovskite family which is of major research interest.

References

[1] M. M. Lee, J. Teuscher, T. Miyasaka, T. N. Murakami, and H. J. Snaith, "Efficient Hybrid Solar Cells Based on Meso-Superstructured Organometal Halide Perovskites," *Science*, vol. 338, pp. 643–647, Nov. 2012.

[2] W. Zhang, M. Saliba, S. D. Stranks, Y. Sun, X. Shi, U. Wiesner, and H. J. Snaith, "Enhancement of perovskite-based solar cells employing core-shell metal nanoparticles," *Nano Letters*, vol. 13, no. 9, pp. 4505–10, 2013. 23947387.

[3] J. M. Ball, M. M. Lee, A. Hey, and H. J. Snaith, "Low-temperature processed meso-superstructured to thin-film perovskite solar cells," *Energy & Environmental Science*, vol. 6, no. 6, pp. 1739–1743, 2013.

[4] D. Weber, "$CH_3NH_3PbX_3$, A Pb(II)-System with Cubic Perovskite Structure," *Zeitschrift fur Naturforschung Section B-A Journal of Chemical Sciences*, vol. 33, no. 12, pp. 1443–1445, 1978.

[5] D. B. Mitzi, *Synthesis, Structure, and Properties of Organic-Inorganic Perovskites and Related Materials*, pp. 1–121. John Wiley & Sons, Inc., 2007.

[6] T. M. Koh, K. Fu, Y. Fang, S. Chen, T. C. Sum, N. Mathews, S. G. Mhaisalkar, P. P. Boix, and T. Baikie, "Formamidinium-containing metal-halide: An alternative material for near-ir absorption perovskite solar cells," *The Journal of Physical Chemistry C*, vol. 0, no. 0, p. null, 0.

[7] G. E. Eperon, S. D. Stranks, C. Menelaou, M. B. Johnston, L. M. Herz, and H. J. Snaith, "Formamidinium lead trihalide: a broadly tunable perovskite for efficient planar heterojunction solar cells," *Energy Environ. Sci.*, vol. 7, pp. 982–988, 2014.

[8] T. Ishihara, J. Takahashi, and T. Goto, "Exciton state in two-dimensional perovskite semiconductor $(C_{10}H_{21}NH_3)_2PbI_4$," *Solid State Communications*, vol. 69, no. 9, pp. 933 – 936, 1989.

[9] G. C. Papavassiliou, "Synthetic Three-and Lower-Dimensional Semiconductors Based on Inorganic Units," *Molecular Crystals and Liquid Crystals Science and Technology. Section A. Molecular Crystals and Liquid Crystals*, vol. 286, pp. 231–238, July 1996.

[10] T. Ogawa and Y. Kanemitsu, *Optical properties of low-dimensional materials*, vol. 1. World Scientific, 1995.

[11] G. Papavassiliou, "Three- and low-dimensional inorganic semiconductors," *Progress in Solid State Chemistry*, vol. 25, no. 3–4, pp. 125 – 270, 1997.

[12] E. Hanamura, N. Nagaosa, M. Kumagai, and T. Takagahara, "Quantum wells with enhanced exciton effects and optical non-linearity," *Materials Science and Engineering: B*, vol. 1, no. 3–4, pp. 255 – 258, 1988.

[13] K. Tanaka, T. Takahashi, T. Ban, T. Kondo, K. Uchida, and N. Miura, "Comparative study on the excitons in lead-halide-based perovskite-type crystals $CH_3NH_3PbBr_3$ $CH_3NH_3PbI_3$," *Solid State Communications*, vol. 127, pp. 619–623, Sept. 2003.

[14] V. D'Innocenzo, G. Grancini, M. J. P. Alcocer, A. R. S. Kandada, S. D. Stranks, M. M. Lee, G. Lanzani, H. J. Snaith, and A. Petrozza, "Excitons versus free charges in organo-lead tri-halide perovskites," *Nature Communications*, vol. 5, pp. –, Apr. 2014.

[15] J.-H. Im, J. Chung, S.-J. Kim, and N.-G. Park, "Synthesis, structure, and photovoltaic property of a nanocrystalline 2h perovskite-type novel sensitizer $(CH_3CH_2NH_3)PbI_3$," *Nanoscale research letters*, vol. 7, no. 1, pp. 1–7, 2012.

[16] K. Chondroudis and D. B. Mitzi, "Electroluminescence from an organic-inorganic perovskite incorporating a quaterthiophene dye within lead halide perovskite layers," *Chemistry of Materials*, vol. 11, no. 11, pp. 3028–3030, 1999.

[17] D. B. Mitzi, K. Chondroudis, and C. R. Kagan, "Organic-inorganic electronics," *IBM journal of research and development*, vol. 45, no. 1, pp. 29–45, 2001.

[18] G. Xing, N. Mathews, S. S. Lim, N. Yantara, X. Liu, D. Sabba, M. Grätzel, S. Mhaisalkar, and T. C. Sum, "Low-temperature solution-processed wavelength-tunable perovskites for lasing," *Nature Materials*, vol. 13, no. 5, pp. 476–480, 2014.

[19] F. Deschler, M. Price, S. Pathak, L. E. Klintberg, D.-D. Jarausch, R. Higler, S. Hüttner, T. Leijtens, S. D. Stranks, H. J. Snaith, M. Atatüre, R. T. Phillips, and R. H. Friend, "High photoluminescence efficiency and optically pumped lasing in solution-processed mixed halide perovskite semiconductors," *The Journal of Physical Chemistry Letters*, vol. 5, no. 8, pp. 1421–1426, 2014.

[20] S. Zhang, P. Audebert, Y. Wei, A. Al Choueiry, G. Lanty, A. Bréhier, L. Galmiche, G. Clavier, C. Boissière, J.-S. Lauret, and E. Deleporte, "Preparations and characterizations of luminescent two dimensional organic-inorganic perovskite semiconductors," *Materials*, vol. 3, no. 5, pp. 3385–3406, 2010.

[21] M. Saliba, K. W. Tan, H. Sai, D. T. Moore, T. Scott, W. Zhang, L. A. Estroff, U. Wiesner, and H. J. Snaith, "The influence of thermal processing protocol upon the crystallization and photovoltaic performance of organic-inorganic lead trihalide perovskites," *The Journal of Physical Chemistry C*, 2014.

[22] K. W. Tan, D. T. Moore, M. Saliba, H. Sai, L. A. Estroff, T. Hanrath, H. J. Snaith, and U. Wiesner, "Thermally induced structural evolution and performance of mesoporous block copolymer-directed alumina perovskite solar cells," *ACS Nano*, vol. 0, no. ja, p. null, 2014.

[23] M. Liu, M. B. Johnston, and H. J. Snaith, "Efficient planar heterojunction perovskite solar cells by vapour deposition," *Nature*, vol. 501, pp. 395–398, Sept. 2013.

[24] J. Burschka, N. Pellet, S.-J. Moon, R. Humphry-Baker, P. Gao, M. K. Nazeeruddin, and M. Gratzel, "Sequential deposition as a route to high-performance perovskite-sensitized solar cells," *Nature*, vol. 499, pp. 316–319, July 2013.

[25] B. Conings, L. Baeten, C. De Dobbelaere, J. D'Haen, J. Manca, and H.-G. Boyen, "Perovskite-based hybrid solar cells exceeding 10reproducibility using a thin film sandwich approach," *Advanced Materials*, vol. 26, no. 13, pp. 2041–2046, 2014.

[26] Q. Chen, H. Zhou, Z. Hong, S. Luo, H.-S. Duan, H.-H. Wang, Y. Liu, G. Li, and Y. Yang, "Planar heterojunction perovskite solar cells via vapor-assisted solution process," *Journal of the American Chemical Society*, vol. 136, no. 2, pp. 622–625, 2014.

[27] D. G. Billing and A. Lemmerer, "Synthesis, characterization and phase transitions in the inorganic–organic layered perovskite-type hybrids $[(C_nH_{2n+1}NH_3)_2PbI_4]$, *n* = 4, 5 and 6," *Acta Crystallographica Section B*, vol. 63, pp. 735–747, Oct 2007.

[28] A. Lemmerer and D. G. Billing, "Synthesis, characterization and phase transitions of the inorganic-organic layered perovskite-type hybrids $[(C_nH_{2n+1}NH_3)_2PbI_4]$, n = 7, 8, 9 and 10," *Dalton Trans.*, vol. 41, pp. 1146–1157, 2012.

[29] N. A. Gippius, E. A. Muljarov, S. G. Tikhodeev, T. Ishihara, and L. V. Keldysh, "Dielectrically confined excitons and polaritons in natural superlattices -perovskite lead iodide semiconductors," *MRS Proceedings*, vol. 328, 1 1993.

[30] D. B. Mitzi, "Synthesis, crystal structure, and optical and thermal properties of $(C_4H_9NH_3)_2MI_4$ (M = Ge, Sn, Pb)," *Chemistry of Materials*, vol. 8, no. 3, pp. 791–800, 1996.

[31] S. J. Jung, R.-Z. Yin, E. J. Oh, U.-I. Cho, K. H. Kim, and C. H. Yo, "Synthesis and characteristics of the organic layered structure material of $(C_4H_9NH_3)_2Fe_xPb_{1-x}Cl_4$," *Bulletin-Korean Chemical Society*, vol. 22, no. 7, pp. 703–708, 2001.

[32] Y. Takeoka, K. Asai, M. Rikukawa, and K. Sanui, "Systematic Studies on Chain Lengths, Halide Species, and Well Thicknesses for Lead Halide Layered Perovskite Thin Films," *Bulletin of the Chemical Society of Japan*, vol. 79, no. 10, pp. 1607–1613, 2006.

[33] T. Ishihara, X. Hong, J. Ding, and A. Nurmikko, "Dielectric confinement effect for exciton and biexciton states in PbI_4-based two-dimensional semiconductor structures," *Surface Science*, vol. 267, no. 1–3, pp. 323 – 326, 1992.

[34] M. Szafranski, "Investigation of phase instabilities in guanidinium halogenoplumbates(ii)," *Thermochimica Acta*, vol. 307, no. 2, pp. 177 – 183, 1997.

[35] M. Szafranski and K. Stahl, "Crystal structure and phase transitions in perovskite-like $C(NH_2)_3SnCl_3$," *Journal of Solid State Chemistry*, vol. 180, pp. 2209–2215, Aug. 2007.

[36] M. Szafranski and M. Jarek, "Origin of spontaneous polarization and reconstructive phase transition in guanidinium iodide," *CrystEngComm*, vol. 15, no. 23, p. 4617, 2013.

[37] M. Szafranski, "Ferroelectricity in the guanidinium compound $[C(NH_2)_3]_4Cl_2SO_4$: Synthesis and characterization," *Physical Review B*, vol. 72, p. 054122, Aug. 2005.

[38] S. Kashiwamura and N. Kitazawa, "Thin films of microcrystalline $(CH_3NH_3)(C_6H_5C_2H_4NH_3)_2)Pb_2Br_7$ and related compounds: fabrication and optical properties," *Synthetic Metals*, vol. 96, no. 2, pp. 133–136, 1998.

[39] K. Liang, D. B. Mitzi, and M. T. Prikas, "Synthesis and Characterization of Organic-Inorganic Perovskite Thin Films Prepared Using a Versatile Two-Step Dipping Technique," *Chemistry of Materials*, vol. 10, pp. 403–411, Jan. 1998.

[40] K. Gauthron, J.-S. Lauret, L. Doyennette, G. Lanty, a. Al Choueiry, S. J. Zhang, a. Brehier, L. Largeau, O. Mauguin, J. Bloch, and E. Deleporte, "Optical spectroscopy of two-dimensional layered $(C_6H_5C_2H_4\text{-}NH_3)_2\text{-}PbI_4$ perovskite.," *Optics express*, vol. 18, pp. 5912–9, Mar. 2010.

[41] Y. Tabuchi, K. Asai, M. Rikukawa, K. Sanui, and K. Ishigure, "Preparation and characterization of natural lower dimensional layered perovskite-type compounds," *Journal of Physics and Chemistry of Solids*, vol. 61, pp. 837–845, June 2000.

[42] G. E. Eperon, V. M. Burlakov, P. Docampo, A. Goriely, and H. J. Snaith, "Morphological Control for High Performance, Solution-Processed Planar Heterojunction Perovskite Solar Cells," *Advanced Functional Materials*, vol. 24, no. 1, pp. 151–157, 2014.

APPENDIX A

Synthesis Protocols, Fitting Parameters, and Mie Theory

A.1 Synthesis Protocols

A.1.1 TiO_2 nanoparticle synthesis

A 16 g batch of TiO_2 NPs with ~25 nm diameter was synthesized as follows.
First, 2.4 g of acetic acid was added slowly (~15 min) and dropwise to a stirring solution of 11.72 g titanium isopropoxide (same material as for the compact layer) and left stirring for an additional 15 min.
Second, the solution was added slowly into 58 ml of stirring MQ water and left stirring for 60 min. The solution turned white and exhibited aggregation.
Third, peptization was achieved by adding 0.8 ml nitric acid to the stirring solution which was transferred to a conical flask placed in a water bath and then heated to 80°C (~10 min) and left for 60 min after which the heating was turned off. The resulting solution was translucent.
Fourth, the solution was filtered (1 µm filters) with a vacuum pump setup.
Fifth, the solution was distributed in appropriate autoclave containers, sealed tightly and left in an oven at 240°C for 12 h.
Sixth, upon cooling to room temperature the solution was retrieved and 0.48 ml nitric acid was added. Then, in order to have optimal dispersion, an ultrasonic bath was applied followed by exposure to an ultrasonic horn for 3 min (20% strength, 2 s on, 2 s off).
Seventh, the solution was washed by centrifugation at 6000 rpm for 60 min. The excess solvent was pipetted out and refilled with MQ water. The ultrasonic horn was used for dispersion. This procedure was repeated 3 times. Then, another 3 centrifugations followed in the same way, only this time the solvent was replaced by ethanol.

A.1.2 SiO_2 nanoparticle synthesis

The chemicals were purchased from Sigma-Aldrich, i.e. tetraethyl orthosilicate (TEOS) (98%), and ammonium hydroxide solution (Sigma-Aldrich, 31.5% in water). Appropriate amounts of DI water, ethanol, and ammonia (see below) were mixed in a flask and left stirring with a magnetic bar for ~5 min. Then, TEOS was added quickly and the solution was left for 12 h to react. The product was washed 3 times by centrifugation and subsequent solvent exchange with ethanol.

Table A.1 lists the the quantities used for a 100 ml solution of SiO_2 nanoparticles of 20,40,80, and 150 nm diameter.

Table A.1 Quantities used for a 100 ml solution of SiO_2 nanoparticles of 20,40,80, and 150 nm diameter.

SiO_2 diameter (nm)	H_2O (ml)	NH_3 (ml)	Ethanol (ml)	TEOS (ml)
20	5.40	3.38	91.08	0.14
40	5.40	3.38	90.67	0.55
80	5.40	3.38	89.03	2.19
150	5.40	3.38	83.52	7.70

A.1.3 Core-Shell Nanoparticle Synthesis

In this section the synthesis of core-shell $Au@SiO_2$ and $Ag@TiO_2$ nanoparticles is presented. The protocols were originally developed and optimized by Yao Sun of Cornell University.

$Au@SiO_2$ Nanoparticles

Bare Au Nanoparticles

The synthesis procedure for 15, 30, 80, and 150 nm Au NPs was adapted from [1–3].
Gold nanoparticles of 15 nm diameter were grown as follows. 52.5 ml of a 0.01 wt% (w/V) solution of chloroauric acid ($HAuCl_4$ x $3H_2O$, Sigma-Aldrich) solubilized in MQ water was prepared followed by heating to 100°C while stirring. Upon reaching the boiling point 2 ml of 1 wt% of sodium citrate (in water) and 2 ml of a 0.05 wt% (in water) of citric acid were quickly added. The solution exhibited a deep red colour indicating the successful formation of the nanoparticles.
Larger nanoparticles of 30 nm diameter were grown by using the previous solution as seed. 3 ml of 15 nm Au NP solution were taken and topped up with MQ water to reach 20 ml.

(A) 2 ml of a 0.2 wt% chloroauric acid solution was diluted with MQ water to reach 10 ml.

(B) A mixture of 0.5 ml 1 wt% ascorbic acid solution and 0.25 ml 1 wt% sodium citrate solution was diluted with MQ water to reach 10 ml.

(A) and (B) were added to the previously prepared seed solution which was kept stirring. The addition had to occur slowly and separately, ideally dropwise with sufficient delay (~3 min) between drops to ensure good mixing so that the whole procedure took up to 40 min.

The solution was then heated until boiling and left boiling for 30 min after which the hot plate was switched off to allow for cooling to room temperature. A colour change occurred towards a more rose coloured tone.

Au NPs of 80 nm diameter were grown by using 4.5 ml of 30 nm NP seed, diluted with MQ water to reach 20 ml. For the rest of the procedure, the previous protocol for the 30 nm Au NPs was followed to the letter. A colour change towards orange occured.

150 nm Au NPs were grown by using 20 ml of 80 nm seed. The same protocol as for the 30 nm Au NPs was followed with the following adjustment. For solution (A), 8 ml (instead of 2 ml) of 0.2 wt% chloroauric acid solution was used.

SiO_2 Shell

A SiO_2 shell was deposited on the gold nanoparticles from the previous section. The main protocols in this work involved shells for 80 and 100 nm gold core diameters. At first, 25.6 g ml^{-1} polyvinylpyrrolidone, average mol wt 40000 (PVP-40) (Sigma-Aldrich) dissolved in MQ water was prepared. 0.25 ml of the PVP-40 solution was added to 10 ml of the 80 nm Au NP seed and stirred for 24 h. Afterwards, centrifugation at 4000 rpm for 10 min was applied, the excess supernatant was pipetted out, and 2 ml of an ammonium solution (0.21 ml of 20-23% stock solution (Sigma-Aldrich) mixed with 5 ml ethanol) was added. The solution was transferred to vials and kept stirring.

Then, 6 µl of 10 vol% TEOS diluted in ethanol was added and left stirring for 12 h. Final cleaning was done with centrifugation at 4000 rpm and dispersion in ethanol.

The SiO_2 shell for the 150 nm Au NPs followed the same procedure with slight adjustments in quantities: 0.5 ml of PVP-40 and 13.75 µl of TEOS.

$Ag@TiO_2$ nanoparticles

The synthesis of 40 nm diameter silver nanoparticles with a 2 nm titania shell is introduced.

Bare Ag Nanoparticles

Silver nanoparticles with 40 nm diameter were synthesized by adding 1 g polyvinylpyrrolidone, average mol wt 10000 (PVP-10) (Sigma-Aldrich) to 50 ml ethylene glycol which is kept stirring until full dissolution. 34 mg silver nitrate ($AgNO_3$) was added.

The solution was heated incrementally over 1 h from 27-120°C, held at 120°C for an additional 1 h, and then left to cool to room temperature.

As a next step, 400 ml of acetone was added, the solution was centrifuged at 3000 rpm for 30 min, the supernatant removed, and the final product redispersed in 60 ml ethanol. An additional centrifugation at 3000 rpm for 1.5 h was applied and the supernatant removed.

This was followed by redispersion in a mixture of 31.5 ml ethanol and 4.5 ml ammonia solution which subsequently was stirred and ultrasonicated for 30 min.

TiO_2 Shell

The TiO_2 shell was grown by adding titanium isopropoxide (TPO) (24 µl in 4ml ethanol) to 40 ml of the above solution of Ag NPs which was left to stir vigorously. Afterwards, moderate stirring was continued for 12 h in the dark. Final cleaning was conducted by centrifugation at 3000 rpm for 1 h, pipetting out the supernatant, and redispersion in 20 ml ethanol.

A.1.4 Mesoporous block copolymer-directed alumina (MBCP-Al_2O_3) and titania (MBCP-TiO_2) films

The MBCP samples in this thesis were prepared by Kwan W. Tan of Cornell University.

All materials were used as received. Anhydrous grades of toluene,*n*-butanol, tetrahydrofuran, chloroform, N,N-dimethylformamide (DMF) and terpineol, 97% aluminum tri-*sec*-butoxide, >97% titanium isopropoxide, 20 wt% aluminum oxide nanoparticles in isopropanol (<50 nm, product number 702129), 57 wt% hydroiodic acid in water, 33 wt% methylamine solution in ethanol, and lead chloride were obtained from Sigma-Aldrich. 70% nitric acid and 37% hydrochloric acid were obtained from Mallinckrodt Baker and EMD Millipore, respectively. 10 cP and 46 cP ethyl cellulose were obtained from TCI America.

MBCP-Al_2O_3 thin films were prepared using 50 mg of poly(isoprene)-*block*-poly(styrene)-*block*-poly(ethylene oxide) (ISO, $M_n = 38.3\,\mathrm{kg\,mol^{-1}}$, with a polydispersity index of 1.07 containing 68.4 wt% PI and 18.0 wt% PS) dissolved in 500 mg of toluene and *n*-butanol solvent mixture (1:1, w/w). In a separate vial, 104 mg of 97% aluminum tri-*sec*-butoxide, 478 mg of *n*-butanol and 478 mg of toluene were added sequentially. The white cloudy suspension was left undisturbed for 15 min, followed by vigorous stirring for 30 min to allow homogenization. 55 µl of 70% nitric acid was added and the mixture was stirred overnight (>12 h). The transparent alumina sol was added into the ISO solution and stirred for 45 min. The ISO-Al_2O_3 solution was processed by spin coating on silicon at 2000 rpm (45 s) in a nitrogen drybox. The MBCP-Al_2O_3 hybrid thin films were baked at 50°C (2 h), 100°C (2 h), and 130°C (2 h) sequentially in the drybox and calcined at 450°C (3 h) with a ramp rate of 1 °C/ min. From scanning electron microscopy, the BCP-Al_2O_3 thin film thickness was 70-80 nm.

MBCP-TiO_2 thin films were prepared using a modified method as described elsewhere [4]. Briefly, 50 mg of ISO was dissolved in 1.35 g of tetrahydrofuran and chloroform solvent

mixture (4:5, w/w). In a separate vial, 53.9 µl of >97% titanium isopropoxide, 16.8 µl of 37% HCl acid, and 216 ml of tetrahydrofuran were mixed and stirred vigorously. The yellow coloured titania sol was added into the ISO solution and stirred for 45 min. The ISO-TiO_2 solution was processed by spin coating on silicon at 2000 rpm (45 s) in the drybox. The MBCP-TiO_2 hybrid thin films were baked at 50°C (2 h), 100°C (2 h), and calcined at 450°C (3 h) with a ramp rate of 1 °C/min.

A.2 Drude-Lorentz and Critical Point Analysis Fitting Parameters

The best fit parameters were calculated in my previous work [5].

Table A.2 Drude-Lorentz parameters gold as calculated in my previous work [5].

ε_∞	=	3.679	
$\omega_{p,D}$	=	8.841	eV
$\omega_{p,L}$	=	9.206	eV
ω_0	=	4.191	eV
γ_D	=	0.053	eV
γ_L	=	3.550	eV

Table A.2 are the best fit parameters for equation 3.17

$$\varepsilon = \varepsilon_\infty - \frac{\omega_{p,D}^2}{\omega^2 + i\omega\gamma_D} + \frac{\omega_{p,L}^2}{\omega_0^2 - \omega^2 - i\omega\gamma_L}$$

Table A.3 Critical point parameters for gold as calculated in my previous work [5].

ε_∞	=	1.730	
$\omega_{p,D}$	=	8.782	eV
$\omega_{p,1}$	=	12.681	eV
$\omega_{p,2}$	=	0.737	eV
$\omega_{0,1}$	=	2.470	eV
$\omega_{0,2}$	=	3.550	eV
γ_D	=	0.090	eV
γ_1	=	1.881	eV
γ_2	=	0.303	eV
Φ_1	=	-1.042	rad
Φ_2	=	-1.745	rad

Table A.3 are the best fit parameters for eq. 3.18

$$\varepsilon_{Au} = \varepsilon_\infty - \frac{\omega_{p,D}^2}{\omega^2 + i\omega\gamma_D} + \frac{\omega_{p,1}\exp(i\Phi_1)}{\omega_{0,1} - \omega - i\gamma_1} + \frac{\omega_{p,2}\exp(i\Phi_2)}{\omega_{0,2} - \omega - i\gamma_2}$$

A.3 Mie Theory

In 1908 Gustav Mie developed a formalism to solve the Maxwell equations for spherical particles under plane wave illumination [6]. Here only a summary of the results is given for the case of isotropic, linear, and homogeneous media following the book by Bohren and Huffman [7] where the detailed calculations can be found. Under such conditions the Maxwell equations 3.1 can be rewritten as electromagnetic wave equations, also known as the Helmholtz equations

$$(\nabla^2 + k^2)\mathbf{H} = 0 \qquad \text{(A.1a)} \qquad\qquad (\nabla^2 + k^2)\mathbf{E} = 0 \qquad \text{(A.1b)}$$

with $k^2 = \omega^2 \tilde{\varepsilon}\mu$

Finding a solution to this starts with writing the scalar wave equation $(\nabla^2 + k^2)\Psi = 0$ in spherical polar coordinates

$$\left(\frac{1}{r^2}\frac{\partial}{\partial r}\left(r^2\frac{\partial}{\partial r}\right) + \frac{1}{r^2\sin(\theta)}\frac{\partial}{\partial\theta}\left(\sin(\theta)\frac{\partial}{\partial\theta}\right) + \frac{1}{r^2\sin(\theta)}\frac{\partial^2}{\partial\phi^2} + k^2\right)\Psi = 0 \qquad \text{(A.2)}$$

A solution can be found by separation of variables with $\Psi(r,\theta,\phi) = R(r)\Theta(\theta)\Phi(\phi)$ resulting in

$$\Psi_{emn} = \cos(m\phi)P_n^m(cos(\theta))z(kr) \qquad \text{(A.3)}$$

where the index 'e' stands for even solutions with $\cos(m\phi)$; 'o'dd solutions are with $\sin(m\phi)$. $P_n^m(cos(\theta))$ are the associated Legendre polynominals. z(kr) are the spherical Bessel functions of the first kind $j_n(kr) = \sqrt{\frac{\pi}{2kr}}J_{n+1/2}(kr)$ (no singularity in the origin), or the second kind $y_n(kr) = \sqrt{\frac{\pi}{2kr}}Y_{n+1/2}(kr)$ (singularity in the origin) with J and Y being the Bessel functions of the first and second kind. Also, linear combinations known as spherical Hankel functions of the first kind $h_n^{(1)}(kr) = j_n(kr) + iy_n(kr)$, and second kind $h_n^{(2)}(kr) = j_n(kr) - iy_n(kr)$ are solutions. Sometimes Hankel functions are also referred to as Bessel functions of the third kind. $j_n(x)$ and $y_n(x)$ can be defined by the recursive relationships $\frac{n}{x}B_n(x) = \frac{1}{2}(B_{n-1}(x) + B_{n+1}(x)) \quad (B = j, y)$ given the starting functions $j_0(x) = \frac{\sin(x)}{x}$, $j_1(x) = \frac{\sin(x)}{x^2} - \frac{\cos(x)}{x}$, and $y_0(x) = -\frac{\cos(x)}{x}$, $y_1(x) = -\frac{\cos(x)}{x^2} - \frac{\sin(x)}{x}$. Additionally, the Ricatti-Bessel functions are defined as $\Psi(x) = xj_n(x)$, and $\xi(x) = xh_n^{(1)}(x)$.

Figure A.1 shows plots of the introduced spherical Bessel functions of the first and second kind.

From these relationships the Helmholtz eq. A.1 can be solved resulting in analytical expressions for the electric and magnetic field.

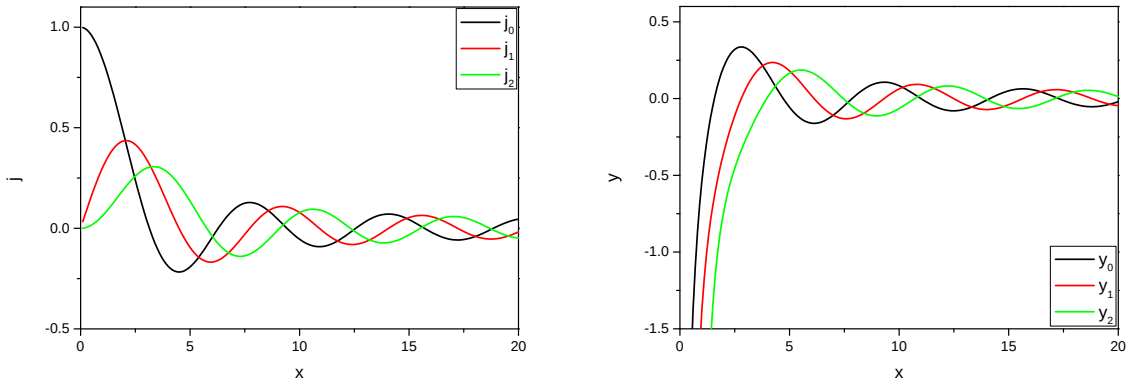

(a) (b)

Fig. A.1 (a) Spherical Bessel functions of the first kind and (b) second kind. Spherical Bessel functions of the second kind exhibit a singularity at the origin.

Furthermore, the scattering and extinction cross sections can be deduced as

$$C_{sca} = \frac{2\pi}{k^2}\sum_{n=1}^{\infty}(2n+1)(|a_n|^2+|b_n|^2) \tag{A.4}$$

$$C_{ext} = \frac{2\pi}{k^2}\sum_{n=1}^{\infty}(2n+1)Re(a_n+b_n) \tag{A.5}$$

with

$$a_n = \frac{m\Psi_n(mx)\Psi_n'(mx)-\Psi_n(x)\Psi_n'(mx)}{m\Psi_n(mx)\xi_n'(mx)-\xi_n(x)\Psi_n'(mx)} \tag{A.6}$$

$$b_n = \frac{\Psi_n(mx)\Psi_n'(x)-m\Psi_n(x)\Psi_n'(mx)}{\Psi_n(mx)\xi_n'(x)-m\xi_n(x)\Psi_n'(mx)} \tag{A.7}$$

where $m = \frac{n_{sphere}}{n_{medium}}$ is the relative index of refraction and $x = kr_{sphere} = \frac{2\pi n_{medium} r_{sphere}}{\lambda}$ is the size parameter .

Quasistatic Approximation

For nanoparticles much smaller than the wavelength of the incoming light the quasistatic approximation ($d << \lambda$) can be used. The excitation field now can be assumed to be spatially homogeneous over the whole object which translates into assuming $kr << 1$. With this it can be shown that the polarizability α is [7, 8]

$$\alpha = 4\pi r^3 \frac{\epsilon - \epsilon_{medium}}{\epsilon + 2\epsilon_{medium}} \tag{A.8}$$

Clearly, α maximizes when $|\epsilon + 2\epsilon_{medium} = 0|$ which is consistent with the Clausius-Mossotti relation. This is known as the Fröhlich condition $Re(\epsilon(\omega)) = -2\epsilon_{medium}$ (for a dielectric medium) and the associated mode is the dipole surface mode.

References

[1] W. Zhang, M. Saliba, S. D. Stranks, Y. Sun, X. Shi, U. Wiesner, and H. J. Snaith, "Enhancement of perovskite-based solar cells employing core-shell metal nanoparticles," *Nano Letters*, vol. 13, no. 9, pp. 4505–10, 2013. 23947387.

[2] C. Ziegler and A. Eychmuller, "Seeded growth synthesis of uniform gold nanoparticles with diameters of 15-300 nm," *Journal of Physical Chemistry C*, vol. 115, no. 11, pp. 4502–4506, 2011.

[3] C. Graf, D. L. J. Vossen, A. Imhof, and A. van Blaaderen, "A general method to coat colloidal particles with silica," *Langmuir*, vol. 19, no. 17, pp. 6693–6700, 2003.

[4] P. Docampo, M. Stefik, S. Guldin, R. Gunning, N. A. Yufa, N. Cai, P. Wang, U. Steiner, U. Wiesner, and H. J. Snaith, "Triblock-terpolymer-directed self-assembly of mesoporous TiO_2: High-performance photoanodes for solid-state dye-sensitized solar cells," *Advanced Energy Materials*, vol. 2, no. 6, pp. 676–682, 2012.

[5] M. Saliba, *Numerical Simulations of Near and Far Field Scattering Processes in Plasmonic Nanostructures (Diplomarbeit).* Stuttgart: Max Planck Institute for Solid State Research, 2009.

[6] G. Mie, "Beiträge zur Optik trüber Medien, speziell kolloidaler Metallösungen," *Annalen der Physik*, vol. 330, pp. 377–445, JAN 1908.

[7] C. F. Bohren and D. R. Huffman, *Absorption and Scattering of Light by Small Particles.* Wiley-VCH, 1983.

[8] J. Jackson, *Classical Electrodynamics.* 2 ed. New York Wiley, 1975.

APPENDIX B

Publications and Conferences

Publications

Bold: First author.
Underlined: co-author

10) **M. Saliba**, and H. J. Snaith, *Characterisation of Highly Excitonic Layered Perovskite Materials for Solar Cell and LED applications*, (in preparation)

9) **M. Saliba**, W. Zhang, S. D. Stranks, Y. Sun, J. M. Ball, M. B. Johnston, U. Wiesner, H. J. Snaith, *Plasmonic Core-Shell Silver-TiO_2 Nanoparticles in Low Temperature Processed Perovskite Solar Cells*, (in preparation)

8) A. Abate, M. Saliba, D. J. Hollman, S. D. Stranks, G. Grancini, A. Petrozza, and H. J. Snaith, *Enhanced organometal-halide perovskite solar cells via supramolecular halogen bond passivation*, Nano Letters (2014)

7) K. W. Tan*, D. T. Moore*, **M. Saliba***, H. Sai, L. A. Estroff, T. Hanrath, H. J. Snaith, and U. Wiesner, *Thermally induced structural evolution and performance of mesoporous block copolymer-directed alumina perovskite solar cells*, ACS Nano (2014)

6) **M. Saliba**, K. W. Tan, H. Sai, D. T. Moore, T. Scott, W. Zhang, L. A. Estroff, U. Wiesner, and H. J. Snaith, *The Influence of Thermal Processing Protocol Upon the Crystallization and Photovoltaic Performance of Organometal Trihalide Perovskites*, The Journal of Physical Chemistry C (2014)

5) K. Wojciechowski, M. Saliba, T. Leijtens, A. Abate and H. J. Snaith, *Sub 150 ˚C Processed Meso-superstructured Perovskite Solar Cells with Enhanced Efficiency*, Energy & Environment Science (2013)

4) J. T.-W. Wang, J. M. Ball, E. M. Barea, A. Abate, J. A. Alexander-Webber, J. Huang, M. Saliba, I. Mora-Sero, J. Bisquert, H. J. Snaith, and R. J. Nicholas, *Low-Temperature Processed Electron Collection Layers of Graphene/TiO2 Nanocomposites in Thin Film Perovskite Solar Cells*, Nano Letters (2013)

3) W. Zhang*, **M. Saliba***, S. D. Stranks, Y. Sun, X. Shi, U. Wiesner, and H. J. Snaith, *Enhancement of Perovskite-Based Solar Cells Employing Core-Shell Metal Nanoparticles*, Nano Letters (2013)

2) M. Hentschel, M. Saliba, R. Vogelgesang, H. Giessen, A. P. Alivisatos, and N. Liu, *Transition from Isolated to Collective Modes in Plasmonic Oligomers*, Nano Letters (2010)

1) M. Mäder, T. Höche, J. W. Gerlach, S. Perlt, J. Dorfmüller, M. Saliba, R. Vogelgesang, K. Kern, and B. Rauschenbach, *Plasmonic activity of large-area gold-nanodot arrays on arbitrary substrates*, Nano Letters (2009)

∗ equal contribution

Conferences and Talks

2014 *Film Formation in Perovskite Solar Cells*, International Conference of Solution Processed Semiconductor Solar Cells, Oxford (poster)

2014 *Enhancement of Perovskite-Based Solar Cells Employing Core-Shell Metal Nanoparticles*, SPIE Optics + Photonics, San Diego (talk)

2014 *Enhancement of Perovskite-Based Solar Cells Employing Core-Shell Metal Nanoparticles*, Ultrafast Nano-Optics, Universität Oldenburg (invited talk)

2014 *The Influence of Thermal Processing Protocol upon the Crystallization and Photovoltaic Performance of Organometal Trihalide Perovskites*, HOPV, Lausanne (oral)

2014 *Plasmonic Enhancement and Thin-film Formation Perovskite Solar Cells*, Helmholtz-Zentrum Berlin, Berlin (invited talk)

2013 *Development and Progress of Perovskite Solar Cells*, 4. Physikalisches Institut, Universität Stuttgart (invited talk)

2013 *Enhancement of Perovskite-Based Solar Cells Employing Core-Shell Metal Nanoparticles*, European Conference on Molecular Electronics, London (poster)

2012 *Plasmonic Light Management in Solid-state Solar Cells*, MRS, San Francisco (poster)

2011 *Plasmonic Dye Sensitized Solar Cells,* Organic Electronics and Applications Summer School, Crete (oral)

Honours and Awards

2012-2013 Light Senior Scholar, St Catherine's College, Oxford

2010 Best Diploma Thesis by Kano Suryoyo

2007-2010 Heinrich Böll scholarship

2007 DAAD scholarship

2007 Baden-Württemberg scholarship

2003 e-fellows.net scholarship for excellent Abitur results

APPENDIX C

Posters

Plasmonic Light Management in Solid-state Solar Cells

Michael Saliba*[1], Wei Zhang[1], Yao Sun[2], Xian Shi[2], Yan Francescato[3], Stefan Alexander Maier[3], Ulrich Wiesner[2], Henry James Snaith[1]
* M.Saliba1@physics.ox.ac.uk
[1]University of Oxford | [2]Cornell University | [3]Imperial College London

Plasmonics

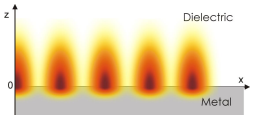

Figure 1a *Surface plasmon propagating parallel to a metal-dielectric interface.*

- *Plasmon*: quasiparticle describing quantization of plasma oscillation
- *Surface plasmon*: electromagnetic wave traveling along metal-dielectric interface
- *plasmon resonance mode*: light coupling to a surface plasmon

Metallic nanoparticles (NPs) show plasmonic modes which can be fine-tuned by the geometry or material of the NPs. This can increase the pathlength of incoming light or assist electron-hole splitting. [1]

Solid-state Solar Cell

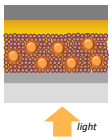

Fig. 1b *Schematics of a solid-state solar cell (SSSC)*

- incoming light reaches photoactive area and creates electron-hole pair
- electron transfers through perovskite and mesoporous titania
- hole transfers to hole transporter

SSSCs have (often) limited thickness because the solid-state hole transporter does not fully penetrate the titania structure. This means incoming light passes through the solar cell without being used. [2]

Gold Nanoparticle Characterisation

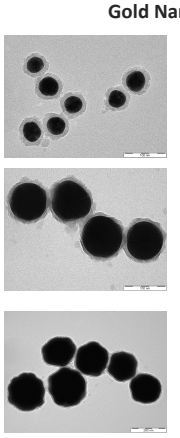

Fig. 3a *(left) TEM image of a 40nm gold NP with a 10nm silica shell. (right) Cross section simulation in water compared to experiment. A plasmonic dipole mode appears at 532nm.*

Fig. 3b. *(l) TEM image. (r) Cross section simulation of a 100nm gold NP with a 10nm silica shell in water compared to experiment. Note how the dipole mode red-shifts to 576nm with increasing size as expected from fig. 2b.*

Fig. 3c *(l) TEM image. (r) Cross section simulation of a 150nm gold NP with a 10nm silica shell in water. The dipole mode red-shifts further to 615nm and additionally a quadrupole mode starts forming at 540nm.*

Simulations: Multiple Multipole Method (MMP)

$$\text{field} = \sum_k A_k \cdot \text{basis}_k + \text{error}$$

- Use solutions of Maxwell's equations: plane waves, **Bessel**, **Hankel** functions,...
- MMP: terminated series of multipoles at multiple locations

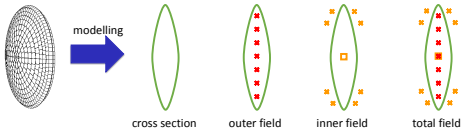

- Surface elements have to follow Maxwell boundary conditions
- Optimize A_k by minimizing *error* in boundaries [3]

Simulation Results for Spheres

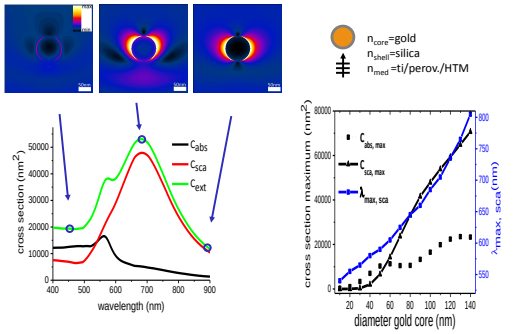

Fig. 2a. *Cross sections and em fields of a 100nm gold core with a 10nm silica shell*

Fig. 2b. *(left) Maximum cross section over gold core diameter. (right) Peak wavelength for maximum scattering cross section.*

Results

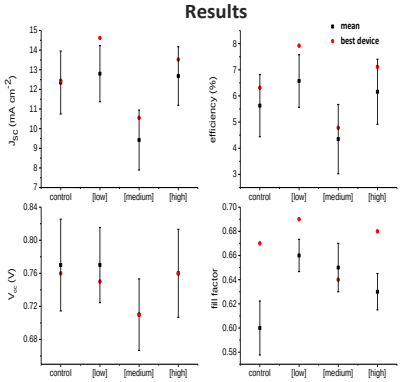

Fig. 4a *Solar cell parameters of different concentrations of Au NPs blend with titania*

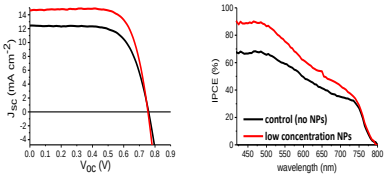

Fig. 4b *(left) JV curves of best devices. (right) Corresponding external quantum efficiency*

Acknowledgment and References

We thank the European Commission and EPSRC for financial support.

[1] *C. F. Bohren and D. R. Huffman,* Absorption and Scattering of Light by Small Particles, *Wiley-VCH (1983)*
[2] *M. M. Lee, J. Teuscher, T. Miyasaka, T. N. Murakami, and H. J. Snaith,* Efficient Hybrid Solar Cells Based on Meso-Superstructured Organometal Halide Perovskites, *Science (2012)*
[3] *M. Hentschel, M. Saliba, R. Vogelgesang, H. Giessen, A. P. Alivisatos, N. Liu,* Transition from isolated to collective modes in plasmonic oligomers, *Nano Letters (2010)*

Fig. C.1 Poster at Spring MRS, San Francisco (2012)

Enhancement of Perovskite Solar Cells Employing Core-shell Metal Nanoparticles

Michael Saliba*[1], Wei Zhang[1], Samuel D Stranks[1], Yao Sun[2], Xian Shi[2], Ulrich Wiesner[2], Henry J Snaith[1]
*M.Saliba1@physics.ox.ac.uk
[1]University of Oxford | [2]Cornell University

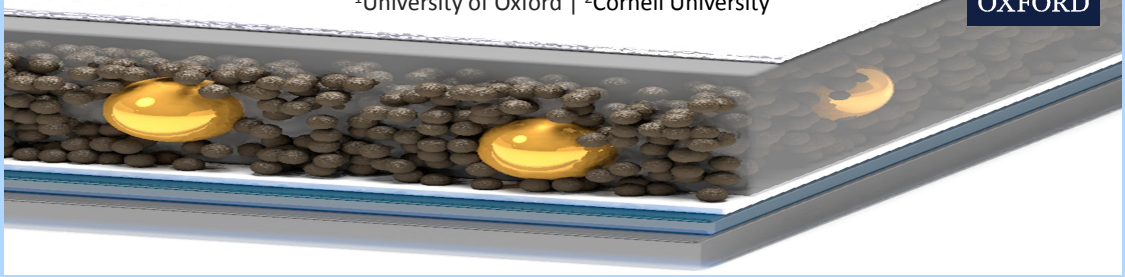

Motivation

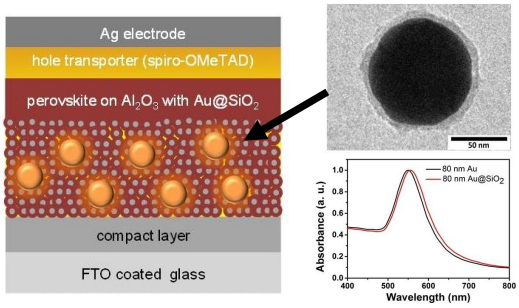

Meso-superstructured perovskite solar cell[2]

- incoming light hits photoactive area and creates electron-hole pair
- electron transfers through perovskite
- hole transfers to hole transporter

Core-Shell metal nanoparticle

- gold-silica nanoparticles
- 80nm core with 8nm shell
- absorption peak at 550nm

Optical measurements and IPCE

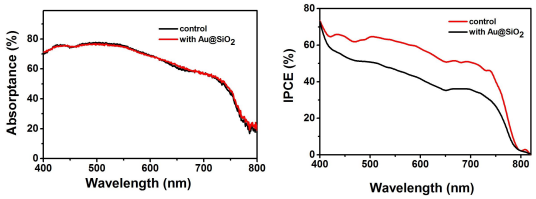

- No obvious absorptance differences between control and Au@SiO_2idevices
- Broad enhancement in IPCE spectrum with no specific sharp peak

Photoluminescence data

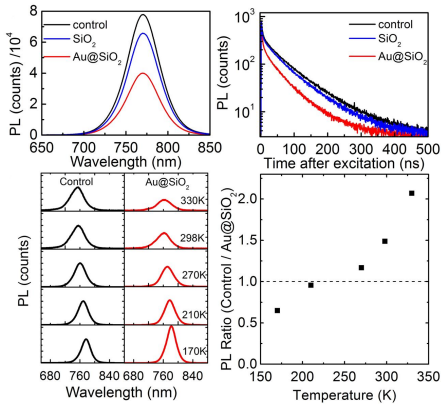

- PL quenching in presence of Au@SiO_2 NPs at room temperature
- Quenching reduced (and even reverted) with decreasing temperature
- Only slight change for pure SiO_2 NPs
- In general, integrated PL decreases with temperature (not shown)

Exciton binding energy (E_{bx}) fitted with an Arrhenius-like equation[3]

$$PL \sim e^{-E_{bx}/(k_b T)}$$

E_{bx} (control) = 98meV
E_{bx} (Au@SiO_2) = 35meV

Device data

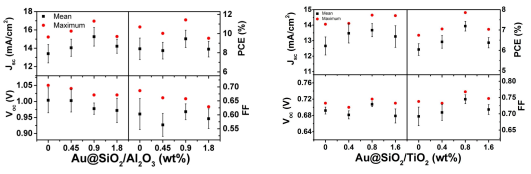

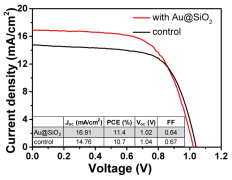

- Overall improvement for Al_2O_3 and TiO_2 mesostructure
- Mainly J_{sc} increase from 14.8 to 16.9 mA/cm²
- Pure silica particles w/out effect.
- 48 devices per parameter

Acknowledgment and References

We thank the European Commission and EPSRC for financial support.

[1] *M. Saliba, W. Zhang, S. D. Stranks, Y. Sun, X. Shi, U. Wiesner, and H. J. Snaith,* Enhancement of Perovskite-Based Solar Cells Employing Core–Shell Metal Nanoparticles, *Nano Letters (2013)*
[2] *M. M. Lee, J. Teuscher, T. Miyasaka, T. N. Murakami, and H. J. Snaith,* Efficient Hybrid Solar Cells Based on Meso-Superstructured Organometal Halide Perovskites, *Science (2012)*
[3] *Z. Chen, C. Yua, K. Shum, J. J. Wang, W. Pfenninger, N. Vockic, J. Midgley, J. T. Kenney,* Photoluminescence study of polycrystalline CsSnI3 thin films: Determination of exciton binding energy, *Journal of Luminescence (2012)*

Outlook

Reduced exciton binding energy leads to more charge generation. Plasmonic heating (local heating in direct vicinity of the NPs)

Further investigation for the precise mechanism is needed, entailing:
- Precise charge dynamics in this (largely uninvestigated) perovskite
- Plasmonic heating (local heating in vicinity of the NPs)
- Exciton-plasmon coupling

Fig. C.2 Poster at European Conference on Molecular Electronics, London (2013)